Lecture Notes

Plasma Interface Physics

Summer Semester 2021

Ruhr-UniversitÃ¤t Bochum

Prof. A. von Keudell

September 9, 2026

Preface

These notes are based on the lecture "Plasma Surface Physics" in the summer semester 2021 and are based on earlier lectures on plasma-surface interaction and layer diagnostics and emerged in 2004/05. As main sources, the books by Liebermann and Lichtenberg (*Principles of Plasma Discharges and Materials Processing*), Zangwill (*Physics at Surfaces*), Venables (*Introduction to Surface and Thin Film Processes*), Barabasi and Stanley (*Fractal Concepts in Surface Growth*) and Nastasi, Mayer, Hirvonen (*Ion Solid Interaction*) were used. The section on vacuum physics is based on Leybold (*Fundamentals of Vacuum Technology*). These notes are not intended to replace these books and are understood as a supplement.

Contents

Chapter 1

Introduction

Reactive plasmas are an essential part of plasma technology. The use of low-temperature plasmas often aims to synthesize a coating from a gaseous compound or to etch a surface. In a plasma discharge, a source gas is dissociated and ionized, and the reaction products are deposited on the surrounding surfaces. The essential advantage of this process is the fact that dissociation already takes place in the gas phase and not only on the surface. In other processes, such as chemical vapor deposition (CVD), the surface to be coated usually has to be hot to initiate the dissociation of the starting molecule. In plasma-enhanced chemical vapor deposition (PCVD), the surface can remain at room temperature. This is an invaluable advantage, as the choice of substrates thus becomes almost arbitrary.

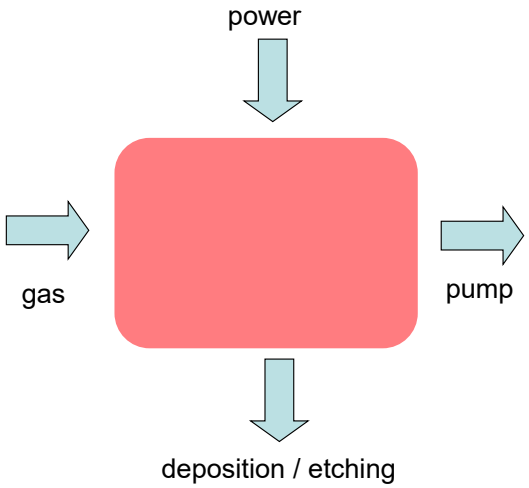

Figure 1.1: Material conversion in reactive plasmas.

The material conversion in reactive plasmas can be schematically written as a balance equation:

$$\frac{dn_x}{dt} = n_e n_g k - \frac{n_x}{\tau} = 0 \tag{1.1}$$

The generation of reactive particles with density n_x essentially occurs through collision reactions of electrons with density n_e with the neutral gas with density n_g with the rate coefficient k. The confinement of the reactive particles in the plasma volume is expressed by a confinement time τ. Thus, the following equilibrium concentration is established:

$$n_x = \underbrace{\tau}_{Reactor}\ \underbrace{n_e}_{Plasma}\ n_g\ \underbrace{k(T_e)}_{Plasma} \tag{1.2}$$

Here, the reactor geometry, the gas flow, and the pumping power determine the residence time of the gas in the reactor. The plasma density is predetermined by the heating power, while the electron temperature depends on the plasma type and the boundary conditions.

If the reactions of the reactive particles among themselves are neglected, the absolute density of a reactive particle n_x is essentially determined by the confinement time τ: if the particles are very reactive, they are lost upon the first wall collision; a high density cannot form in the plasma. Without additional information, one cannot distinguish from the observation of a low density n_x whether the production rate of these particles is low or whether they have a high loss probability upon a wall collision. This contradiction is often overlooked in the literature.

When considering the interface between a plasma and a solid, several established disciplines of physics meet:

- *Plasma Physics:* In plasma physics, the plasma edge layer is described by several models. In these models, the particle flux of ions and neutral particles onto a surface can be predicted in terms of the number of particles and the energies of the particles. However, the boundary condition of the surface for the incident particle flux is often only roughly captured with simple loss probabilities (often 1, i.e. every incident particle is lost).

- *Ion Beam Physics:* There is the very established discipline of ion beam techniques in which the course of a collision cascade of an incident ion in a solid is described. This physics is needed to describe the sputtering of solids as it occurs in accelerators and in nuclear physics in the interaction of high-energy ion beams with a target. The codes and

models are very well developed, but they contain no chemical component. Furthermore, these codes often model processes that only occur on the time scale of a collision cascade from fs to ps. Slower processes such as diffusion are not captured.

- *Surface Physics:* In surface physics, the nature of the interfaces is investigated in great detail. Here, the adsorption of a molecule on a reactive surface (e.g. CO on ruthenium) is often considered. Depending on the temperature and surface structure, different adsorption and dissociation channels result. The consideration of these systems is almost inverse to those in the interaction of a plasma with an interface. In the case of a plasma, the particles are often the reactive reaction partners (e.g. H atoms, SiH_3 radicals), so that the surface itself can initially be inert (e.g. Si crystal). In this sense, one must invest a lot of effort in the preparation of the plasma in a plasma experiment, while in pure surface physics, a lot of effort is invested in the preparation of the surfaces (e.g. preparation of a metal single crystal in ultra-high vacuum at 10^{-12} mbar). The exposure is then very simple by setting a gas pressure of stable molecules as reaction partners; with the impingement rate according to gas kinetics, the flux of reaction partners is automatically set.

However, several difficulties arise in the processes at the plasma-solid interface:

- *Surface establishes itself:* At the plasma-surface interface, the intense particle flux generates a modification of the surface, which settles at a certain equilibrium value. This is the end of the reaction partners for the incident particles. For this reason, the base pressure of an experiment, which is so important for pure surface physics, is not so significant for the consideration of the plasma-surface interaction, since the plasma first creates the exact surface (e.g. the growing film or the etched surface). Therefore, it is also essential to observe these interfaces as in-situ and in real-time as possible. If a surface is analyzed only after plasma exposure, many changes may have already occurred.

- *Heterogeneous processes:* In the processes at the plasma surface, synergies and anti-synergies between the incident particle species can often occur. For example, there is the process of chemical sputtering, in which the simultaneous interaction of ions and reactive neutrals first leads to erosion. i.e. the separate investigation of the ion-solid and the neutral-solid interaction alone will not bring the desired clarification.

- *Complex particle spectra:* A reactive plasma is initially generated from a simple source gas. However, plasma chemistry leads to the formation of a variety of species, all of which can impinge on a surface and react there. The complexity of these surface processes is significantly higher than that of a simple adsorption process of e.g. CO on a metal surface (from the perspective of surface physics, such a reaction is already very complex).

Chapter 2

Surfaces

In the following, some fundamental laws and concepts of surface physics will be introduced. With this knowledge, it is possible to check the plausibility of hypotheses for individual plasma-surface processes. Direct experimental verification is often not possible, as there is usually no precisely defined and well-studied surface physics experiment for these processes. For example, the surface reactions of molecular radicals are decisive for plasma deposition, but there are no precisely defined single-particle experiments for these reactions under ultra-high vacuum conditions.

2.1 Basic Concepts

2.1.1 Coverage

The **coverage** of a surface with a surface density of adsorbed atoms or molecules n_{ads} is generally expressed as:

$$\boxed{\Theta = \frac{n_{ads}}{n_0}} \tag{2.1}$$

Here, it should be noted that the total number of adsorption sites n_0 depends on the system and does not necessarily correspond to the surface density of the surface atoms. n_0 is thus a normalization and often denotes the maximum surface density that can be achieved for an adsorbate.

2.1.2 Sticking Coefficient

The interaction of neutral plasma species can generally be divided into several classes. A particle can chemisorb on the surface, which is characterized

by a probability s, the **sticking coefficient** . As another possibility, the particle can be reflected with probability r or form a new particle that desorbs with probability γ through a reaction with the surface. Together, these probabilities must sum to 1:

$$s + r + \gamma = 1 \tag{2.2}$$

For plasma technological processes, one often wants to determine the probability with which a certain particle species contributes to film growth or film erosion. However, numerous measurement methods only allow the determination of the so-called **surface loss probability** β , which corresponds to the sum

$$\beta = s + \gamma \tag{2.3}$$

i.e. on the basis of a measurement of β, one can only estimate the actually interesting quantity s. These different reaction pathways are illustrated in Fig. 3.1.

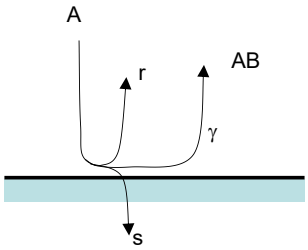

Figure 2.1: The surface reaction can be divided into a fraction for sticking s, reflection r, and surface reaction γ.

2.2 Thermodynamics of Surfaces

2.2.1 Surface Energy and Surface Tension

The simplest description of surfaces is based on thermodynamics. The internal energy in a closed system is given by:

$$U = TS - pV + \mu N \tag{2.4}$$

The change in internal energy as a function of the extrinsic quantities S, V and N is defined as:

$$dU = TdS - pdV + \mu dN \tag{2.5}$$

If a solid is split into two parts, the change in internal energy required for this is the **surface tension** γ multiplied by the newly created surface A. i.e. the change in internal energy by increasing the surface by an amount dA is

$$dU = TdS - pdV + \mu dN + \gamma dA \tag{2.6}$$

However, the surface tension has two contributions:

- **Breaking of individual bonds**

  First, energy must be expended when splitting the solid to break the individual bonds. This energy is referred to as **surface energy** .

- **Segregation in multi-component systems**

  In multi-component systems, phase separation can also occur, as, for example, component A in a system AB accumulates at the surface after splitting. This is referred to as **segregation** of component A. Through this phase separation, component A undergoes a phase transition from a dissolved state within the solid to a dense phase at the surface. With the change per phase i is respectively a term $\mu_i dn_i$ associated.

In summary, the energy that must be expended to split the solid is the surface energy and the change in energy during the phase transition in multi-component systems. Both together are the **surface tension** γ:

$$\underbrace{\gamma dA}_{surfacetension} = \underbrace{f_s dA}_{surfaceenergy} + \underbrace{\sum_i \mu_i dn_i}_{segregation} \tag{2.7}$$

The geometric structure of the surface always tries to adjust itself in such a way that the surface tension is minimized. The condition for this is

$$\oint \gamma dA = \text{minimum} \tag{2.8}$$

The surface tension has the unit [Nm^{-1}]. It corresponds to a force per boundary line of a surface. Each crystal direction is associated with a different surface tension γ. If a crystal is *not* split along preferred directions, many

step edges are created on the surface. At these step edges, more bonds have been broken during the splitting of the crystal compared to a surface without step edges. Therefore, the surface tension γ is very high in the former case due to a large value for f_s (see Fig. 3.2).

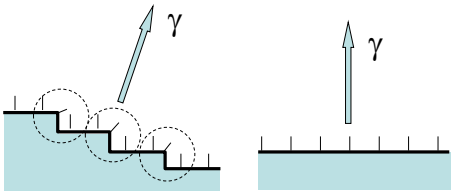

Figure 2.2: The surface tension depends strongly on the plane under which the crystal was split.

The minimization of condition 2.8 can be observed from the external shape of a solid if it is brought close to its melting point. In the experiment, a small droplet of the material to be observed is placed on a heated surface. Due to the high temperature, the individual atoms have sufficient mobility to enable any change in shape of the solid. Without the boundary condition of a crystal, the minimization of the surface would lead to the formation of a sphere, as in a soap bubble or a raindrop. However, in the case of a crystal, many bonds at the surface are not satisfied and a spherical shape is not the energy minimum in the microscopic sense. Therefore, the resulting shape can be determined using the so-called **Wulff plots** , as illustrated in Fig. 3.3: for each crystal direction, a vector is drawn with a length corresponding to the surface tension. Then, planes are constructed with a surface normal corresponding to the γ-vectors. The smallest enclosed volume then also corresponds to the shape of the crystal that is observed in the experiment.

2.2.2 Determination of Surface Tension

The determination of the surface tension on plasma-treated surfaces is often carried out in so-called wetting experiments. The idea of this measurement is to analyze the conditions for the force equilibrium at the boundary line of a droplet on a surface. The so-called contact angle (see Fig. **??**) is set in such a way that the surface tensions at the boundary line droplet-vacuum γ_{DV}, the boundary line surface-vacuum γ_{SV} and at the boundary line surface-droplet γ_{SD} cancel each other out. The curvature of the droplet is observed with a

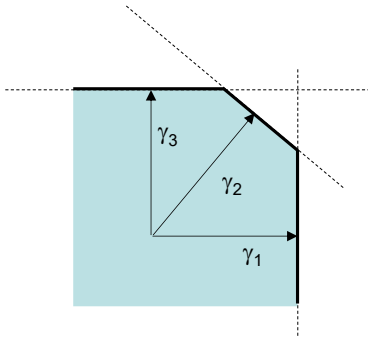

Figure 2.3: Wulff Plot. The surface tension determines the shape of a crystal near the melting point.

suitable microscope and the value for γ_{SV} can be inferred from the contact angle (see Fig. 3.4).

$$\gamma_{SV} = \gamma_{SD} + \gamma_{DV} \cos \Phi \tag{2.9}$$

In many systems of plasma technology, the surface tension is dominated by the surface energy. This surface energy is a measure of the energy that must be expended to break bonds. In non-polar carbon-fluorine compounds, this energy is much lower than in strongly polar oxygen-containing films. Therefore, a very large contact angle is observed in C:F films and the films are usually *hydrophobic, water-repellent*. In oxidized surfaces, the contact angle will be small and the films are usually *hydrophilic, water-attractive*.

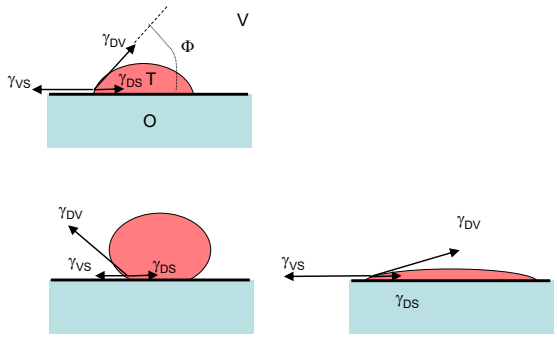

Figure 2.4: The contact angle Φ is essentially determined by the surface tension of the surface/vacuum boundary γ_{SV}.

In plasma technology, the case often occurs that the surfaces can become very rough. The contact angle of these rough surfaces is characterized by the **Wenzel equation** .

$$\cos \Phi^* = r \cos \Phi \tag{2.10}$$

which links the contact angle of the smooth surface Φ with the contact angle Φ^* of the rough surface. i.e., in the experiment on a rough surface, a contact angle of Φ^* is observed, which is different from that of a smooth surface. Since the surface tension is a force per circumference, the influence of a rough surface can be interpreted as a change in the force effect at the boundary line where the three media meet.

The proportionality constant r is the ratio of the projected area A' to the actual area A, as illustrated in Fig. 6.1.

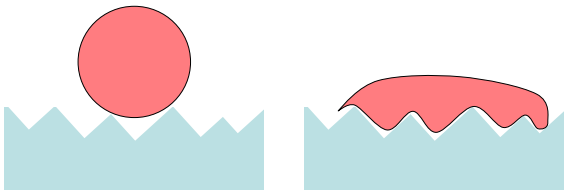

Figure 2.5: In the case of rough surfaces, the contact angle can be either reduced or increased.

The morphology of the surface amplifies, according to Eq. 2.10, both the hydrophobic and the hydrophilic properties of a surface. On a rough, hydrophobic surface, the contact area can be further reduced if the contact angle is further increased. Conversely, in the case of a hydrophilic surface, the contact area is maximized (see Fig. 6.1).

This can also be shown by a graphical representation of Eq. 2.10 (see Fig. 6.2). Point 1 and point 3 correspond to the angles on a smooth surface. If this surface is roughened, point 1 shifts to 2 and 3 to 4, i.e. the surface becomes either more hydrophilic or more hydrophobic.

2.2.3 Crystal Growth

In surface physics, different forms of crystal growth can be explained by the respective variation of the surface tension. Three typical morphologies can be distinguished. The surface tension of the adsorbed film is γ_F; the

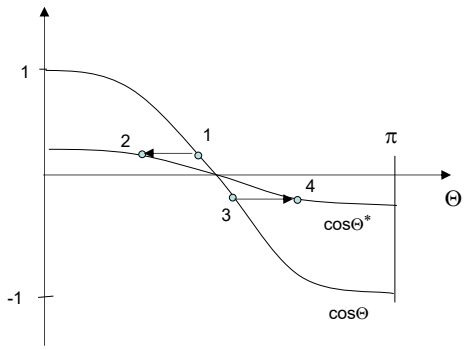

Figure 2.6: Graphical representation of Eq. 2.10.

surface tension of the substrate is γ_s; the surface tension at the film/substrate interface is $\gamma_{S/F}$:

- **Vollmer-Weber** $\gamma_S < \gamma_F + \gamma_{S/F}$

  If the surface tension of the substrate γ_S is small, the energy gain by wetting this surface is low. Therefore, film growth usually occurs in the form of islands.

- **Frank van der Merwe** $\gamma_S > \gamma_F + \gamma_{S/F}$

  If the surface tension γ_S is very large, wetting the surface can effectively reduce the free energy of the system. Therefore, layer-by-layer growth is observed.

- **Stranski-Krastanov**

  This mixed form between island and layer growth occurs when layer-by-layer growth is initially preferred on a substrate, e.g. to compensate for a lattice mismatch. However, the surface tension of the adsorbate then predominates and island growth is observed.

2.2.4 Nucleation

Film growth is not necessarily a process that begins instantaneously, but may require a nucleation phase. Certain equilibrium conditions between the surface and the gas phase must exist for film growth to begin. The internal energy of a system is given by:

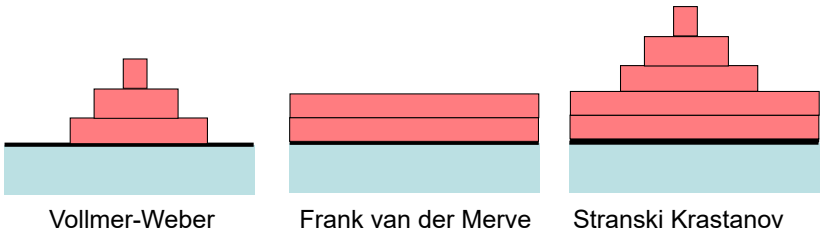

Figure 2.7: Depending on the surface tension, different forms of crystal growth are obtained.

$$U = TS - pV + \sum_i \mu_i n_i \tag{2.11}$$

and

$$dU = TdS - pdV + \sum_i \mu_i dn_i \tag{2.12}$$

From the comparison between the total differential of Eq. 2.11 and Eq. 2.12, one can immediately conclude that:

$$\boxed{0 = SdT - Vdp + \sum_i n_i d\mu_i} \tag{2.13}$$

This is referred to as the **Gibbs-Duhem relation** . This equation links the intrinsic quantities of a system, temperature, pressure, and chemical potential. If one now introduces a change in one of these parameters, one can calculate its effect on the other intrinsic quantities. The variation of the chemical potential with variation of pressure or temperature is therefore:

$$d\mu = \frac{1}{N}\left[-SdT + Vdp\right] \tag{2.14}$$

If the pressure of a system is changed from a pressure p_0 to a pressure p, at constant temperature, a change in the chemical potential is obtained according to:

$$\Delta\mu = \frac{1}{N}\int_{p_0}^{p} Vdp = \frac{1}{N}\int_{p_0}^{p} Nk_BT\frac{1}{p}dp = k_BT\ln\frac{p}{p_0} \tag{2.15}$$

This equation can now be used to describe a system of gaseous particles in front of a surface. The gaseous particles have a pressure p. In equilibrium with the surface, the gas particles in both systems, adsorbed and gaseous, have the same chemical potential. Therefore, the pressure p_0 can be interpreted as the saturation vapor pressure, since then $\Delta\mu = 0$ applies.

If the pressure is now increased above the saturation vapor pressure p_0, the chemical potential of the gaseous particles increases, and it becomes more favorable for them to condense on the surface. This *gas-solid* phase transition is described by the Gibbs enthalpy. This is reduced because the gaseous particles with high chemical potential become condensed particles with lower chemical potential. Therefore, the change in Gibbs enthalpy due to the condensation of N gaseous particles is given by:

$$\Delta G = -\Delta\mu N \tag{2.16}$$

However, the change in surface tension must also be considered in this condensation. Additional terms result from two new interfaces, the interface condensate-vacuum A_{OF} and condensate-substrate $A_{Kontakt}$ with the respective surface tensions (see Fig. 2.8). Thus, the total change in Gibbs enthalpy is:

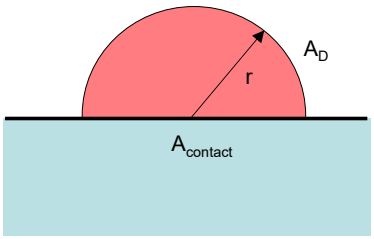

Figure 2.8: Nucleation in the form of hemispherical nuclei.

$$\Delta G = -N\Delta\mu + A_{OF}\gamma_F - A_{contact}\gamma_S A_{contact}\gamma_{S/F} \tag{2.17}$$

For particles to condense from the gas phase, the change in Gibbs enthalpy must be negative. Let us assume that the condensate can be described by hemispherical nuclei with radius r. The change in Gibbs enthalpy is given by the condensation of N gaseous particles into a nucleus with radius r. The surface and contact area are each quantities that scale with $\propto r^2$, while the number of particles in the nucleus scales with $\propto r^3$.

$$\Delta G \propto -\frac{4\pi}{3} r^3 \Delta\mu + \pi r^2 \left[2\gamma_F - \gamma_S + \gamma_{S/F}\right] \tag{2.18}$$

The variation of ΔG with the nucleus radius r is shown in Fig. **??**. It can be seen that for very small radii, the Gibbs enthalpy rather increases. Only for nuclei with a radius greater than a critical radius r_c does the Gibbs enthalpy decrease, $r > r_{krit}$.

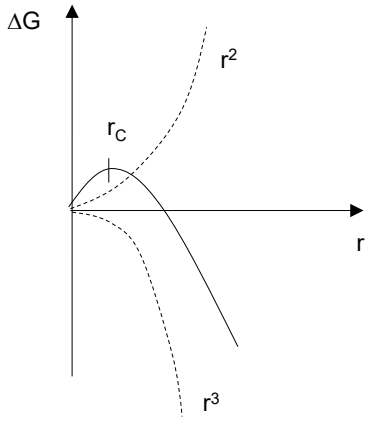

Figure 2.9: The change in Gibbs enthalpy during nucleation as a function of the radius of hemispherical nucleation nuclei.

If the pressure in a system is increased above the saturation vapor pressure p_0, $\Delta\mu$ is increased. Nevertheless, it may *not* be favorable for the system to condense gaseous particles on the surface, since the decrease in G according to $-\Delta\mu N$ is overcompensated by the creation of new surface according to $+\gamma_F A_{OF}$. Thus, no nucleation takes place! Only when, through statistical fluctuations, a nucleus has *randomly* formed with a radius r that is larger than the critical radius r_c, does nucleation occur and these larger nuclei can grow further by continuous condensation.

The radius r_c can be reduced by a strong increase in $\Delta\mu$, i.e. the vapor is supersaturated. Thus, one reaches regions in which r_c approximately reaches the diameter of an adsorbate atom. When this point is reached, condensation sets in abruptly.

Nucleation often initiates condensation processes. For example, spontaneous condensation in a supersaturated vapor only occurs when nuclei are present. Example: condensation trails of airplanes.

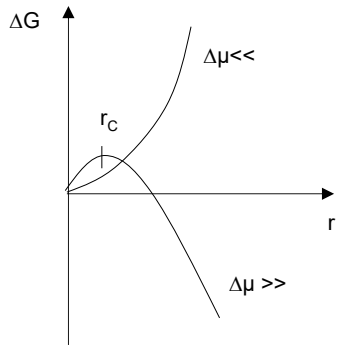

Figure 2.10: If the gain in ΔG through the condensation of gas atoms is large, nucleation sets in. The shape changes with a supersaturation of the vapor, which leads to a greater change in the chemical potential $\Delta\mu$ upon condensation.

2.2.5 Roughness Transition

Finally, we want to consider another result of the thermodynamics of surfaces. So far, the morphology of the surface has always been considered with regard to a minimum of the surface tension. This was derived from a minimum of the energy.

In many systems, however, one often has the situation that the temperature is kept constant by a temperature bath. These isothermal systems are better described by the free energy, which is a function of T, V, N. This *free energy* in a system is given by:

$$F = U - TS \tag{2.19}$$

The free energy depends on the internal energy and the entropy according to:

$$dF = -SdT - pV \tag{2.20}$$

i.e. a system with a different temperature compared to the external temperature bath undergoes irreversible processes until the free energy is minimized. To this end, consider an island on a surface that is to be characterized by its edge. This island edge represents an increase in energy in the system, since the atoms at the edge lack a neighbor and their surface energy is greater. If the energy per surface site of width a is defined as E_0, the energy of a step edge of length l is:

$$U = E_0 \frac{l}{a}. \tag{2.21}$$

How many possibilities are there for the shape of the island? We describe a closed line of length l on the surface as an iteration from atom to atom, where the number of possible new directions at each step is equal to the number z of neighboring atoms. The total number of steps until the length l is reached is l/a. Thus, we obtain for the number of possible island contours:

$$\Omega = z^{l/a} \tag{2.22}$$

With this number of possibilities, the entropy of an island with circumference l can be calculated as $S = k_B \ln \Omega$. Together, we obtain for the free energy:

$$F = E_0 \frac{l}{a} - T k_B \ln z^{l/a} = \frac{l}{a} \left[E_0 - k_B T \ln z \right] \tag{2.23}$$

What does this equation mean? At low temperatures, the term E_0 dominates and the surface remains atomically flat. However, at a certain temperature T, the entropy term dominates and the surface becomes spontaneously rough, effectively reducing the free energy. This is the **roughness transition** . However, this is only observed for a few elements, since the temperature for this transition must be lower than the evaporation temperature of the material.

2.3 Surface structure

The structure of surfaces is determined by the minimization of the free energy. For example, if one considers a silicon surface that has been created by the cleavage of a crystal, the large number of open bonds represents an unfavorable free energy. This can be reduced by a so-called **reconstruction** of the surface. In this case, open bonds on the surface are connected. The exact surface reconstruction depends on the temperature of the surface.

A famous example is the reconstruction of a silicon surface that was created by cleavage in the crystal direction (100). The open bonds are assumed to be saturated by hydrogen atoms at room temperature. If the substrate temperature is increased, the surface undergoes three reconstructions as illustrated in Fig. 2.11:

- 1×1 **Reconstruction**

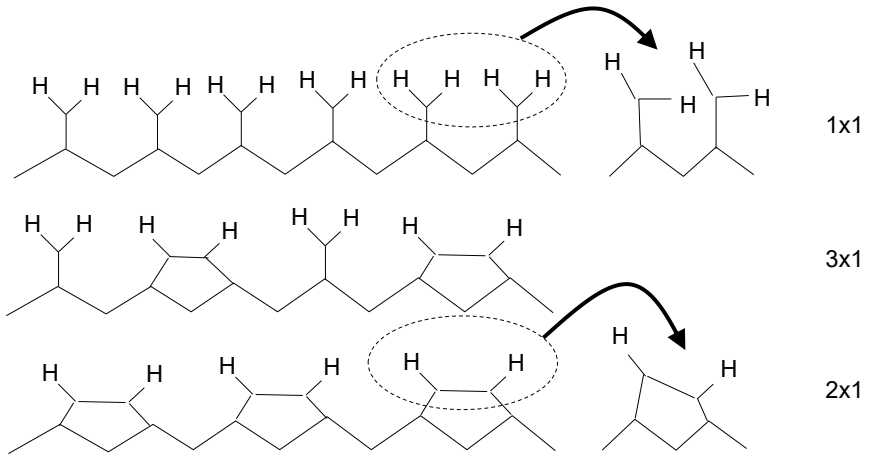

Figure 2.11: The reconstruction of a hydrogen-covered silicon surface undergoes several stages with increasing temperature.

At room temperature, two hydrogen atoms are bound to each silicon atom on the surface. However, adjacent hydrogen atoms come so close that their mutual repulsive interaction bends the silicon-silicon bonds of the binding partners. Stress builds up in the surface.

- 3×1 **Reconstruction**

  If the temperature is increased to about 150 °, the system has the possibility to reduce this stress by desorption of H_2 molecules. In doing so, two adjacent SiH_2 groups reconstruct to form a new Si-Si bond and release an H_2 molecule. This new Si-Si bond is, however, strongly strained. Through this type of reconstruction, the distance between the H atoms increases, and the formerly energetically unfavorable adjacent SiH_2 groups can relax.

- 2×1 **Reconstruction**

  At 250 ° finally, the system gains by the formation of H_2 molecules. However, no open bonds may be created, so that all SiH_2 groups reconstruct with each other. Now, each silicon surface atom has only one hydrogen as a binding partner. At even higher substrate temperatures, the hydrogen then begins to desorb completely and open bonds remain on the surface.

2.4 Electronic Structure of Surfaces

In chemical reactions on surfaces, the charge transfer from an adsorbate to the surface or vice versa is decisive. Therefore, the electronic structure of surfaces is important for evaluating their reactivity.

2.4.1 Metals - Work Function

First, let us consider the electronic structure of metal surfaces. The consideration is similar to that of a plasma edge layer. The atomic cores are immobile, while the electrons can move as a free electron gas. As the energy of the electrons, one has contributions from the kinetic energy, the potential energy, and the electron-electron interaction.

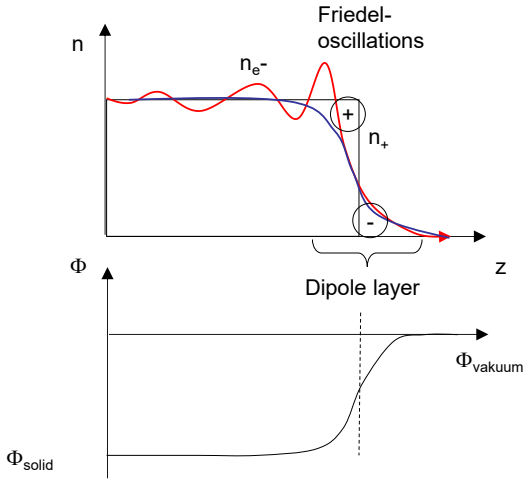

Figure 2.12: Thomas-Fermi model of the electronic structure of a metal surface.

$$\epsilon(k) = \frac{\hbar^2 k^2}{2m} - e\Phi(r) - \underbrace{\int \frac{n(r)}{r - r'} dr'}_{NN-interaction} \tag{2.24}$$

If the electrons are described as a distribution function in real and momentum space, the local electron density is obtained by integration over the momentum space according to the density of states and Fermi-Dirac statistics:

$$n(\epsilon) = \int d^3k \frac{1}{e^{\beta(\epsilon(k)-\epsilon_F)}+1} \tag{2.25}$$

The total number of possible electron states in a volume L^3 results from the boundary conditions of the solid. The number of modes up to a maximum wave vector k_F in the volume is given by:

$$N = \frac{2\left(\frac{4\pi}{3}k_F^3\right)}{\left(\frac{2\pi}{L^3}\right)^3} \tag{2.26}$$

The factor 2 in the numerator corresponds to the two spin settings. The term $(2\pi/L)^3$ corresponds to the volume that a mode occupies in phase space. The derivative of Eq. 2.26 with respect to the energy $\frac{dN}{dE}$ with $E = \frac{\hbar 2k2}{2m}$ is referred to as **density of states**. The electron density is obtained with this density of states as:

$$n_e = \frac{N}{L^3} = \frac{1}{L^3}\int \frac{2\cdot 4\pi k^2 dk}{\left(\frac{2\pi}{L}\right)^3}\frac{1}{e^{\beta(\epsilon(k)-\epsilon_F)}+1} \tag{2.27}$$

or

$$n_e = \int_{k=0}^{\infty} \frac{1}{\pi^2}k^2 dk \frac{1}{e^{\beta(\epsilon(k)-\epsilon_F)}+1} \tag{2.28}$$

This electron density is inserted into the Poisson equation. The solution of this equation at the solid-vacuum transition is shown in Fig. **??**. If the electron-electron interaction is taken into account, oscillations in the electron density at the interface occur, which are referred to as *Friedel oscillations*. It can be seen that the course of the electron density at the surface is blurred and a characteristic **dipole layer** is formed. If one integrates over this density distribution, one obtains a potential well. This dipole layer causes the confinement of the electrons in the solid. This is analogous to the edge layer of a plasma. The difference lies in the fact that the characteristic lengths depend on the electron density, i.e. mm for plasmas and $\mathring{A}$ for solids. In addition, the Boltzmann relation suffices for the description of plasmas, while Fermi statistics are applied in solids.

The depth of the potential well corresponds to the so-called **work function** , as the energy required to remove an electron from the solid.

Adsorbates on this surface can now either enhance or weaken the dipole layer, depending on the orientation of the dipole moment in the adsorbate. The best-known example is the adsorption of cesium, which counteracts the dipole layer of the solid and thus reduces the work function. This is particularly important for the generation of **negative ions**.

2.4.2 Semiconductors - Surface States

In the electronic structure of semiconductor surfaces, the transition of the band structure through the boundary condition surface must be considered. In the simplest case, the potential profile in the solid is given by

$$V(z) = -V_0 + 2V_g \cos gz \tag{2.29}$$

(see Fig. 2.13), with $g = \frac{2\pi}{a}$ and a the lattice constant. V_0 is the depth of the potential well and V_g is the periodic modulation of the potential in the solid lattice. This potential is inserted into the Schrödinger equation[1]:

$$\left[-\frac{d^2}{dz^2} + V(z)\right] \Psi(z) = E\Psi(z) \tag{2.30}$$

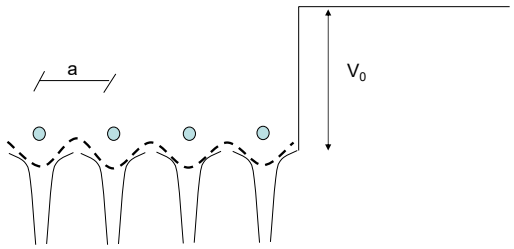

Figure 2.13: Model for band structure calculation.

As an ansatz, so-called **Bloch wave functions** are used

$$\Psi_k(z) = u(z)e^{\imath kz} \tag{2.31}$$

with a prefactor $u(r)$, which takes into account the periodicity of the lattice. A simple example for $u(z)$ would be $u(z) \propto e^{-\imath gz}$. The simplest ansatz for a wave function of this type is:

$$\Psi_k(z) = \alpha e^{\imath kz} + \beta e^{\imath(k-g)z} \tag{2.32}$$

This ansatz is inserted into the Schrödinger equation, and one obtains:

$$\begin{bmatrix} k^2 - V_0 - E & V_g \\ V_g & (k-g)^2 - V_0 - E \end{bmatrix} \begin{bmatrix} \alpha \\ \beta \end{bmatrix} = 0 \tag{2.33}$$

From this, the eigenvalues are obtained:

[1]Here, the factor $\frac{\hbar^2}{2m}$ is omitted.

$$E = -V_0 + \left(\frac{g}{2}\right)^2 + \left(k - \frac{g}{2}\right)^2 \pm \left(g^2 \left(k - \frac{g}{2}\right)^2 + V_g^2\right) 1/2 \tag{2.34}$$

and the wave function:

$$\Psi_k = e^{i\left(k - \frac{g}{2}\right)z} \cos\left(\frac{1}{2} g z + \delta\right) \tag{2.35}$$

with $ei\delta = \frac{E-k2}{V_g}$. The solutions can now be interpreted depending on the absolute magnitude of the individual parameters as follows:

- $V_g = 0$**:**

  If V_g is equal to zero, there is no periodic potential in the potential well. One obtains the solution for free electrons whose potential energy is $-V_0$.

$$E = -V_0 + k^2 \tag{2.36}$$

- $k = \frac{g}{2}$**:**

  For a wave vector corresponding to the Brillouin zone boundary, one obtains two eigenvalues, corresponding to the band gap, as sketched in Fig. 2.14.

$$E = -V_0 \pm V_g + \left(\frac{g}{2}\right)^2 \tag{2.37}$$

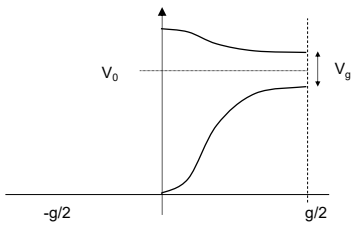

Figure 2.14: Solutions for the energy eigenvalues as a function of the electron wave vector.

- $z > \frac{a}{2}$**:**

  The solutions for $z > a/2$ correspond to a location outside the potential well. Here, the wave function is exponentially decaying. The wave function inside and outside the potential well must be continuously differentiable.

$$\Psi_k = e^{i\left(k-\frac{g}{2}\right)z} \cos\left(\frac{1}{2}gz + \delta\right) \qquad z < \frac{a}{2} \tag{2.38}$$

$$\Psi_k = e^{-\sqrt{V_0 - E}z} \qquad z > \frac{a}{2} \tag{2.39}$$

- **Band Gap:**

  The solutions for states with energies that lie in the band gap can be derived from:

$$E = -V_0 + \left(\frac{g}{2}\right)^2 + \left(k - \frac{g}{2}\right)^2 \pm \left(g^2\left(k - \frac{g}{2}\right)^2 + V_g^2\right) 1/2 \tag{2.40}$$

  With $x = \left(k - \frac{g}{2}\right)^2$ one obtains

$$E = -V_0 + \left(\frac{g}{2}\right)^2 + x \pm \left(g^2 x + V_g r\right) 1/2 \tag{2.41}$$

  If x becomes negative according to Fig. 2.15, the term $k - g/2$ is automatically imaginary. i.e. for the solution of the wave function, one obtains real exponential functions, which do not represent a solution for the volume of the solid, but for the surface. These states are referred to as **surface states** .

  From Fig. 2.16 it is evident that x is largest in the middle of the band gap. Therefore, the prefactor $(k - g/2)$ also becomes large, which corresponds to a small decay length. This means that surface states with energy eigenvalues in the middle of the band gap are strongly localized. This has a great influence on the strength of the chemical bond of the adsorbate to the surface, as shown in Chap. 4.

Bibliography

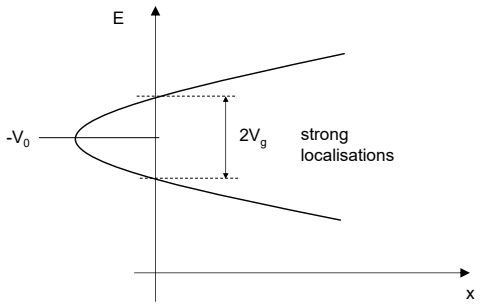

Figure 2.15: Strong localization of surface states.

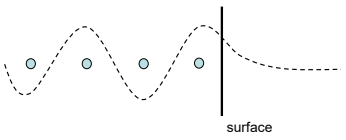

Figure 2.16: Continuous, differentiable continuation of the WF into the vacuum.

Chapter 3

Particle Fluxes on Surfaces

3.1 Ions

In reactive plasmas, the bombardment of the surface with ions is a fundamental characteristic and a unique feature of material synthesis. The following section briefly reviews the transition between the plasma and an adjacent surface before focusing on the energy distributions of the incident ions.

Review of Plasma sheaths

Consider a quasi-neutral plasma in front of a surface. This surface is not grounded. Since the electrons are much more mobile, they leave the plasma at the edge. This locally violates the quasi-neutrality and a sheath potential forms that counteracts the loss of electrons. A new equilibrium is established. In this sheath, the electron density is much smaller than the ion density, as illustrated in Fig. 3.1.

Initially, the energy conservation for the ions is given by:

$$\frac{1}{2}Mv^2(x) + e\Phi(x) = \frac{1}{2}Mv_0^2 \tag{3.1}$$

v_0 is the velocity with which ions enter this space charge zone. In addition, current conservation applies:

$$n_i(x)v_i(x) = n_0 v_0 \tag{3.2}$$

Solving for $n_i(x)$ with $E_0 = \frac{1}{2}Mv_0^2$ gives:

$$n_i(x) = n_0\left(1 - \frac{2e\Phi(x)}{Mv_0^2}\right) = n_0\left(1 - \frac{e\Phi(x)}{E_0}\right)^{-1/2} \tag{3.3}$$

For the description of the electron density, the Boltzmann relationship is used again:

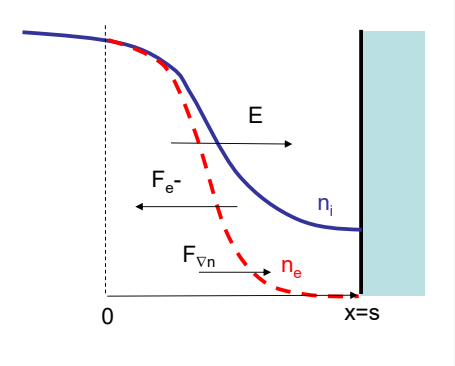

Figure 3.1: Charge carrier density profile in the sheath

$$n_e(x) = n_0 e^{\frac{e\Phi(x)}{k_B T_e}} \tag{3.4}$$

Substituting both into the Poisson equation gives:

$$\frac{d^2\Phi(x)}{dx^2} = e\frac{n_0}{\epsilon_0}\left[\exp\left(\frac{e\Phi(x)}{k_B T_e}\right) - \left(1 - \frac{e\Phi(x)}{E_0}\right)^{-1/2}\right] \tag{3.5}$$

This equation corresponds to a differential equation for the potential profile $\Phi(x)$ in the sheath. This equation is multiplied by $\frac{d\Phi(x)}{dx}$ and integrated over x. The left side becomes

$$\begin{aligned}\int_0^x \frac{d\Phi(x)}{dx}\frac{d^2\Phi(x)}{dx}dx &= \\ \int_0^x \frac{d\Phi(x)}{dx}\frac{d}{dx}\frac{d\Phi(x)}{dx}dx &= \\ \int_0^x \frac{d\Phi(x)}{dx}d\left(\frac{d\Phi(x)}{dx}\right) &= \\ \frac{1}{2}\left(\frac{d\Phi(x)}{dx}\right)^2 &\end{aligned} \tag{3.6}$$

The right side becomes

$$\begin{aligned}\int_0^x \frac{d\Phi(x)}{dx}e\frac{n_0}{\epsilon_0}\left[exp\left(\frac{e\Phi(x)}{k_B T_e}\right) - \left(1 - \frac{e\Phi(x)}{E_0}\right)^{-1/2}\right]dx &= \\ \int_0^{\Phi(x)} e\frac{n_0}{\epsilon_0}\left[exp\left(\frac{e\Phi(x)}{k_B T_e}\right) - \left(1 - \frac{e\Phi(x)}{E_0}\right)^{-1/2}\right]d\Phi &\end{aligned} \tag{3.7}$$

Thus, with integration over Φ under the assumption that $\Phi(0) = \partial\Phi\partial x|_{x=0} = 0$, we obtain:

$$\frac{1}{2}\left(\frac{d\Phi(x)}{dx}\right)^2 = \frac{en_0}{\epsilon_0}\left[k_B T_e e\frac{e\Phi}{k_B T_e} - k_B T_e + 2E_0\left(1-\frac{e\Phi}{E_0}\right)^{1/2} - 2E_0\right] \tag{3.8}$$

This equation requires that the right side becomes greater than zero for meaningful solutions. Assuming that $e\Phi \ll k_B T_e$, the right side can be expanded to the second order:

$$k_B T_e\left(1+\frac{e\Phi}{k_B T_e}+\frac{1}{2}\left(\frac{e\Phi}{k_B T_e}\right)^2\right)k_B T_e + \tag{3.9}$$

$$2E_0\left(1-\frac{1}{2}\frac{e\Phi}{E_0}-\frac{1}{8}\left(\frac{e\Phi}{E_0}\right)^2\right)2E_0 \tag{3.10}$$

This term must be greater than zero. Therefore, it can be concluded:

$$\frac{1}{2}\frac{(e\Phi)^2}{k_B T_e} - \frac{1}{4}\frac{(e\Phi)^2}{E_0} > 0 \tag{3.11}$$

With $E_0 = \frac{1}{2}Mv_0^2$, the condition for the initial velocity v_0 is obtained:

$$\boxed{v_0 > \sqrt{\frac{k_B T_e}{M}} = v_B} \tag{3.12}$$

This is referred to as the **Bohm velocity**. In describing the space charge zone, we have assumed the energy conservation of the ions and found a boundary condition, the Bohm velocity, which must be satisfied for the entry of the ions into this sheath. This naturally raises the question of how the ions are brought to this velocity.

The acceleration of the ions to the Bohm velocity occurs in the so-called **presheath** (Fig. 3.2). In this region, quasi-neutrality must prevail:

$$n_i(x) = n_e(x) \tag{3.13}$$

From this, it can be derived:

$$\frac{1}{n_i(x)}\frac{dn_i(x)}{dx} = \frac{1}{n_e(x)}\frac{dn_e(x)}{dx} \tag{3.14}$$

With $j_i = n_i e v_i(x)$, we obtain:

$$\frac{1}{n_e(x)}\frac{dn_e(x)}{dx} = \frac{ev_i(x)}{j_i(x)}\frac{d}{dx}\frac{j}{ev_i(x)} = \frac{1}{j_i(x)}\frac{dj_i(x)}{dx} - \frac{1}{v_i(x)}\frac{dv_i(x)}{dx} \tag{3.15}$$

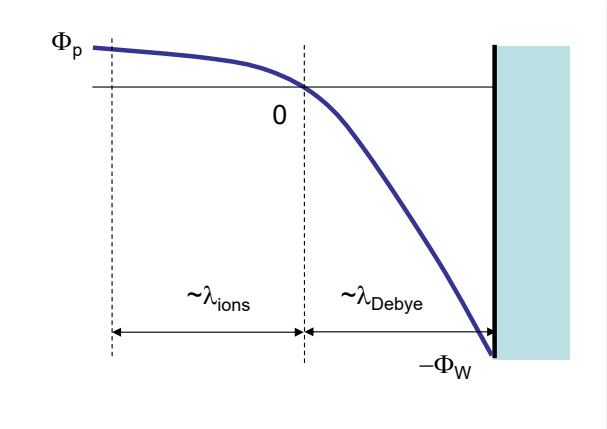

Figure 3.2: Potential profile in the presheath and sheath. The extent of the presheath is of the order of the mean free path of the ions λ_{Ionen} and the sheath is of the order of the Debye length λ_D.

Using the Boltzmann relationship for the electrons, we finally obtain:

$$\frac{1}{v_i(x)}\frac{dv_i(x)}{dx} + \frac{e}{k_B T_e}\frac{d\Phi(x)}{dx} = \frac{1}{j_i(x)}\frac{dj_i(x)}{dx} \tag{3.16}$$

In the presheath, the local ion velocity $v_i(x)$ must always be less than the Bohm velocity v_B. Therefore, from Eq. 3.16, the inequality is obtained as follows:

$$\frac{1}{v_B}\frac{dv_i(x)}{dx} + \frac{e}{k_B T_e}\frac{d\Phi}{dx} < \frac{1}{j_i}\frac{dj_i}{dx} \tag{3.17}$$

This equation can be satisfied by several conditions:

- **Ion friction**: In the case of current conservation ($\frac{dj_i(x)}{dx} = 0$), the left side must explicitly become less than 0. This can be achieved if the increase in ion velocity is reduced by ion friction. That is, the change in $v_i(x)$ is not equivalent to a change in $\Phi(x)$.
- **Geometry, contraction:** Geometric effects can cause the current density to increase as the sheath is penetrated. For example, $\frac{dj_i}{dx} > 0$ in a cylindrical arrangement.
- **Ionization:** The current through the presheath can increase by assuming additional ionization. Here, too, $\frac{dj_i}{dx} > 0$ applies.

Surface without Bias Voltage

Due to the violation of quasi-neutrality in the sheath, a potential difference builds up. If we denote the charge carrier density at the edge of the sheath with n_0, we can

determine the currents that hit the surface. The ion current is given by the Bohm flux:

$$\Gamma_i = en_0 v_B \tag{3.18}$$

and the electron flux that hits the surface is given by:

$$\Gamma_e = \frac{1}{4} n_s v_{e,th} = \frac{1}{4} n_0 v_{e,th} e^{\frac{e\Phi_W}{k_B T_e}} \tag{3.19}$$

For the case of a so-called **floating** surface, (i.e., the surface is not grounded), $\Gamma_e = \Gamma_i$ must hold. This implies:

$$n_0 v_B = \frac{1}{4} n_0 v_{e,th} e^{\frac{e\Phi_W}{k_B T_e}} \tag{3.20}$$

$$\left(\frac{k_B T_e}{M}\right)^{1/2} = \frac{1}{4}\left(\frac{8 k_B T_e}{\pi m}\right)^{1/2} e\frac{e\Phi_W}{k_B T_e} \tag{3.21}$$

Thus, the so-called **floating potential** is obtained:

$$\boxed{\Phi_W = -T_e \ln\left(\frac{M}{2\pi m}\right)^{1/2}} \tag{3.22}$$

A potential drop must also occur between the edge of the sheath and the plasma volume, in which the ions are brought to the Bohm velocity. This can be easily derived from:

$$\frac{1}{2} M v_B^2 = e\Phi_P \tag{3.23}$$

This gives the so-called **plasma potential**

$$\Phi_P = \frac{k_B T_e}{2} \tag{3.24}$$

All potentials are defined here with respect to the layer edge ($v_i = v_B$). The entire potential difference between the plasma potential and an external experimental mass of a plasma reactor includes the entire sheath voltage.

Surface with Applied Voltage

Matrix Sheath

In plasma processes, a voltage is often explicitly applied to an electrode. This results in a high voltage drop across the sheath. This high voltage pushes the electrons back further and accelerates the ions. In the simplest approximation, the violation of quasi-neutrality in the sheath can be described as a step function. If it is assumed that the ion density in the sheath is constant, it is referred to as the so-called **matrix**

layer (Fig. 3.3). The electric field for this case is calculated from the Maxwell equations as follows:

$$\frac{dE}{dx} = \frac{1}{\epsilon_0} e n_0 \tag{3.25}$$

$$E(x) = \frac{1}{\epsilon_0} e n_0 x \tag{3.26}$$

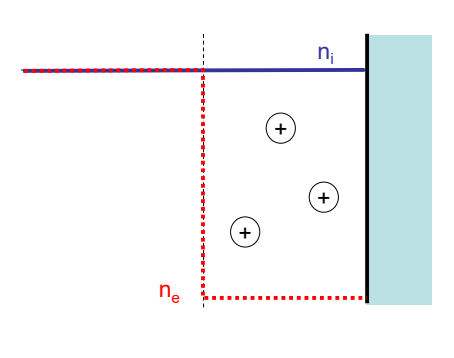

Figure 3.3: Charge carrier density profile in the matrix sheath

This gives the potential profile:

$$\Phi(x) = -\frac{e}{\epsilon_0} n_0 \frac{1}{2} x^2 \tag{3.27}$$

With $\Phi(s) = -V$, the density s of the sheath is obtained:

$$s = \left(\frac{2\epsilon_0 eV}{en_0} \right)^{1/2} = \lambda_D \left(\frac{2eV}{k_B T_e} \right)^{1/2} \tag{3.28}$$

This result shows that the sheath can be many Debye lengths thick.

Child-Langmuir Sheath

The assumption of a constant ion density in the sheath is only valid if collisions in the sheath counteract the acceleration of the ions. In the case of a collision-free sheath, the ion density decreases with increasing acceleration. As an approach, we obtain:

$$\frac{1}{2} M v^2(x) = -e\Phi(x) \tag{3.29}$$

Here, we have neglected v_0, as the ions in the sheath are strongly accelerated and their initial energy (according to v_0) is of minor importance.

$$en(x)v(x) = j_0 \tag{3.30}$$

This gives

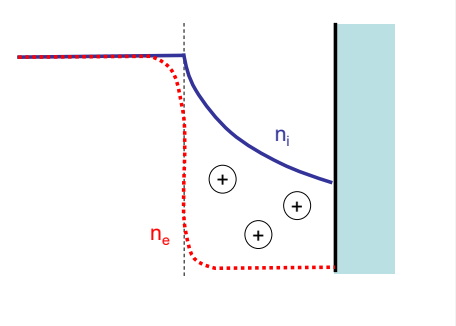

Figure 3.4: Charge carrier density profile in the Child-Langmuir sheath

$$n(x) = \frac{1}{e} j_0 \left(-\frac{2e\Phi(x)}{M} \right)^{-1/2} \tag{3.31}$$

Thus, the Poisson equation gives:

$$\frac{d^2\Phi(x)}{dx^2} = -\frac{j_0}{\epsilon_0} \left(-\frac{2e\Phi(x)}{M} \right)^{-1/2} \tag{3.32}$$

At this point, the electron density in the sheath is neglected. This is a good approximation at high sheath voltage, as the electrons are effectively pushed back into the plasma volume.

After multiplying by $\frac{d\Phi(x)}{dx}$ and integrating over x, we obtain:

$$\frac{1}{2} \left(\frac{d\Phi}{dx} \right) 2 = 2\frac{j_0}{\epsilon_0} \left(\frac{2e}{M} \right)^{-1/2} (-\Phi)^{1/2} \tag{3.33}$$

The integration used the fact that $\Phi(0) = 0$ and $\frac{d\Phi(x)}{dx}|_{x=0} = 0$. This gives for $\Phi(s) = -V$:

$$\boxed{j_0 = \frac{4}{9}\epsilon_0 \left(\frac{2e}{M} \right)^{1/2} \frac{V^{3/2}}{s^2}} \tag{3.34}$$

This corresponds to the space charge-limited current according to the **Child-Langmuir law**, or the $V^{3/2}$ law. With current conservation, we must have:

$$j_0 = e n_0 v_B \tag{3.35}$$

and we obtain for the sheath thickness:

$$s = \frac{\sqrt{2}}{3} \lambda_D \left(\frac{2eV}{k_B T_e} \right)^{3/4} \tag{3.36}$$

Collision dominated sheath

So far, we have always assumed a sheath without collisions, in which the velocity of the ions increases according to energy conservation. The other limiting case arises from the assumption that collisions in the sheath limit the velocity, as expressed by the mobility. Initially, of course, flux conservation applies in the sheath.

$$n_i(x)v_i(x) = n_0 v_B \tag{3.37}$$

but the velocity is described by

$$v_i(x) = \mu E \tag{3.38}$$

In the following, two cases can be distinguished:

- **Constant mean free path λ = const.**
  If the mean free path is constant, the mobility of the ions can be expressed as:

$$v_i(x) = \mu E = \frac{e}{M\nu_m}E = \frac{e\lambda}{v_i(x)}E \tag{3.39}$$

  This gives for a velocity-independent mean free path:

$$v_i(x) = \left(\frac{e\lambda}{M}E(x)\right)^{1/2} \tag{3.40}$$

  Thus, the ion density is:

$$n_i(x) = \frac{v_B}{v_i(x)}n_0 = v_B n_0 \left(\frac{e\lambda}{M}E(x)\right)^{-1/2} \tag{3.41}$$

  Substituting this into the Poisson equation, neglecting the electron density in the sheath:

$$\frac{dE}{dx} = \frac{e}{\epsilon_0}n_0 v_B \left(\frac{e\lambda}{M}E(x)\right)^{-1/2} = \frac{1}{\epsilon_0}j_0 \left(\frac{e\lambda}{M}E\right)^{-1/2} \tag{3.42}$$

  The dependence obtained from this is:

$$j_0 = \frac{2}{3}\left(\frac{5}{3}\right)^{3/2}\epsilon_0 \left(\frac{e\lambda}{M}\right)^{1/2}\frac{V^{3/2}}{s^{5/2}} \tag{3.43}$$

  It can be seen that the scaling is very similar to the Child-Langmuir law. Only the dependence on the sheath thickness s is somewhat different, since the ion density in comparison to free fall cannot decrease as quickly. Another difference is the mean free path λ in the expression for the current. If this becomes small, the current across the sheath is also small.

- **Constant mobility ν_m = const.**
  A constant mobility implies a velocity-independent collision frequency. Thus, we obtain:

$$\frac{dE}{dx} = \frac{e}{\epsilon_0}\mu^{-1}E^{-1} \tag{3.44}$$

  This solves to:

$$j_0 = \frac{9}{8}\epsilon_0\mu\frac{V^2}{s^3} \tag{3.45}$$

It can be seen that depending on the boundary condition and prior assumption, the relationship between potential, voltage, and layer thickness is different. However, the formation of a sheath between plasma and surface complicates the homogeneous surface coating of three-dimensional workpieces (Fig. 3.5). If the sheath thickness is large, the ion beam incident perpendicularly no longer illuminates the surface conformally, and an anisotropic coating is obtained, especially in small structures (in CVD, synthesis occurs on the hot surface, which is almost independent of the shape of the workpiece).

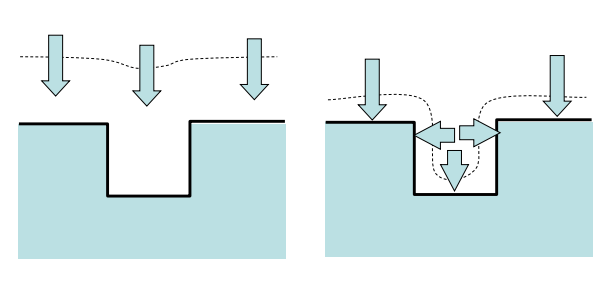

Figure 3.5: Coating of three-dimensional bodies is only possible at high electron density.

3.1.1 Energy and Current of Incident Ions

Ion Energy Distribution in a DC Discharge

The ion energy distribution in a DC discharge is initially quite simple, as all ions fall through the sheath voltage V and thus singly charged ions have the energy eV. Charge exchange collisions (CX charge exchange) in the sheath can change the distribution, as the newly formed ions see a correspondingly smaller remaining potential drop within the sheath. This contribution from charge exchange collisions leads to an exponentially increasing contribution to lower ion energies (see Fig. 3.6). This exponential

dependence can be easily visualized. The mean free path λ for such a collision changes the particle number N over a flight distance dx according to $dN = 1/\lambda N dx$. Therefore, the number of original ions decreases exponentially with the path x in the sheath. At the same time, the number of formed charge exchange neutrals increases. In total, this exponential increase to small energies remains, as the probability of experiencing *no* collision on the flight from the sheath edge to the surface is exponentially smaller than experiencing many collisions.

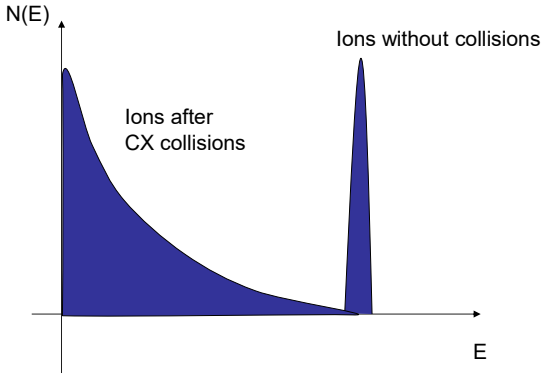

Figure 3.6: Ion energy distribution from a DC sheath where charge exchange collisions (CX) contribute to ions that hit at lower energies than the sheath voltage.

Ion Energy Distribution in an RF Discharge

The ions that fall through the sheath can follow the oscillating field to varying degrees depending on their mass. In the case of very light ions (H^+), the ion energy distribution is correspondingly broad. A characteristic double peak structure is formed, as shown in Fig. 3.7.

The width of this energy distribution is determined by the ratio of the transit time τ through the sheath and the frequency of the rf. The transit time is calculated from:

$$\frac{dv}{dt} = \frac{e}{M}\vec{E} \tag{3.46}$$

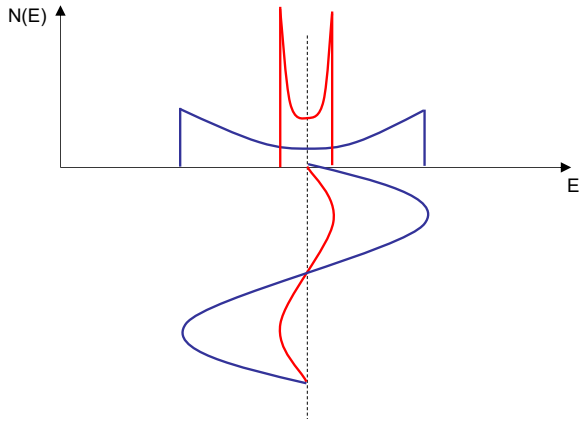

Figure 3.7: Depending on the mass of the ions, they can follow the oscillating field in the sheath more or less. Their energy upon impact on the surface depends on their phase relation to the electric field in the rf cycle. Since the E-field remains at its maximum or minimum for a longer time, a characteristic double peak structure of the ion energy distribution is formed.

Given a thickness of the sheath s, a transit time τ is obtained for a constant E-field in the sheath:

$$\tau = \left(\frac{s^2 M}{eE} \right)^{1/2} \tag{3.47}$$

The width of the energy distribution can be well described by a scaling factor $\xi = \omega_{rf}\tau$. There are two limiting cases:

- $\tau \gg \omega_{rf}^{-1}$, $\xi \gg 1$**:** With a long transit time, the high and low E-fields that the ion sees on its trajectory through the sheath are averaged out. The energy distribution becomes very sharp and its maximum lies at the average sheath voltage corresponding to the DC self-bias.

- $\tau \ll \omega_{rf}^{-1}$, $\xi \ll 1$**:** With a very short transit time, the ion sees either a high or low E-field, depending on the phase relation to the rf period in which it enters the sheath; the energy distribution becomes very broad. The shape of the energy distribution is shown in Fig. 3.7. The width is given by:

$$\Delta E \propto \frac{1}{\xi} \propto \frac{1}{\omega_{rf}} \left(\frac{s2M}{eE} \right)^{-1/2} \propto \frac{1}{\omega_{rf}\sqrt{M}} \tag{3.48}$$

Since the sheath voltage varies sinusoidally, the E-field remains at its maximum or minimum for a longer time, forming a characteristic double peak structure of the ion energy distribution.

In the case of collisions in the sheath, one would expect in the simplest case that the energy distribution would broaden and smear out. However, in the case of rf plasmas, the interesting observation is made that a whole series of new peaks appears: if a charge exchange collision occurs in the sheath, a new stationary ion is obtained, which is accelerated from this point in the sheath and hits with an energy corresponding to the phase relation to the field and the remaining transit time. This behavior is shown in Fig. 3.8.

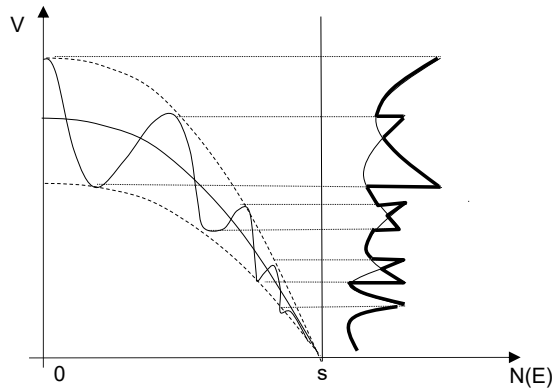

Figure 3.8: Structured broad ion energy distributions are created in the case of charge exchange collisions within an rf sheath.

Neutral Particles In reactive plasmas, a variety of radicals are formed from the source gas, which contribute to film growth or erosion. The fluxes of these reactive particles to the surfaces are discussed below.

3.1.2 Diffusion

Density Profiles

The essential transport process is diffusion for the neutral particles. To describe diffusion, we initially start from the momentum balance of a type of particle. This is extended by a simple approach for the collision term, the relaxation approximation. The change in momentum in a fluid element is given by the momentum lost in a collision ($\sim m\vec{v}$), multiplied by the frequency of this process ($\sim n\nu_m$). Thus, we obtain:

$$mn\left[\frac{\partial}{\partial t}\vec{v} + (\vec{v}\nabla)\vec{v}\right] = qn\vec{E} - \nabla p - m\vec{v}n\nu_m \tag{3.49}$$

In the steady state, the time derivative is set to zero. Assuming that $\nu_m \gg v$ (we consider the case of high collision frequency), the second term on the left side proportional to v^2 can also be neglected. Thus, we obtain:

$$\vec{v} = \frac{1}{mn\nu_m}\left(\pm en\vec{E} - \nabla p\right) \tag{3.50}$$

Using the ideal gas law, two cases arise. For an isothermal change of state, we have:

$$\nabla p = kT\nabla n \tag{3.51}$$

For an adiabatic change of state (i.e., the temperature does not remain constant with a change in pressure), the adiabatic equation applies:

$$\frac{\nabla p}{p} = \gamma\frac{\nabla n}{n} \tag{3.52}$$

Here, γ is given by

$$\gamma = \frac{2+N}{N} \tag{3.53}$$

with N the number of degrees of freedom.

For an isothermal change of state, the following expression for the velocity of the plasma species in the fluid picture is obtained:

$$\vec{v} = \pm\frac{e}{m\nu_m}\vec{E} - \frac{k_BT}{m\nu_m}\frac{\nabla n}{n} \tag{3.54}$$

$$\vec{j} = n\vec{v} = n\frac{\pm e}{m\nu_m}\vec{E} - \frac{k_BT}{m\nu_m}\nabla n \tag{3.55}$$

The first term describes the particle flux driven by a drift term, such as ions and electrons by the electric field. The second term corresponds to a particle flux driven by a density gradient, diffusion. Accordingly, the so-called **mobility** is obtained to describe the drift:

$$\boxed{\mu = \frac{|q|}{m\nu_m}} \tag{3.56}$$

and the **diffusion constant** as:

$$\boxed{D = \frac{k_B T}{m\nu_m}} \tag{3.57}$$

The connection between drift and diffusion is given by the **Einstein relation**:

$$\boxed{\mu = \frac{|q|}{k_B T} D} \tag{3.58}$$

As an example, we consider the solution of the continuity equation in planar geometry for a neutral gas (i.e., the drift term falls away). The geometry is sketched in Fig. B.1.

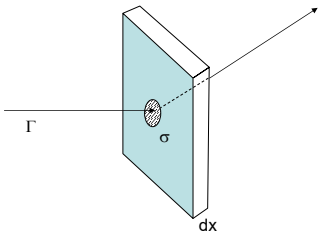

Figure 3.9: Geometry for solving the diffusion equation in 1-dim

The approach is:

$$\frac{\partial n}{\partial t} + \nabla(-D\nabla n) = 0 \tag{3.59}$$

Assuming that D is spatially constant (e.g., a constant temperature profile), we obtain:

$$\frac{\partial n}{\partial t} = D\nabla^2 n \tag{3.60}$$

We make a separation approach for the density n according to

$$n = u(t)w(x) \tag{3.61}$$

and separate the variables.

$$\frac{1}{u}\frac{\partial u}{\partial t} = D\frac{1}{w}\nabla^2 w = \text{const.} = -\frac{1}{\tau} \tag{3.62}$$

Since the left side depends only on time and the right side only on location, both sides must each result in a constant. We define this as -1/τ. The time dependence is obtained from the solution of

$$\frac{\partial u}{\partial t} = -\frac{1}{\tau}u \tag{3.63}$$

with

$$u(t) = u_0 e^{-\frac{t}{\tau}} \tag{3.64}$$

The solution of the spatial dependence is obtained from

$$-\frac{1}{D\tau} = \frac{1}{w}\nabla^2 w \tag{3.65}$$

With the definition of a geometry constant $\Lambda = \sqrt{D\tau}$ we obtain

$$-\frac{1}{\Lambda^2}w = \nabla^2 w \tag{3.66}$$

with the solution

$$w(x) = w_0 \cos\frac{x}{\Lambda} + ...+ \tag{3.67}$$

In planar geometry with the boundary condition $n = 0$ for $x = \pm l/2$, the geometry constant Λ is obtained:

$$\Lambda = \frac{l}{\pi} \tag{3.68}$$

For other geometries such as cylindrical geometry or spherical problems, correspondingly different geometry constants are obtained (in cylindrical geometry, the spatial dependence is given, for example, by Bessel functions). The solution in one dimension is:

$$n(x,t) = n_0 e^{-\frac{t}{\tau}} \cos\left(\frac{\pi}{l}x\right) \tag{3.69}$$

That is, the density profile that arises from diffusion of neutrals corresponds to a cosine. This is referred to as the fundamental mode of diffusion. This density profile decays exponentially over time. Even if an initial density distribution deviates from the cosine profile, the cosine distribution quickly forms due to the decay of higher modes, whose amplitude then becomes exponentially smaller.

Diffusion Coefficients

The question to be clarified here is how large this diffusion coefficient is. Initially, a hypothetical boundary surface in a gas volume is considered. The fluxes that pass through this boundary surface collision-free from both sides are, at a distance λ, according to Fig. 3.10:

$$j_z = \frac{1}{6}\bar{v}n_1(z-\lambda) - \frac{1}{6}\bar{v}n_1(z+\lambda) = \frac{1}{6}\bar{v}\left(-\frac{\partial n}{\partial z}2\lambda\right) \tag{3.70}$$

The factor $\frac{1}{6}$ corresponds to one spatial direction out of six possible ones. We obtain:

$$j_z = -D\frac{\partial n}{\partial z} = \qquad\qquad D = \frac{1}{3}\bar{v}\lambda \tag{3.71}$$

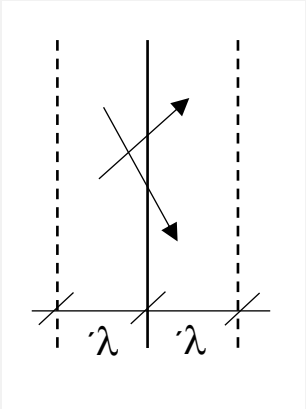

Figure 3.10: Diffusion through a boundary surface.

With

$$\lambda = \frac{1}{n\sigma} \tag{3.72}$$

Thus, the diffusion coefficient is given as:

$$\boxed{D = \frac{1}{3}\bar{v}\frac{1}{n\sigma}} \tag{3.73}$$

To calculate the diffusion coefficient, we first need the average velocity of the particles in the gas volume. This is calculated from the averaging over the velocity distribution.

$$\langle v\rangle \int v f d^3v \tag{3.74}$$

With a sufficient number of collisions, the distribution function f has the form of a Maxwell distribution, as it is a distribution of maximum entropy, as shown further below. The distribution function is:

$$\boxed{f(\vec{v}) = \left(\frac{m}{2\pi k_B T}\right)^{3/2} e^{-\frac{1/2mv^2}{k_B T}}} \tag{3.75}$$

From this distribution function, the average velocity is obtained as:

$$\langle v \rangle = \left(\frac{8k_B T}{\pi m}\right)^{1/2} \tag{3.76}$$

The average velocity in one direction x is:

$$|\langle v_x \rangle| = \left(\frac{2k_B T}{\pi m}\right)^{1/2} = \frac{1}{2}\langle v \rangle \tag{3.77}$$

Thus, the particle flux onto a hypothetical boundary surface in a gas volume, after considering only the positive x-direction, for example, is:

$$\Gamma = n\frac{1}{2}\frac{1}{2}\langle v \rangle = \frac{1}{4}n\langle v \rangle \tag{3.78}$$

The diffusion coefficient D is obtained after these preliminary considerations as:

$$D = \frac{1}{3}\frac{1}{n\sigma}\langle v \rangle = \frac{1}{3}\frac{1}{n\sigma}\left(\frac{8k_B T}{\pi m}\right)^{1/2} = \frac{1}{2}\sqrt{\frac{8}{\pi}}\frac{1}{n\sigma}\left(\frac{k_B T}{m}\right)^{1/2} \tag{3.79}$$

Finally, the effective cross-section for the collision process must be determined. In general, the collision between hard spheres is assumed, with a distance r_{12} as the sum of the radii. With the reduced mass μ, we obtain:

$$D = \frac{3}{8}\sqrt{\pi}\frac{1}{n r_{12}^2 \Omega}\left(\frac{k_B T}{2\mu}\right)^{1/2} \tag{3.80}$$

Here, Ω is the Lenard-Jones parameter, which is tabulated for many combinations of collision particles. It corresponds to a correction to the assumption of hard spheres.

Diffusion Profile with Surface Reactions

When considering spatially bounded plasmas, we have so far assumed perfectly absorbing walls. This can be taken into account with a boundary condition according to a density $n = 0$ directly at the location of the wall. For unreactive particles, the wall is not a sink and they are simply reflected; no variation in density occurs. For reactive particles, on the other hand, the wall of a plasma is only partially a sink. This is expressed by a reflection coefficient r, which lies in a range $0 < r < 1$.

The particle fluxes across a boundary surface that lies within a mean free path in front of a wall are given by two components: a flux j_{out} towards the wall and a flux j_{in} away from the wall. The flux j_{loss} that is lost at the wall corresponds exactly to the difference of these two parts according to [**?**, Cha87]:

$$j_{loss} = j_{out} - j_{in} \tag{3.81}$$

Now consider the density of the particles at the location of this hypothetical boundary surface. This is calculated from the fluxes passing through this boundary surface:

$$n = \frac{1}{\langle v_x \rangle}(j_{out} + j_{in}) \tag{3.82}$$

Here, the average velocity in one spatial dimension according to Eq. 3.77 is decisive. Thus, we obtain:

$$n = \frac{1}{\frac{1}{2}\langle v \rangle}(j_{out} + j_{in}) \tag{3.83}$$

Finally, we introduce that the fluxes j_{out} and j_{in} are linked via the reflection coefficient:

$$j_{in} = r j_{out} \tag{3.84}$$

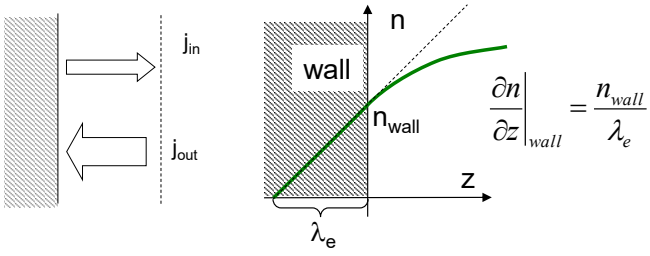

Figure 3.11: Geometry for considering the diffusion profile of reactive particles.

We have three equations 3.81, 3.83, and 3.84 for the three unknowns j_{in}, j_{out}, and j_{loss}. These can be eliminated and we obtain as a relationship for the flux j_{loss} that is lost at the surface:

$$\boxed{j_{loss} = \frac{1}{2} n v \frac{1-r}{1+r} = \frac{1}{4} n v \frac{\beta}{1-\beta/2}} \tag{3.85}$$

We now consider the two limiting cases of large and small reflection coefficients, according to Fig. B.6:

- **Wall reflects almost perfectly,** $r \sim 1$

  If $r \sim 1$ (i.e., the particles are not lost at the surface), the fraction of particles passing through the boundary surface is:

$$j_{loss} \simeq \frac{1}{2} nv \frac{1}{2} \underbrace{(1-r)}_{=s} \tag{3.86}$$

  That is, the fraction s that sticks to the wall is $j = \frac{1}{4}nv$ in accordance with gas kinetics. With a reflecting wall, no density profile forms in front of the surface. Thus, the incident particle flux onto the boundary surface is simply the directed particle flux in a homogeneous gas volume.

- **Wall absorbs almost perfectly,** $r \sim 0$

  If $r \sim 0$ (i.e., the particles are lost at the surface), the fraction of particles passing through the boundary surface is:

$$j_{loss} \simeq \frac{1}{2} nv \tag{3.87}$$

  In discussing this dependence, it should be noted that the density in Eq. 3.87 is to be taken at the boundary surface in front of the surface. n is *not* the density in the volume and *not* identical to the density in Eq. 3.86. This is illustrated in Fig. B.6: the fact that the wall acts as a sink causes a density gradient to form in front of the surface, which leads to a lower local density compared to the density in the volume. Eq. 3.87 can be considered composed of two parts:

$$j_{loss} = \underbrace{\frac{1}{4} nv}_{gaskinetic} + \underbrace{\frac{1}{4} nv}_{gradient\ density} = \frac{1}{2} nv \tag{3.88}$$

  The second term arises from the fact that the flux directed into the volume $\frac{1}{4}nv$ is exactly compensated by the diffusion according to the density gradient towards the wall. That is, the gradient adjusts itself so that *no* net flux occurs away from the wall.

By determining the particle densities in a pulsed plasma in a time-resolved manner, the reflection coefficient can now be determined. The idea of this measurement is to observe the decay time of a particle species: if this is short, the surfaces act as a sink and the reflection coefficient is correspondingly

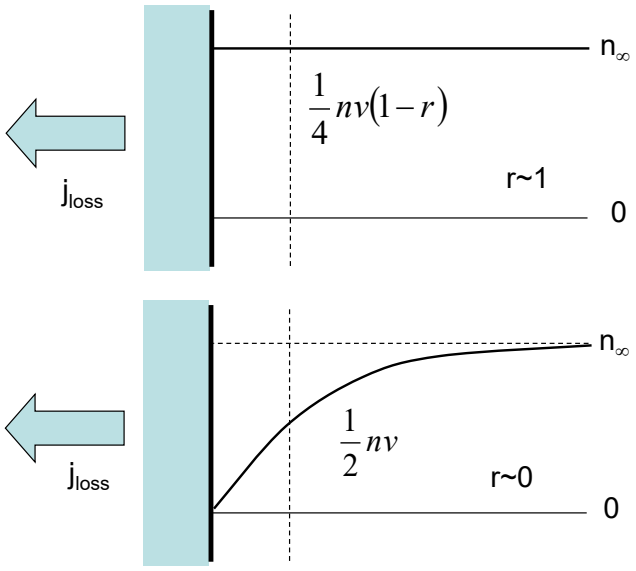

Figure 3.12: Depending on the size of the reflection coefficient, a different density profile forms in front of the surface. The relationship between the flux of reactive particles lost at the surface and the local density in front of the surface is given by Eq. 3.87.

small. If it is large, the reactive particles are reflected at the surfaces and their reflection coefficient must therefore be large. The temporal variation of a particle species is given by the continuity equation:

$$\frac{\partial n}{\partial t} + \nabla j = 0 \tag{3.89}$$

Now, two cases can be distinguished:

- **Free fall**

  In the case of neglecting collisions, the continuity equation can be linearized as:

$$\frac{n}{\tau} = \frac{1}{\Delta x} j_{loss} = -\frac{1}{\Delta x}\frac{1}{2} nv \frac{1-r}{1+r} \tag{3.90}$$

  Thus, for the decay time τ with $\frac{1}{\Delta x} = \frac{A}{V}$

$$\frac{1}{\tau} = \frac{A}{V}\frac{1}{4}\langle v\rangle \frac{\beta}{1-\beta/2} \tag{3.91}$$

- **Transport-limited**

  If it is assumed that diffusion decisively influences the transport to the wall, the linearized continuity equation is:

$$\frac{n}{\tau} = D\frac{n}{\Lambda^2} \tag{3.92}$$

  Empirically, it has been shown that the characteristic length Λ can be written as:

$$\Lambda^2 = \Lambda_0^2 + \lambda\frac{V}{A} \tag{3.93}$$

  Here, Λ_0 is the geometry constant resulting from the solution of the continuity equation without considering wall effects (e.g., π/l in planar-parallel geometry). The value for λ is obtained from the approach:

$$j_{loss} = D\nabla n = D\frac{n}{\lambda} = \frac{1}{2}nv\frac{1-r}{1+r} \tag{3.94}$$

  This implies that λ:

$$\frac{1}{\lambda} = \frac{1}{D}v\frac{1}{4}\frac{\beta}{1-\beta/2} \tag{3.95}$$

  Thus, the approach is:

$$\frac{1}{\tau} = D\frac{1}{\Lambda_0^2 + \lambda\frac{V}{A}} \tag{3.96}$$

  The value for β is contained in the expression for λ.

Bibliography

[Cha87] P. Chantry. *J. Appl. Phys.*, 62:1141, 1987.

Chapter 4

Neutral Particle-Solid Interaction

4.1 Adsorption

In general, a distinction is made between **physisorption** and **chemisorption**. In physisorption, the adsorbate retains its chemical identity, and the binding energy is < 0.5 eV. In chemisorption, the adsorbate loses its original identity, as a new covalent or ionic bond is formed with the solid. The binding energy in this case is usually > 0.5 eV.

4.1.1 Physisorption

In physisorption, the binding is determined by the induced dipole-dipole interaction, the **van der Waals bond**. Both in the adsorbate and in the substrate, a respective dipole moment is induced. A prominent example of this type of bond is the adsorption of noble gases on metals at low temperatures.

There are two variants to calculate this induced dipole-dipole interaction.

- **Lenard-Jones Potential**

  The potential energy of the interaction of two dipoles is:

$$E_{pot} \propto -\vec{p}_{adsorbats}\vec{p}_{substrate} \tag{4.1}$$

  The electric field of a dipole scales with the distance r as:

$$\vec{E} \propto \frac{1}{r^3} \tag{4.2}$$

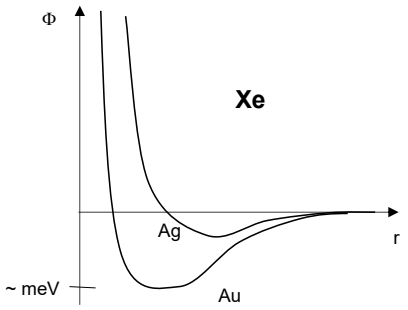

Figure 4.1: Physisorption of Xe on silver or gold surfaces. The binding energy is usually in the meV range and proportional to the electron density in the metal.

In the case of induced dipole-dipole interaction, the electric field of the dipole in the adsorbate now induces a dipole moment in the substrate through polarization. The polarization of the substrate is described by the polarizability $\alpha_{Substrat}$ as follows:

$$\vec{p}_{substrat} = \alpha_{substrat}\vec{E}_{adsorbate} \tag{4.3}$$

Here, we assume that the adsorbate carries a dipole moment that is linked to a corresponding electric field $\vec{E}_{adsorbate}$. Conversely, the dipole moment of the adsorbate is given by the electric field of the substrate as:

$$\vec{p}_{adsorbate} = \alpha_{adsorbate}\vec{E}_{Substrate} \tag{4.4}$$

If these equations are taken together, the potential energy of the bond between adsorbate and substrate through the induced dipole-dipole interaction is obtained as:

$$E_{pot} \propto -\vec{p}_{adsorbate}\vec{p}_{substrate} = -\alpha_{substrate}\alpha_{adsorbate}|E|^2 \propto -\frac{\alpha_{substrate}\alpha_{adsorbate}}{r^6} \tag{4.5}$$

The repulsive part of the interaction arises from the Pauli exclusion principle. This part is arbitrarily designated with a scaling of $1/r^{12}$. This gives the Lenard-Jones potential as:

$$\boxed{E_{pot} = \frac{c_1}{r^{12}} - \frac{c_2}{r^6}} \tag{4.6}$$

According to this consideration, the binding energy in the case of van der Waals interaction is particularly large when the corresponding polarizabilities are large. Thus, Xe has a higher binding energy because its polarizability is large compared to He due to the high number of electrons. The adsorption on metals with high electron density such as Au is greater compared to Ag.

- **Image Force**

  In the case of very conductive substrates, one can assume that the moving electron in the adsorbate atom creates an electrostatic image of itself in the substrate, as illustrated in Fig. 4.2.

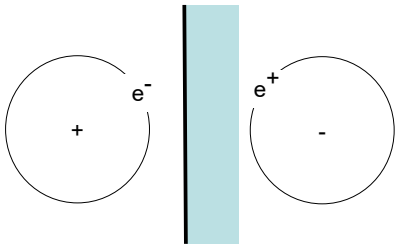

Figure 4.2: Image potential.

The potential energy is composed of the individual contributions of the repulsive interaction between like charges and the attractive interaction between unlike charge carriers:

$$E_{pot} = \frac{1}{2}\left[-\frac{e^2}{2r} - \frac{e^2}{2(z-r)} + \frac{e^2}{2z-r} + \frac{e^2}{2z-r}\right] \tag{4.7}$$

The distance between the atomic nucleus and the surface is z and the radius of the electron orbit is r. If the expression for the potential energy is developed into small terms $r/z \ll 1$, one obtains:

$$E_{pot} = -\frac{1}{8}\frac{e^2 r^2}{z^3} \tag{4.8}$$

One can see that the potential energy scales with the distance z^{-3} and thus has a greater range than the classical Lenard-Jones potential.

Nevertheless, the absolute value of the binding energy always remains in the meV range.

4.1.2 Chemisorption

Compared to physisorption, a direct chemical bond is formed in chemisorption, in which the identity of the adsorbing molecule is lost. Let us first consider the chemical bond in a molecule.

The H_2^+ Ion

In the hydrogen molecule ion H_2^+, the distance of the protons is given as r, the distance r_1 of the electron to proton 1 and r_2 to proton 2, as illustrated in Fig. 4.3.

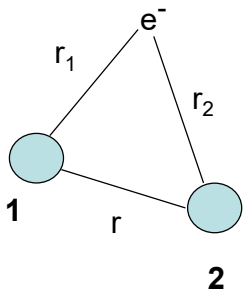

Figure 4.3: Coordinate system for the H_2^+-ion.

The potential energy of the system has an attractive contribution of the electron to the two protons and a repulsive part of the protons to each other.

$$E_{pot} = \frac{e^2}{4\pi\epsilon_0}\left(-\frac{1}{r_1} - \frac{1}{r_2} + \frac{1}{r}\right) \tag{4.9}$$

To determine the wave function of the electron, we make the assumption that it arises from a linear combination of atomic wave functions (**LCAO Linear Combination of Atomic Orbitals**). Since both protons are indistinguishable, the probability of presence of the total wave function must be symmetric with respect to the plane of symmetry of the molecule. There are two possible linear combinations for this.

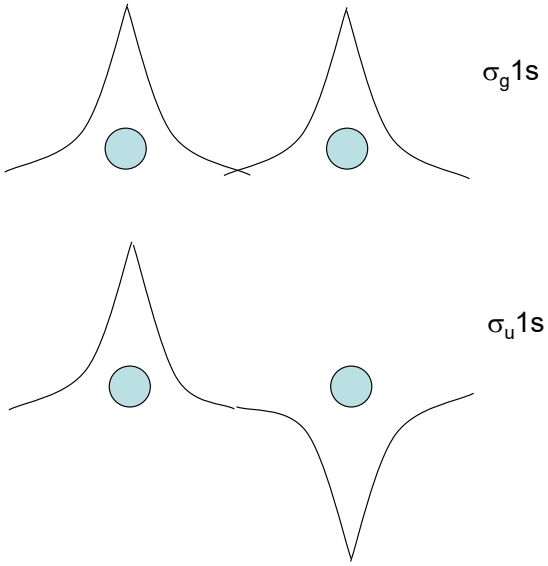

Figure 4.4: Linear Combination of Atomic Orbitals LCAO. Superposition of 1s wave functions as even and odd total wave function.

$$\Psi_1 \propto \Phi_A + \Phi_B \tag{4.10}$$
$$\Psi_2 \propto \Phi_A - \Phi_B \tag{4.11}$$
$$\tag{4.12}$$

In homonuclear molecules, the total wave function has different symmetry behavior. One distinguishes even and odd wave functions for which the following must apply:

$$\Psi_{\text{even}}(\vec{r}) = \Psi_{\text{even}}(-\vec{r}) \tag{4.13}$$
$$\Psi_{\text{odd}}(\vec{r}) = -\Psi_{\text{odd}}(-\vec{r}) \tag{4.14}$$

In Fig. 4.4, the case of the superposition of 2 1s wave functions is shown. The case of the linear combination $\Phi_A(1s) + \Phi_B(1s)$ results in an even wave function. The case of the linear combination $\Phi_A(1s) - \Phi_B(1s)$ results in an odd wave function. If the probability of presence of the electron $|\Psi^2|$ is formed, it can be seen that only in the case of the even total wave function

a finite electron density *between* the two atoms is created. This finite electron density reduces the repulsive interaction of the two protons with each other. Consequently, the function Ψ_{even} describes the bonding molecular state and the function Ψ_{odd} the anti-bonding state. The energy difference of the molecular levels between a bonding and a non-bonding state depends on the overlap of the wave functions.

A more detailed analysis yields the variation of the total energy with the distance of the protons r, once for the bonding state and once for the anti-bonding state in Fig. 4.5. Only in the state Ψ_{even} a minimum in the potential energy occurs at an atomic core distance of 1.06 $\mathring{A}$.

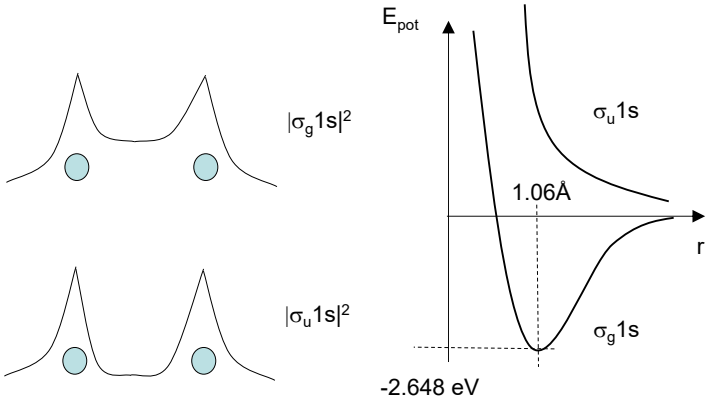

Figure 4.5: Electron density in the H_2^+-ion for the even and odd total wave function. Potential energy as a function of the atomic core distance R.

Bond Atom-Metals

When an atom or molecule bonds with a substrate, a splitting of the levels occurs, which can be large or small depending on the overlap of the wave functions. In many metals, on the one hand, there are the s-electrons, which are responsible for the chemical bond, but also the localized d-electrons. Both states contribute differently to the bond between atom and adsorbate. If the band in the solid is broad as in s-band metals (Na, Mg,...) e.g., the overlap is small and the level of the adsorbate broadens at most. If the band in the solid is narrow, since the states are localized as e.g. in the d-band metals, a strong splitting of the levels is observed.

When an atom or molecule comes into contact with a surface, a **charge transfer** can occur and electrons from the solid occupy the bonding or non-

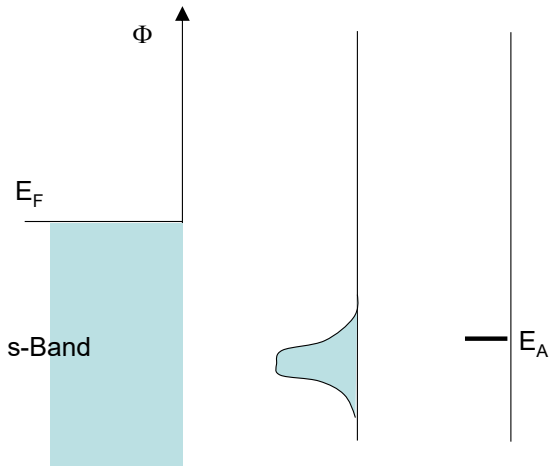

Figure 4.6: Level broadening when the atomic level overlaps with the s band in metals.

bonding states of the adsorbate atom. The possibility of charge transfer, however, depends on the position of the Fermi level relative to the ionization energy in the adsorbate. If the non-bonding state in the atom is occupied by charge transfer, the bond of this atom to the substrate is weak. In the case of a molecule, this can mean that when the non-bonding molecular state is occupied, the breaking of this molecule is initiated.

If, on the other hand, the ionization energy in the adsorbate is small compared to the work function in the solid, the bond is strong, since in the case of charge transfer usually only the bonding state is occupied.

A similar consideration can also be made for the comparison of the binding energies of adsorbates on noble metals compared to transition metals. With filled d bands, the occupation of the non-bonding level is dominant and the bond of the adsorbate is usually weak. With only half-filled d-bands, the bond is strong, as shown in Fig. 4.9.

Molecules, Catalysis

When molecules bond to the surface, this picture becomes more complicated, as one must consider both the bonding and non-bonding states in the molecule as well as their respective overlap with the states of the solid.

As a molecule approaches the surface, a splitting occurs both of the bonding and the non-bonding *molecular state*. The comparison of the levels

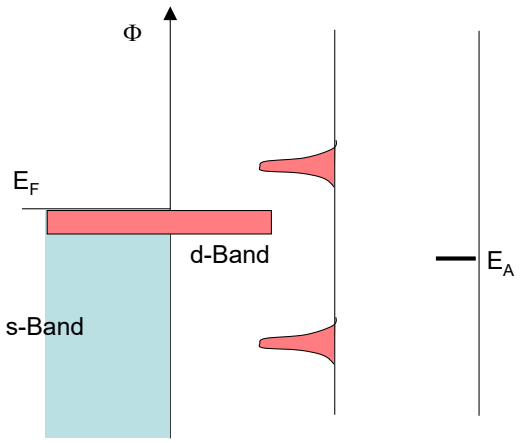

Figure 4.7: Level splitting when the atomic level overlaps with the localized d band in metals.

with the Fermi energy then determines whether the non-bonding level of the molecule can be occupied. If this is the case, the molecular bond breaks and the levels of the atom must be used for the new consideration. This course of the adsorption of a molecule is shown in Fig. 4.10:

Semiconductors

In semiconductors, the charge carrier density at the Fermi edge is very low. Consequently, the reactivity for catalysis is also very low, since the induction of reactions is always associated with a charge transfer.

4.2 Surface Processes

4.2.1 Adsorption, Desorption

The strength of the bond is visible in an experiment in which particles are adsorbed or desorbed from the surface. To calculate the rates, we first consider the total number n_0 of particles that are bound in the potential well of depth ϵ. From the convolution of the density of states $g(\epsilon)$ with the occupation $f(\epsilon)$, we obtain:

$$n_0(T) = \int_{-E}^{0} d\epsilon g(\epsilon) f(\epsilon) \tag{4.15}$$

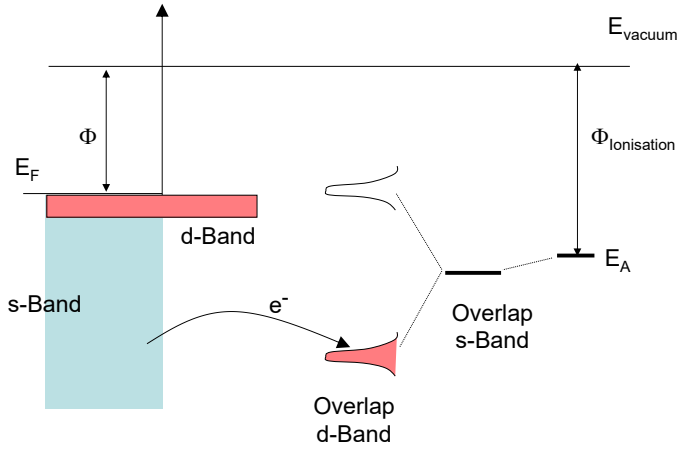

Figure 4.8: Splitting of atomic states in a d-band metal

The occupation in the potential well is given as:

$$f(\epsilon) = Z_{ads} e^{-\frac{\epsilon-\mu}{k_B T}} \tag{4.16}$$

with Z_{ads} the partition function in the adsorbed state, which results from the possible internal degrees of freedom (rotation, vibration). The density of states of a harmonic oscillator is derived from its energy ϵ:

$$\epsilon = \hbar\omega_0 \left(n + \frac{1}{2} \right) \tag{4.17}$$

The density of states is the number of possible states at an energy ϵ in the energy interval $\Delta\epsilon$. The number of states is obtained, neglecting the factor $1/2$, as:

$$N(E) = \frac{\epsilon}{\hbar\omega_0} \tag{4.18}$$

Here, it is additionally assumed that the frequency does not change with energy. Since the states are only occupied within $k_B T$ in the minimum of the potential well, the parabolic approximation applies and an explicit dependence $\omega(\epsilon)$ does not need to be considered. The density of states is thus:

$$g(\epsilon) = \frac{dN}{d\epsilon} = \frac{1}{\hbar\omega_0} \tag{4.19}$$

By integrating Eq. 4.15, the number of particles in the well is obtained as:

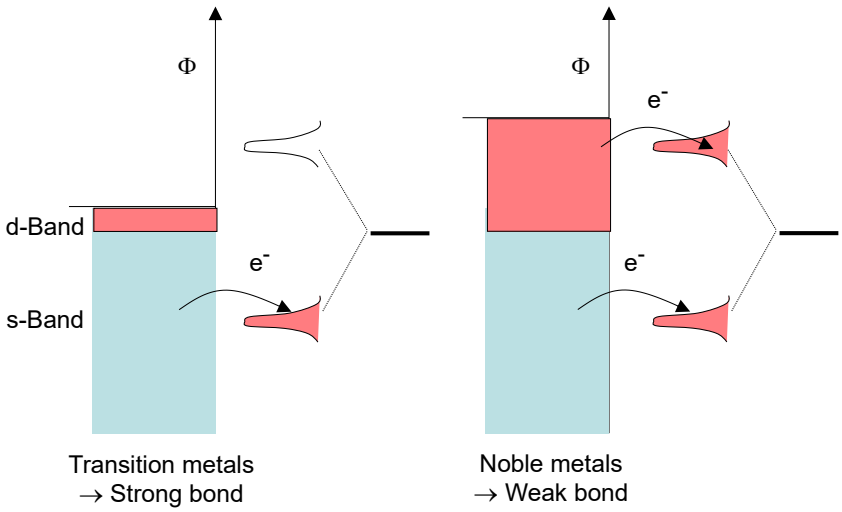

Figure 4.9: The strength of the bond depends on the width of the d-band.

$$n_0(T) = \frac{k_B T}{\hbar\omega_0} Z_{ads} e^{\frac{\mu+E}{k_B T}} \tag{4.20}$$

The flux of particles $J_{out,1}$ that desorb is given as the number of particles in the potential n_0 times a rate R. This rate is the desorption rate that we want to determine.

$$J_{out,1} = n_0(T) R \tag{4.21}$$

When these particles have moved away from the surface, they occupy states in the phase space of free particles. This number given as flux ($\frac{\Delta n}{dt}$) times dt becomes:

$$\begin{aligned} \frac{\Delta n}{\Delta t} dt = J_{out,2} dt &= \int_0^\infty \frac{dx dp}{h} f(\epsilon) \\ &= \frac{1}{h} \int_0^\infty \frac{dx}{dt} dp f(\epsilon) dt \\ &= \frac{1}{h} \int_0^\infty \frac{p}{m} dp f(\epsilon) dt \\ &= \frac{k_B T}{h} Z_{frei} e^{\frac{\mu}{k_B T}} dt \end{aligned} \tag{4.22}$$

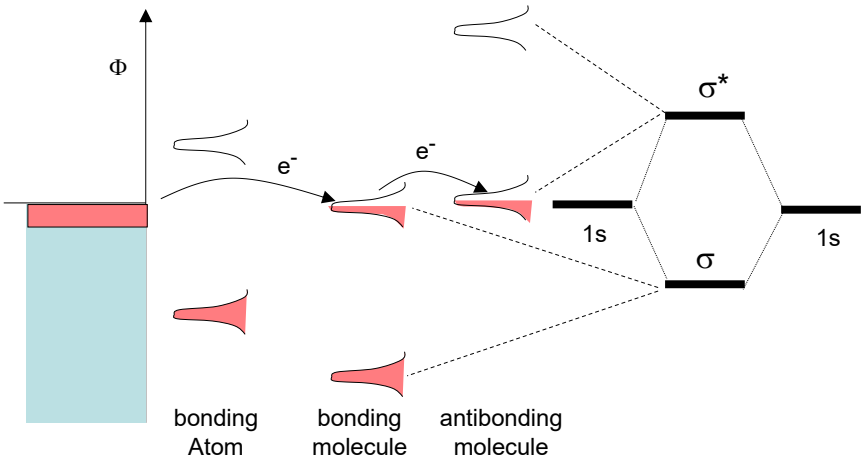

Figure 4.10: Dissociation of a molecule on the surface is only possible if the anti-bonding orbital of the molecule can be occupied by charge transfer.

Due to particle conservation, the particle fluxes according to Eq. 4.21 and Eq. 4.22 must be equal:

$$J_{out,1} = J_{out,2} \tag{4.23}$$

Thus, the **Arrhenius law** for the desorption rate is obtained with:

$$\boxed{R_{Desorption} = R_0 = \frac{\omega_0}{2\pi}\frac{Z_{frei}}{Z_{ads}}e^{-\frac{E}{k_B T}}} \tag{4.24}$$

One can see that the rate R follows an exponential law with an activation energy E. The prefactor scales with the vibrational frequency of the adsorbed atom. This can be understood intuitively, since the atom moves away from the surface once in every vibrational period and thus tries to overcome the potential barrier.

4.2.2 Sticking Coefficient

In the sense of time reversal, one could also equate the rate of desorption with a rate of adsorption. However, the probability that a particle with energy ϵ upon impact on the wall falls into the potential well is less than 1. This is described by the so-called **sticking coefficient** $s(\epsilon)$ or $s(T)$:

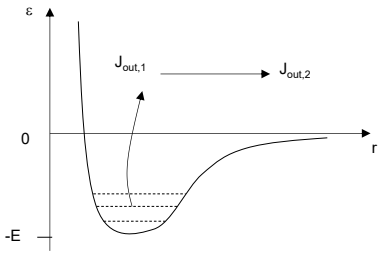

Figure 4.11: Desorption by excitation of particles from the chemisorption potential

$$R_{adsorption} = R_0 \underbrace{\int_0^\infty s(\epsilon) e^{-\frac{\epsilon}{k_B T}} d\left(\frac{\epsilon}{k_B T}\right)}_{s(T)} \tag{4.25}$$

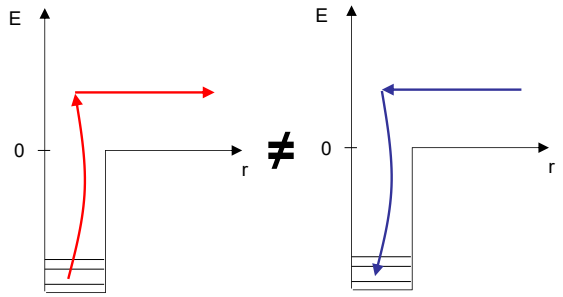

Figure 4.12: The rate of desorption and adsorption differ by the sticking coefficient.

$s(\epsilon)$ denotes the probability for a particle with kinetic energy ϵ to be trapped in the potential well. $s(T)$ takes into account that at a temperature T only a part of all particles have the energy ϵ.

How can a finite sticking coefficient $s(\epsilon)$ now be calculated? For this purpose, a box potential is illustrative. We consider the geometry as sketched in Fig. 4.13. A particle of mass M and energy E_{kin} hits a surface atom of mass m and temperature T_s. On the surface, there is a chemisorption potential of depth ϵ.

The velocity v_h of the incident particle upon impact on the surface atom

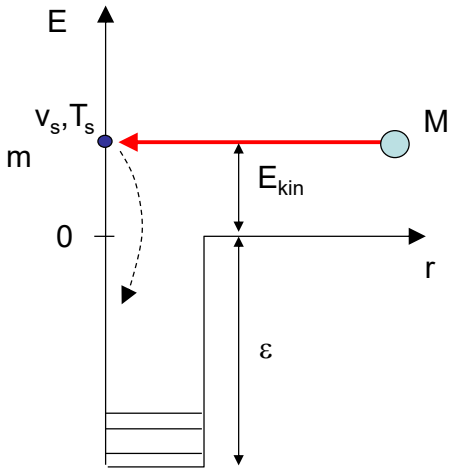

Figure 4.13: Estimation of the sticking coefficient based on a box potential. The incident particle has the mass M and kinetic energy E_{kin}. The surface atom has the mass m and the temperature T_s.

is[1]:

$$v_h = -\left[\frac{2}{M}(E_{kin} + \epsilon)\right]^{1/2} \tag{4.26}$$

That is, as the particle approaches the surface, its kinetic energy initially *increases* in the chemisorption potential. The probability of a collision with a surface atom with velocity v (expressed by a Maxwell distribution $\propto \exp(-a^2v^2)$) is given as:

$$p(v)dv = (v_h - v)\exp(-a^2v^2)dv \tag{4.27}$$

If the velocities of the substrate atom v and the adsorbate atom v_h point in the same direction, collisions are less frequent than if the two velocities are oppositely directed.

For the sticking coefficient, it is now decisive how great the probability is that a particle *after* the collision has an energy less than ϵ. Then it remains trapped in the potential well. The kinematics require for the velocity v_h' after the collision of an adsorbate particle with the surface atom:

[1] we consider the one-dimensional case; therefore v_h is negative according to the chosen coordinate system.

$$v_h' = \frac{\mu - 1}{\mu + 1} v_h + \frac{2}{\mu + 1} v \qquad mit \qquad \mu = \frac{M}{m} \tag{4.28}$$

The kinematic factor γ describes the fraction of energy that can be transferred to a substrate atom:

$$\gamma = 4 \frac{mM}{(m + M)^2} \tag{4.29}$$

At a critical velocity v_c, the energy after the collision will be less than ϵ. That is, $\frac{1}{2} m v_c^2 = \epsilon$. Thus, the condition is obtained:

$$v_c = \frac{1}{2} \left[(1 + \mu) \left(\frac{2\epsilon}{M} \right)^{1/2} + (1 - \mu) v_h \right] \tag{4.30}$$

The sticking coefficient $s(\epsilon)$ is given as:

$$s = \frac{\int_{-\infty}^{v_c} (v_h - v) \exp(-av^2) dv}{\int_{-\infty}^{\infty} (v_h - v) \exp(-av^2) dv} \tag{4.31}$$

The solution of the integrals gives:

$$s(v_h, \epsilon, a) = \frac{1}{2} + \frac{1}{2} \mathrm{erf}(av_c) + \exp(-a^2 v_c^2) \frac{1}{2av_h \pi^{1/2}} \tag{4.32}$$

The dependence of the sticking coefficient 4.32 on the parameters of our model can be illustrated as follows:

- **Depth of the potential well, according to ϵ**

  If the depth of the potential well becomes larger, the kinetic energy of the particle increases. In the momentum transfer, energy is transferred according to the kinematic factor γ. The absolute amount of this energy transfer becomes larger, and the greater reduction of the potential energy of the particle leads to it being trapped in the potential well. The sticking coefficient increases with increasing depth of the potential well.

- **Higher particle energy, according to v_h**

  At a higher particle energy, more energy must be lost in the surface collision in order for the particle to be trapped. The sticking coefficient decreases with increasing particle energy.

- **Mass difference according to μ**

  The kinematic factor γ becomes unfavorable with a large difference in the masses of the collision partners. Consequently, the sticking coefficients for hydrogen atoms are usually very small. In the microscopic sense, the possibility of energy transfer upon collision with a surface atom depends on the coupling to the phonon spectrum of the solid.

- **Substrate temperature according to a**

  At a high substrate temperature, the sticking coefficient decreases, since according to the Maxwell distribution, the velocity of the surface atoms increases. Since collision processes with surface atoms whose velocity is oppositely directed occur more frequently, the energy loss of the adsorbate particles is smaller. The sticking coefficient decreases with increasing temperature.

4.2.3 Adsorption Isotherms

The determination of the sticking coefficient can be done in different ways. The simplest is the direct measurement by a scattering experiment in which a quantified beam of particles is reflected from a surface and the particle loss or the growth rate is measured. However, it is also possible to determine the sticking coefficient from a determination of the surface coverage Θ in equilibrium.

The coverage of a surface depends on the incident particle flux j_{in}, the sticking coefficient s, and the desorption rate R. In the simplest case, the density of adsorbed particles on the surface is given as:

$$\frac{dn_{ads}}{dt} = j_{in} \underbrace{s_0(1-\Theta)}_{s(\Theta)} - \Theta n_0 R \tag{4.33}$$

with n_0 the number of surface sites. s_0 is the sticking coefficient on the uncovered surface. The differential equation for Θ gives:

$$\frac{dn_0\Theta}{dt} = j_{in} s_0(1-\Theta) - \Theta n_0 R \tag{4.34}$$

Langmuir Isotherm

As a measurement, one either considers the change in coverage Θ as a function of the particle flux (isotherm) or as a function of the substrate temperature as the determining quantity for the desorption rate R.

If one starts with the exposure of a surface at constant temperature, the surface coverage initially changes according to:

$$\frac{d\Theta}{dt} \propto s_0 j_{in} \qquad \Theta \ll 1 \tag{4.35}$$

In the case of a Langmuir isotherm, it is assumed that the sticking coefficient $s(\Theta)$ depends in a simple way on whether the surface site is occupied or not. This approach was chosen in Eq. 4.34 and one obtains:

$$\frac{s(\Theta)}{s_0} = (1 - \Theta) \tag{4.36}$$

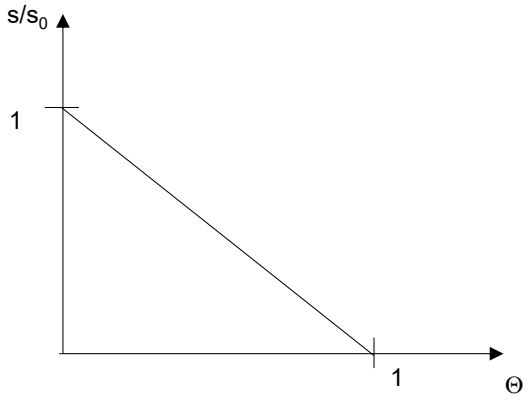

Figure 4.14: Dependence of the sticking coefficient on the coverage in the case of Langmuir adsorption.

Hot Precursor

In adsorption processes, it is often possible that either surface diffusion occurs or that several free adsorption sites are needed to chemisorb all atoms of a molecule, for example (e.g., dissociative chemisorption). These cases can be described in general by considering the adsorption process as a sequence of reaction steps.

Initially, the probability of an adsorbed particle to chemisorb is given as p_a. The probability to diffuse to an adjacent site is given as p_m. The probability to desorb, if the surface site is unoccupied, is p_d, if it is occupied p'_d. The sum of these probabilities is one. Now, the adsorption at a surface site 1 is considered:

$$p_a(1) = p_a(1-\Theta) \quad (4.37)$$
$$p_d(1) = p_d(1-\Theta) + p'_d\Theta \quad (4.38)$$
$$p_m(1) = 1 - p_a(1) - p_d(1) \quad (4.39)$$

With a probability $p_m(1)$, the particle diffuses to an adjacent site 2. At this site, new probabilities arise:

$$\begin{aligned} p_a(2) &= p_m(1)p_a(1-\Theta) \\ p_d(2) &= p_m(1)\left(p_d(1-\Theta) + p'_d\Theta\right) \\ p_m(2) &= 1 - p_a(2) - p_d(2) \end{aligned}$$

One can see that for a given coverage Θ, the total probability to chemisorb (corresponding to the sticking coefficient) is obtained as:

$$s = p_a(1-\Theta)\left[1 + p_m(1) + p_m(2) + ...\right] \quad (4.40)$$

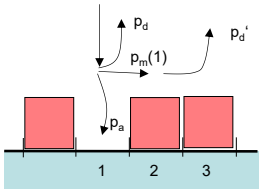

Figure 4.15: Probability p_a describes adsorption, p_m diffusion to an adjacent surface site, and p_d for desorption.

This leads to a geometric series with the limit:

$$s = \frac{p_a(1-\Theta)}{1 - p_m(1)} \quad (4.41)$$

This can be solved to the so-called **Kisliuk model**:

$$\frac{s}{s_0} = \left(1 + \kappa\frac{\Theta}{1-\Theta}\right)^{-1} \quad (4.42)$$

with

$$s_0 = \frac{p_a}{p_a + p_d} \qquad \kappa = \frac{p'_d}{p_a + p_d} \tag{4.43}$$

The form of the sticking coefficient s as a function of κ is shown in Fig. 4.16. The number κ^{-1} corresponds to the number of adsorption sites that are visited before chemisorption takes place. Three cases can be distinguished:

- $\kappa^{-1} \gg 1$

  The number of adsorption sites is high; the number of sites an incident particle visits before chemisorption takes place is high. Even at high coverage, the probability of chemisorption is high, since the adsorbed particle can find the few free sites through surface diffusion. One speaks of *associative adsorption*.

  This form of the model is also referred to as the *hot precursor* model. On corrugated[2] surfaces, the perpendicular momentum of an incident particle can easily be converted into a transverse momentum.

- $\kappa^{-1} = 1$

  For a value of $\kappa = 1$, the above description reduces to the simple expression for the Langmuir isotherm 4.36:

  $$\frac{s}{s_0} = \left(1 + \frac{\Theta}{1-\Theta}\right)^{-1} = 1 - \Theta \tag{4.44}$$

  The Langmuir isotherm corresponds to a surface mechanism in which a particle does not diffuse, i.e., $p_m(1) = 0$, and in which the particle is not adsorbed at an occupied surface site, i.e., $p'_d = 1$. This gives for Eq. 4.39:

  $$0 = 1 - p_a(1-\Theta) - p_d(1-\Theta) - \Theta \tag{4.45}$$

  This solves to:

  $$p_a + p_d = 1 \tag{4.46}$$

  Thus, we obtain:

  $$\kappa = \frac{p'_d}{p_a + p_d} = \frac{1}{p_a + p_d} = 1 \tag{4.47}$$

[2]Corrugation refers to a strong variation of the potential energy with the lateral position on the surface

- $\kappa^{-1} \ll 1$

  In this case, several surface sites are needed for the adsorption of a particle. One speaks of *dissociative adsorption*. An example is the chemisorption of H_2 or O_2 on metals.

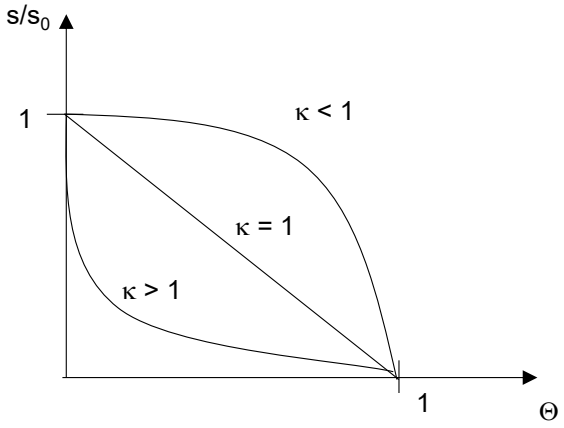

Figure 4.16: General dependence of the sticking coefficient on the coverage. κ^{-1} describes the number of surface sites visited by the incident particle or consumed in the adsorption event.

4.2.4 Activated Adsorption

In considering the sticking coefficient, we initially assumed the simple model of a box potential for chemisorption on the surface.

Let us now consider the dissociative adsorption of a molecule A_2. On the surface M, there is initially the chemisorption potential. The depth of this potential well corresponds to the chemical bonds $A - M$ in the order of several eV. However, there is also a physisorption potential for the binding of the entire molecule A_2 to the surface $A_2 - M$. The depth of this potential well is much smaller, in the order of $< 0.5eV$. As a molecule approaches the surface, it is first accelerated in the respective potential well. If it can give off enough kinetic energy to the solid, the particle can be trapped in the potential well. It adsorbs. Now, two cases can be distinguished, according to Fig. 4.17:

If an atom is initially in the physisorption minimum, the sticking coefficient depends on whether the particle can overcome the barrier to the

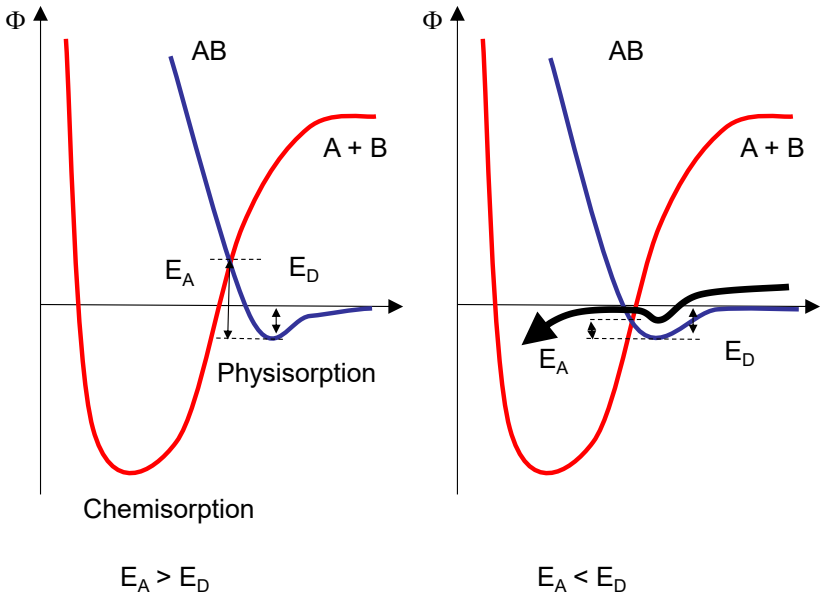

Figure 4.17: Thermally activated chemisorption occurs if the activation energy between the physisorption potential and the chemisorption potential is greater than the binding energy of the physisorption potential.

chemisorption well (this corresponds to the probability p_a), or whether the particle desorbs from the surface again (this corresponds to the probability p_d). The corresponding probabilities with the activation energies from Fig. 4.17 are:

$$p_a = \nu_a e^{-\frac{\epsilon_A}{k_B T}} \tag{4.48}$$

$$p_d = \nu_d e^{-\frac{\epsilon_D}{k_B T}} \tag{4.49}$$

ν_a and ν_d are prefactors. This results in a temperature dependence for the sticking coefficient s_0 of the uncovered surface:

$$s_0 = \frac{p_a}{p_a + p_d} = \left[1 + \frac{\nu_d}{\nu_a} e^{-\frac{\epsilon_d - \epsilon_a}{k_B T}}\right]^{-1} \tag{4.50}$$

- **Intersection point chemisorption potential/physisorption potential > 0 or $\epsilon_a > \epsilon_d$**

Now the molecule A_2 is first trapped in the physisorption potential well. At finite temperature, the particle can either overcome the potential barrier to the chemisorption potential well or desorb again. When overcoming the potential barrier, dissociation occurs. One speaks of *thermally activated adsorption*.

Contrary to the expectation from the consideration of Eq. 4.32, the sticking coefficient increases with increasing temperature.

- **Intersection point chemisorption potential/physisorption potential < 0 or $\epsilon_a < \epsilon_d$**

  Now the molecule A_2 can be trapped directly in the chemisorption potential well. Upon approaching the surface, the molecule enters the region of the chemisorption potential for the constituents of the molecule and dissociation occurs. This is the decisive reaction step in catalysis.

  As with the simple box potential according to Eq. 4.32, the sticking coefficient decreases with increasing temperature.

The previous consideration was one-dimensional, since only the distance to the surface was directly included. In general, however, the adsorption process is a higher-dimensional process, since the system can have many degrees of freedom that can influence the reaction rate. The simplest extension of the above picture is the two-dimensional consideration with the distance of the molecule to the surface and with the distance of the atoms in the molecule to each other. Now the potential energy can be described as a function of these two coordinates, as shown in Fig. 4.18. One can see two minima, the physisorption minimum[3] and the chemisorption minimum[4]. The trajectory through the space of potential energy is referred to as **reaction coordinate**.

As a molecule approaches the surface, the distance of the atoms in the molecule initially remains constant **entrance channel**, upon approaching the surface, the distance of the atoms in the molecule would have to increase to meet the chemisorption potential for each of the atoms **exit channel**. The exact course of the reaction depends on where the saddle is located between the physisorption and chemisorption minima in the two-dimensional potential landscape. If the saddle is in the (entrance channel), a greater kinetic energy of the molecule helps to overcome this saddle. If the saddle is in the (exit channel), a vibrational excitation helps to increase the probability

[3]large distance to the surface, but distance of the atoms in the molecule as in the free molecule

[4]small distance to the surface but large distance of the atoms from each other, the molecule is dissociated

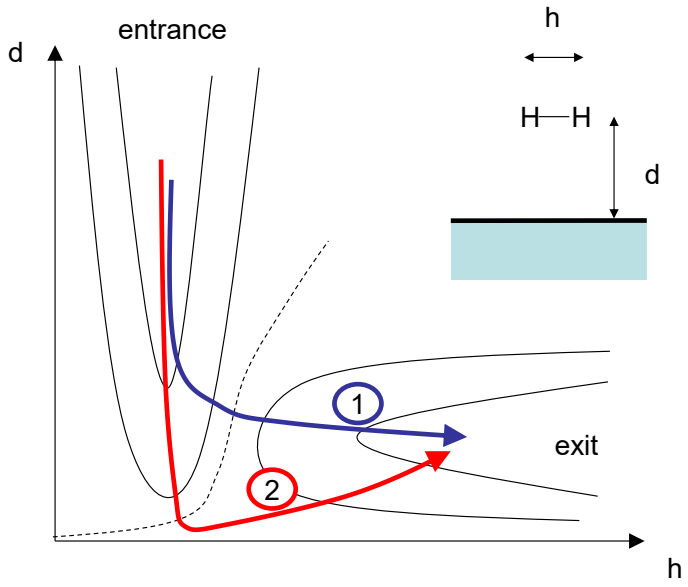

Figure 4.18: Reaction coordinates in the contour plot with the coordinates distance in the molecule h and distance d of the molecule from the surface.

of overcoming the saddle by varying the distance of the atoms in the molecule. This is shown in Fig. 4.19.

4.2.5 Surface Reactions

Surface reactions are a key goal in the application of surface physics. The most prominent example is catalysis, where the interaction of reactants with a surface catalytically accelerates the conversion of substances. The best-known example is the synthesis of ammonia, where hydrogen and nitrogen are converted into ammonia with the help of iron catalysts. The catalytic role of the surface is defined such that it enables the course of the reaction, but is not consumed in it.

In catalysis, the essential role of the surface is that it initially breaks the molecular bond through dissociative chemisorption. Then the new molecule is associated and can desorb.

For the surface reactions of two reactants A and B to a new product AB, two essential reaction pathways can be distinguished:

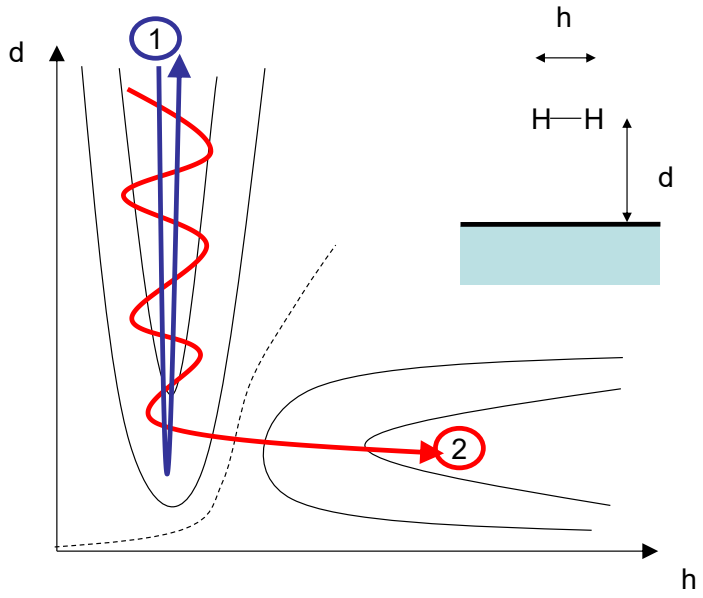

Figure 4.19: Vibrationally assisted chemisorption.

Eley-Rideal

In an Eley-Rideal reaction, the reactant A directly interacts with the adsorbed reactant B on the surface and produces the product AB that desorbs. The rate is therefore:

$$R = kp_A\Theta_B \tag{4.51}$$

p_A is the pressure of constituent A and is a measure of the flux of incident particles. Θ_B is the coverage of particle species B. k is the rate coefficient. The rate equation for Θ_B gives:

$$\frac{d\Theta_B}{dt} = s_B(1-\Theta_B)p_B - k_d\Theta_B \tag{4.52}$$

Here, p_B is the pressure of constituent B as a measure of the incident flux. s_B is the sticking coefficient of B. k_d is the desorption rate. One obtains with

$$\Theta_B = \frac{k_B p_B}{1 + k_B p_B} \tag{4.53}$$

with $k_B = \frac{s_B}{k_d}$. The rate is:

$$R = k\frac{p_A p_B k_B}{1 + k_B p_B} \tag{4.54}$$

An Eley-Rideal reaction is characterized by several things:

- **Reaction products are hyperthermal:**

  Since the reaction proceeds directly, the reaction products do not come into thermal equilibrium with the surface. This results in the desorbing particles being hyperthermal.

- **Small cross section:**

  The direct reaction, e.g., abstraction from a surface atom by an incident atom, occurs on a short time scale. Since a bond must be broken here, the probability is very small and the cross section for the reaction is small.

- **Dependence of the reaction rate:**

  Since the reactant A reacts directly, the reaction rate 4.54 increases continuously with the coverage of B until complete coverage is reached and the rate saturates (see Fig. 4.20).

Langmuir-Hinshelwood

In the Langmuir-Hinshelwood reaction, both constituents A and B first adsorb on the surface and react there to form a new molecule AB. The rate is:

$$R = k\Theta_A\Theta_B \tag{4.55}$$

p_A is the pressure of constituent A and a measure of the flux of incident particles. Θ_B is the coverage of particle species B. k is the rate coefficient. From the rate equations for Θ_B and Θ_A, one obtains:

$$\Theta_A = \frac{k_A p_A}{1 + k_A p_A + k_B p_B} \qquad \text{and} \qquad \Theta_B = \frac{k_B p_B}{1 + k_A p_A + k_B p_B} \tag{4.56}$$

Here, p_B/p_A is the pressure of constituent B/A as a measure of the incident flux. $k_A = \frac{s_A}{k_d}$ and $k_B = \frac{s_B}{k_d}$. The rate is:

$$R = k\frac{k_A k_B p_A p_B}{(1 + k_A p_A + k_B p_B)^2} \tag{4.57}$$

The Langmuir-Hinshelwood reaction has the following characteristics:

- **Reaction products thermal**

  Since the reactants A and B are in thermal equilibrium with the surface, the temperature of the desorbing products AB is equal to the substrate temperature.

- **Large cross section**

  The cross sections for the Langmuir-Hinshelwood reaction are usually large, since the reaction times of the adsorbed reactants A and B can become sufficiently long.

- **Dependence of the reaction rate**

  The rate for the formation of the product AB depends on the *simultaneous* coverage of the surface with reactant A and B. Only then does one obtain an optimum in the rate (see Fig. 4.20).

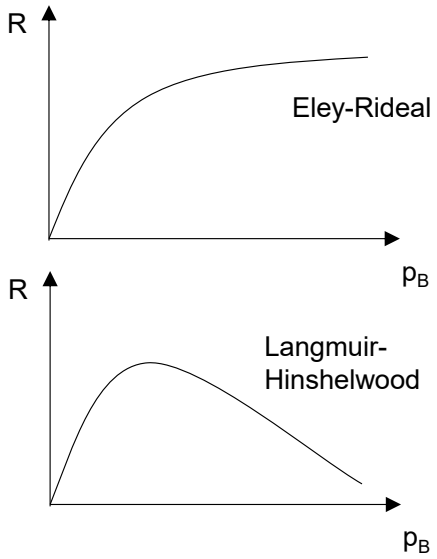

Figure 4.20: Reaction rates as a function of the pressure p_B of the constituent B in the case of an Eley-Rideal (ER) or Langmuir-Hinshelwood (LH) mechanism.

4.3 Example: a-Si:H Deposition

Amorphous silicon is an important component of plasma technology, as it is the only thin-film material from which electronic components can be manufactured. Pure amorphous silicon is initially a material with poor electronic properties. However, it has been shown that the addition of hydrogen greatly increases the conductivity [Abe93]. Hydrogen incorporated into the amorphous network thus saturates defects in the band center. This material can be produced in different ways:

- **PECVD in Silane Plasmas**

  The most established method for producing amorphous silicon films is coating from silane plasmas. Here, electron impact-induced dissociation of silane initially dominates, according to:

  $$e^- + SiH_4 \rightarrow SiH_2 + 2H + e^- \tag{4.58}$$

  In this dissociation, excited silane is initially formed, which relaxes under *evaporation* of two hydrogen atoms. This is in contrast to the dissociation of methane, which directly leads to CH_3.

  $$SiH_4^* \rightarrow SiH_2 + 2H \tag{4.59}$$

  If the partial pressure of SiH_4 is high enough, the very reactive SiH_2 reacts with SiH_4.

  $$SiH_2 + SiH_4 \rightarrow Si_2H_6 \tag{4.60}$$

  Finally, disilane is then dissociated into silyl radicals.

  $$e^- + Si_2H_6 \rightarrow 2SiH_3 + e^- \tag{4.61}$$

  According to this reaction scheme, two important reaction partners can be formed that are important for film synthesis: (i) SiH_2 if the SiH_4 partial pressure is low (ii) SiH_3 and Si_2H_6 if the partial pressure of SiH_4 is high. In the experiment, it was shown that only in the latter case can films with good electronic properties also be produced. Therefore, one must ensure in silicon coating that the plasma is operated so that only a small part of SiH_4 is consumed or converted. Typically, this is only 10

- **Reactive Magnetron Sputtering (RMS)**

  In contrast to PECVD, it is also possible to deposit a-Si:H films in reactive magnetron discharges. For this purpose, hydrogen is added to the argon discharge. Remarkable about this process is the fact that, despite the direct deposition of silicon atoms compared to SiH_3 as in PECVD, the intensive hydrogen flux is sufficient to saturate the defects in the material and actually produce a film with good electronic properties.

- **Hot filament**

  Finally, there is also the possibility to produce a-Si:H with the hot filament method. Here, the hot filament essentially serves to dissociate hydrogen. This reacts via:

$$H + SiH_4 \rightarrow SiH_3 + H_2 \tag{4.62}$$

  to form silyl radicals. The advantage over PECVD is the better scalability of the discharges.

Since the production of a-Si:H films is essentially carried out in silane plasmas with low depletion, the growth models have particularly focused on scenarios for the incorporation of SiH_3 into an a-Si:H surface.

First, the experimental observations are summarized:

- Surface loss probability β remains constant at 0.3: Numerous experiments showed that the surface loss probability for SiH_3 is constant at 0.3. This is surprising, as one would expect that processes such as surface diffusion are strongly temperature-dependent with variable substrate temperature.

- Sticking coefficient s constant at $s = 0.1$ for substrate temperatures less than 350 °C: In addition to β, s is also constant over a wide temperature range. Only above 350 °C, it increases to 0.3.

- Hydrogen concentration: The hydrogen concentration in a-Si:H decreases continuously with the substrate temperature. The hydrogen concentration on the surface, however, remains high over a wide temperature range, only the composition with respect to the proportion of SiH, SiH_2 and SiH_3 surface groups changes.

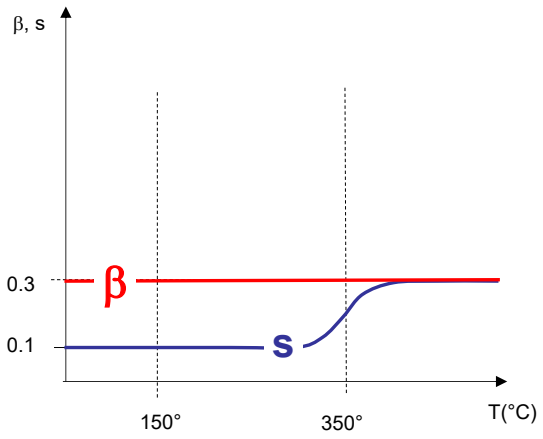

Figure 4.21: Surface loss probability and sticking coefficient as a function of the growth temperature.

Against the background of these boundary conditions, a model has initially been established that, on the one hand, brings a high sticking coefficient but also a high hydrogen coverage into harmony. By postulating a *hot precursor* mechanism, one can achieve that SiH_3 is first adsorbed on a fully covered surface and diffuses until it finds a free bond as an adsorption site. After that, desorption is classified as unlikely in this model, additionally achieving a constant incorporation probability that is independent of the substrate temperature.

This model is strictly dependent on the requirement that SiH_3 can only be incorporated at a free bond. However, it subsequently turns out that SiH_3 can also be incorporated in *strained bonds* on the surface according to:

$$SiH_3 + Si - Si \rightarrow Si - SiH_3 - H \tag{4.63}$$

The excess hydrogen is then thermally released by reconstruction of the surface.

In addition to the deposition of amorphous silicon films, it is also possible to deposit microcrystalline silicon at high hydrogen dilution of the plasmas.

4.4 Surface Roughness

The investigation of plasma-surface phenomena is made difficult in practice by the fact that the reactants and surfaces are often poorly defined. In

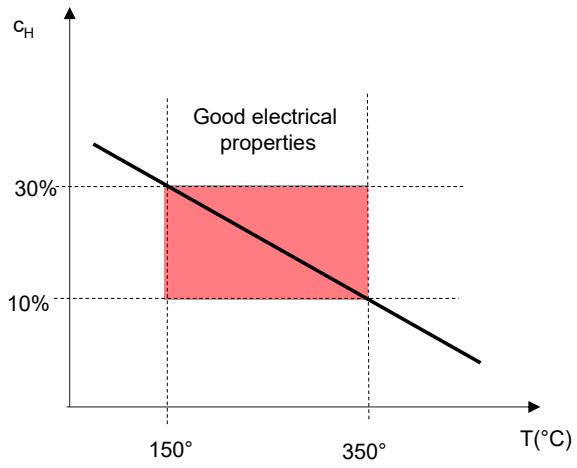

Figure 4.22: Hydrogen concentration in a-Si:H as a function of the growth temperature.

pure surface physics, one can usually refer to well-characterized surfaces and adsorbates.

An elegant way to learn something about surface processes is, on the other hand, the observation of surface roughness and its temporal development during film growth. The idea is that depending on the growth process, the surface can become very smooth or, on the contrary, rough. If a growth precursor, for example, has a large surface diffusion length, epitactic films are formed in the limit, while growth precursors with a very short surface diffusion length lead to very rough films, as illustrated in Fig. 4.24.

The mathematical tool to quantify these phenomena is described below:

4.4.1 Basic Concepts

The average film thickness in one dimension[5] is obtained by averaging the heights $h(i,t)$ over a distance L according to:

$$\langle h(t) \rangle = \frac{1}{L} \sum_{i}^{L} h(i,t) \tag{4.64}$$

[5]The dimensionality of an interface (here the surface) between the film and the environment in three dimensions is 2. In two dimensions, the interface becomes a line and the dimension of this boundary is 1.

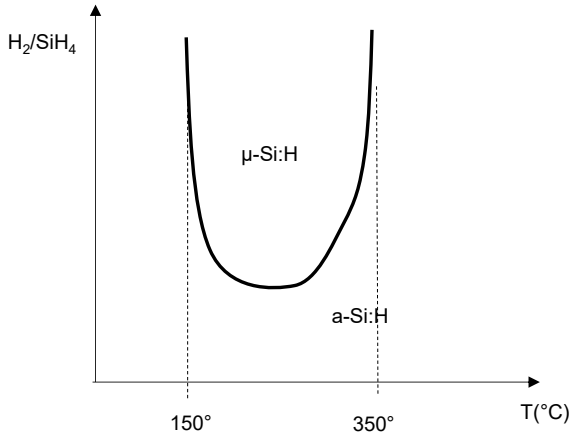

Figure 4.23: By H_2 dilution, it is possible to deposit microcrystalline silicon in silane plasmas.

This interface is created by the random impact of particles that lead to an increase in the film thickness. If the particle flux is constant over time, the following must apply:

$$\langle h(t) \rangle \propto t \tag{4.65}$$

The roughness $w(L,t)$ is defined as the quadratic deviation from the mean value, and one obtains:

$$w(L,t) = \left(\langle h^2 \rangle - \langle h \rangle^2 \right)^{1/2} = \left[\frac{1}{L} \sum_i^L \left(h(i,t) - \langle h \rangle \right)^2 \right]^{1/2} \tag{4.66}$$

This notation of a one-dimensional interface is illustrated in Fig. 4.25.

If one now lets a layer (in the computer model) grow and observes the resulting roughness, one makes the following observations (see Fig. 4.26):

- **Dynamic growth exponent** β

  The roughness begins to increase with a characteristic exponent, the dynamic growth exponent β:

$$\boxed{w \propto t^{\beta} \qquad L \to \infty} \tag{4.67}$$

  The exact value of β depends on the growth process, as will be shown further below.

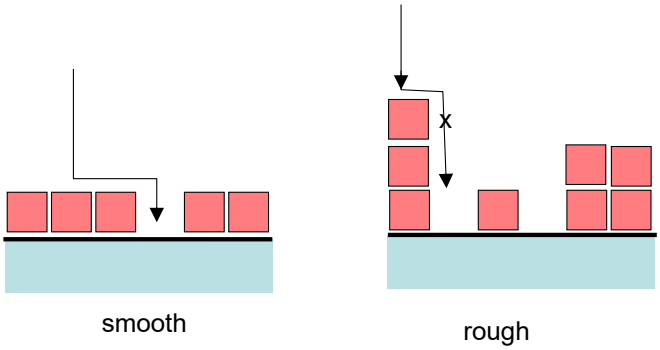

Figure 4.24: The roughness of a surface provides information about the formation mechanism of the thin film.

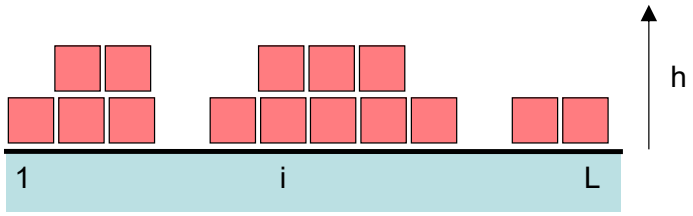

Figure 4.25: Notation for describing the surface contour.

- **Static growth exponent** α

  At a given scale of observation L, one finds that after a certain coating duration, the roughness apparently no longer changes. This is due to the fact that, for example, roughnesses become larger in scale with increasing growth, and the observation size no longer captures the morphology of the surface. If the observation scale L is changed, larger-scale roughnesses can be observed again, and the temporal change in roughness becomes visible again. Thus, the saturation value w_{sat} of the roughness depends on the scale of observation. This dependence follows a scaling according to the static growth exponent :

$$\boxed{w_{sat} \propto L^{\alpha} \qquad t \to \infty} \tag{4.68}$$

- **Exponent z for the time t_x at which saturation occurs:**

  The time t_x from which saturation occurs can also be expressed by a scaling that depends on the length scale of observation L:

$$\boxed{t_x \propto L^z} \tag{4.69}$$

  The parameters α, β and z are not independent of each other. At the point where saturation occurs, the dynamic (4.67) and static scaling (4.68) must coincide. Therefore, the following must apply:

$$w = t_x^\beta = L^\alpha \tag{4.70}$$

  With equation 4.69 one obtains

$$L^{z\beta} = L^\alpha \tag{4.71}$$

  From this it follows:

$$z = \frac{\alpha}{\beta} \tag{4.72}$$

The scaling laws for roughness can be expressed in summary as a unique function:

$$w(L,t) \propto \underbrace{L^\alpha}_{Scale} \quad \underbrace{f\left(\frac{t}{t_x}\right)}_{Time\ dependence} \tag{4.73}$$

Growth Mechanisms The absolute size of the growth exponents depends on the growth mechanism of thin films. In the experiment, one observes the roughness over time and compares the plot of this quantity with Eq. 4.67. Alternatively, one can also observe a given film on different scales and determine the respective roughness. The comparison with Eq. 4.68 then provides information about the static growth exponent.

As possible growth mechanisms, some are highlighted (see Fig. 4.27):

- **Random Deposition**

  In random deposition, the incident particle is directly incorporated. Since the point of impact is statistically distributed, this process follows Poisson statistics (see below). The roughness increases continuously.

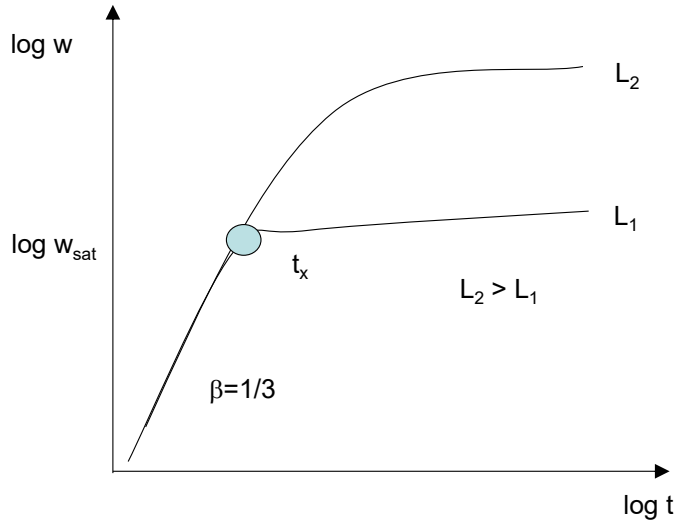

Figure 4.26: Average roughness as a function of the scale of observation L and the growth time t.

- **Surface Diffusion**

  In surface diffusion, the particle can diffuse over several surface sites after adsorption to find a suitable site. This leads to smoother surfaces. A prominent example is epitaxy, in which absorbed particles are only incorporated at step edges, and layer-by-layer film growth is observed.

- **Ballistic Deposition**

  In ballistic deposition, a particle is incorporated if it finds a nearest neighbor. This creates a non-linear effect, since the incorporation probability also depends on neighboring surface sites.

4.4.2 Single Particle Modeling

For the modeling of growth phenomena, there are two fundamentally different approaches. In the single particle approach, a microscopic picture of the growth process consisting of activation barriers for surface diffusion, etc. is developed, and the resulting roughness is then calculated in a Monte Carlo computer program. In the continuum approach, one tries to encode the physics into an equation and then tries to determine the scaling properties of this equation. From this, the growth exponents then result.

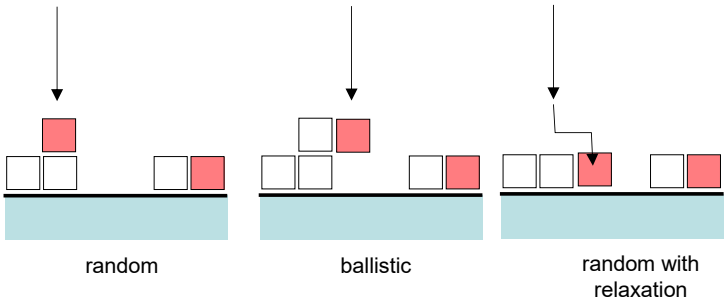

Figure 4.27: Different variants of film growth.

In the single particle picture, the random deposition can still be described analytically. The probability of reaching a height h_i at a certain location i when N particles hit over a distance L is given by the following probability:

$$P(h,N) = \left(\begin{array}{c} N \\ h \end{array} \right) p_i^h (1-p_i)^{N-h} \tag{4.74}$$

The average film thickness is therefore:

$$\langle h \rangle = \sum_i^N h_i P(h,N) = Np = \frac{N}{L} = t \tag{4.75}$$

The mean value of the square of the height is:

$$\langle h^2 \rangle = \sum_i^N h_i^2 P(h,N) = Np(1-p) + N^2 p^2 \tag{4.76}$$

From this, the roughness is obtained as:

$$w^2 = \langle h^2 \rangle - \langle h \rangle^2 = Np(1-p) = \frac{N}{L}\left(1 - \frac{1}{L}\right) = t\left(1 - \frac{1}{L}\right) \tag{4.77}$$

Finally, one obtains the dynamic growth exponent for random deposition $\beta = 1/2$. That is, the roughness increases continuously with an exponent of $1/2$. This is also referred to as *runaway roughness*:

$$w^2 \propto t \qquad bzw. \qquad w \propto t^{1/2} \tag{4.78}$$

In-Depth - Determination of Scaling via Solution of Continuum Equations

In the continuum approach, one tries to describe the physics of roughness development by a differential equation. Here, $G(h,x,t)$ describes the physics of film growth and $\eta(x,t)$ describes the fact that the incident particle flux F is a statistically fluctuating quantity.

$$\frac{\partial h}{\partial t} = G(h,x,t) + F + \eta(x,t) \tag{4.79}$$

The form of $G(h,x,t)$ can be derived from several boundary conditions. For example, the validity of the equation must not depend on the sign of x and h, etc. From this, the leading terms for G are obtained as:

$$\frac{\partial h}{\partial t} = \nabla^2 h + \nabla^4 h + \left(\nabla^2 h\right)\left(\nabla h\right)^2 + ... + \eta(x,t) \tag{4.80}$$

Random Deposition

First, consider random deposition in the continuum picture. Let F be the average flux of incident particles:

$$\frac{\partial h}{\partial t} = F + \eta(x,t) \tag{4.81}$$

The static nature of the incident flux implies that:

$$\langle \eta(x,t) \rangle = 0 \tag{4.82}$$

The incident particle flux is characterized by uncorrelated noise:

$$\langle \eta(x,t)\eta(x',t') \rangle = 2D\delta^d(x-x')\delta(t-t') \tag{4.83}$$

Here, D is a constant that is a measure of this noise, while d denotes the dimension of the problem. This term only gives a finite value if $x = x'$ and/or $t = t'$ applies. That is, events that are separated in space or time lead to $\langle \eta(x,t)\eta(x',t') \rangle = 0$ and are therefore uncorrelated.

The average film thickness after a time t is again:

$$\langle h(x,t) \rangle = \int_0^t (F+\eta)dt = Ft \tag{4.84}$$

or the average square of the height:

$$\begin{aligned} \langle h^2(x,t) \rangle &= \left(\int_0^t (F + \eta dt \right)^2 \\ &= \int_0^t F \int_0^t F + \int_0^t \int_0^t F\eta + \int_0^t \int_0^t \eta\eta \end{aligned}$$

$$\begin{aligned} &= F^2t^2 + \int_0^t 2D \\ &= F^2t^2 + 2Dt \end{aligned} \tag{4.85}$$

From this, the roughness is calculated as:

$$w^2 = \langle h^2 \rangle - \langle h \rangle^2 = 2Dt \tag{4.86}$$

One obtains again:

$$w = (2Dt)^{1/2} \tag{4.87}$$

One can see that the roughness again scales with the dynamic exponent $\beta = 1/2$, just as in the single particle approach.

$$\Delta\mu N = \gamma dA \tag{4.88}$$

If this situation is considered for a hemispherical body, one obtains the change in the chemical potential as:

$$\Delta\mu = \gamma \frac{4\pi\left((r+dr)2 - r2\right)}{4\pi r^2 dr \frac{1}{V_{Atom}}} \tag{4.89}$$

This can be shortened to the **Thomson-Gibbs formula**:

$$\boxed{\Delta\mu = 2\gamma \frac{V_{Atom}}{r}} \tag{4.90}$$

Thus, the rate of adsorption is proportional to the change in the chemical potential and inversely proportional to the curvature radius of the surface. That is, more strongly curved surfaces grow faster than less strongly curved ones. Intuitively, this can be explained by the fact that in strongly curved surfaces, a change in this curvature corresponds to a strong change in the surface tension, which is favored.

The factor $1/r$ corresponds to the curvature of a surface. Thus, one obtains the continuum approach as:

$$\frac{\partial h}{\partial t} \propto \gamma \nabla^2 h \tag{4.91}$$

Determination of the Scaling Exponents via Analysis of the Scaling of the Equations

For the description of the development of roughness, it is important to define the scaling properties of the surfaces when the observation or description scale is changed. One distinguishes self-similar and self-affine surfaces:

- **self-similar**

  In self-similar surfaces, the equations describing the physics are preserved if the quantities location x, height h, and time t are scaled as follows.

$$\begin{aligned} x &\rightarrow bx \\ h &\rightarrow bh \\ t &\rightarrow bt \end{aligned}$$

- **self-affine**

  In self-affine surfaces, on the other hand, the equations describing the physics are only preserved if the individual dimensions of the problem are scaled differently. An increase in the length scale by the factor b transforms into a scaling of the quantities height h and time t according to:

$$\begin{aligned} x &\rightarrow bx \\ h &\rightarrow b^{\alpha}h \\ t &\rightarrow b^{z}t \end{aligned}$$

We want to use the property of scaling the quantities to determine the exponents. For this purpose, the quantities α and β are chosen in such a way that the solutions become *independent* of b. We want to illustrate this with a simple example. For the derivation of the scaling properties, the transformation of the equation

$$\boxed{\frac{\partial h}{\partial t} = \gamma \nabla^2 h + \eta(x,t)} \tag{4.92}$$

is considered in the following. For a self-affine surface, we replace the quantities x, h and t according to the following rule:

$$\begin{aligned} x &\rightarrow bx \\ h &\rightarrow b^{\alpha}h \\ t &\rightarrow b^{z}t \end{aligned}$$

and arrive at the transformed equation:

$$b^{\alpha - z}\frac{\partial h}{\partial t} = \gamma b^{\alpha-2}\nabla^2 h + b^{-\frac{1}{2}(d+z)}\eta \tag{4.93}$$

Here, η was calculated as follows:

$$\langle \eta(bx, bzt)\eta(bx', bzt')\rangle = 2D\delta^d(bx - bx')\delta^2(bzt - bzt') = b^{-(d-z)}\langle \eta\eta'\rangle \tag{4.94}$$

Here, it was used that $\delta^d(bx) = b{-}d\delta^d(x)$. Thus, one finally obtains:

$$\frac{\partial h}{\partial t} = \gamma b^{(\alpha-2)-(\alpha-z)}\nabla^2 h + b^{-\frac{1}{2}(d+z)-(\alpha-z)}\eta \tag{4.95}$$

This equation must be independent of the absolute size of b, since the equation describes the physics of the mechanism and should not depend on the scale of observation. Therefore, the following must apply:

$$\begin{aligned}(\alpha - z) - (\alpha - 2) &= 0 \\ -\frac{1}{2}(d + z) - (\alpha - z) &= 0\end{aligned}$$

From this it follows that:

$$\alpha = \frac{2 - d}{2} \tag{4.96}$$

$$\beta = \frac{2 - d}{4} \tag{4.97}$$

Surface Diffusion

In the case of film growth by surface diffusion, one obtains a continuum equation according to:

$$\boxed{\frac{\partial h}{\partial t} = -K\nabla^4 h + F + \eta(x,t)} \tag{4.98}$$

The exponent ∇^4 can be motivated as follows. In surface diffusion, a material transport along the surface takes place. This particle flux is driven by a difference in the chemical potential. Thus, adsorbed atoms diffuse from a region with high chemical potential to a region with low chemical potential, according to:

$$j = -\frac{\partial \mu}{\partial x} \tag{4.99}$$

The change in height at a location x due to this surface diffusion is given by the continuity equation with:

$$\frac{\partial h}{\partial t} + \nabla j = 0 \tag{4.100}$$

Since the chemical potential scales as $\nabla^2 h \propto \mu$, one obtains overall:

$$\frac{\partial h}{\partial t} \propto \nabla^4 h \tag{4.101}$$

To derive the scaling properties of this equation for self-affine surfaces, however, the scaling properties of the prefactors must also be considered[a]. As a result, one obtains:

$$\alpha = \frac{4 - d}{2} \tag{4.102}$$

$$\beta = \frac{4 - d}{8} \tag{4.103}$$

	static α	dynamic β
Random Deposition	does not saturate	$\frac{1}{2}$
Evaporation Condensation	0	0
Ballistic Deposition	0.38	0.24
Surface Diffusion	1	$\frac{1}{4}$

Table 4.1: Scaling exponents for a 2-dim surface depending on the growth mechanism

Nonlinear Effects

The simplest case of a nonlinear effect is ballistic deposition. Here, the environment of the point of impact is decisive for the deposition as illustrated in Fig. 4.27.

The dependencies in the continuum equation can be illustrated with the help of Fig. **??**. The change in height h at a location x due to an incident flux F is given by:

$$\delta h^2 = (F\delta t)^2 + (F\delta t \tan\Theta)^2 \tag{4.104}$$

$$\delta h^2 = (F\delta t)^2 + (F\delta t \nabla h)^2 \tag{4.105}$$

$$\delta h = F\delta t \left(1 + (\nabla^h)2\right)^{1/2} \tag{4.106}$$

For $\nabla h \ll 1$ one thus obtains:

$$\boxed{\frac{\partial h}{\partial t} = F\frac{1}{2}\left(\nabla h\right)^2 + \eta(x,t)} \tag{4.107}$$

This is referred to as the **KPZ equation**. In one dimension, an analytical solution for the scaling exponents is known:

$$\alpha = \frac{1}{2} \tag{4.108}$$

$$\beta = \frac{1}{3} \tag{4.109}$$

[a] This is achieved by the renormalization group theory

In summary, the individual growth mechanisms have different scaling properties, which are summarized in Table 4.1 for the case of the two-dimensional interface.

4.4.3 Measurement Methods

There are two approaches to measuring the scaling exponents. The dynamic scaling exponent β can be determined in-situ by optical methods, e.g., ellipsometry, or ex-situ by atomic force microscopy, which is performed on films with different layer thicknesses.

The static scaling exponent α can be determined with the AFM, in which different scan areas are chosen. The comparison with Eq. 4.68 then provides information about the static growth exponent.

Bibliography

[Abe93] J.R. Abelson. *Appl. Phys. A*, 56:493, 1993.

Chapter 5

Ion-Solid Interaction

The ion-solid interaction can be separated into a nuclear and an electronic component for the case of plasma-typical energies and ions. The interaction through collisions with the target atoms describes the nuclear collision process, which leads to momentum and energy transfer. The interaction with the electrons in the solid only becomes important at high particle velocities and is usually only associated with energy loss.

The interaction of ions with the solid atoms can be considered as a consequence of individual collisions or as a collective effect [Sig81]:

- **Linear Cascade**

  If the interaction is considered as a sequence of independent individual collisions, one speaks of a linear cascade. The probability of a three-body collision at the energies considered does not come into play. This type of description is referred to as the theory of the **linear cascade**, or as BCA (binary collision approximation).

- **Heat Spike**

  In a collision process in which a lot of energy is locally deposited, the collective movement of the atoms in the target can become important. This can be considered as a local heating and one therefore speaks of a **heat spike**. However, this only becomes important for large or highly charged ions and will not be considered further.

5.1 Neutralization

As an ion approaches the surface, neutralization usually occurs well before the surface. For further consideration, it is irrelevant whether the projectile

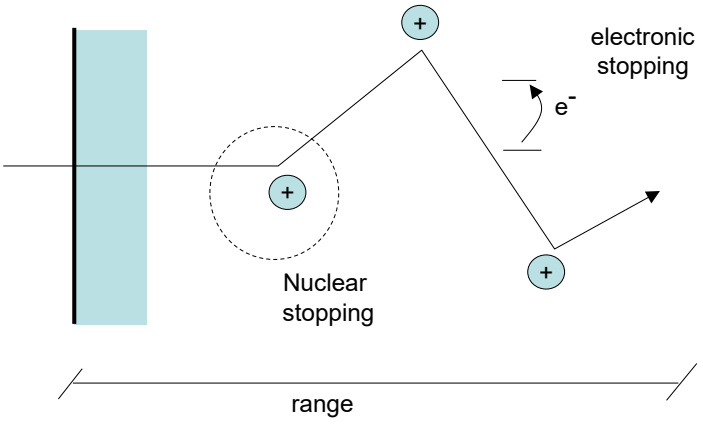

Figure 5.1: In the ion-solid interaction, one distinguishes small momentum losses due to electronic excitation and large momentum losses when scattering off the target atoms.

is considered as an ion or not, since the shielding by the solid electrons is decisive in the collision processes.

Interaction Potentials

The potential of the target atoms is characterized by their shielding by the surrounding electron gas, similar to Debye shielding in plasmas. If the electrons in a solid of length L are described as plane waves with an energy ϵ and a wave vector $\vec{k}$, one obtains:

$$\epsilon = \frac{\hbar^2 k^2}{2m_e} \tag{5.1}$$

The number N of electrons at the location $\vec{x}$ is calculated by counting in the sphere with radius $|\vec{k}|$ in the phase space at temperature $T = 0$ as follows (see Fig. 5.2):

$$\underbrace{2}_{Spins} \frac{1}{8} \frac{4\pi}{3} k^3 \frac{1}{\left(\frac{2\pi}{L}\right)^3} = N(\vec{x}) \tag{5.2}$$

Here, it is taken into account that due to the Pauli exclusion principle, each wave occupies a volume of $\left(\frac{2\pi}{L}\right)^3$ in phase space, and we only count in an octant (factor 1/8) since we consider standing waves. The connection between energy ϵ and electron density $n = \frac{N}{L^3}$ is therefore:

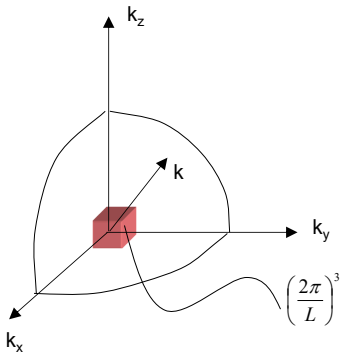

Figure 5.2: Phase space for electronic states in a solid.

$$\epsilon = \frac{\hbar^2}{2m}\left(\frac{3\pi^2}{L^3}N\right)^{2/3} = \frac{\hbar^2}{2m}\left(3\pi^2 n\right)^{2/3} \tag{5.3}$$

The density of states is given as:

$$g(\epsilon) = \frac{dn}{d\epsilon} = \frac{V}{2\pi^2}\left(\frac{2m}{\hbar^2}\right)^{3/2}\epsilon^{1/2} \tag{5.4}$$

The local variation of the kinetic energy of the electrons is a reflection of the potential energy. After the total energy remains constant, the kinetic energy ϵ increases in regions where the potential energy V is negative. With the substitution $\epsilon = -V$ one obtains:

$$n = \frac{(2m)^{2/3}}{3\pi^2\hbar^3}(-V)^{3/2} \tag{5.5}$$

By means of the Poisson equation, the potential energy V and the potential Φ for electrons are linked as $\Phi = -eV$.

$$\nabla^2\Phi = -\frac{e}{\epsilon_0}(n_+ - n_-) \tag{5.6}$$

With respect to the density n_+ of the immobile positive ions, we then obtain through a local change in the electron density n_-:

$$\nabla^2\Phi = \frac{e}{\epsilon_0}n_- \tag{5.7}$$

or as an expression for the potential energy V:

$$-\nabla^2 V \propto n \tag{5.8}$$

or as a differential equation:

$$\nabla^2 V \propto -(-V)^{3/2} \tag{5.9}$$

and with an approach according to:

$$V = \frac{Ze^2}{4\pi\epsilon_0 r}\chi \tag{5.10}$$

If we substitute this into the radially symmetric differential equation, we initially obtain:

$$\frac{1}{r^2}\frac{\partial}{\partial r}\left(r^2\frac{\partial V}{\partial r}\right) \propto -(-V)^{3/2} \tag{5.11}$$

From Eqs. 5.5, 5.10, and 5.10, the shielding of the Coulomb potential in the vicinity of a target atom, the so-called **Thomas-Fermi equation**:

$$\boxed{x^{1/2}\frac{d^2\chi}{dx^2} = \chi^{3/2}} \tag{5.12}$$

with the abbreviation

$$r = a_{TF}x \qquad\qquad a_{TF} = 0.885\frac{a_0}{Z^{1/3}} \tag{5.13}$$

For the case where the two collision partners have different nuclear charges, one uses:

$$a_{TF} = 0.885\frac{a_0}{Z_{eff}^{1/3}} \qquad\qquad Z_{eff} = \left(Z_1^{1/2} + Z_2^{1/2}\right)^2 \tag{5.14}$$

The exact solution of the Thomas-Fermi equation is complex. In particular, it is not suitable for the numerical calculation of projectile trajectories as a sequence of scattering processes on shielded potentials. To have simpler potentials for solving the scattering integral, as described below, different approximations are used:

- **Power Law**

  The shielding function $\chi(x)$ can be written as a power law with an integer exponent s. However, this type of solution is only valid in a limited range of distances between the projectile and the target atom.

Therefore, the solutions must be joined together, as illustrated in Fig. 5.3.

$$\chi(x) = \frac{k}{s}\left(\frac{a_{TF}}{r}\right)^{s-1} = \frac{k}{s}\left(\frac{1}{x}\right)^{s-1} \tag{5.15}$$

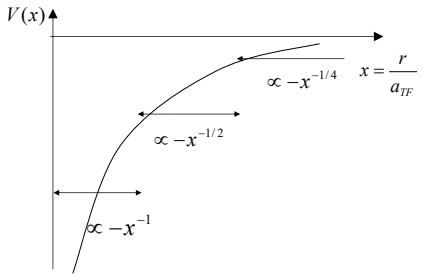

Figure 5.3: Shielding function according to the Thomas-Fermi equation.

with s an integer and k a constant.

- **Universal Law**

  A more general form of the shielding function was developed by Ziegler, Biersack, Littmark (ZBL), which corresponds to an empirical approximation for the solution of the Thomas-Fermi equation. As a shielding function, one uses an approach:

$$\chi(x) = a_0 e^{-b_0 x} + ... + a_3 e^{-b_3 x} \tag{5.16}$$

  with 8 coefficients a and b. The distance x is:

$$x = \frac{r}{a_U} \tag{5.17}$$

  with

$$a_U = 0.8854 a_0 \frac{1}{Z_1^{0.23} + Z_2^{0.23}} \tag{5.18}$$

  The exact form of the ZBL shielding is:

$$\chi(x) = 0.1818e^{-3.2x} + 0.5099e^{-0.9423x} + 0.2802e^{-0.4028x} + 0.02817e^{-0.2016x} \tag{5.19}$$

Review of Scattering Physics

Kinematics

So far, the type of scattering process has not been specified. In solving the scattering problem, the goal is to determine the dependence between the impact parameter b and the scattering angle Θ. For this purpose, one practically starts from the **center-of-mass system**. The center-of-mass velocity is:

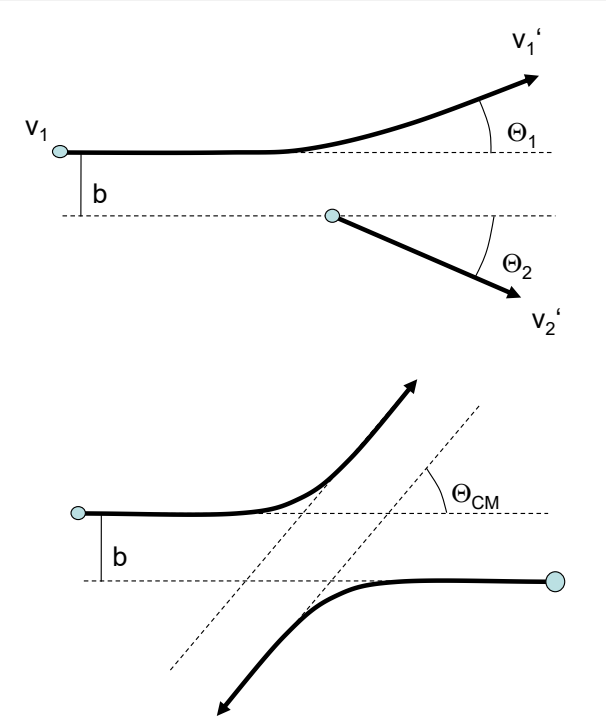

Figure 5.4: Laboratory system - center-of-mass system

$$v_{cm} = \frac{m_1 v_1 + m_2 v_2}{m_1 + m_2} \tag{5.20}$$

The reduced mass m_{cm} is:

$$m_{cm} = \frac{m_1 m_2}{m_1 + m_2} \tag{5.21}$$

The relative velocity is:

$$v_r = v_1 - v_2 \tag{5.22}$$

The scattering angles Θ_1 and Θ_2 in the laboratory system are related to the scattering angle in the center-of-mass system Θ_{cm} according to Fig. 5.4 as:

$$\tan\Theta_1 = \frac{m_2 \sin\Theta_{cm}}{m_1 + m_2\cos\Theta_{cm}} \tag{5.23}$$

$$\Theta_2 = \frac{1}{2}(\pi - \Theta_{cm}) \tag{5.24}$$

The energy loss is obtained from the solution of energy and momentum conservation for a given scattering angle. This is referred to as the **kinematic factor** γ.

$$\boxed{\frac{\Delta E}{E} = \gamma = \frac{2m_1m_2}{(m_1+m_2)^2}(1-\cos\Theta_{cm})} \tag{5.25}$$

The kinematic factor is maximized in a central collision. One obtains:

$$\gamma = 4\frac{m_1m_2}{(m_1+m_2)^2} \tag{5.26}$$

After introducing these new quantities for the center-of-mass system, the energy conservation must be solved on the trajectory:

$$\frac{1}{2}m_{cm}\left(\dot{r}^2 + r^2\dot{\Theta}_{cm}^2\right) + \Phi(r) = \frac{1}{2}m_{cm}v_R^2 \tag{5.27}$$

as well as the angular momentum conservation:

$$m_{cm}v_0 b = m_{cm}r^2\dot{\Theta}_{cm} \tag{5.28}$$

Equations 5.27 and 5.28 can be inserted into each other using the relationship:

$$\frac{d\Theta}{dr} = \frac{d\Theta}{dt}\frac{1}{\frac{dr}{dt}} \tag{5.29}$$

One finally obtains the so-called **scattering integral**:

$$\boxed{\Theta_{cm} = \pi - 2b\int_{r_{min}}^{\infty} \frac{1}{r^2\left[1 - \frac{\Phi(r)}{\frac{1}{2}m_{cm}v_R^2} - \left(\frac{b}{r}\right)^2\right]1/2}dr} \tag{5.30}$$

Here, the scattering potentials $V(r)$ are inserted according to the type of interaction and the integral is solved. This results in the dependence $\Theta(b)$, from which the differential cross section is subsequently determined.

Cross Section

To describe the cross section for a collision, the differential cross section is first introduced as the fraction of the cross section that leads to scattering into a certain solid angle element $d\Omega$:

$$\Gamma 2\pi b db = \Gamma\frac{d\sigma}{d\Omega}\underbrace{2\pi R\sin\Theta}_{Radius\ Ring}\underbrace{Rd\Theta}_{Solid\ angle\ d\Omega}\underbrace{\frac{1}{R^2}}_{Correction\ Distance} \tag{5.31}$$

Particle conservation requires that the flux through a ring of width db and radius b is identical to the flux through a ring with opening angle $d\Theta$ on the surface of a sphere with radius R. Solving gives:

$$\frac{d\sigma}{d\Omega} = \frac{b}{\sin\Theta}\frac{db}{d\Omega} \tag{5.32}$$

That is, for the determination of the differential cross section, we need a relationship between the so-called **impact parameter** b and the angle at which the particle is scattered.

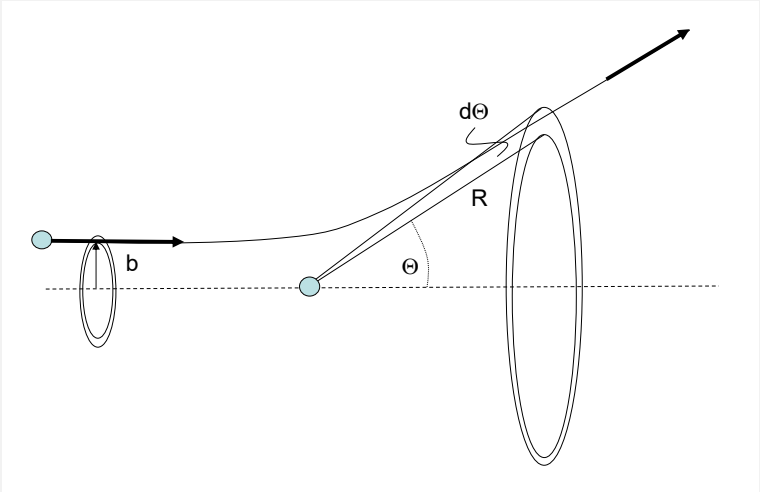

Figure 5.5: Differential cross section

The total cross section is finally obtained by integrating over the entire solid angle:

$$\sigma_{sc} = 2\pi \int_0^{\pi} \frac{d\sigma}{d\Omega} \sin\Theta d\Theta \tag{5.33}$$

However, for transport, it is not the loss of the particle that is interesting or the probability that a scattering process has occurred, but rather how much this scattering process has reduced the momentum. The corresponding cross section for momentum transfer must be corrected by the factor:

$$dp = p - p\cos\Theta \tag{5.34}$$

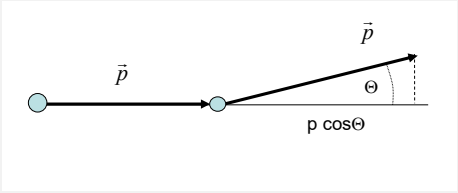

Figure 5.6: Cross section for momentum loss

$$\frac{dp}{p} = 1 - \cos\Theta \tag{5.35}$$

Thus, one obtains:

$$\sigma_m = 2\pi \int_0^{\pi} (1 - \cos\Theta) \frac{d\sigma}{d\Omega} \sin\Theta d\Theta \tag{5.36}$$

That is, if the particle is hardly deflected, i.e., $\Theta \sim 0$, $\cos\Theta$ becomes zero and the cross section σ_m vanishes.

5.2 Energy Loss

The energy loss of an ion on its trajectory in the solid is characterized by two quantities:

- **Stopping Power**

  The so-called stopping power denotes the energy loss of a projectile per path length in a solid:

$$B = \frac{dE}{dx} \left[\mathrm{eVm}^{-1}\right] \tag{5.37}$$

- **Stopping Cross Section**

  If this stopping power is related to the particle density n, the stopping cross section can be given:

$$\sigma = \frac{1}{n} \frac{dE}{dx} \left[\mathrm{eVm}^{2}\right] \tag{5.38}$$

5.2.1 Nuclear Energy Loss

As mentioned at the beginning, the nuclear energy loss refers to the energy and momentum loss during scattering off the target atoms. The probability of scattering a particle with energy E over a path length dx is given as:

$$p(E) = n\sigma(E)dx \tag{5.39}$$

The fraction of collisions in which an energy T is transferred to the target atom is:

$$\frac{dp(E)}{dT} dT = n dx \frac{d\sigma(E)}{dT} dT \tag{5.40}$$

Now, one must still integrate over all possible energy losses T and one obtains the average energy loss $\langle dE \rangle$ over a path length dx with:

$$\langle dE \rangle = \int_T T \frac{dp(E)}{dT} dT = n \int_{T_{min}}^{T_{max}} T \frac{d\sigma(E)}{dT} dT dx \tag{5.41}$$

Thus, the stopping power becomes:

$$\boxed{\langle \frac{dE}{dx} \rangle = n \int_{T_{min}}^{T_{max}} T \frac{d\sigma(E)}{dT} dT} \tag{5.42}$$

At low energies, the energy loss increases because T increases linearly. At high energies, the cross section for scattering becomes small and the energy loss decreases again (see Fig. 5.7).

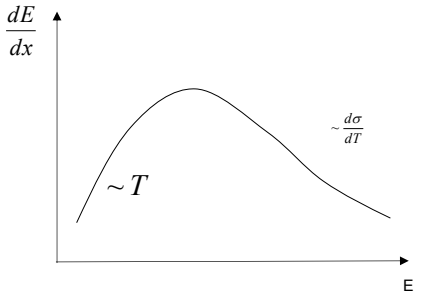

Figure 5.7: Behavior of the stopping power in the case of nuclear energy loss.

5.2.2 Electronic Energy Loss

In the case of electronic energy loss, the excitation of the electrons by the projectile is decisive. The type of approximation is determined by the velocity v of the projectile:

- $v \gg$ and $\Theta \simeq 0$

  At high particle energies, the deflection is small and the energy loss is calculated according to the **Bethe-Bloch formula**. Initially, the momentum loss due to the motion in the field of the Coulomb force is given as:

$$\Delta p = \int_{-\infty}^{\infty} \vec{F} dt \tag{5.43}$$

Since the momentum loss is small, the velocity v of the projectile can be assumed to be almost constant and approximated as:

$$\Delta p = \frac{1}{v} \int_{-\infty}^{\infty} \vec{F} dx \tag{5.44}$$

The small momentum loss also means that the direction of the projectile hardly changes and thus no change in b occurs, i.e., the integration in dt can be directly converted into the integration in db. The force in the Coulomb potential is given as:

$$\vec{F} = -\frac{d\Phi)(r)}{db} \tag{5.45}$$

With an electron as a collision partner, the change in direction of the projectile is small and b remains constant on the trajectory (see Fig. 5.8). This gives:

$$\Delta p = -\frac{1}{v} \frac{d}{db} \int_{-\infty}^{\infty} \Phi \left((x^2 + b^2)^{1/2} \right) dx \tag{5.46}$$

or

$$\Delta p = \frac{Z_1 Z_2 e^2}{v 4\pi\epsilon_0 b} \underbrace{\int_{-\infty}^{\infty} \frac{b^2}{(x^2 + b^2)^{3/2}} dx}_{\approx 2} \tag{5.47}$$

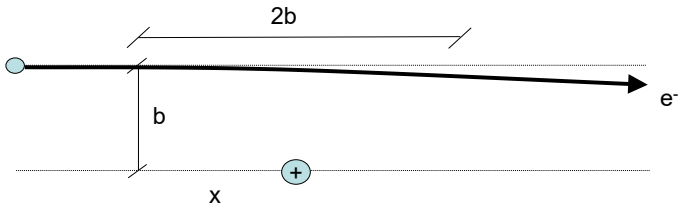

Figure 5.8: In the case of electronic energy loss, no deflection of the projectile occurs, since the collision partner is the electron in the solid.

and finally:

$$\Delta p = \frac{2Z_1 Z_2 e^2}{4\pi\epsilon_0 v b} \tag{5.48}$$

with $Z_2 = 1$

$$T = \frac{\Delta p^2}{2m} = \frac{2Z_1^2 e^4}{(4\pi\epsilon_0)^2 v^2 b^2 m} \tag{5.49}$$

The stopping power is obtained from an averaging over all possible energy losses, as explained in Eq. 5.42:

$$\langle \frac{dE}{dx} \rangle = n_e \int_{T_{min}}^{T_{max}} T \frac{d\sigma(E)}{dT} dT dx = n_e \int_{b_{min}}^{b_{max}} T 2\pi b db \tag{5.50}$$

or

$$-\langle \frac{dE}{dx} \rangle = \frac{4\pi Z_1^2 e^4 n_e}{(4\pi\epsilon_0^2) m_e v^2} \ln \frac{b_{max}}{b_{min}} \tag{5.51}$$

Now, the integration limits are needed, given as minimum and maximum impact parameters. The maximum transferred energy corresponds to the central collision on an electron, given as:

$$T_{max} = 4\frac{1}{2} m_e v^2 = 2 m_e v^2 \tag{5.52}$$

With Eq. 5.49 one obtains:

$$b_{min} = \frac{Z_1 e^2}{4\pi\epsilon_0 m_e v^2} \tag{5.53}$$

The minimum transferred energy corresponds to the ionization potential that must be provided to be able to excite an electron of the target atom at all.

$$T_{min} = \langle \text{Excitation energy} \rangle = I \tag{5.54}$$

or

$$b_{max} = \frac{2Z_1 e^2}{4\pi\epsilon_0 \sqrt{2 m_e v^2 I}} \tag{5.55}$$

In addition, the maximum impact parameter cannot be larger than half the distance between the solid atoms.

$$-\langle\frac{dE}{dx}\rangle = \frac{4\pi Z_1^2 e^4 n_e}{(4\pi\epsilon_0)^2 m_e v^2} \ln\frac{2m_e v^2}{I} \tag{5.56}$$

- $v \simeq v_F$ and $\Theta \ll$

  At low energies, the energy transfer is limited by the fact that not all electrons can participate in the scattering, as they are bound in the Fermi sea.

$$\Delta E = m_e v_F \Delta v \tag{5.57}$$

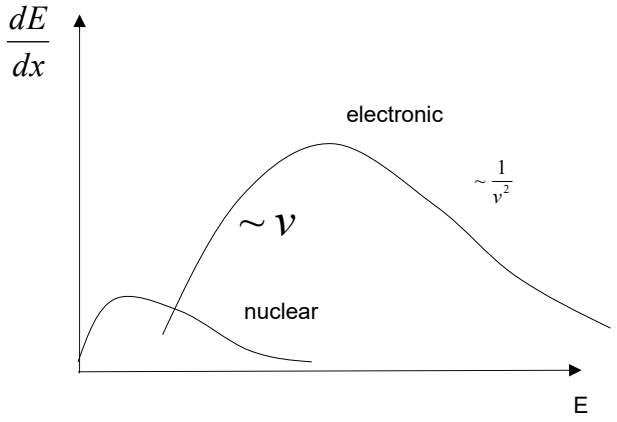

Figure 5.9: Behavior of the stopping power for electronic energy loss.

5.3 Sputtering

In the case of sputtering a solid, one considers the case where surface atoms are struck in a collision cascade and may be able to leave the solid. This is expressed by a sputtering yield Y:

$$Y = \frac{N_{sputtered}}{N_{incident}} \tag{5.58}$$

with $N_{sputtered}$ the number of atoms released and $N_{incident}$ the number of incident energetic ions. This sputtering yield is generally a function of the

energy of the incident ions and the material considered. Sputtering in turn produces particles that leave the surface with a characteristic energy and angular distribution. This will be discussed below.

Consider the sputtering process in which an ion penetrates the solid and there, through nuclear energy loss, strikes the solid atoms. The number N of struck solid atoms (= **recoils**) with an energy greater than E_0 is, given a total energy of the projectile E, given as:

$$N(E, E_0) \sim \Gamma \frac{E}{E_0} \tag{5.59}$$

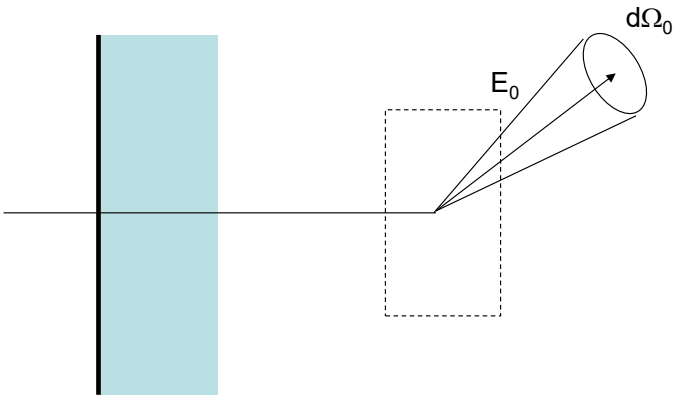

Figure 5.10: In the collision cascade, secondary particles of energy E_0 are generated in a solid angle $d\Omega_0$.

Γ is a function of the interaction potential for the specific combination of projectile and target. This is a linear approximation in which it is assumed that the energy E is divided equally among recoils of energy E_0 (a 1000 eV ion can only generate 5 recoils of energy 200 eV due to energy conservation, etc.). The number of recoils $n(E, E_0)$ within the energy interval dE_0 is given as:

$$n(E, E_0) = \frac{dN(E, E_0)}{dE_0} \sim \Gamma \frac{E}{E_0^2} = F(E, E_0) \tag{5.60}$$

The total number $G(E, E_0)$ of particles that are moved per unit time and are in the energy interval dE_0 is given by the flux of incident projectiles Φ times the number of recoils $n(E, E_0)$ generated thereby and the unit of time dt_0.

$$G(E, E_0)dE_0 = \Phi n(E, E_0)dt_0 \tag{5.61}$$

dt_0 is formally replaced by:

$$dt_0 = \frac{dE_0}{\left|\frac{dE_0}{dt}\right|} = \frac{dE_0}{v_0 \left|\frac{dE_0}{dx}\right|} \tag{5.62}$$

Thus, one obtains:

$$G(E, E_0)dE_0 = \Phi\Gamma_m \frac{E}{E_0^2} \frac{dE_0}{v_0 \left|\frac{dE_0}{dx}\right|} \tag{5.63}$$

These are the particles *within* the solid that are released. Now, however, we only need the recoils that are moving towards the surface, as only these have the possibility to leave the solid. The flux of particles J is given by the product of recoils $G(E, E_0)$ times velocity v_0. In addition, this flux must be projected onto the surface direction by multiplication with $\cos\Theta$, as illustrated in Fig. 5.11. Thus, one finally obtains:

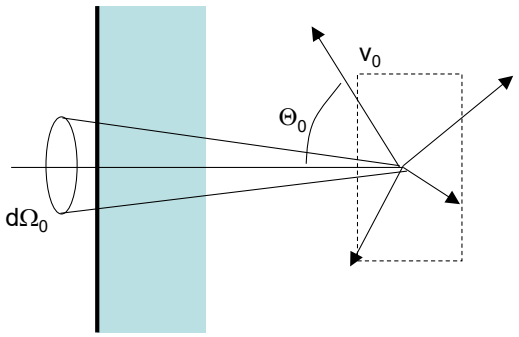

Figure 5.11: The outward-directed flux of secondary particles is obtained by projection onto a direction.

$$J(E, E_0)dE_0d\Omega = G(E, E_0)dE_0d\Omega v_0 \cos\Theta = \Phi\Gamma_m \frac{E}{E_0^2} \frac{dE_0}{v_0 \left|\frac{dE_0}{dx}\right|} v_0 \cos\Theta d\Omega \tag{5.64}$$

When the recoils pass through the surface of the solid, the barrier corresponding to the surface binding energy E_{SB} must still be overcome. This can be described within the framework of elastic scattering.

From the conservation of momentum for the velocity component parallel to the surface, which remains unchanged, the following condition is obtained:

$$v_0 \sin \Theta_0 = v_1 \sin \Theta_1 \tag{5.65}$$

or

$$E_1 \sin^2 \Theta_1 = E_0 \sin^2 \Theta_0 \tag{5.66}$$

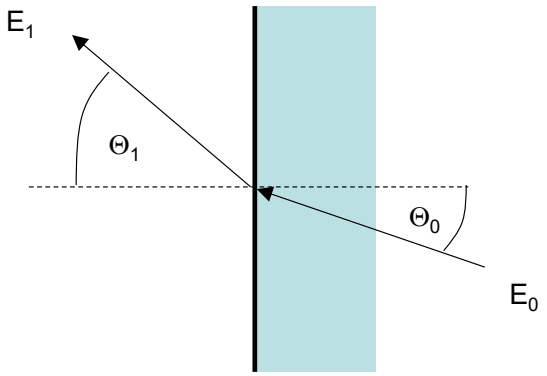

Figure 5.12: Barrier model of sputtering.

The conservation of energy gives:

$$E_1 = E_0 - E_{SB} \tag{5.67}$$

From the derivative of the conservation of momentum with respect to the solid angle, one can derive:

$$E_1 2 \sin \Theta_1 \cos \Theta_1 d\Theta_1 d\Phi_1 = E_0 \sin \Theta_0 \cos \Theta_0 d\Theta_2 d\Phi_2 \tag{5.68}$$

With the solid angle $d\Omega = 2\pi \sin \Theta d\Theta d\Phi$ one thus obtains the relationship:

$$E_1 \cos \Theta_1 d\Omega_1 = E_0 \cos \Theta_0 d\Omega_0 \tag{5.69}$$

Thus, one can convert the flux of directed particles J into a yield $Y = J/\Phi$ as:

$$dY = \Gamma_m \frac{E}{E_0^2} \frac{dE_1}{\left|\frac{dE_0}{dx}\right|} \frac{E_1}{E_0} \cos \Theta_1 d\Omega_1 \tag{5.70}$$

If one now replaces E_0 with $E_1 + E_{SB}$, one obtains

$$dY = \Gamma_m E \frac{dE_1}{\left|\frac{dE_0}{dx}\right|} \frac{E_1}{(E_1 + E_{SB})^3} \cos\Theta_1 d\Omega_1 \tag{5.71}$$

The differential sputtering yield is thus [Tho68]:

$$\boxed{\frac{dY}{dE_1 d\Omega_1} = \Gamma_m \frac{E}{\left|\frac{dE_0}{dx}\right|} \frac{E_1}{(E_1 + E_{SB})^3} \cos\Theta_1} \tag{5.72}$$

This is referred to as the **Thompson distribution**. This dependence in the sputtering yield is characterized by several peculiarities:

- **Energy distribution** E_1

  If one considers the maximum of the energy distribution of the sputtered particles, one finds that this does not depend on the energy of the incident ions E. That is, by measuring the maximum, one can determine the surface binding energy E_{SB}.

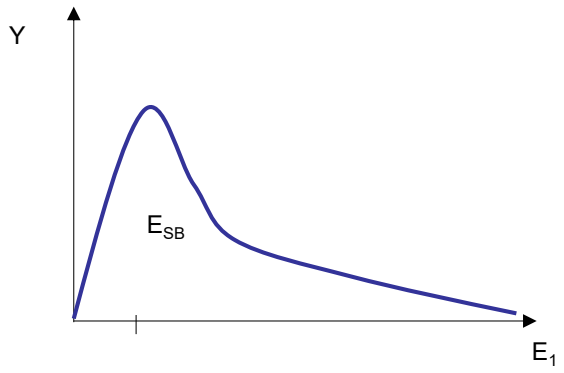

Figure 5.13: Energy distribution of the sputtered particles.

- **Angular distribution** Θ_1

  The emission of the particles follows a cosine distribution in the first approximation. That is, the sputtering behaves like an emitting surface. This can be explained by the fact that the generation of the particles in the volume is assumed to be isotropic generation of recoils.

- **Energy dependence** E

The sputtering yield increases linearly with the energy of the ions E. This simple statement must be corrected at two points. On the one hand, the sputtering yield decreases again at very high energies, since the ions penetrate deeply into the material and the recoils are only generated at great depth, from where they can hardly reach the surface anymore. On the other hand, sputtering is a threshold process, since the kinematics of the collision partners specifies a minimum energy of the ions above which sputtering can occur.

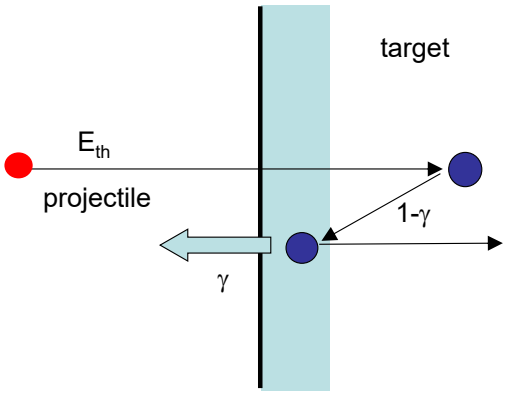

Figure 5.14: Sputtering as a threshold process.

This threshold energy can be derived intuitively. Consider an ion of energy E that falls onto the surface. This ion must first change its direction in a first collision. In doing so, a percentage γ of energy, the kinematic factor, is transferred to the target atom. That is, the backscattered ion has only an energy of $E(1-\gamma)$. This backscattered ion must now transfer its energy to a surface atom. The percentage is now directly the kinematic factor γ. This energy transfer must at least transfer the surface binding energy E_{SB} for sputtering to occur, or:

$$E(1-\gamma)\gamma > E_{SB} \tag{5.73}$$

This thus gives a threshold E_{SB} for sputtering of:

$$E_{th} > \frac{E_{SB}}{(1-\gamma)\gamma} \tag{5.74}$$

This equation only applies to projectiles that are lighter than the target, since backscattering had to occur in the first step. For heavier projectiles, the first step is more complicated, since the projectile can only reverse its momentum through multiple scattering (momentum reversal). The threshold energies typically range from 10 eV to several hundred eV, depending on the projectile/target combination.

- **Angle of the incident ions** α

  The sputtering of the target also depends on the angle of the incident ion. Here, one obtains two contributions. On the one hand, the sputtering yield increases with a flatter angle of incidence, since the cascade of recoils reaches closer to the solid surface. That is, more particles have the opportunity to reach the surface. However, at very flat angles, the number of target atoms within which the projectile is decelerated becomes very small. And the sputtering yield becomes zero at $\alpha = 90°$.

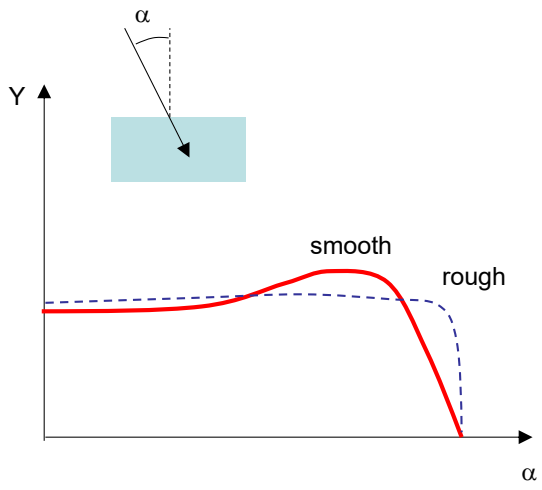

Figure 5.15: Angle dependence of sputtering with α the angle of the incident ion to the surface normal.

- **Rough surfaces**

  In the case of rough surfaces, the angle dependence almost disappears, since the angle of incidence α, as well as the emission angle Θ_1, are no longer uniquely defined.

Empirical Formulas for Sputtering In principle, the recommendation is to calculate the sputtering yield with the corresponding computer codes (e.g., *TRIM.SP*[Eck91]). As an approximation formula, the so-called Bohdansky formula has become established, which is structured as follows. The sputtering yield as a function of the energy of the ions at perpendicular incidence on the surface is:

$$Y(E_{ion}, \alpha = 0^\circ) = Q s_n(\epsilon) \left(1 - \left(\frac{E_{th}}{E_0}\right)^{2/3}\right) \left(1 - \frac{E_{th}}{E_0}\right) \tag{5.75}$$

The absolute value is determined by the adjustable parameter Q. The energy dependence can be directly derived from the mass ratio of the projectile and the target. The individual parameters are the reduced ion energy ϵ:

$$\epsilon = \frac{E_{ion}}{E_{TF}} \tag{5.76}$$

with the Thomas-Fermi energy E_{TF}:

$$E_{TF} = \frac{Z_1 Z_2 e^2}{a_L} \frac{M_1 + M_2}{M_2} \tag{5.77}$$

with the length scale a_L

$$a_L = \left(\frac{9\pi^2}{128}\right)^{1/3} a_B \left(Z_1^{2/3} + Z_2^{2/3}\right)^{-1/2} = 0.4685 \left(Z_1^{2/3} + Z_2^{2/3}\right)^{-1/2} [\mathring{A}] \tag{5.78}$$

and the parameter for the nuclear stopping s_n

$$s_n(\epsilon) = \frac{3.441\sqrt{\epsilon}\ln(\epsilon + 2.718)}{1 + 6.355\sqrt{\epsilon} + \epsilon(6.882\sqrt{\epsilon} - 1.708)} \tag{5.79}$$

The threshold energy E_{th} at a given surface binding energy E_{SB} finally depends on whether the projectile is lighter or heavier than the target:

$$E_{th} = \begin{cases} \frac{E_{SB}}{\gamma(1-\gamma)} & M_1 < 0.2 M_2 \\ 8 E_{SB} \left(\frac{M_1}{M_2}\right)^{0.4} & M_1 > 0.2 M_2 \end{cases} \tag{5.80}$$

5.4 Chemical Sputtering

5.4.1 Fundamentals

Etching using plasmas is a key application in the semiconductor industry. For the production of integrated circuits, it is necessary to create lateral structures on a silicon wafer. In some cases, it is also necessary to create trenches or holes with a high aspect ratio, i.e., great depth compared to the diameter. For the production of structures, there is an *additive* and a *subtractive* method, as illustrated in Fig. 5.16: (i) in the additive method, a mask is first applied to the silicon wafer. This mask consists of a polymer that can be exposed (lithography). The exposed polymer can then be removed by means of an etching process. A film is deposited on this structured surface. Subsequently, the mask is removed, which thereby exposes the previously covered areas of the silicon wafer (lift off); (ii) in the subtractive method, the film is first deposited and then the mask is applied. In an etching step, the film is now removed that was not covered by the mask.

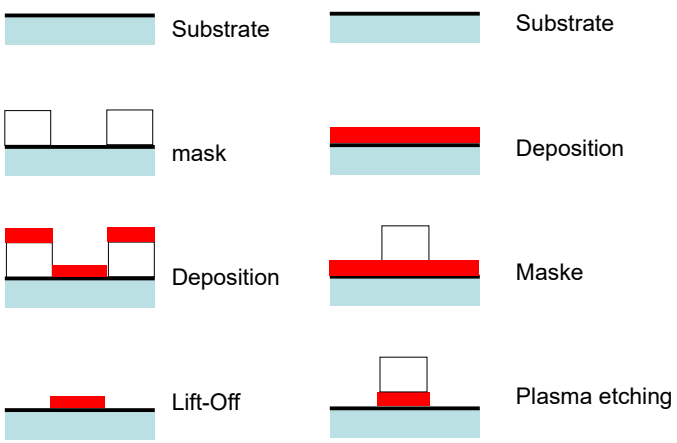

Figure 5.16: Typical process sequence for etching structures in semiconductor technology.

This described structuring can be realized for lateral structures with wet chemical methods. However, to create holes or trenches with a high aspect ratio, a high anisotropy of the etching process is required. This can only be achieved by plasma etching (also referred to as dry etching). In conventional wet chemical etching, the material removal occurs isotropically, which limits the transfer of a mask to a silicon substrate.

Material	Etch plasma	Etch product
Al	BCl_3+Ar,He	$AlCl_3$, Al_2Cl_6
	CCl_4	$AlCl_3$, Al_2Cl_6
	Cl_2	$AlCl_3$, Al_2Cl_6
	$SiCl_4$	$AlCl_3$, Al_2Cl_6
	$CHCl_3$	$AlCl_3$, Al_2Cl_6
Si	CF_4+O_2	SiF_4
	SF_6+O_2	SiF_4
	XeF_2	SiF_4
	F_2	SiF_4
	Cl_2	SiF_4
SiO_2	CF_4	SiF_4+CO_2
	C_2F_6	SiF_4+CO_2
	C_3F_8	SiF_4+CO_2
W	CF_4, SF_6	WF_6
Ta	NF_3,F_2	WF_6
Nb	NF_3,F_2	WF_6
Mo	NF_3,F_2	WF_6

Table 5.1: Selected examples of common etch plasmas

The structuring of nanometer-sized structures in the semiconductor industry is a central part of the technology and is used for many components on the μm scale, such as MEMS (Micro-Electro-Mechanical-Systems): a prominent example is the micro-mirrors used in projection devices. But also micropumps and sensors.

The combination of material and reactive plasma is shown for some typical examples in Table **??**.

Plasma processes are primarily required to be anisotropic and selective, i.e., that a material such as SiO_2 is etched much more strongly compared to Si. Plasma processes have the advantage that the mask production also defines the minimum structure size, that the use of chemicals is low. The disadvantage compared to wet chemical processes is, however, the necessity of a vacuum arrangement.

When etching silicon or silicon oxide, fluorine-containing plasmas are generally used. In the plasma, fluorine is dissociated and reacts with silicon to form SiF_4. The selectivity and the anisotropy of the etching process can be better controlled if pure fluorine F_2 is not used but fluorine-carbon compounds C_xF_y. In addition, it is possible to add up to 20% O_2 to form stable volatile compounds such as COF_2, etc. In addition, the etch rate increases

as $O_2 + CF_4 \rightarrow CO_2 + 4F$.

A particular feature of etching in fluorine-containing plasmas is the clear dependence of the etch rate on the doping. n-doped silicon is etched much faster than p-doped silicon. This effect is initially initiated by adsorbed fluorine atoms, which, due to their strong electronegativity, can easily polarize the high electron density in n-doped silicon. A charge transfer occurs and an F^--ion is formed on the surface. Due to the image charge that is created in the conductive silicon, the F^--ion is drawn deeper into the material (see Fig. 5.17).

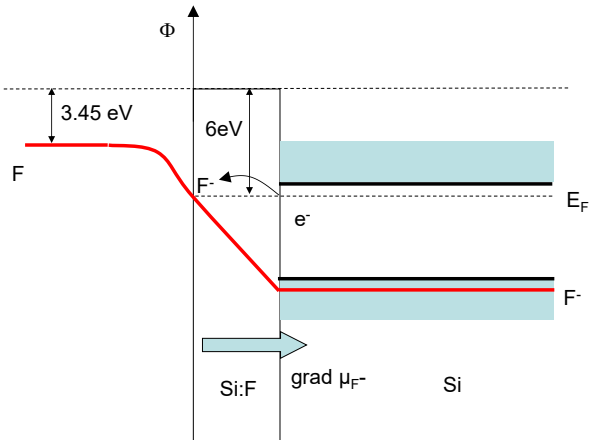

Figure 5.17: Doping dependence of silicon etching.

5.4.2 Anisotropic Etching

Anisotropy in plasma etching is ensured by the fact that the reaction rate on a given surface is only high if reactive particles and ions simultaneously impinge, as illustrated in Fig. 5.18. In this famous experiment, a silicon surface was etched with selective particle beams of energetic argon ions and thermal fluorine atoms: (i) if only fluorine atoms impinge, a slight chemical etching occurs. A Si:F polymer forms on the surface, which has a passivating effect; (ii) if the ion bombardment is added, the Si:F polymer is efficiently sputtered and the erosion rate increases dramatically. The flux of fluorine atoms is still essential, since the volatile compound SiF_4 must be formed; (iii) without the addition of fluorine atoms, one only has physical sputtering. This is not very efficient in the considered energy range. That is, one recognizes

that the erosion rate is only high if ions and reactive atoms impinge on the surface *simultaneously*.

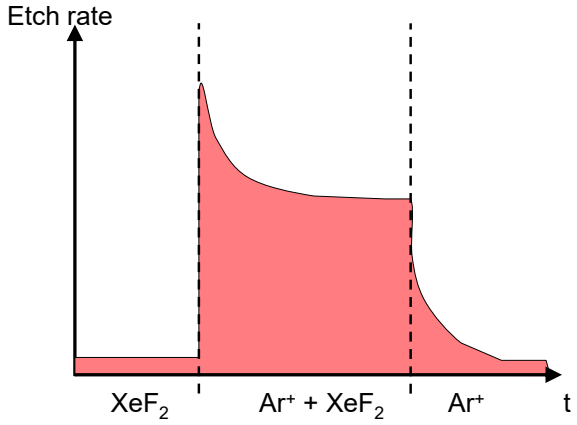

Figure 5.18: Synergism in the etching of silicon in XeF_2 and argon ions.

One recognizes that the formation of the Si:F surface layer is essential for the erosion behavior. Depending on the ratio of the flux of F atoms to the surface and the set ion bombardment, one observes the growth of this fluorine polymer or the efficient erosion of the substrate, as illustrated in Fig. 5.19.

Since the ions have a preferred direction through the sheath, they ensure not only an efficient erosion rate but also the anisotropy of the etching process. For the production of integrated circuits, it is necessary to create narrow lateral structures. The individual memory cells are arranged vertically rather than planar. This makes it necessary to be able to produce trenches with a high aspect ratio. Plasma etching can exactly achieve this. Conventional wet chemical etching processes with an isotropic etching direction are unsuitable.

If one considers a trench, the ions and the neutral atoms only impinge simultaneously on the bottom of this trench. On the sidewalls, the ion bombardment is greatly reduced. There, a stable Si:F polymer forms and significantly reduces the erosion of the sidewalls.

This sidewall passivation is highly sensitive to the choice of process parameters. If, for example, the etching of aluminum in chlorine plasmas is considered, the etching effect is still quite isotropic in pure chlorine. Only when using CCl_4 does a stable Al:C:Cl polymer form on the sidewalls. Only at the bottom of the trench does one then again obtain the preferential etching effect.

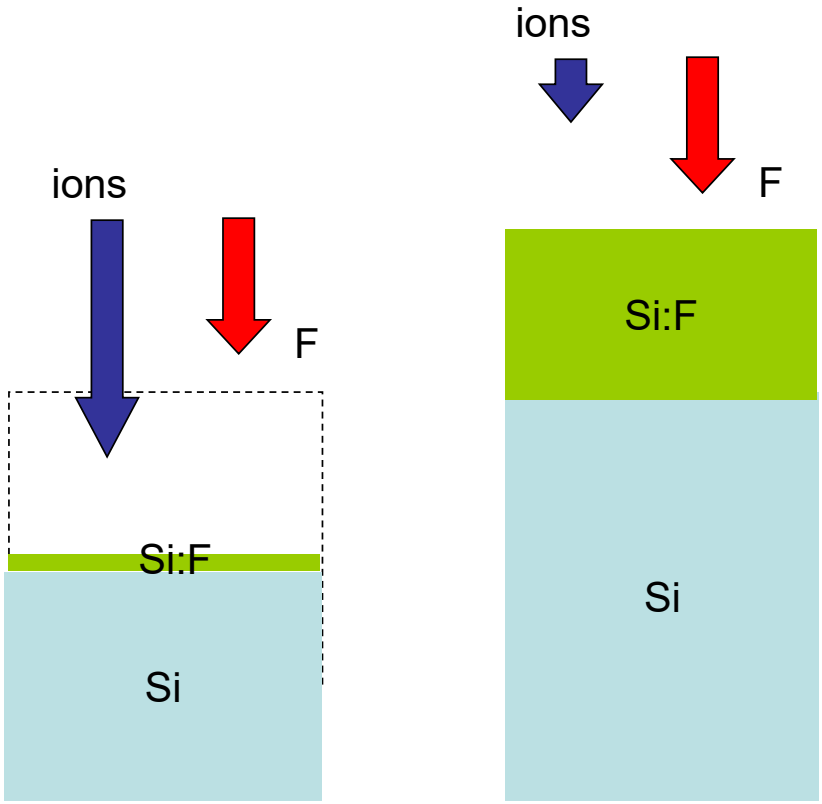

Figure 5.19: Anisotropic etching through the balance of erosion and polymerization.

The formation of surface polymers is a self-limiting process. This is mainly due to the efficient momentum reversal of the incident ions. The incident ions cannot reverse their momentum because of the unfavorable mass ratio to the fluorine atoms. This happens much more efficiently on silicon atoms. That is, for example, an argon ion penetrates the Si:F polymer and is only reflected at the Si:F interface. The reversal of momentum increases the sputtering effect and thus represents a self-limitation of the Si:F layer thickness.

5.4.3 Selectivity

The plasma etching can additionally act selectively, in the sense that Si is etched while SiO_2 is not attacked. This is particularly important since a

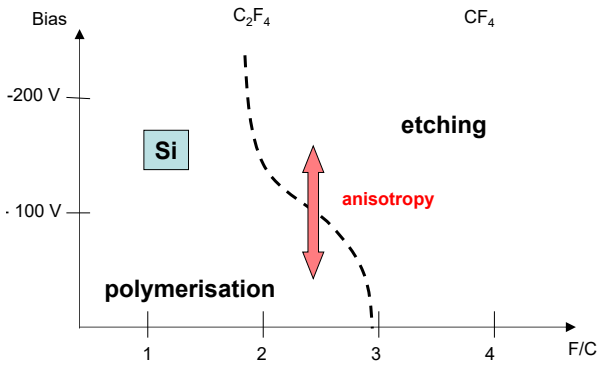

Figure 5.20: Formation of a polymer layer on the surface.

uniform flux of reactive particles to all surfaces cannot be guaranteed for different structure sizes. Therefore, it is important that in structures that, for example, have already been freed of SiO_2, no further etching of Si occurs, so that other structures on the wafer can be completely structured during this time.

Depending on the substrate material, one obtains different graphs according to Fig. 5.18. By skillfully choosing the operating point, one can achieve that either only SiO_2 or only Si is etched.

5.4.4 Limits of Plasma Etching

When etching microstructures, the following points must be considered:

- **Loading**

  If an etching process is optimized for a given reactor with a single silicon wafer, large differences arise when one wants to transfer the same process to a reactor with several wafers. Since the exposed silicon surface of the wafers is now many times larger, more reactive gas is consumed. Accordingly, the etch rate per wafer is reduced. This is referred to as loading.

- **Damaging**

  High-energy ions that impinge during etching lead to lattice defects and thus reduce the conductivity in the materials. This is compensated by a thermal annealing step. The problem of damage is particularly important for the gate area in a field-effect transistor, where the current transport must proceed undisturbed in a small volume.

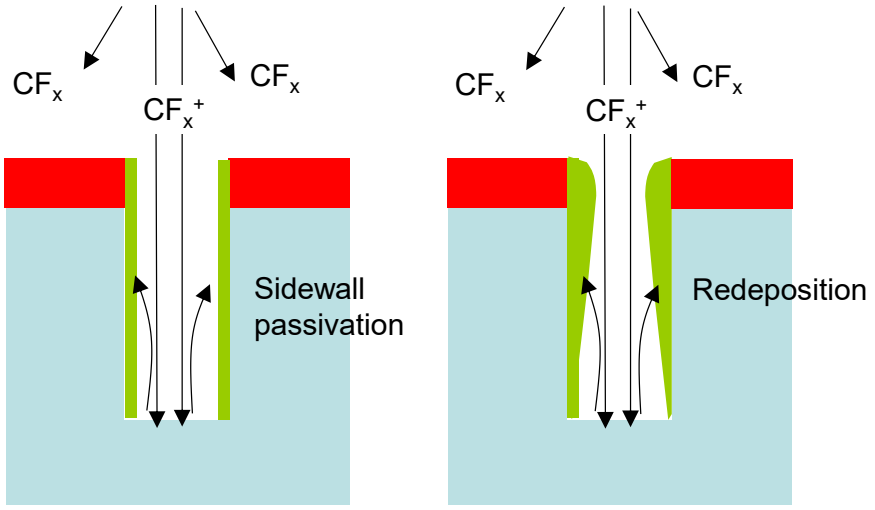

Figure 5.21: Sidewall passivation.

- **Microtrenching**

  The incident ions in plasma etching have a small but finite opening angle. Ions that hit the sidewalls are scattered at a small angle. This locally increases the flux to the corners in the trench: an inhomogeneous etch rate is created, as illustrated in Fig. 5.23.

- **Notching**

  When etching structures in insulators, a charging can occur, since the electrons impinge from a larger solid angle compared to the ions. Thus, the upper end of a trench becomes negatively charged and the bottom positively charged. The fields thus created deflect the incident ions, which leads to a flux enhancement at the sidewalls at the bottom of the trench, as illustrated in Fig. 5.24.

- **Etch Lag**

  In plasma etching, a sufficient flux of ions and reactive particles is necessary. Since the reactive particles impinge on the surface from all spatial directions, the flux within a narrow trench is much smaller than within a wide trench. Thus, a wide trench is etched much faster than a narrow trench. This results in different depths of the structures after a given process duration. This can only be compensated by over-etching.

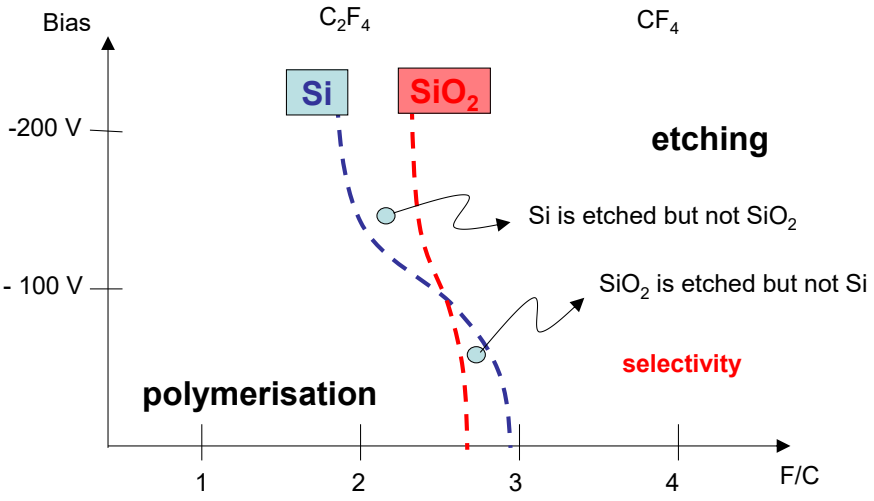

Figure 5.22: Selective etching by choosing the operating point

However, this requires that the etching step in the wide trenches is stopped by a boundary surface in the material. This is illustrated in Fig. 5.25.

- **Dust formation in plasmas**

  In many processes of semiconductor technology, reactive precursors are used. However, under unfavorable process parameters, negative ions form in the plasma, which are trapped in the enclosing plasma potential. These negative ions undergo ion-molecule reactions and finally form macroscopic dust particles. If these dust particles fall onto the wafer surface, they can destroy the corresponding structures there.

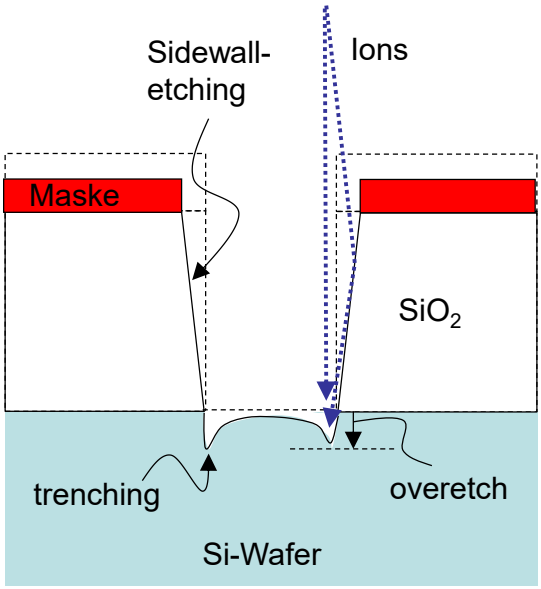

Figure 5.23: Microtrenching: due to the reflection of ions on the sidewalls of a trench, an etch enhancement occurs at the bottom.

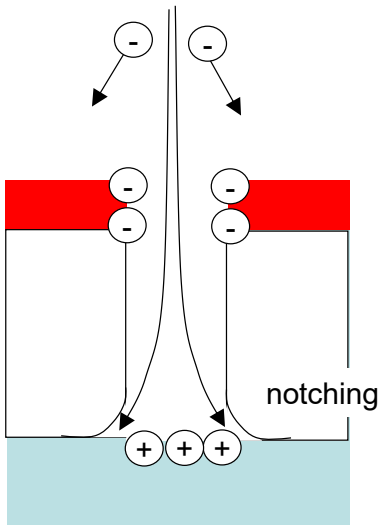

Figure 5.24: Notching.

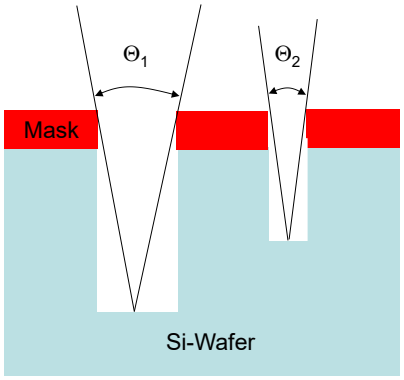

Figure 5.25: Etch depth depends on the aspect ratio of the holes.

5.5 Secondary Electron Emission

5.5.1 Secondary Electron Emission by Ions

Ions impinging on surfaces not only lead to sputtering and material removal but also knock electrons out of the solid, which is referred to as secondary electron emission by ions. Here, electronic excitation in the solid becomes visible through the emission of an electron that exits the surface. The energy input is initially the electronic energy loss of the incident ion or the neutralization of the ion directly in front of the surface. Similarly, secondary electrons can also be triggered by impinging electrons or other excited species. The rate and energy of the secondary electrons are essentially determined by the density of states of the involved states. The following discusses the classical Hagstrum model [**?**].

First, consider the energy scheme of an ion in front of a surface in Fig. 5.26. Here, two scales can be considered. On the one hand, relative to the vacuum level E_{Vakuum} and on the other hand, relative to the bottom of the Fermi sea, which describes the metal.

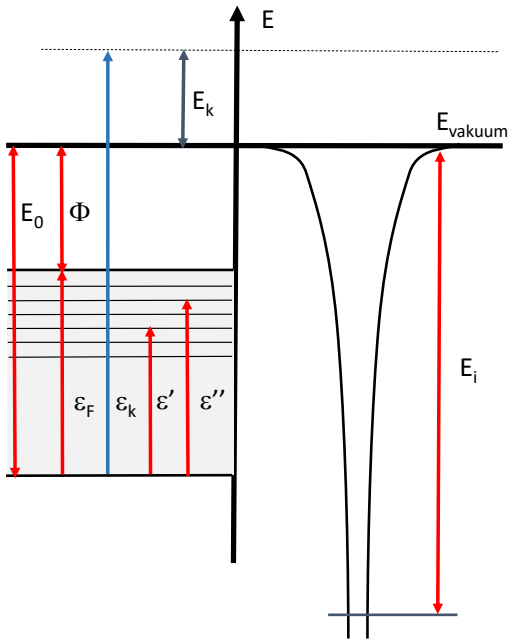

Figure 5.26: Energy scheme of the generation of secondary electrons. The energies in the Fermi sea of depth ϵ_F with the bottom E_0 below the vacuum level and E_i the ionization energy of the ion.

Auger Neutralization

Rate of Secondary Electron Emission

In the so-called Auger neutralization, the ion is neutralized at the surface by an electron in the state ϵ'. The energy released is transferred to an electron in the state ϵ''. The kinetic energy of the electron that leaves the surface is E_k relative to the vacuum level:

$$E_k = \epsilon' + \epsilon'' - 2\epsilon_0 + E_i \tag{5.81}$$

or ϵ_k relative to the bottom of the Fermi sea:

$$\epsilon_k = \epsilon' + \epsilon'' - \epsilon_0 + E_i \tag{5.82}$$

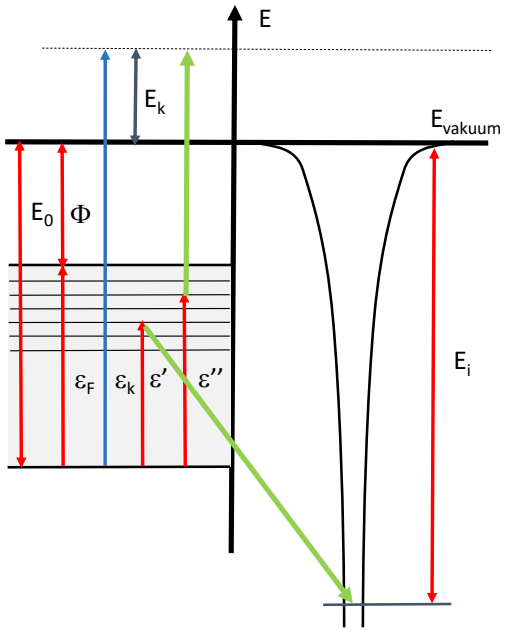

Figure 5.27: Auger neutralization: An ion with ionization energy E_i transfers its energy upon neutralization to the electronic system of the solid while capturing an electron at energy ϵ'

The rate of generation of these secondary electrons is determined using Fermi's Golden Rule.

$$\text{Rate}_i = \frac{2\pi}{\hbar} \langle i|H|f\rangle^2 \, N(\epsilon_k) N(\epsilon') N(\epsilon'') d\epsilon_k d\epsilon' d\epsilon'' d\Omega \tag{5.83}$$

Here, the density of states of the involved states $N(\epsilon_k)$, $N(\epsilon')$, $N(\epsilon'')$ is important for the energy dependence of the rate. In particular, more states become accessible at higher energies and the secondary electron emission coefficient increases. The absolute size when comparing different metals is determined by the differences in the density of states. To calculate the rate for all possible states that lead to an electron at energy ϵ_k, one must integrate over all states ϵ' and ϵ''.

$$\begin{aligned} Rate_{\epsilon_k} &= \int\int\int \frac{2\pi}{\hbar} \langle i|H|f\rangle^2 N(\epsilon_k)N(\epsilon')N(\epsilon'')d\epsilon' d\epsilon'' d\Omega \\ &\quad \delta\left(\epsilon' + \epsilon'' + E_i - \epsilon_0 - \epsilon_k\right) P_\Omega(\theta, \epsilon_k) \end{aligned} \tag{5.84}$$

This integral can be calculated more easily by using the following substitution.

$$\epsilon'' = \epsilon + \Delta \tag{5.85}$$

$$\epsilon' = \epsilon - \Delta \tag{5.86}$$

That is, when integrating over Δ, the sum of ϵ' and ϵ'' remains the same (see eq. 5.81), thus the energy of the electron ϵ_k is also fixed. The integral over the average energy ϵ is divided into two parts. Once between 0 and $\epsilon_F/2$ and between $\epsilon_F/2$ and ϵ_F. The appropriate integration limits for Δ are then 0 to ϵ and 0 to $\epsilon_F - \epsilon$. By substitution, it can be seen that all states ϵ' and ϵ'' between 0 and ϵ_F are included.

$$Z = \int_0^{\epsilon_F/2}\int_0^{\epsilon} N(\epsilon-\Delta)N(\epsilon+\Delta)\delta\left(2\epsilon + E_i - \epsilon_0 - \epsilon_k\right) d\Delta d\epsilon \tag{5.87}$$

$$+ \int_{\epsilon_F/2}^{\epsilon_F}\int_0^{\epsilon_F-\epsilon} N(\epsilon-\Delta)N(\epsilon+\Delta)\delta\left(2\epsilon + E_i - \epsilon_0 - \epsilon_k\right) d\Delta d\epsilon \tag{5.88}$$

This can be written more concisely as:

$$Z = \int_0^{\epsilon_F} T(\epsilon)\delta\left(2\epsilon + E_i - \epsilon_0 - \epsilon_k\right) d\epsilon = T\left[\frac{1}{2}\left(\epsilon_k + \epsilon_0 - E_i\right)\right] \tag{5.89}$$

with the so-called **Auger transform** T. The argument of this function corresponds exactly to the value for ϵ at which the argument of the delta function $\delta(2\epsilon + E_i - \epsilon_0 - \epsilon_k)$ becomes zero and thus $\delta = 1$.

$$T(\epsilon) = \int_0^{\epsilon} N(\epsilon-\Delta)N(\epsilon+\Delta)d\Delta \qquad \epsilon < \epsilon_F/2 \tag{5.90}$$

$$T(\epsilon) = \int_0^{\epsilon_F-\epsilon} N(\epsilon-\Delta)N(\epsilon+\Delta)d\Delta \qquad \epsilon_F/2 < \epsilon < \epsilon_F \tag{5.91}$$

Here, the quantities $N(\epsilon)$ are the occupation of the states in the solid at energy ϵ and result from the product of the density of states times the Fermi-Dirac distribution. For these excitations at high energies due to neutralization, however, the temperature dependence can be neglected and it is sufficient to consider the density of states up to the Fermi energy. In the simplest model of a free electron gas, this would be:

$$N(\epsilon) = \frac{3}{2}\frac{n}{E_F}\sqrt{\frac{\epsilon}{E_F}} \tag{5.92}$$

The total rate of excited electrons per ion is now obtained by integrating over all states. The coefficient C combines the prefactors or the matrix element. Here, the energy dependence is very small.

$$\text{Rate}_{\text{total}} = C\int\int N(\epsilon_k)T\left[\frac{1}{2}\left(\epsilon_k+\epsilon_0-E_i\right)\right]P\Omega(\theta,\epsilon_k)d\Omega d\epsilon_k \tag{5.93}$$

The probability of exciting an electron to energy ϵ_k is for $\epsilon_k > \epsilon_F$:

$$P_k(\epsilon_k) = \frac{N(\epsilon_k)T\left[\frac{1}{2}\left(\epsilon_k+\epsilon_0-E_i\right)\right]}{\int_{\epsilon_F}^{\infty} N(\epsilon_k)T\left[\frac{1}{2}\left(\epsilon_k+\epsilon_0-E_i\right)\right]d\epsilon_k} \tag{5.94}$$

The final number of electrons that are created in the solid must still take into account the probability $P_t(s,v_0)$ of the absorption of the ion's energy with velocity v_0 at location s, as well as the angular distribution of the emission $P_\Omega(\theta,\epsilon_k)$

$$N_i(\epsilon_k) = \int_s^{\infty}\int_0^{2\pi}\int_0^{\pi} P_t(s,v_0)P_k(\epsilon_k,s)P_\Omega(\theta,\epsilon_k)\sin\theta d\theta d\phi ds \tag{5.95}$$

Angular Distribution of Emission

Finally, the probability that the released electron leaves the solid must be considered. Here, only a part of the angular distribution must be integrated up to a critical angle θ_c as illustrated in Fig. 5.28.

$$P_e(\epsilon_k) = \int_0^{2\pi} \int_0^{\theta_c} P_\Omega(\theta, \epsilon_k) \sin\theta d\theta d\phi \tag{5.96}$$

The secondary electron emission coefficient γ is finally:

$$\gamma = \int_0^{\infty} N_i(\epsilon_k) P_e(\epsilon_k) d\epsilon_k \tag{5.97}$$

By passing an electron of energy ϵ_k, which is emitted at an angle θ through the surface barrier with height ϵ_0, an electron is obtained at energy $\epsilon_k - \epsilon_0$ and angle θ' in vacuum.

$$\epsilon_k \cos\theta^2 = \epsilon_0 + (\epsilon_k - \epsilon_0) \cos\theta'^2 \tag{5.98}$$

Experiments show that the angular distribution of the emission is not homogeneously distributed over 4π.

$$\frac{P_\omega(\theta < \theta_c)}{P_\omega(\theta > \theta_c)} = f^2 \tag{5.99}$$

For $f = 1$, from the consideration of the density of states for free particles $\propto \sqrt{\epsilon}$

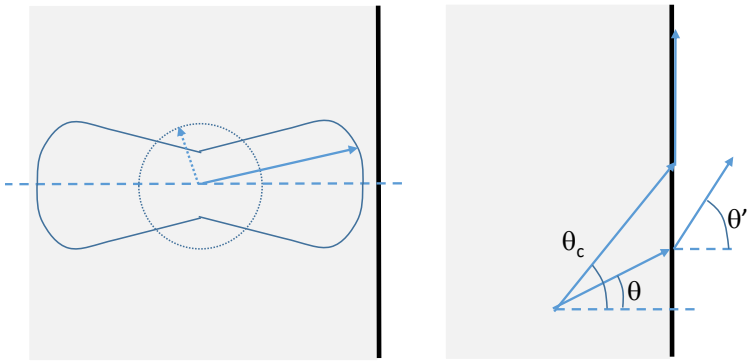

Figure 5.28: Angular distribution of emission

$$P_e = \frac{1}{2}\left[1 - \left(\frac{\epsilon_0}{\epsilon_k}\right)^{1/2}\right] \tag{5.100}$$

That is, for $\epsilon_k = \epsilon_0$ we get $P_e = 0$ and for $\epsilon_k \to \infty$ we get $P_e = 1$. This expression is modified by the preference for forward scattering:

$$P_e = \frac{1}{2}\left[\frac{1-\left(\frac{\epsilon_0}{\epsilon_k}\right)^{1/2}}{1-\left(1-\frac{1}{f^2}\right)\left(\frac{\epsilon_0}{\epsilon_k}\right)^{1/2}}\right] \tag{5.101}$$

For $f = 1$, i.e., an isotropic distribution, we get the simple expression 5.100 again.

Energy Loss of Ions as a Function of Depth s

$$P_t(s, v_0) = R(s)\frac{1}{v_0}ds \exp\left(-\int_s^\infty R_s \frac{ds}{v_0}\right) \tag{5.102}$$

Energy Distribution of Emitted Electrons

The final number of free electrons generated outside the solid at energy ϵ_k is

$$N_0(\epsilon_k) = N_i(\epsilon_k)P_e(\epsilon_k) \tag{5.103}$$

The secondary electron coefficient γ is then the integral over all possible energies of the free particles E_k:

$$\gamma = \int_0^\infty N_0(E_k)dE_k \tag{5.104}$$

The energy distribution of the emitted electrons is shown in Fig. 5.29. It can be seen that this distribution has a characteristic shape that is shifted to higher energies for larger ionization energies. The energy distribution of the emitted electrons is obtained by convolving the density of states of the free particles.

Fig. 5.30 shows the energy distribution of the secondary electrons for the case of argon ions on copper. The energy scale begins with the bottom of the Fermi sea. The distribution of the electrons in the solid as well as the emission probability is shown.

Fig. 5.31 shows the dependence of the secondary electron emission on the ionization energy of the incident ions. γ generally increases with E_i. In this parameter, there is also a small dependence on the kinetic energy of the ions. In the range up to 100 eV, for example, at high energies, neutralization takes place closer to the surface. Here, the lower level of the ion is slightly shifted upwards, so that E_i can decrease by e.g. about 2 eV for helium ions and thus also γ.

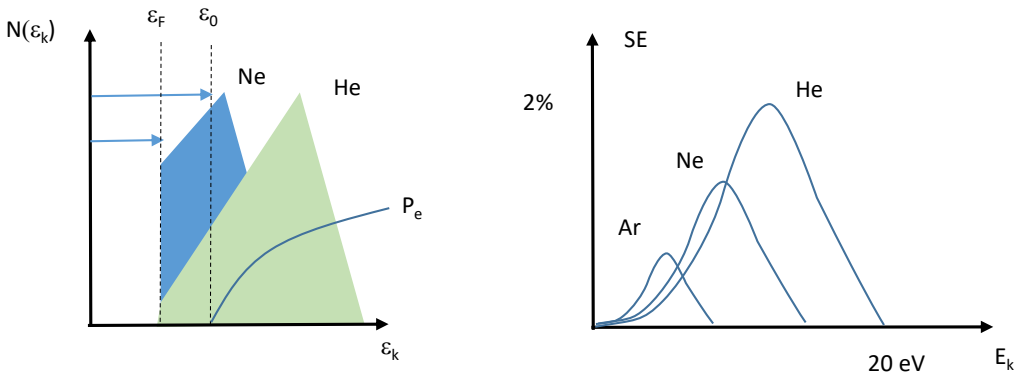

Figure 5.29: Schematic energy distribution of the electrons inside the solid relative to the bottom of the Fermi sea (left). Energy distribution of the emitted electrons.

Auger De-excitation

In addition to Auger neutralization, there is the process of Auger de-excitation. Here, the first step is the transition of an electron from the solid into an unoccupied level in the ion, see Fig. 5.32 (green arrow). An energy E_x is released during the transition to the ground state of the ion, the neutralization. The released energy E_x is then used to trigger an electron from the solid or the adsorbate atom. The process of Auger de-excitation has only a small contribution compared to Auger neutralization.

5.5.2 Secondary Electron Emission by Metastable Particles

Secondary electron emission by the impact of metastable particles is very similar to ion-induced secondary electron emission. Here, an ion is first generated in a first step. There is the process of resonant ionization and Auger de-excitation:

- *Resonant Ionization:* In the so-called resonant ionization, the overlap of the excited state of the metastable particle with a free state in the solid is very large. As a result, the metastable particle is quickly ionized. Subsequently, this ion is then neutralized again by Auger neutralization and a free electron is created. This process has a large cross section.

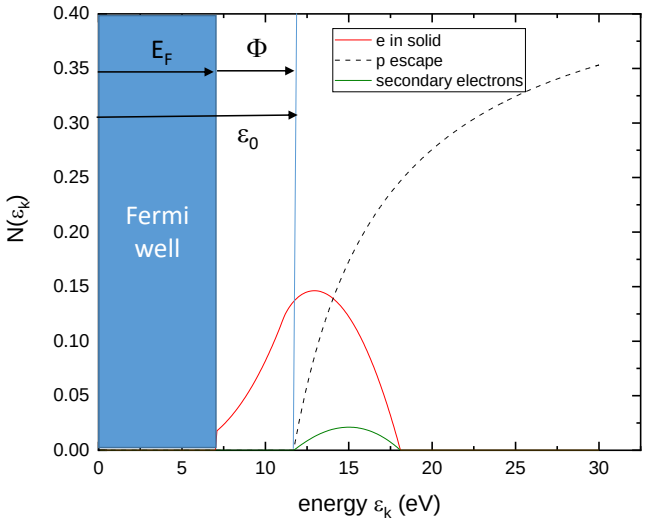

Figure 5.30: Calculated energy distribution of the electrons inside the solid or outside for argon ions on copper.

- *Auger De-excitation:* In Auger de-excitation, the ground state is created because an electron from the solid transitions into the state of the metastable particle. A negative ion is created. This immediately neutralizes itself with the emission of an electron. This process has a small cross section.

The two processes depend on the relationship between the energy of the upper excited state and the Fermi energy. As an example, the reaction of helium metastables is shown in Fig. 5.33. The ionization energies are 24.8 eV and the upper level is at about 20 eV. That is, for work functions greater than 4.8 eV, resonant ionization occurs, for smaller work functions Auger de-excitation.

Bibliography

[Eck91] W. Eckstein. *Computer Simulation of Ion Solid Interactions.* Springer Series in Materials Science, Berlin and Heidelberg, 1 edition, 1991.

[Sig81] P. Sigmund. Sputtering by ion bombardment: Theoretical concepts. In R. Behrisch, editor, *Sputtering by Particle Bombardment I*, pages 9–71. Springer, Berlin, 1981.

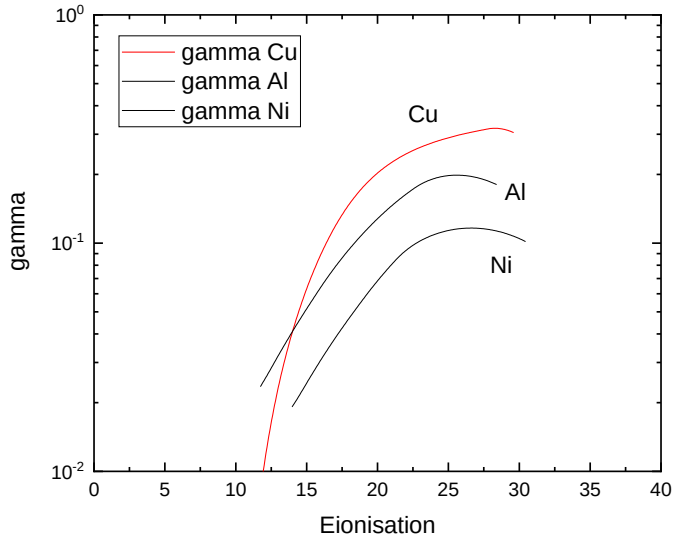

Figure 5.31: Dependence of γ on the ionization energy of the ions for copper, aluminum, and nickel.

[Tho68] M.W. Thompson. *Philos. Mag.*, 18:377, 1968.

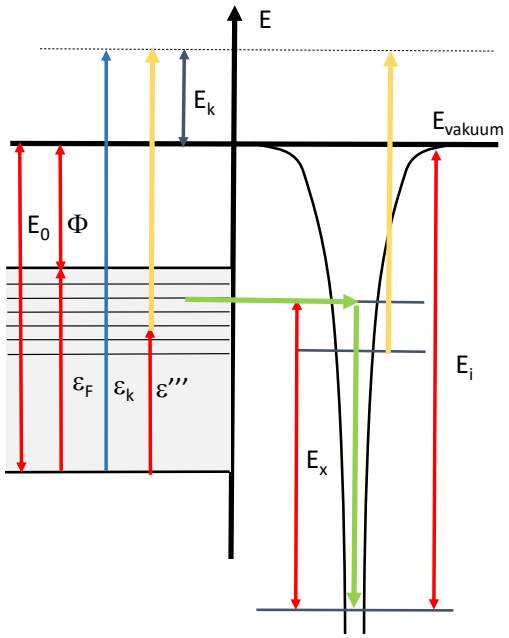

Figure 5.32: Auger de-excitation. The energy during de-excitation can either be emitted by an electron of the adsorbate (self-excitation) or an electron of the solid.

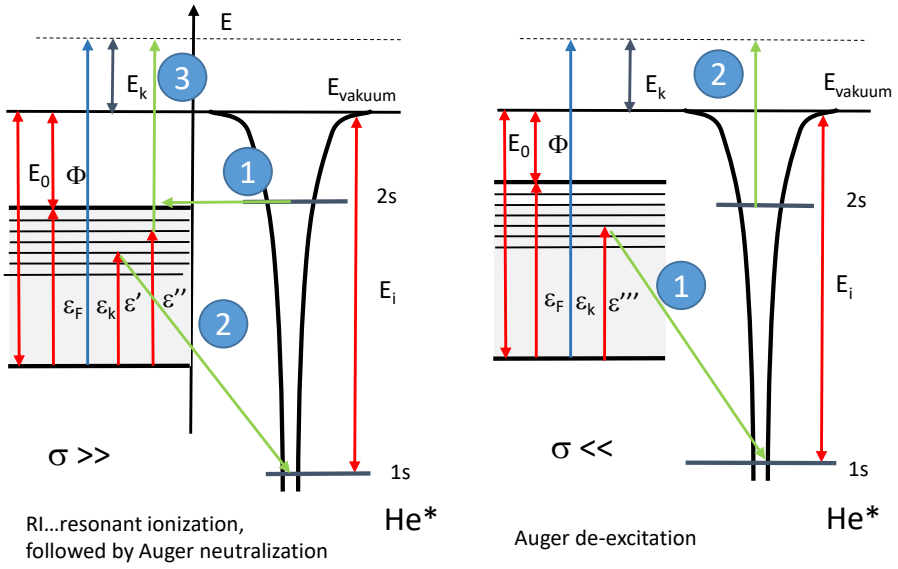

Figure 5.33: Energy distribution of the electrons inside the solid relative to the bottom of the Fermi sea (left). Energy distribution of the emitted electrons.

Chapter 6

Measurement Methods for Surface Fluxes

6.1 Measurement of Ions

6.1.1 Measurement of Ions Using Probes

The currents through a boundary layer on a surface depend on the potential of this surface and the electron temperature according to the Bohm velocity. That is, by recording a current-voltage characteristic, it should be possible to obtain information about the distribution function of the charge carriers and their density. A probe measurement utilizes this fact:

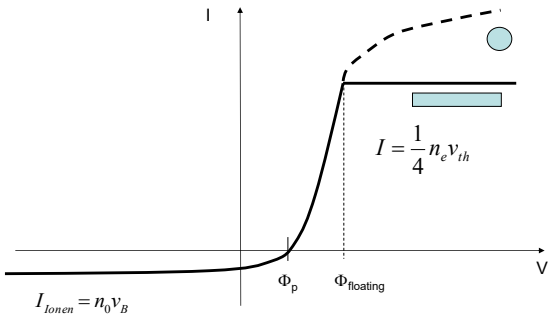

Figure 6.1: Probe characteristic

Three regions in the current-voltage characteristic can be distinguished (probe is planar) (see Fig. 6.1).

- **Ion saturation current**

  With a strongly negative bias of the surface, the electrons are repelled and the current is essentially carried by the ions. From this region, the charge carrier density is usually determined. The current density is given by.

$$j_{\text{Ionen}} = -en_0 v_B \tag{6.1}$$

- **Running area**

  At medium voltages, the electrons are no longer completely repelled, and the electron current can partially compensate for the ion current. At the floating potential, this is exactly fulfilled because $j_e = j_{Ionen}$. When the potential reaches the plasma potential, the electrons are no longer repelled. The electron current is proportional to:

$$j_{\text{e}} = \frac{1}{4} en_0 v_{e,th} \exp\left(\frac{V - \Phi_P}{k_B T_e}\right) \tag{6.2}$$

  The total current that the probe sees is, of course, the ion current plus the electron current; i.e., to correctly determine the electron current, the ion current must still be subtracted in the running area.

- **Electron saturation current**

  At voltages above the plasma potential, all electrons are collected, and the current obtained is

$$j_{\text{e}} = \frac{1}{4} en_0 v_{e,th} \tag{6.3}$$

In general, from the running area, not only the electron temperature can be determined but, of course, also the distribution function of the electrons. With increasing voltage V, fewer and fewer electrons are repelled. Therefore, from the velocity space of the electrons, an increasingly larger volume in phase space contributes to the current:

$$j_e = e \int_{v_{min}}^{\infty} v^2 f(v) dv \int_0^{2\pi} d\phi \int_0^{\Theta_{min}} \underbrace{v \cos\Theta}_{z-projection} \sin\Theta d\theta \tag{6.4}$$

The connection between azimuthal angle and minimum velocity is:

$$\cos\Theta_{min} = \frac{v_{min}}{v} \tag{6.5}$$

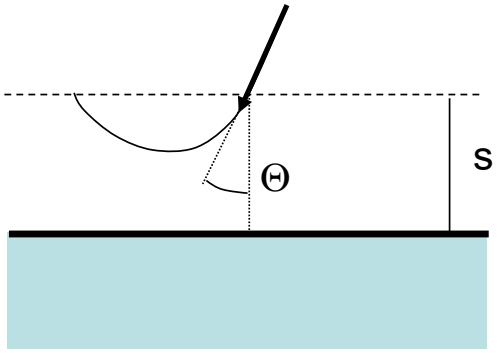

Figure 6.2: The boundary layer as a velocity filter of the incident ions or electrons

Thus, we obtain:

$$j = e\pi \int_{v_{min}}^{\infty} v^3 \left(1 - \frac{v_{min}^2}{v^2}\right) f(v) dv \tag{6.6}$$

We now consider the distribution function not as a function of velocity, but as a function of energy ϵ with

$$\epsilon = \frac{1}{2} m v^2 \tag{6.7}$$

Furthermore, we consider the minimum velocity v_{min}, expressed by the potential difference V, which drops between the probe and plasma ($V = \Phi_p - V_{probe}$) and which holds back the electrons with velocities smaller than v_{min}. Through this coordinate transformation, we obtain:

$$I = \frac{2\pi}{m^2} A \int_{V}^{\infty} \epsilon \left(1 - \frac{V}{\epsilon}\right) f(\epsilon) d\epsilon \tag{6.8}$$

The derivative with respect to the potential difference V yields:

$$\frac{dI}{dV} = -\frac{2\pi}{m^2} A \int_{V}^{\infty} f(\epsilon) d\epsilon \tag{6.9}$$

or:

$$\frac{d^2 I}{dV^2} = \frac{2\pi}{m^2} A f(\epsilon) \tag{6.10}$$

That is, the second derivative of the characteristic is directly proportional to the distribution function of the electrons. In practice, this determination of the distribution function is made difficult by the necessity (i) to subtract the ion current from the measured total current, (ii) to determine the plasma potential, and (iii) to form the second derivative with noisy data.

In addition to these aspects of evaluation, it must also be noted that often a small cylindrical probe is chosen in order not to disturb the plasma. With a cylindrical probe, however, when considering the electron and ion current, the conservation of angular momentum and the expansion of the boundary layer with increasing negative voltage of the probe must be taken into account. Here, two cases can be distinguished: (i) in the collisionless case, the currents result from the OML (orbital motion limited) theory, while in the case with collisions in the boundary layer, the current is determined by the radial transport. These two cases are illustrated in Fig. 6.3.

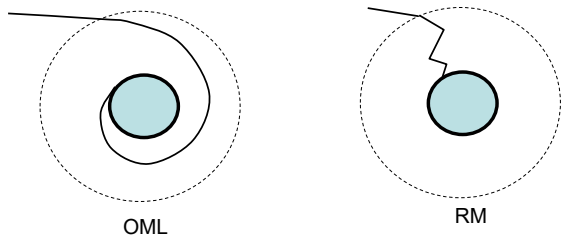

Figure 6.3: Orbital-Motion-Limited (OML) current, Radial-Motion-Limited (RML) current

6.1.2 Retarding Field Analyzer (RFA)

When measuring a probe characteristic, the signal is dominated by the electron current. Therefore, with the probe methods, the energy distribution of the electrons is determined. The energy distribution of the ions, on the other hand, is better measured with a retarding field analyzer (RFA). Here, ions are extracted from the plasma and must run against a retarding field. The derivative of the current-voltage characteristic then yields the velocity distribution of the ions. In addition, the total ion flux is determined. The setup of an RFA is shown schematically in Fig. 6.4: Ions enter through a grounded grid or a small opening (0). A first grid (1) serves to retain the plasma electrons. A second grid (2) is varied in its potential and serves as a barrier for the incoming ions. A third grid (3) in front of the collector Â©

serves to retain the secondary electrons triggered at the collector. When constructing a retarding field analyzer, the following things must be considered [BP93, WRMA96, WRM+97]:

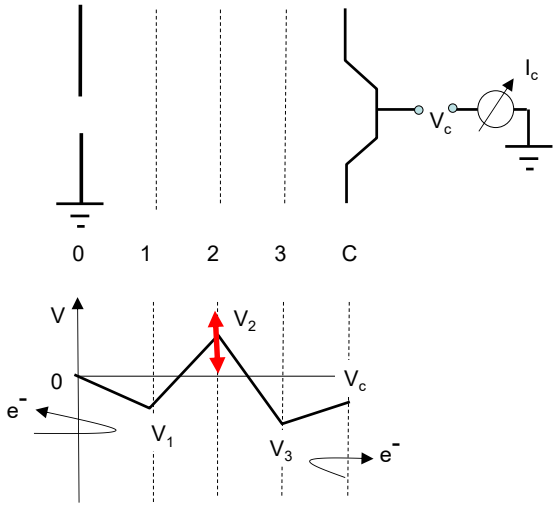

Figure 6.4: Connection of a retarding field analyzer. Grid 0 to the plasma. Grids 1, 2 and 3 inside the RFA and area C as collector.

- **Entrance opening:**

  The entrance opening of the RFA should be smaller than the Debye length to avoid disturbing the energy of the ions by a local disturbance of the electric field distribution in the boundary layer in front of the entrance opening.

  If a grid (0) is used, on the one hand the mesh width must be smaller than the Debye length. In addition, from the assembly, the grid should be flush with the surface. Otherwise, a local field distortion would occur and the ions would not be injected axially into the RFA. This leads to a broadening of the energy distribution. The field distortion at the grid (0) is the determining factor for the energy resolution of the RFA (see Fig. 6.5). This field distortion can be given by the unfavorable assembly of the grid as well as by the field inhomogeneities in the meshes of the grid itself.

- **Plasma electrons:**

  Behind the entrance opening, a negatively biased grid (1) is needed to separate the electrons from the plasma ions. Assuming an electron

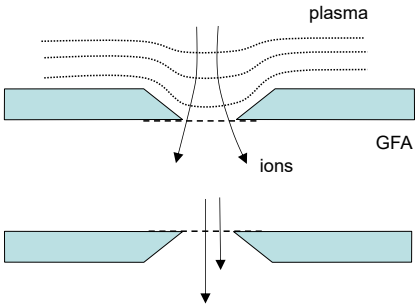

Figure 6.5: The field distortion at the entrance to the RFA is decisive for the energy resolution.

temperature of 4 eV, about -55 V is needed to hold back 99.98% of the electrons.

If these electrons are not repelled, they can advance into the region of grid (2) and are attracted by it. This leads to a high electron density in the RFA between grid (1) and (3), which causes ionization of the residual gas in the RFA. These additional ions contribute to additional energy channels in the spectrum.

- **Collector:**

  When the ions hit the collector, secondary electrons can be triggered. These apparently increase the incident ion current. To avoid this, a potential difference must exist between the collector ÂⒸ and the last grid (3) that always pushes the electrons back to the collector. The energy of the secondary electrons can be very roughly estimated as:

$$E_{\text{secondary electron}} = E_{\text{ionisation}} - 2\Phi_a \tag{6.11}$$

  with Φ_A the work function from the collector. This secondary electron generation is essentially triggered by the neutralization process of the ion (potential emission), therefore the potential energy of the ion (ionization energy) is decisive here. Only at kinetic energies in the keV range are secondary electrons triggered according to the electronic energy loss of the incident ion.

  The voltage at the grid (3) in front of the collector should be more negative than all others, so that secondary electrons generated at the different grids are also pushed back into the plasma.

If the capture of the secondary electrons by the collector Â© is not ensured by suitable wiring, a signal offset is observed even at a large retarding voltage at which no ion should reach the collector anymore. This signal is caused by secondary electrons triggered by photons or metastables that can reach the collector unobstructed (see Fig. 6.6).

- **Transmission of the grids:**

  If grids are used, their transmission must be taken into account. The mesh width should also be small compared to the distance l of the grids to realize optimal decelerating or accelerating potential curves. Otherwise, the field penetration leads to deflection of the ion trajectories. This influence on the width of the energy distribution scales as:

$$\frac{\Delta E}{E} \propto l^{-1} \tag{6.12}$$

- **Plan-parallel grids:**

  The grids should be as parallel as possible to each other in order to measure narrow energy distributions.

- **Mean free path in the RFA:**

  The mean free path in an RFA should be larger than its dimensions; otherwise, the energy resolution is impaired by collisions between the grids. This can be achieved by two measures: (i) on the one hand, the retarding field analyzer can be differentially pumped, and on the other hand (ii) one can try to make the RFA so small that the dimension becomes smaller than the mean free path. The latter has become possible through microstructuring technology. However, it is then no longer possible to work with grids, but simple holes in a conductive silicon layer are used. For the analysis of the measured energy distributions, a detailed description of the ion trajectories in the given potential profile must then be performed.

If the mentioned criteria for the wiring of the RFA are not considered, some artifacts become visible as shown in Fig. 6.6.

In RFA measurement, a current is measured which results from a velocity distribution $f(v)$ to:

$$I = e \int v f(v) dv = \frac{e}{M} \int f(v) dE \tag{6.13}$$

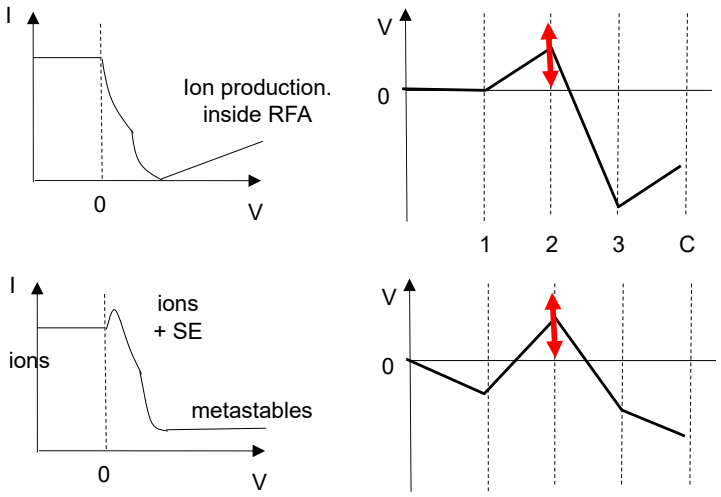

Figure 6.6: Artifacts in RFA measurement arise on the one hand due to insufficient suppression of plasma electrons (top): Electrons that penetrate the RFA can ionize there and thus contribute to the ion flux. In the same way, the inadequate suppression of secondary electrons at the collector leads to a background of secondary electron generation by metastables.

with $E = \frac{1}{2}Mv^2$. That is, the derivative of the current curve with respect to the voltage or energy of the ions is:

$$\frac{dI(E)}{dE} = \frac{e}{M} f(v) \tag{6.14}$$

Plotting $\frac{dI(V)}{dV}$ versus the voltage V thus corresponds to plotting a velocity distribution $f(v)$ versus an energy (corresponding to v^2).

The energy distribution is obtained by deriving the current-voltage characteristic. Since it is noisy data, a point-by-point derivation does not yield meaningful data. It is better to perform the derivation by convolution with a derived Gaussian function:

$$\frac{dI(V_0)}{dV_0} = \int_{V=0}^{\infty} I(V) \frac{V_0}{\sigma^2\sqrt{2\pi\sigma}} \exp\left(\frac{(V-V_0)^2}{2\sigma^2}\right) dV \tag{6.15}$$

Here, the parameter σ can be used to set the degree of averaging over the data.

In general, the incident ions have an angular distribution with respect to the surface normal. While the angular distribution in the plasma is still

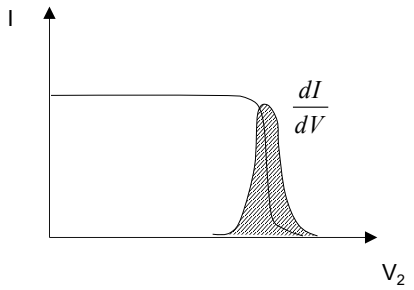

Figure 6.7: Determination of the IED by derivation of the characteristic.

isotropic, it is strongly narrowed by the acceleration in the pre- and boundary layer. The width of this distribution depends on the ratio of the ion temperature in the plasma and the boundary layer voltage as illustrated in Fig. 6.8. This narrow angular distribution can be broadened by collisions in the boundary layer. A narrow angular distribution is the basic prerequisite for the anisotropic etching of structures in semiconductor technology.

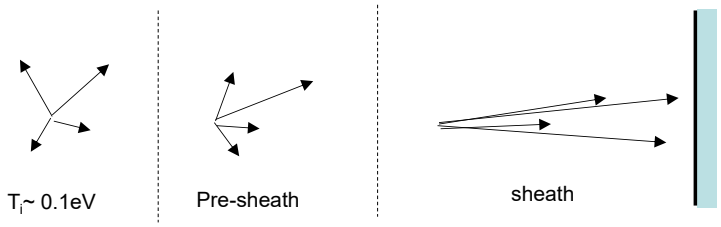

Figure 6.8: Narrowing of the angular distribution by acceleration in the boundary layer.

Measurement of this narrow angular distribution is possible by using an RFA whose collector is divided into individual elements. This, however, also requires the individual grids to be designed hemispherically. This is sketched in Fig. 6.9.

The generation of secondary electrons at the different points in the RFA can also be utilized to determine the secondary electron emission coefficient. For this purpose, grid 2 and 3 are connected equally. A current-voltage characteristic is observed which can be divided into three regions (i) only ions are measured as current I_1. Due to the negative bias, secondary electrons are pushed back to the collector. (ii) Now all ions are still collected but the

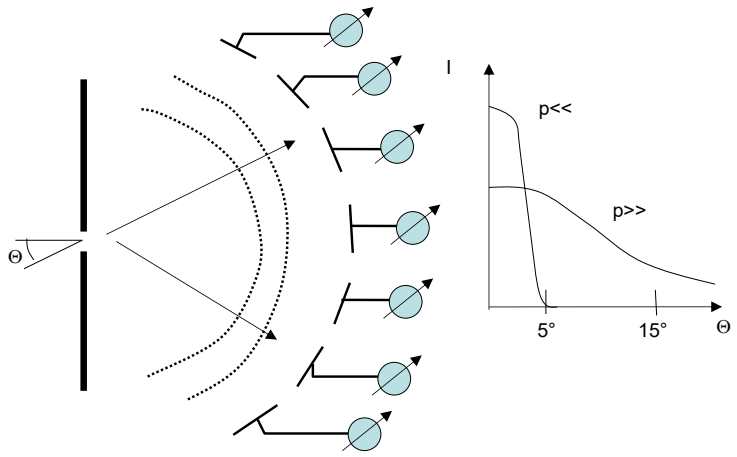

Figure 6.9: Measurement of the angular distribution by a spherical retarding field analyzer.

retarding voltage is no longer sufficient to push the secondary electrons back to the collector. An additional secondary electron current becomes visible as *apparently* higher ion current I_2. Therefore, the secondary electron emission coefficient γ_i is given as:

$$\gamma_i = \frac{I_2 - I_1}{I_1} \tag{6.16}$$

6.1.3 Plasma Monitor

In an RFA, the energy distribution is obtained only by deriving a current measurement. This measurement can be achieved much more accurately by using an energy filter. As a rule, this is additionally combined with a mass filter, so that an energy-dispersive mass spectrometer, the *plasma monitor* [ZNM97b, ZNM97a], is obtained.

A plasma monitor consists of several elements, as shown in Fig. 6.11: (i) a single lens to inject the ions into the energy filter, (ii) an energy filter that only allows ions of a certain energy to pass, (iii) a mass filter, usually a quadrupole filter, (iv) and a detector, either a Faraday cup or continuous (channeltron) or discrete secondary electron multiplier (dynodes). These elements are discussed below.

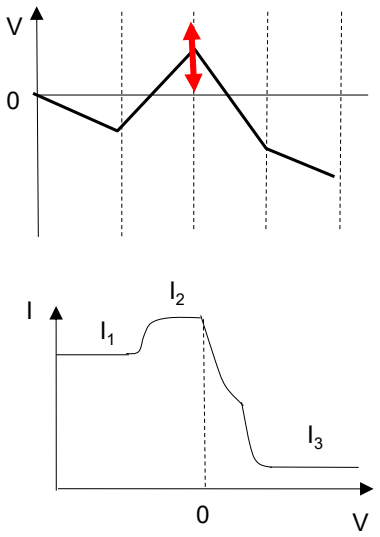

Figure 6.10: Determination of the secondary electron emission coefficients by derivation of the characteristic.

Ion Optics of the Single Lens

The deflection of a charged particle in an electric field, which is limited to the space between two grids (half-space left and right is field-free, see Fig. 6.12) results from the conservation of energy:

$$\frac{m}{2}v_2^2 = \frac{m}{2}v_1^2 + eU \tag{6.17}$$

with $\sin\alpha = \frac{v_{1x}}{v_1}$ and $\sin\beta = \frac{v_{2x}}{v_2}$ it follows because $v_{1x} = v_{2x}$:

$$\frac{\sin\alpha}{\sin\beta} = \frac{v_2}{v_1} \tag{6.18}$$

We obtain the law of refraction for charge carriers, similar to the law of refraction of light. The imaging law of an electrostatic lens can be calculated simply if the assumption of parabolic potential curves is made. The axis of the lens runs in the z-direction, and the potential has the form:

$$\Phi(r,z) = a(z^2 - \frac{1}{2}r^2) \tag{6.19}$$

Since now $\Phi(0,z) = az^2$ and $\Phi''(0,z) = 2a$ it follows:

$$\Phi(r,z) = \Phi(0,z) - \frac{1}{4}\Phi''(0,z)r^2 \tag{6.20}$$

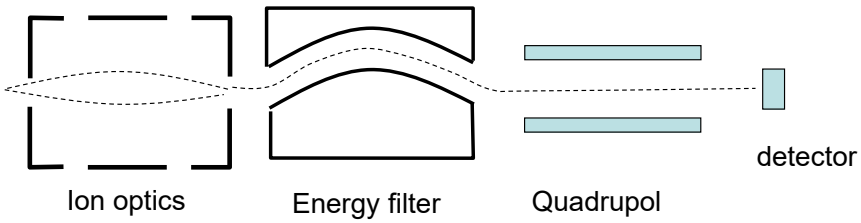

Figure 6.11: Connection of a plasma monitor.

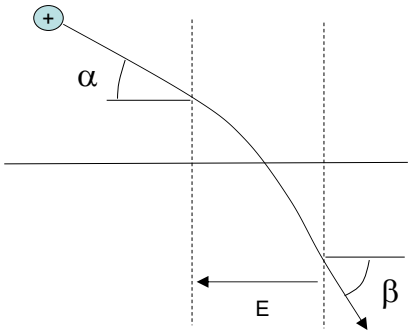

Figure 6.12: Passage of a particle through a region with constant field strength $\vec{E}$.

i.e. to get the potential for arbitrary r it is only necessary to know the course of the potential on the axis ($z = 0$). The equations of motion thus yield:

$$m\frac{d^2r}{dt^2} = e\frac{\partial\Phi}{\partial r} = -\frac{e}{2}\Phi''(0,z)r \tag{6.21}$$

$$m\frac{d^2z}{dt^2} = e\frac{\partial\Phi}{\partial z} = -\frac{e}{2}\Phi'(0,z)r \tag{6.22}$$

For an electrostatic lens, the following applies:

$$\frac{1}{a} + \frac{1}{b} = \frac{1}{f} = \frac{1}{r_m}\left[\frac{dr}{dz}_{z=z_1}\frac{dr}{dz}_{z=z_2}\right] \tag{6.23}$$

The focal length of a lens then results in

$$f = \frac{4\sqrt{\Phi_0}}{\int_{z_1} z_2 \frac{1}{\sqrt{\Phi}} \frac{d2\Phi}{dz^2} dz} \tag{6.24}$$

To optimally inject the collected ions into the energy and mass filter in a plasma monitor, it is necessary to adjust the optics of this single lens so that the ion trajectories are as parallel as possible when they hit the energy filter. A single lens is typically constructed as shown in Fig. 6.13.

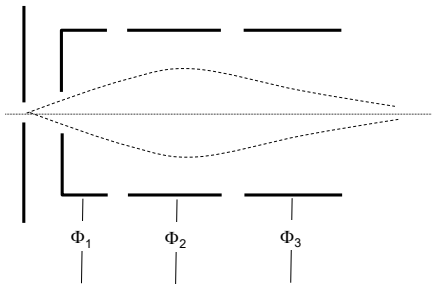

Figure 6.13: Structure of a single lens.

The energy filter is usually set to a constant pass energy, so that the transmitted ion is also injected into the mass filter with constant energy. Ions that enter the plasma monitor with arbitrary energy must first be decelerated or accelerated to this constant pass energy. This is done either in the space *before* the first single lens or *in* the first single lens. In the latter concept, the first lens element is grounded and the potential of the remaining lens elements is varied. If this shift of the potentials is not coordinated, the focusing condition of this first single lens changes and the injection conditions change with the set deceleration or acceleration voltage in the first lens. Chromatic aberration occurs. For a given plasma monitor, it is therefore advisable to optimize the ion optics with corresponding codes (SIMION).

Energy Filter

In an energy filter, the ions are deflected in an electric field with defined geometry. There are several arrangements for this filtering:

- **Sector field**

  In an electric sector field, consisting of two concentric cylinders, an ion is deflected. If the entrance and exit openings are at an angle of 127°

to each other, this element acts focusing, as shown in Fig. 6.14. The condition for imaging the entrance to the exit slit is:

$$2eV = E_0 \frac{R_o}{R_i} \tag{6.25}$$

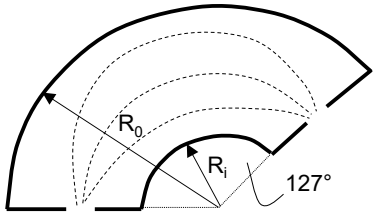

Figure 6.14: A sector field focuses ions if exit and entrance slits are mounted at 127 ° to each other.

with V the potential difference between the two cylinders, E_0 the energy of the incident ion and R_o and R_i the outer and inner radius of the concentric cylinder. This arrangement provides very good resolution but low transmission. The transmission can be increased if a hemispherical capacitor is used.

In the technical implementation of a sector field in a plasma monitor, however, it is often not spatially possible to realize the 127°, since the energy filter is still followed by the mass filter and ion detection. With 127° deflection angle, these components would usually project back into the plasma chamber. Therefore, a deflection angle of only 45° is typically chosen.

- **CMA**

  Another variant of the energy filter is the cylindrical mirror analyzer (CMA Cylindrical Mirror Analyzer). Here, starting from an axial position, the ions are injected into a cylindrical capacitor at 42.3°, as shown in Fig. 6.15. The ions are deflected and reach a second focus. The condition for focusing the entrance to the exit point is given as:

$$eV = E_0 \ln \frac{R_o}{R_i} \tag{6.26}$$

This form of analyzer has the advantage of a compact design and high transmission, since ions can in principle be collected over 2π of the circumference. In practice, however, a smaller solid angle is also used here. A disadvantage of the CMA is its lower energy resolution compared to the sector field. The distance between the focused entrance and exit points is:

$$l_0 = 6.1 R_i \tag{6.27}$$

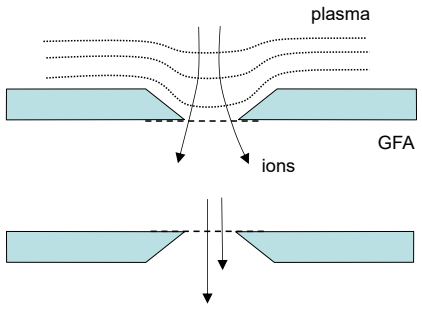

Figure 6.15: A cylindrical mirror analyzer has high transmission with medium energy resolution.

Mass Filter

The mass filter of a quadrupole mass spectrometer consists of a rod system of 4 cylindrical, parallel rods, with the opposite rods being connected equally, as shown in Fig. 6.16. The axial quadrupole field has the form:

$$\Phi(x, z) = \frac{\Phi_0}{2r_0^2}\left(x^2 - z^2\right) \tag{6.28}$$

The absolute surface accuracy of the rods is determined by manufacturing technology (typically μm). The absolute diameter of the rods (several mm) thus determines up to which accuracy the electric field on the axis can be realized. An electric alternating field Φ_0 is applied to this rod system, which is characterized by a direct voltage component U and an alternating voltage component V.

$$\Phi_0 = U + V\cos\omega t \tag{6.29}$$

The equations of motion of a charged particle with charge q and mass m, which moves through this filter, are given as:

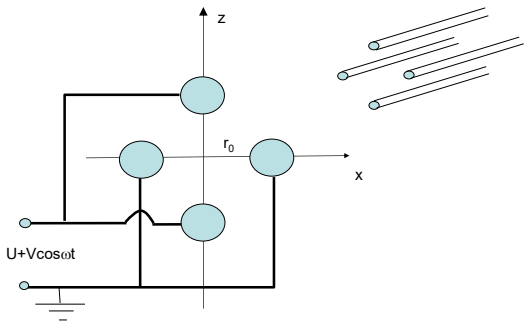

Figure 6.16: Quadrupole mass spectrometer

$$\frac{d^2x}{dt^2} + \frac{q}{mr_0^2}(U + V\cos\omega t)x = 0 \tag{6.30}$$

$$\frac{d^2z}{dt^2} - \frac{q}{mr_0^2}(U + V\cos\omega t)x = 0 \tag{6.31}$$

This equation of motion can be formulated more compactly after introducing the following new quantities:

$$a = \frac{4qU}{mr_0^2\omega^2} \tag{6.32}$$

$$b = \frac{2qV}{mr_0^2\omega^2} \tag{6.33}$$

$$\tau = \frac{1}{2}\omega t \tag{6.34}$$

Thus, we obtain the so-called **Mathieu differential equations**:

$$\frac{d^2x}{d\tau^2} + (a + 2b\cos 2\tau)x = 0 \tag{6.35}$$

$$\frac{d^2z}{d\tau^2} - (a + 2b\cos 2\tau)z = 0 \tag{6.36}$$

These equations have stable solutions for the trajectory of a particle in the rod system depending on the choice of the parameters a and b. This is illustrated in Fig. 6.17.

If the ratio of the direct and alternating voltage components is kept constant, a straight line is obtained in the stability diagram. The absolute choice of the direct voltage determines the mass of the ion that can pass the filter:

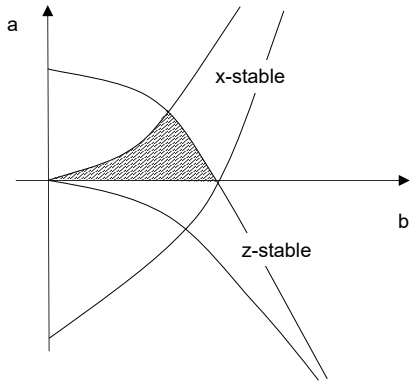

Figure 6.17: Stability diagram for the trajectory in a quadrupole mass spectrometer.

$$\frac{a}{b} = \frac{2U}{V} = \text{const.} \tag{6.37}$$

$$m = 4q\frac{U}{ar_0 2\omega^2} \tag{6.38}$$

If you want to increase the mass resolution, you can change the ratio of the direct and alternating voltage components and thus limit the number of permissible trajectories, as shown in Fig. 6.18.

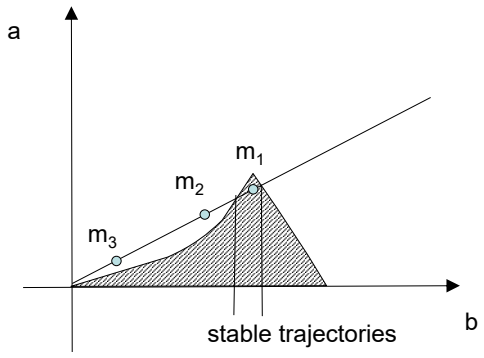

Figure 6.18: Region of permissible trajectories for a given ratio between direct and alternating voltage amplitude, $m_3 > m_2 > m_1$.

A mass scan is realized by increasing the amplitudes starting from small values of U and V while keeping the ratio of U and V constant.

The speed at which ions pass through this quadrupole filter of length L determines the mass separation that can be achieved. The unstable trajectories are characterized by the fact that the amplitudes of the oscillatory motion in the quadrupole field increase exponentially. With a small deviation of the mass from the target mass for which the transmission condition is satisfied, the exponential increase of the amplitude occurs only slowly. That is, the mass resolution becomes better if the rod system is made longer. On the other hand, if the velocity in the direction of the rod system becomes large, the trajectory does not have the opportunity to pass through many rf cycles of the quadrupole field at a given length, and the exponential increase of the amplitude may not be sufficient to deflect the ion permanently. Therefore, the *dwell time* of the ion in the quadrupole filter is decisive for the mass resolution. If the velocity of the ions becomes too small, they become susceptible to deviations from the ideal quadrupole field and lose the confinement, or can no longer be well controlled by the optics. A compromise must therefore be found between stable trajectories and achievable mass resolution. The size of the rod system essentially determines the achievable resolution, since it is easier to realize the required surface roughness in the μm range for larger rods, which is necessary to generate an ideal quadrupole field on the axis.

Ion Detection

The detection of ions is done via secondary electron generation in a channeltron or the first dynode of a SEM. This efficiency depends on the velocity of the ions, and therefore, at higher masses, the detection becomes less sensitive at the same energy. This must first be determined by calibration. If a Faraday detector is used, it is insensitive to the velocity of the ions. However, the sensitivity of the Faraday detector is much lower than that of a SEM. In addition, the Faraday detector is slower than a SEM. Finally, it depends on the design of this Faraday cup whether the ion-induced secondary electrons are trapped within this Faraday detector. Sometimes, the respective manufacturer only designates a simple metal sheet in the beam path as a Faraday detector, although the capture of the secondary electrons *is not* ensured there.

The performance of a SEM can vary greatly with the coating of the respective surfaces, as this coating changes the work function and thus the efficiency for the production of secondary electrons. Therefore, it is necessary to calibrate the SEM signal *daily* with the signal of the Faraday detector or another standard very frequently.

Calibration of a Plasma Monitor

The calibration of the mass and energy transmission of a plasma monitor is usually done by comparison with an RFA measurement.

- **Energy transmission** $T(E)$

  To determine the relative energy transmission of a plasma monitor, noble gas plasmas are suitable, which are operated at different powers and pressures. Depending on the plasma operation, the sheath voltage changes and thus the average energy of the ions. By comparison with retarding field measurements, the energy transmission can be determined. This naturally only applies to plasmas in which the incident ions have a sharp energy distribution. In general, the transmission is lower at high energies than at low energies. This is mainly due to the necessary deceleration of the ions to the pass energy of the energy filter. This deceleration is realized in a simple retarding field and changes the angular distribution of the ions. Since the acceptance angle of the plasma monitor is usually small, only a small part of the angular distribution is captured with strong deceleration. This is illustrated in Fig. 6.19.

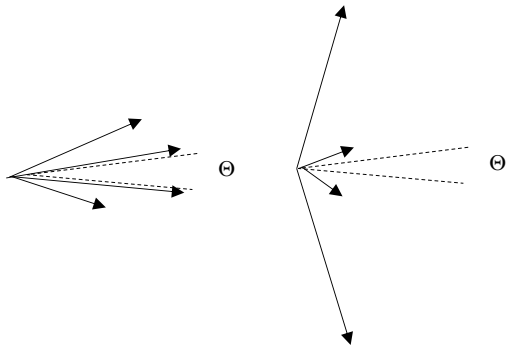

Figure 6.19: The deceleration of the ions in a retarding field changes their angular distribution. Since a plasma monitor has only a small acceptance angle Θ, the number of ions captured changes drastically with their deceleration.

- **Mass transmission** $T(m)$

  For the determination of the relative mass transmission, plasmas must be used in which only one ion species occurs (such as in noble gases,

for example). By comparison with the RFA measurements, a mass transmission for the individual ions is then obtained. Here, however, the energy dependence must still be subtracted.

- **Detection sensitivity of the system C**

  The detection sensitivity of the entire system determines the absolute signal height. The detection sensitivity now includes the collection problem of the differential pumping stage, the ion optics, the transmission of the quadrupole, and the detection sensitivity of the chosen detector.

In summary, the true detection capability N results from the product:

$$N = CT(E)T(m) \tag{6.39}$$

The relative mass and energy transmission can be determined once for a given instrument. The detection sensitivity should be calibrated more often. The daily fluctuations of the signal are mainly caused by the performance of the detector. This influence can be corrected by comparison with the Faraday measurement.

Error Sources in Quantitative Ion Spectrometry

In ion spectrometry, several error sources can be defined:

- **Acceptance of the spectrometer:**

  For the operation of a mass spectrometer, this must be differentially pumped. Usually one or two pumping stages are required. Since the angular distribution of the incident ions is very narrow due to the acceleration in the boundary layer, the alignment of the apertures must be very precise. This is particularly difficult since the opening is usually in the range $> 100\mu$ while the distance of the individual apertures is in the range mm.

- **Chromatic aberration:**

  Energy filtering is usually done in such a way that the filter (sector field, Bessel box, Cylindrical Mirror Analyzer (CMA)) is set to a fixed pass energy, and the ions are first decelerated or accelerated to this energy. This deceleration/acceleration usually takes place within the single lens directly after the ions enter the plasma monitor.

  The imaging properties of this first single lens change with its wiring. Often, the first aperture of this single lens is grounded and the potential

of the middle and second aperture is varied. That is, the deceleration of the ions to a fixed energy also changes the focus of this lens and thus the absolute ion transmission of the plasma monitor. This can be compensated by suitable wiring of this lens [HvSB+98].

- **Detector sensitivity:**

  The detection of ions is done via secondary electron generation in a channeltron or the first dynode of a SEM. This efficiency depends on the velocity of the ions, and therefore, at higher masses, the detection becomes less sensitive. This must first be determined by calibration.

- **Absolute measurement, by comparison with RFA:**

  An absolute measurement of the ion current is only possible by comparison with an RFA measurement.

- **Linearity of the scale**

  The linearity of the sensitivity scale can be easily checked with isotope mixtures. These isotope mixtures result in intensity peaks on closely spaced masses, the ratio of which must exactly correspond to the isotope ratio after the ionization probability of the isotopes is equal.

- **Afterglow SEM detector**

  With a defective SEM detector, afterglow can occur. This becomes visible when a small peak is measured after a large one. With an afterglowing detector, the order in which the peaks are measured makes a big difference.

6.2 Measurement of Neutrals

6.2.1 Standard Mass Spectrometry

The detection of neutral particle fluxes on surfaces is done directly using mass spectrometry. To filter particles according to their mass, they must first be ionized and then filtered according to their mass in a magnetic sector field or in an rf quadrupole field. Quadrupole mass spectrometers have become established as standard diagnostics for low-temperature plasmas because they enable a simple, compact design for mass spectrometers.

Ionization

For detection, collected neutral particles are first ionized in an ionizer. There are several designs for this. An ideal ionizer leads to electron impact ionization of the incident neutral at a fixed energy. A hot filament is used as an electron emitter, which is placed at a negative potential relative to an ionization volume to accelerate the electrons. The ionization process in the ionizer is the cause of a number of problems in mass spectrometry:

- **Chemistry at the hot filament:**

  Particles can be thermally dissociated at the hot filament. These particles can be ionized because they can easily enter the ionization volume and thus contribute to the background signal in the mass spectrometer. This can only be prevented by realizing as high a pumping capacity as possible at the location of the ionizer or by using special filaments (low work function = lower temperature necessary to produce the same electron current).

- **Electron-stimulated desorption:**

  With a simple wiring of the ionizer, the electrons are accelerated into the ionization space and ionize the neutral particles there. If the ionizer as a whole is not shifted to a positive potential, the electrons also reach other areas of the ionizer's surroundings. There, electron-stimulated desorption (ESD) can then take place, which contributes to the neutral gas background in the ionizer.

  If, on the other hand, a wiring is used in which the entire ionizer is shifted to a positive potential, the electrons are always pushed back to the anode, and electron-stimulated desorption can only take place there. With a special design of this surface, the contribution by ESD

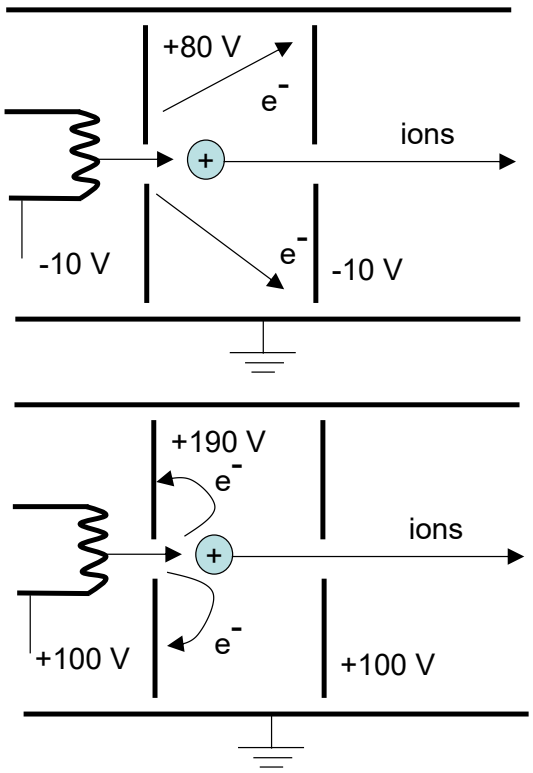

Figure 6.20: If the entire ionizer of a mass spectrometer is placed at a positive potential compared to the surroundings, the generation of secondary particles by electron-stimulated desorption can be strongly suppressed.

can thus be greatly reduced. A corresponding wiring of the ionizer is shown in Fig. 6.20.

- **Electron energy not sharp:**

  The heating of the filament is realized by current flow. This, however, leads to the fact that a voltage also drops across this filament, which is added to the acceleration voltages, depending on whether the electron was emitted at the beginning or at the end of the filament (see Fig. 6.21). This leads to a blurring of the electron energy. This is particularly disadvantageous in ionization threshold spectroscopy (see below). The optimal ionizer is a so-called cross-beam ion source in which a mono-energetic electron beam is crossed with the incident neutral particle beam.

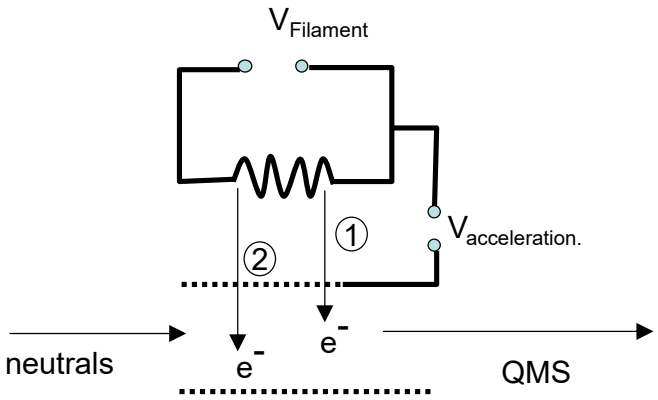

Figure 6.21: Blurring of the energy of the electrons in the ionizer of the mass spectrometer due to unfavorable wiring or design of the filament.

- **Extraction of the ions from the ionizer:**

  In the ionizer, ions are formed by electron impact-induced ionization. These ions must be extracted from the ionizer. The kinetic energy of these ions at the extraction opening consists of the difference between the extraction voltage and the potential at the location where the ions were formed. In order to define the energy of the ions more precisely, it is therefore necessary that the extraction optics collect the ions from a small localized location. That is, the image point for the extraction optics should be small. This can be realized by strong potential gradients. In these, the ions formed are strongly accelerated, and only a strongly localized part of the ions is injected into the mass filter. Due to the strong acceleration, the ions become very stiff on their trajectories and inaccuracies in the potential profile of the device do not lead to a deterioration of the transmission properties of the device. Such a wiring of the ionizer is shown in Fig. 6.22.

- **Extraction of hot ions:**

  Usually, a small volume within the ionizer is extracted with ion optics and injected into the mass filter. The density of the ions formed in the extraction volume is thus a measure of the signal. This becomes particularly problematic with *hot ions*: in the ionization process, ions with high kinetic energy can be formed, which have only a small density in the extraction volume and therefore contribute only slightly to the

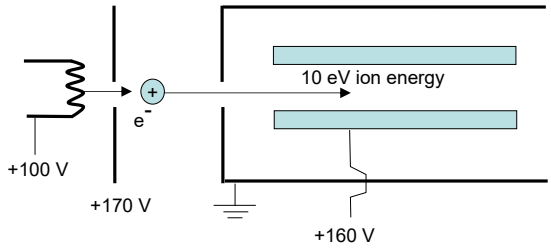

Figure 6.22: By skillful wiring of the ionizer, the ions are extracted with high energy and can thus be injected into the mass filter with high efficiency.

signal.

- **Fragmentation:**

  The electron energy in an ionizer is usually 70 eV. At this energy, the ionization cross sections for most compounds reach their maximum. The disadvantage is the strong fragmentation of the neutral particles. That is, not only the primary mother ion is formed, but a whole series of fragment ions with different fractions, a so-called fragmentation pattern is created. These fragmentation patterns overlap. To extract the densities or fluxes of the original neutral particles from these data again, the spectra must be decomposed into the individual contributions.

The Collection Problem

The pressure in a mass spectrometer should be as small as possible to reduce contributions to the background due to dissociation at the hot filaments, etc. Furthermore, the mean free path of the particles must be larger than the dimensions of the spectrometer. Finally, a SEM only works at pressures below 10^{-6} mbar. This makes a vacuum separation between plasma and mass spectrometer necessary. Here, an optimum must be found between ever better vacua and decreasing signal strength. If several differential pumping stages are used, the vacuum in the mass spectrometer becomes better, but at the same time the distance between the extraction opening and the mass spectrometer increases. The proportion of particles in the molecular beam decreases with r^{-2}. The following things must be considered:

- **Measurement of flux or density?**

The incident flux on the opening in the pumping stage that separates the mass spectrometer from the plasma is given as:

$$\Gamma_{IN} = \frac{1}{4} n v_{therm} \tag{6.40}$$

If many collisions occur in the ionizer, that is, the incident flux thermalizes there, the signal *does not* explicitly depend on the velocity v_{therm} and the measurement of a count rate is thus directly proportional to the influx of particles through the opening and thus to Γ. That is, **the signal corresponds to a flux measurement.**

If, on the other hand, the ionizer is ideally pumped, the probability of ionizing increases with increasing velocity, since the residence time in the ionizer becomes smaller. Although the flux increases with v_{therm}, the detection sensitivity decreases with v_{therm}. Thus, the signal is then proportional to the density n. That is, **the signal corresponds to a density measurement.**

Whether one measures a flux or a density can be tested using noble gases that are introduced into the main chamber at different pressures.

- **Number of pumping stages:**

  The number of differential pumping stages determines the achievable beam-to-background ratio [SCG99, CK71]. The conductance of an opening between two pumping stages is denoted by C. For a simple infinitesimally thin aperture with a round opening of radius r this is:

$$C = 11.7 \pi r^2 [cm] \sqrt{\left(\frac{28}{M[amu]}\right)\left(\frac{T[K]}{298}\right)} \frac{l}{s} \tag{6.41}$$

  The pumping capacity at the location of the aperture is denoted by S. The background pressure after m individual pumping stages is given as:

$$n_{\text{background}} = n_0 \prod_{i=1}^{m} \frac{C_i}{S_i} \tag{6.42}$$

  The density in the molecular beam, which is separated from the plasma, is:

$$n_{beam} = \frac{1}{2} n_0 \left(\frac{\pi r^2}{2\pi x^2} \right) = \frac{1}{4} n_0 \left(\frac{r^2}{x^2} \right) \tag{6.43}$$

This expression is obtained as follows: initially, the density in the opening is only half as large as the density in the volume, because for a location in the aperture opening only particles pass through from the plasma side, not from the side of the mass spectrometer. Particles passing through the aperture area πr^2 distribute themselves over the half-spherical surface $2\pi x^2$, according to the radius x. The ratio of beam to background is thus calculated as:

$$R = \frac{n_{beam}}{n_{background}} = \frac{1}{4} n_0 \frac{r^2}{x^2} \prod_{i=1}^{m} \frac{C_i}{S_i} \tag{6.44}$$

In practice, it turns out that the distance x, the distance between the individual apertures, cannot be made arbitrarily small with simultaneously high pumping capacity. Therefore, there is an optimum which lies at about 2 to 3 pumping stages.

6.2.2 Ionization Threshold Mass Spectrometry

The energy in the ionizer is usually 70 eV. To reduce fragmentation, the energy of the electrons in the ionizer is reduced in ionization threshold mass spectrometry. The disadvantage, however, is that the signal is smaller by orders of magnitude. With this method, it is possible to distinguish the contribution of radicals in a particle stream from that of the neutral parent molecules [KN95, SCG00, PJ98]. The fact is utilized that the following reactions have different threshold energies:

$CH_3 + e^-$	$\rightarrow CH_3^+ + 2e^-$	direct ionization
$CH_4 + e^-$	$\rightarrow CH_3^+ + H + 2e^-$	dissociative ionization

The threshold energy of the first reaction is 9.8 eV, while that of the second reaction is 13.6 eV, since in addition to ionization, a bond break also occurs. That is, if the electron energy is set to a value between 10 and 13 eV, only contributions from CH_3 radicals are obtained on the mass channel 15 amu.

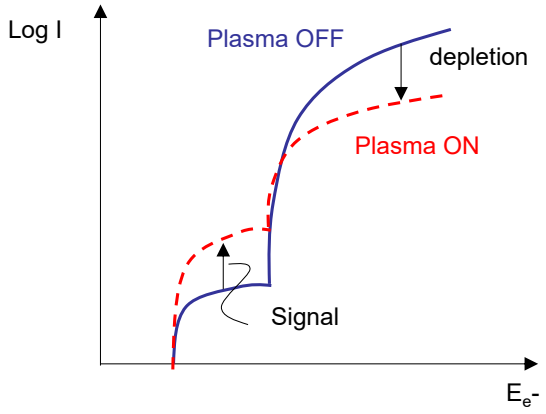

Figure 6.23: Signal curve in ionization threshold mass spectrometry.

6.2.3 Attachment Spectroscopy

An alternative to ionization threshold mass spectrometry is attachment spectrometry, in which negative ions are formed by electron attachment. In this process, fragmentation is very low. The disadvantage is that the electron energies must be very small, and conventional mass spectrometers can only generate the electron current by strongly heating the filaments at these operating modes, which makes frequent filament changing necessary. On the other hand, the cross sections for electron attachment are often not known, and thus a quantification of the data is made difficult.

6.2.4 Cavity Method

A fundamentally different approach to the detection of particle fluxes from a plasma is the cavity method [NDA94, HSSJvK00, KvdSSS00]. Here, a particle flux is directed into a defined geometry. In this geometry, particles can be reflected between the walls and are deposited on the surfaces according to their sticking coefficient. With this method, the surface loss probability of growth precursors in a reactive plasma can be determined. However, their identity cannot be determined.

In the simplest case, we consider the ratio of the layer thicknesses on the inner surfaces in a cavity at the top and bottom, as sketched in Fig. 6.24. We consider the case of a rectangular cavity into which the particles can enter through a slit. Furthermore, it is assumed that the distance of the side walls is much larger than the height of the cavity and the mean free path of

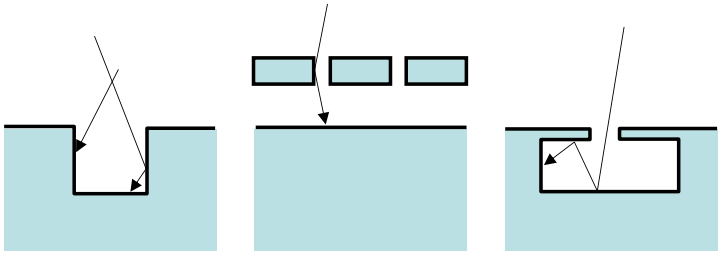

Figure 6.24: Cavity method.

the neutral particles is much larger than the dimensions of the cavity. Gas phase collisions are thus neglected, and the particles can be considered as ballistic. It is assumed that a fraction β is lost at each reflection (either by layer growth according to a sticking coefficient s or by reaction to a stable molecule with the probability γ, see Chap. 2), while a fraction $(1-\beta)$ is reflected. Thus, the following series results for the coating at the bottom of the cavity:

$$N_{bottom} = \beta N_p + (1-\beta)(1-\beta)\beta N_p + (1-\beta)^4 \beta N_p \ldots \quad (6.45)$$

$$N_{bottom} = \beta N_p + N_p \sum_{i=1}^{\infty} \beta(1-\beta)^{2i} = \quad (6.46)$$

$$= \beta N_p + \frac{(1-\beta)^2}{\beta(2-\beta)} N_p \quad (6.47)$$

In the same way, the coating on the inner surface at the top of the cavity can be determined, according to:

$$N_{top} = (1-\beta)\beta N_p + (1-\beta)^3 \beta N_p + (1-\beta)^5 \beta N_p \ldots \quad (6.48)$$

$$N_{top} = N_p \sum_{i=1}^{\infty} \beta(1-\beta)^{2i-1} = \quad (6.49)$$

$$= \frac{(1-\beta)}{\beta(2-\beta)} N_p \quad (6.50)$$

If the ratio of the number of particles lost at the top and bottom is formed, we obtain:

$$\frac{N_{top}}{N_{bottom}} = \frac{(1-\beta)}{\beta(2-\beta)} \left(\beta N_p + \frac{(1-\beta)2}{\beta(2-\beta)} \right)^{-1} = (1-\beta) \quad (6.51)$$

This derivation does not yet take into account the lateral layer thickness distribution on the inside of the cavity. For this purpose, for each reflection, either a specular reflection can be approximated, or a cosine distribution for the particles desorbing from the surface can be postulated. From the corresponding modeling of this local distribution of the layer thicknesses in the cavity, β can be determined exactly.

A simpler estimate is already possible on the basis of the comparison of the integral over the layer thickness distribution on the lower and upper inner side of the cavity. The ratio of these integrated layer thicknesses is a measure of the surface loss probability β (β includes the sticking coefficient s, according to $\beta = s + \gamma$, see Chap. 2). The ratio of the integrated layer thickness distributions is directly proportional to the factor $(1-\beta)$. If $\beta \to 0$, the layer thicknesses at the top and bottom are equal, since the particles almost survive an arbitrary number of collisions. The probability of being deposited somewhere on an inner surface of the cavity is thus equal. If $\beta \to 1$, the particles have no chance of surviving the first reflection on the lower inner side of the cavity. Therefore, the integral layer thickness on the upper inner side of the cavity becomes almost zero $N_{oben} = 0$.

This description shows that the comparison of the deposition rates at the top and bottom in a cavity is a direct measure of the surface loss probability β. This method has the advantage that it is particularly sensitive to particles with a high sticking coefficient, since $\beta = 0.8$ and $\beta = 0.9$ can be clearly distinguished. For small values of $\beta < 0.01$, a homogeneous coating in the cavity will always be observed, and a difference corresponding to $\beta = 10^{-3}$ and $\beta = 10^{-4}$ cannot be resolved. For the latter particles, mass spectrometry with the method of decay time is advantageous.

Bibliography

[BP93] C. Böhm and J. Perrin. *Rev. Sci. Instr.*, 64:31, 1993.

[CK71] J.W. Coburn and E. Kay. *J. Vac. Sci. Technol.*, 8:738, 1971.

[HSSJvK00] C. Hopf, T. Schwarz-Selinger, W. Jacob, and A. von Keudell. *J. Appl. Phys*, 87:2719, 2000.

[HvSB+98] E.A.G. Hamers, W.G.J.H.M. van Sark, J. Bezemer, W.J. Goedheer, and W.F. van der Weg. *Int. J. Mass. Spec.*, 173:91, 1998.

[KN95] P. Kae-Nune. *Plasma Sources Sci. Technol.*, 4:250, 1995.

[KvdSSS00] W. M. M. Kessels, M. C. M. van de Sanden, R. J. Severens, and D. C. Schram. *J. Appl. Phys.*, 87:3313, 2000.

[NDA94] A. Nuruddin, J. R. Doyle, and J. R. Abelson. *J. Appl. Phys.*, 76:3123, 1994.

[PJ98] P. Pecher and W. Jacob. *Appl. Phys. Lett.*, 73:31, 1998.

[SCG99] H. Singh, J.W. Coburn, and D.B. Graves. *J. Vac. Sci. Technol.*, 17:2447, 1999.

[SCG00] H. Singh, J.W. Coburn, and D.B. Graves. *J. Vac. Sci. Technol.*, 18:299, 2000.

[WRM+97] J.R. Woodworth, M.E. Riley, P.A. Miller, G.A. Hebner, and T.W. Hamilton. *J. Appl. Phys.*, 81:5950, 1997.

[WRMA96] J.R. Woodworth, M.E. Riley, D.C. Meister, and B.P. Aragon. *J. Appl. Phys.*, 80:1304, 1996.

[ZNM97a] M. Zeuner, H. Neumann, and J. Meichnser. *Vacuum*, 48:443, 1997.

[ZNM97b] M. Zeuner, H. Neumann, and J. Meichsner. *J. Appl. Phys.*, 81:2985, 1997.

Chapter 7

Measurement Methods in Surface Physics

7.1 Measurement Methods in Ultra-High Vacuum (UHV)

7.1.1 Electron Spectroscopy

Many measurement methods in surface physics use electrons as probes. Due to the limited penetration depth, the energy and direction of reflected electrons or electrons generated by the photoelectric effect carry information directly about the surface. When photons are used as probe particles, the information depth is often much greater.

The mean free path of electrons in the solid is described by the so-called **universal curve**. Almost independent of the element being investigated, the same mean free path is established. This has a minimum at 100 eV with a penetration depth of approximately 10 $\mathring{A}$. The derivation of this universal curve is as follows:

- **Density of States at Low Energies**

  At low energies, the mean free path increases because fewer and fewer electrons in the solid can participate in scattering processes. In a scattering process of an incident electron with energy E with an electron of the solid, this must be scattered into an unoccupied state according to the Pauli exclusion principle. Only states within a spherical shell of the Fermi sphere with a thickness E are accessible for this scattering process. The volume of the phase space of this spherical shell scales with

E^2. Therefore, the mean free path increases with increasing energy according to $1/E^2$.

- **Energy Dependence of Scattering at High Energies**

  At high energies, the effect comes into play that small-angle scattering scales with the particle velocity (see Bethe-Bloch formula). That is, at high electron velocities, the deflection is small and thus the mean free path is larger.

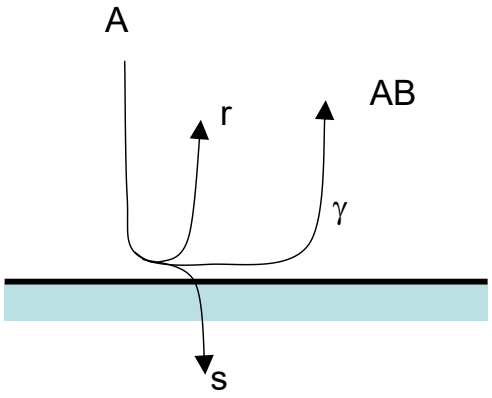

Figure 7.1: Universal curve for the penetration depth of electrons in a solid.

The success of electron-based surface diagnostics is essentially linked to the development of improved vacuum methods. In the early phase, the signals of these methods were superimposed by contamination of the surfaces, and an accurate elucidation of structures and mechanisms was not possible. Table 7.1 provides an overview of the most important electron-based methods.

- **Photoelectron Spectroscopy (XPS)**

  In photoelectron spectroscopy, electrons are emitted from the surface by X-ray photons through the photoelectric effect. The kinetic energy of these electrons is measured, which results from the difference between the photon energy, the binding energy, and the work function of the solid, as illustrated in Fig. 7.2.

$$E_{kin} = h\nu - E_B - \Phi \tag{7.1}$$

Quantity	Acronym	Physical Effect
Structure	LEED (Low-energy electron diffraction)	Diffraction
	ISS (Ion surface scattering)	Scattering
	STM (Scanning Tunneling Microscopy)	Tunneling Effect
Composition	XPS (X-ray photoelectron spectroscopy)	Photoelectric Effect
	AES (Auger electron spectroscopy)	Photoelectric Effect
	EELS (Electron energy loss spectroscopy)	Inelastic Scattering
Band Structure	PE (Photoemission)	Photon Absorption
	IPE (Inverse Photoemission)	Inverse Photon Emission

Table 7.1: A selection of electron spectroscopy methods

If the electrons originate from inner shells, the peaks in the electron energy spectrum are sharp, as these deep energy levels in the solid do not participate in the chemical bonding in the solid. Thus, they are characteristic of the individual elements.

However, the position of these sharp photoelectron peaks of the inner electrons can be slightly shifted, as the binding energy depends on the neighboring atoms: if, for example, electronegative atoms are present in the vicinity of an atom, the peak is shifted to higher binding energies in a characteristic manner. Thus, in the **C1S** peak, two neighboring peaks appear at higher binding energies if graphite is oxidized and CO and CO_2 groups are present on the surface. Due to the electronegativity of oxygen, a charge shift occurs, resulting in a δ^- at the location of the oxygen atom and a δ^+ at the location of the carbon. The δ^+ charge at the location of the carbon atom causes a higher binding energy for the core electron. Due to this sensitivity, XPS is also referred to as ESCA for this application (ESCA - Electron Spectroscopy for Chemical Analysis).

The cross section for the generation of photoelectrons can be tabulated, as it is almost independent of the chemical environment. Therefore, XPS is used for the quantification of the composition of samples.

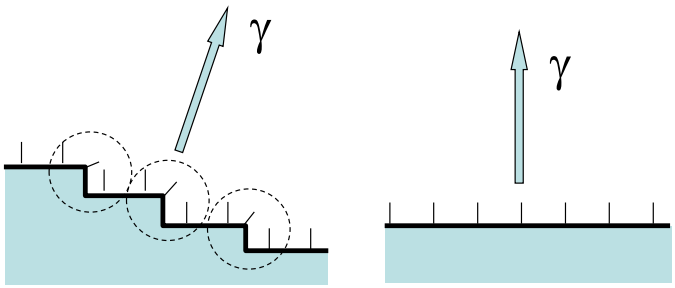

Figure 7.2: Term scheme for XPS.

When analyzing the kinetic energy of the emitted electrons in an XPS spectrum, it should be noted that in Eq. 7.1, the work function of the detector and not that of the sample is decisive.

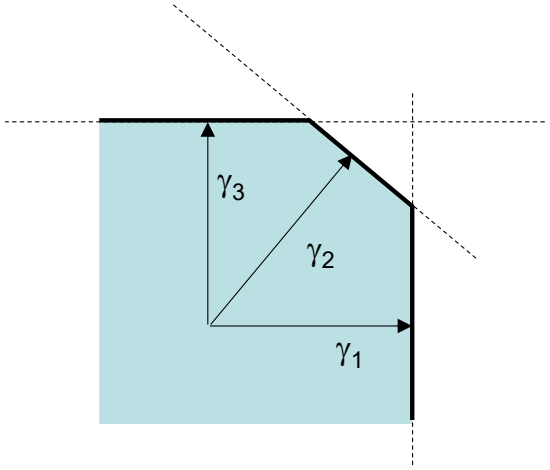

Figure 7.3: For determining the kinetic energy, the work function of the spectrometer is crucial.

In XPS measurement, the sample and the detector are electrically connected to each other, i.e., the Fermi levels equalize. An electron that is emitted from the sample must re-enter another solid on the surface of a detector to be measured as current. Fig. 7.3 makes it clear that the work function of the detector is important for this.

Furthermore, it should be noted that when using a simple X-ray tube

as a source, peaks may appear multiple times in the spectra, as the X-ray lines are split by the fine structure and several lines contribute to the signal simultaneously. This can only be excluded by using an X-ray tube with an additional monochromator.

- **Auger Electron Spectroscopy (AES)**

  In Auger electron spectroscopy, a core electron (K) is first removed by photons. The core hole (energy E_k) is filled by an electron in a higher shell (E_{L_1}); the energy released ($E_K - E_{L_1}$) is used to release another electron (energy E_{L_2}) given a work function Φ. The notation of the transitions follows the notation of the individual shells. In this example, it is a KLL transition, as shown in Fig. 7.4. The kinetic energy of the released electron is therefore:

$$E_{kin} = E_K - E_{L_1} - E_{L_2} - \Phi \tag{7.2}$$

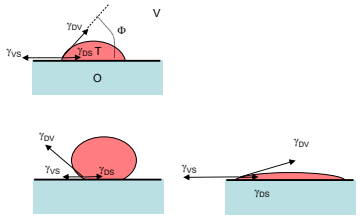

Figure 7.4: Term scheme of AES.

The quantification of Auger spectra is not straightforward, as the electrons released are outer electrons and the cross section strongly depends on the chemical bonding in which these electrons are located. Therefore, Auger spectra must generally be calibrated with other methods.

- **Electron Diffraction (LEED)**

  For the structural determination of crystalline surfaces, the diffraction of low-energy electrons is a standard method (LEED, low energy electron diffraction). It occurs similarly to X-ray diffraction in bulk crystals. For elastic scattering, the following applies:

$$\vec{k}_{OUT} = \vec{k}_{IN} + \vec{g} \tag{7.3}$$

  Here, $\vec{k}IN$ and $\vec{k}OUT$ are the wave vectors of the incident and outgoing electrons, which are equal in magnitude, and the vector $\vec{g}$ is the crystal

momentum. Since the penetration depth of the electrons is small, the diffraction occurs only at the topmost monolayers. This has the consequence that in the scattering, the crystal momentum perpendicular to the surface $\vec{g}\perp$ is *not* a conserved quantity, and only the periodicity of the wave vector in the surface $\vec{g}|$ must be considered. The following applies:

$$\vec{k}_{OUT} = \vec{k}_{IN} + \vec{g}\| + \vec{g}\perp \tag{7.4}$$

with an arbitrary length for the vector $\vec{g}\perp$. As in X-ray diffraction, an Ewald sphere (see Fig. 7.5) is constructed in reciprocal space. Each allowed $\vec{g}\|$ vector at the surface corresponds to a rod perpendicular to the surface, corresponding to arbitrary lengths for $\vec{g}\perp$. Where these rods intersect the Ewald sphere is the endpoint of the allowed vectors $\vec{k}OUT$. These vectors thus indicate the direction of the diffraction peaks.

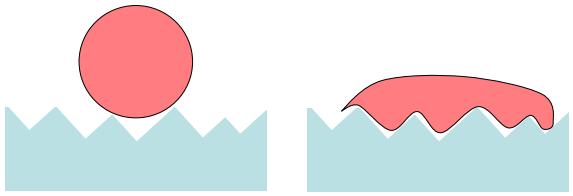

Figure 7.5: Ewald construction for electron diffraction at surfaces. The crystal momentum perpendicular to the surface is not a conserved quantity.

7.1.2 Structure Determination with Ion Beams

In structure determination by electron diffraction, only information about the large-scale order is obtained, as the method is based on the coherent superposition of electron waves.

However, if low-energy (keV) ions are scattered at the surfaces, information about the local short-range order is obtained, as, unlike in diffraction, the kinematics of the individual collisions are important. Ion scattering is element-sensitive, surface-sensitive, and structure-sensitive:

- **Element-Sensitive**

  Based on the kinematics of a collision between an ion and a surface atom (given by the masses, energy, and scattering angle), the mass of

the surface atoms can be determined from the energy of the scattered ion. The chemical information is derived from this.

- **Surface-Sensitive**

  The probability of neutralizing ions becomes very high if they penetrate into the solid. Therefore, reflected **ions** can only originate from scattering processes at the surface.

  By selecting the ion, the information depth of the diagnostics can be determined. If ions with high ionization energy are used, the unoccupied level in the ion is much deeper than the Fermi edge in the solid. Accordingly, the probability is high that this hole is filled (see Fig. 7.6). This neutralization usually occurs as Auger neutralization, as the released potential energy is consumed for the emission of a secondary electron. If an ion is still observed in the scattered signal, it is ensured that the scattering has indeed only occurred at the topmost atomic layer. Such a probe ion is, for example, helium.

  In contrast, alkali ions have a low ionization energy. In these ions, the probability is finite that the ion is not neutralized. That is, if ions are measured in the scattered signal, they can originate from scattering processes within the first atomic layers.

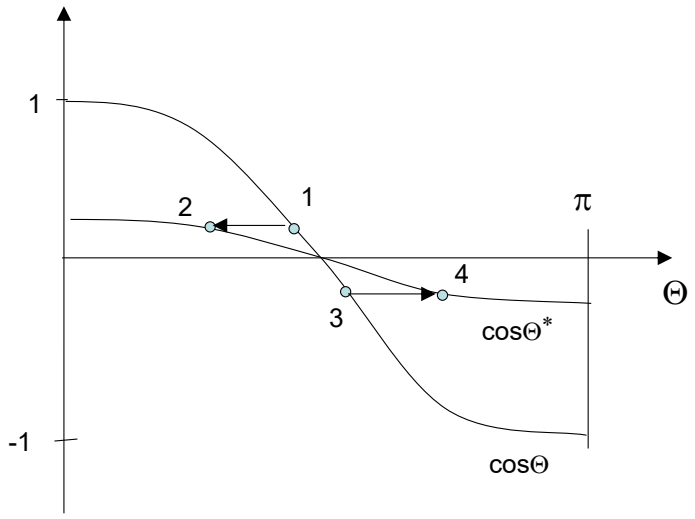

Figure 7.6: Depending on the ratio between ionization energy and work function, neutralization or ionization occurs.

- **Structure-Sensitive**

  The cross section for scattering of ions with energies in the keV range is of a suitable size so that when the angle of incidence of the ions is varied, the scattering at the topmost ions produces a shadow cone in which atoms of the second and third layers can disappear or appear, as illustrated in Fig. 7.7. That is, when measuring under variation of the angle of incidence or exit, a strong variation of the scattering intensity is obtained, depending on how many scattering partners are available.

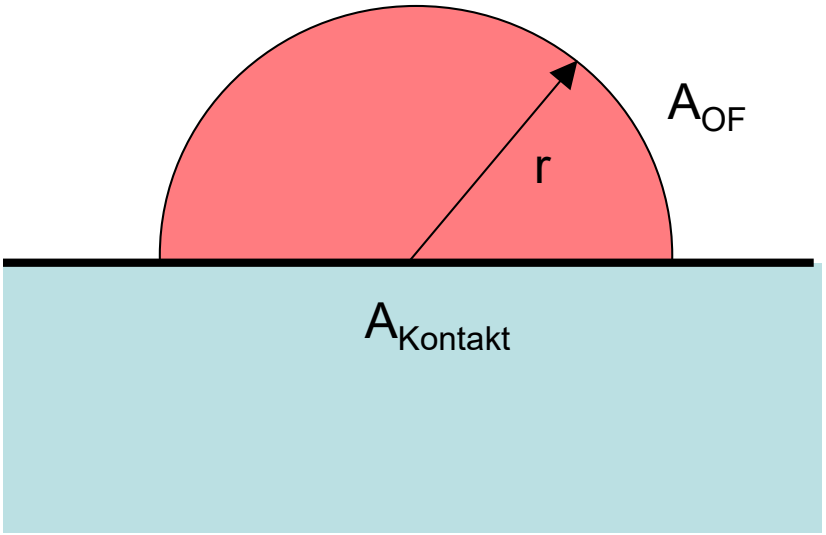

Figure 7.7: Structure determination by ion scattering. If the second layer enters the shadow cone of the first, a reduction of the signal occurs.

  This is in contrast to the scattering of MeV ions as in the Rutherford Backscattering (RBS) method. Here, the cross section is very small, and shadowing only occurs in certain crystal directions (channeling), where ions penetrate deep into the solid.

Chapter 8

Measurement Methods for Optical Properties

The following discusses the essential optical measurement methods that are crucial in plasma technology.

8.1 General

8.1.1 Optical In-Situ Diagnostics

Optical diagnostics have the great advantage that they are compatible with the pressures of a plasma. By coupling a diagnostic beam, the interface between plasma and workpiece can be examined without contact. The geometry of this observation immediately defines an incidence plane of the light, spanned by the direction of incidence and the surface normal of the surface. As the angle of incidence, an angle near 70° is often chosen, close to the Brewster angle, so that as much light as possible is directed into the sample and exits again through reflection at the back. Thus, the reflected light beam contains the maximum information about the film.

The disadvantage of optical methods is that the analysis requires an optical model that can be ambiguous. Furthermore, optical methods require a reflection geometry, i.e., two windows in the plasma system, which are often not available in a commercial context.

Optical measurement methods can be broadly divided into reflectometry and ellipsometry. In reflectometry, an intensity measurement is performed, which changes continuously, for example, by interference during the growth of a film. Here, the sensitivity is limited. However, in polarization-resolved methods such as ellipsometry, the change in the polarization state is measured

and is independent of the absolute intensity. These are much more sensitive.

8.1.2 Description of the Polarization State of Light

Alternatively, the polarization state can also be derived from the description of the shape of the ellipse.

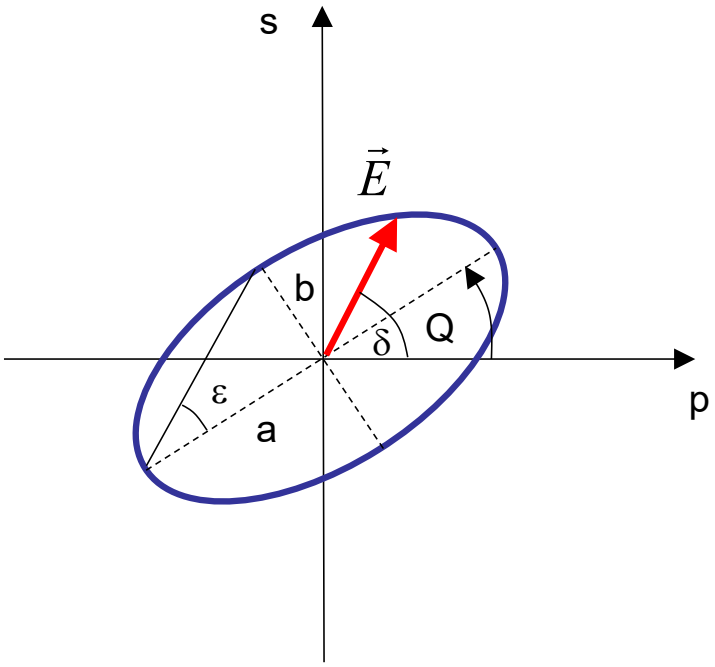

Figure 8.1: Description of the polarization state of light.

$$\chi = \frac{E_p}{E_s} = \frac{|E_p|}{|E_s|} e^{i(\delta_p - \delta_s)} \tag{8.1}$$

This quantity χ is related to the tilt of the ellipse Q and the ellipticity ϵ via:

$$\chi = \frac{\tan Q + i \tan \epsilon}{1 - i \tan Q \tan \epsilon} \tag{8.2}$$

This ellipticity ϵ is related to the semi-axes of the ellipse via:

$$\pm \frac{b}{a} = \pm \tan \epsilon \tag{8.3}$$

The sign distinguishes between left-handed and right-handed polarization. Thus, for Q and ϵ we obtain:

$$\tan 2Q = \frac{2\Re\chi}{1-|\chi|^2} \tag{8.4}$$

and

$$\sin 2\epsilon = \frac{2\Im\chi}{1+|\chi|^2} \tag{8.5}$$

8.2 Reflectometry

The simplest way to determine the optical properties is to measure the reflectivity. This can be done spectrally resolved in a transmission or reflection measurement, but also in-situ during a plasma process.

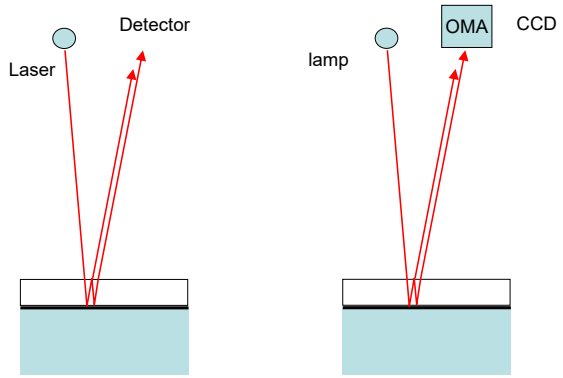

Figure 8.2: Typical arrangement of an interferometry measurement.

Transmission measurement is difficult to realize in-situ in a plasma process. A special case is the temperature measurement of heated wafers. Here, the band gap of a wafer is determined, which depends on the temperature. The empirical relationship is:

$$E_{gap}(T) = E_{gap}(0) - \frac{\alpha T^2}{T+\beta} \tag{8.6}$$

Here, α and β are empirical parameters. In the measurement setup, the radiation source is the heating coil located below the wafer, while the optics view the wafer from the outside. The band edge is then obtained from the

wavelength at which this optics no longer sees the emission of the heating coil.

For the evaluation of transmission or reflection measurements, it is essential to create a complete optical model of the film or the measurement. With the help of this model, the measurements can be evaluated quantitatively. An example of such an evaluation is shown in Fig. 8.3, where the transmission of a 100 nm thick film was fitted using a Tauc-Lorentz model.

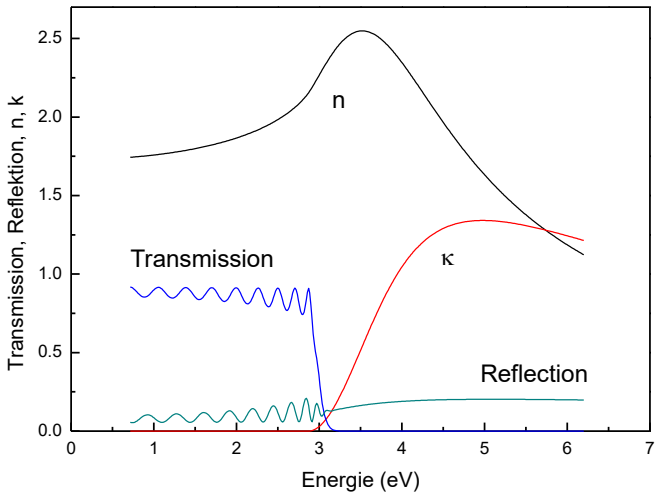

Figure 8.3: Transmission measurement of a 100 nm film assuming a Tauc-Lorentz dispersion.

What possibilities are there for in-situ measurement? Here, a laser is often reflected on the sample and a photodiode measures the interference during the plasma process. Alternatively, it is also possible to use a white light source and perform spectral resolution on the receiver side using a spectrograph. This has the advantage that redundant information about the film thickness is measured.

In a single-wavelength interferometer, the measurement signal is typically as shown in Fig. 8.4. A periodic change in the reflected intensity is observed as a thin film grows. From the angle of incidence and the phase shift, the optical thickness nd can be derived from the distance of the maxima or minima. However, this evaluation is much more accurate if a direct optical model of the measurement is used. Here, the absolute change in reflectivity is evaluated. At the beginning, the intensity corresponds to the reflectivity of the substrate. For an infinitely thick film, the reflectivity is then determined

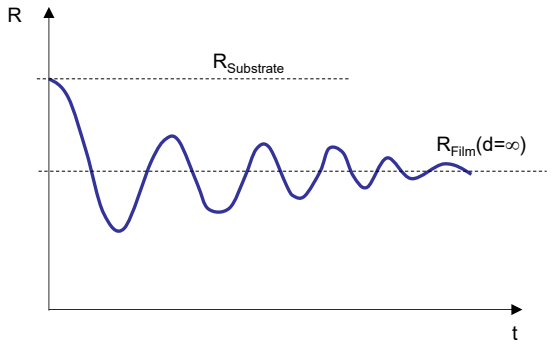

Figure 8.4: Interference signal of a single-wavelength interferometer.

by the refractive index of the film. During coating, a transition between these two boundary cases occurs. Only with quantitative modeling is it possible to obtain information about the absolute refractive index or the extinction.

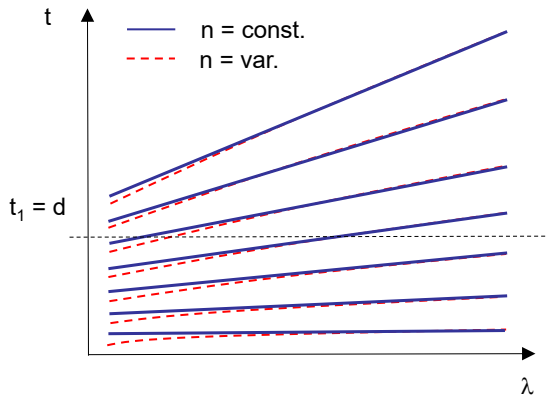

Figure 8.5: Distribution of the maxima of a spectrally resolved interference measurement.

This evaluation of a single-wavelength interferogram can still be ambiguous. In a spectrally resolved measurement, a distribution of the intensity maxima is obtained as shown in Fig. 8.5. It can be seen that with increasing wavelength, the distance between the maxima becomes larger. This is understandable since the difference in film thickness between the maxima becomes larger at large wavelengths. For a constant refractive index, straight lines are obtained in the plot of time versus wavelength. If the refractive index

varies (in the figure, the refractive index is higher at small wavelengths), a characteristic curvature of these lines results.

This type of measurement can also be performed spatially resolved by using a CCD camera as a detector in the laser interferometer. This type of measurement method is often used to evaluate photoresist coating in the semiconductor industry. Here, it is essential that a defined thickness of the layer is set to ensure the selectivity of the subsequent etching process (end-point detection). Reflectometry is particularly suitable for this, as the polymers used are transparent in the visible range and thus produce pronounced interferences.

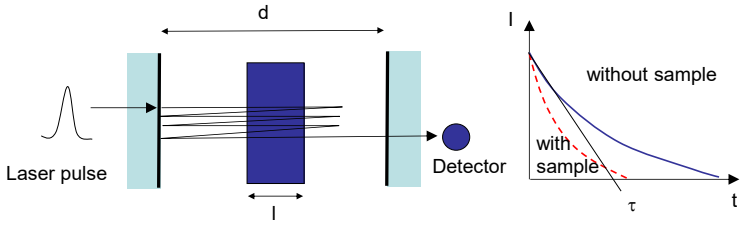

Figure 8.6: Cavity-Ring-Down-Spectroscopy.

If the absorption is very weak, more sensitive methods can be used to determine the optical properties. A particularly sensitive absorption measurement is Cavity Ring Down Spectroscopy (CRDS, Fig. 8.6). Here, a laser pulse is trapped in a high-quality laser cavity. It is multiply reflected and is only weakly coupled out on a mirror. If a detector is placed behind this mirror, an exponentially decaying signal is observed. If a sample is now placed between the mirrors, the laser pulse is additionally attenuated and the decay of the intensity occurs faster. From the difference between the decay time with and without the sample, the absorption can be inferred. It is essential that the absorption measurement is realized via a *time measurement*. The direct measurement of an intensity change with and without the sample is too insensitive. For the decay time τ the following applies:

$$\tau = \frac{d}{(1-R)+kl} \tag{8.7}$$

Here, d is the length of the cavity, l is the length of the sample, R is the reflectivity of the laser mirrors, and k is the extinction. It can be seen that the decay time becomes very long if R is close to 1. Only then is the laser pulse trapped in the cavity long enough to lead to an evaluable signal through the attenuation.

Another sensitive method is Photothermal Deflection Spectroscopy (PDS). Here, a laser beam is guided just past a sample (see Fig. 8.7). The sample is located in a liquid. A monochromatic light source is incident on the sample. If light from this source is absorbed, the sample heats up slightly. This heating leads to a gradient in the refractive index within the liquid above the sample. In the region of this refractive index gradient, the laser beam is deflected. This deflection is made visible on a position-sensitive detector.

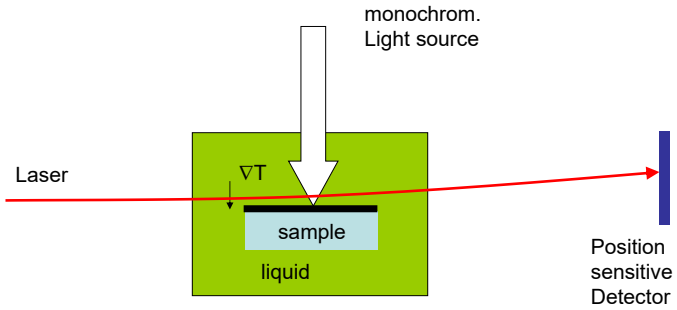

Figure 8.7: Photothermal Deflection Spectroscopy.

8.3 Ellipsometry

Unlike reflectometry, ellipsometry additionally measures the degree of polarization of the reflected light. This increases the accuracy of the method by orders of magnitude.

8.3.1 Calculation of the Beam Path

Jones Formalism

The propagation of light through an optical system can be described by matrices within a coordinate system relative to the plane of incidence (see Fig. 8.1). The directions are parallel p and perpendicular s to the plane of incidence. The reflection coefficients are the eigenvalues of this coordinate system r_p and r_s. The transmission axis of the polarizer is at an angle P to the plane of incidence. The analyzer is at A. We first consider a plane wave that can be described by a so-called Jones vector with components E_p and E_s corresponding to the electric field amplitudes.

$$\vec{E}_{in} = \left[\begin{array}{cc} E_p & E_s \end{array} \right] \tag{8.8}$$

The transmission through a polarizer is given by a matrix $\hat{T}$. If this transmission axis is parallel to the plane of incidence, we obtain:

$$\hat{T} = \left[\begin{array}{cc} 1 & 0 \\ 0 & 0 \end{array} \right] \tag{8.9}$$

However, this transmission axis could be tilted relative to the plane of incidence. The necessary rotation transformation is accomplished by a matrix $\hat{D}$ with an angle α as the rotation angle.

$$\hat{D}(\alpha) = \left[\begin{array}{cc} \cos\alpha & \sin\alpha \\ -\sin\alpha & \cos\alpha \end{array} \right] \tag{8.10}$$

The reflection at the sample is given by:

$$\hat{R} = \left[\begin{array}{cc} r_p & 0 \\ 0 & r_s \end{array} \right] \tag{8.11}$$

MÃ¼ller Matrix Formalism

The propagation of only partially coherent light can be described using the MÃ¼ller matrix formalism, which is based on intensities and not field amplitudes. The light is described here by means of a Stokes vector:

$$S = \left[\begin{array}{c} I_0 \\ I_x - I_y \\ I_{+\frac{1}{4}\pi} - I_{-\frac{1}{4}\pi} \\ I_{\text{right}} - I_{\text{left}} \end{array} \right] \tag{8.12}$$

Each optical element has a corresponding MÃ¼ller matrix. A linear polarizer is:

$$M_{\text{polarizer}} = \left[\begin{array}{cccc} 1 & 1 & 0 & 0 \\ 1 & 1 & 0 & 0 \\ 0 & 0 & 0 & 0 \\ 0 & 0 & 0 & 0 \end{array} \right] \tag{8.13}$$

The rotation by an angle Θ is:

$$M_{\text{rotation}} = \frac{1}{2} \left[\begin{array}{cccc} 1 & 0 & 0 & 0 \\ 0 & \cos 2\Theta & \sin 2\Theta & 0 \\ 0 & -\sin 2\Theta & \cos 2\Theta & 0 \\ 0 & 0 & 0 & 1 \end{array} \right] \tag{8.14}$$

The reflection of light on a sample, which is described by the ellipsometric angles Ψ and Δ, is:

$$M_{\text{sample}} = \begin{bmatrix} 1 & -\cos 2\Psi & 0 & 0 \\ -\cos 2\Psi & 1 & 0 & 0 \\ 0 & 0 & \sin 2\Psi \cos \Delta & \sin 2\Psi \sin \Delta \\ 0 & 0 & -\sin 2\Psi \sin \Delta & \sin 2\Psi \cos \Delta \end{bmatrix} \tag{8.15}$$

The outgoing Stokes vector for light that is linearly polarized at 45 degrees to the plane of incidence is:

$$S_{OUT} = M_{sample} M_{rotation} \left(-\frac{\pi}{4}\right) M_{polarization} M_{rotation} \left(\frac{\pi}{4}\right) S_{IN} \tag{8.16}$$

This results in:

$$S_{OUT} = \begin{bmatrix} 1 & -\cos 2\Psi & \sin 2\Psi \cos \Delta & -\sin 2\Psi \sin \Delta \end{bmatrix} \tag{8.17}$$

Depolarization is taken into account by assuming that not all intensities contribute to the polarization state. That is, the sum of the individual components of S_{out} does not add up to 1. A portion μ is depolarized.

8.3.2 Ellipsometer Types

Method of the Rotating Analyzer

The currently simplest and most widely used design of an ellipsometer is the one with a rotating analyzer (see Fig. 8.8). The light first passes through a stationary polarizer, is reflected by the sample, then passes through a stationary compensator that can be folded into the beam path, and then through a rotating analyzer.

The complete optical system gives the electric field strength of the outgoing light $\vec{E}_{out}$:

$$\vec{E}out = \left[\hat{D}(-A)\hat{T}_{analyser}\hat{D}(A)\right] \hat{R} \left[\hat{D}(-P)\hat{T}_{polariser}\hat{D}(P)\right] \vec{E}_{in} \tag{8.18}$$

The change in the degree of polarization is expressed as a complex number ρ, which is given by:

$$\rho = \frac{E_{s,in}/E_{p,in}}{E_{s,out}/E_{p,out}} = \frac{E_{p,out}/E_{p,in}}{E_{s,out}/E_{s,in}} = \frac{r_p}{r_s} \tag{8.19}$$

ρ can also be expressed by the **ellipsometric angles** Ψ and Δ as:

$$\rho = \frac{r_p}{r_s} = \tan\Psi e^{i\Delta} \tag{8.20}$$

The intensity on the detector is given as the product of the field amplitudes $\vec{E}\text{out}\vec{E}^*\text{out}$:

$$\begin{aligned} I_{detector} &= g\left[1 - \cos 2\Psi\left(\cos 2A + \cos 2P\right) + \right. && (8.21)\\ &\quad \left. \cos 2A \cos 2P + \sin 2\Psi \cos\Delta \sin 2A \sin 2P\right] && (8.22) \end{aligned}$$

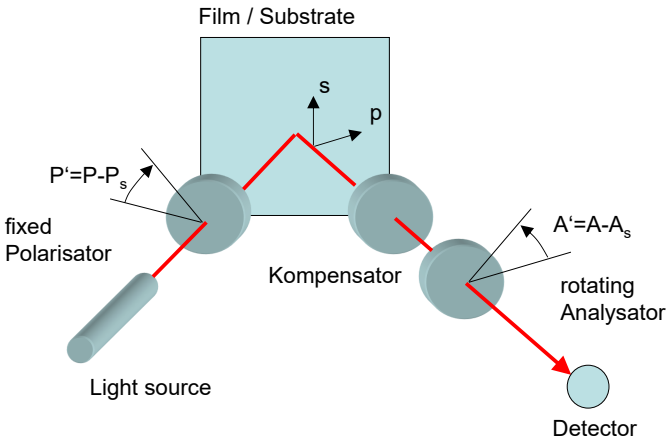

Figure 8.8: Ellipsometer with rotating analyzer

g is a scaling factor. This equation has the form of:

$$I_{detector} = f\left[1 + \alpha \cos 2A + \beta \sin 2A\right] \tag{8.23}$$

with a scaling factor f and

$$\alpha = \frac{\cos 2P - \cos 2\Psi}{1 - \cos 2\Psi \cos 2P} \qquad \text{and} \qquad \beta = \frac{\sin 2P \sin 2\Psi \cos\Delta}{1 - \cos 2\Psi \cos 2P} \tag{8.24}$$

In a rotating analyzer ellipsometer, the intensity is measured N times per revolution. By Fourier transformation of the signal, the coefficients a and b can be determined:

$$\alpha = \frac{2}{N\langle I\rangle}\sum_{i=1}^{N} I_i \cos\left(\frac{2\pi(i-1)}{N}\right) \qquad \text{and} \qquad \beta = \frac{2}{N\langle I\rangle}\sum_{i=1}^{N} I_i \sin\left(\frac{2\pi(i-1)}{N}\right) \tag{8.25}$$

From these coefficients a and b, the ellipsometric angles Ψ, Δ are obtained as:

$$\cos 2\Psi = \frac{\cos 2P - \alpha}{1 - \alpha\cos 2P} \qquad \text{and} \qquad \cos\Delta = \frac{\beta}{\sqrt{1-\alpha^2}} \tag{8.26}$$

It is important to note that only Ψ has a unique solution. For Δ, there are two solutions, as this angle can take values between 0° and 360°. This ambiguity can be resolved within a kinetic ellipsometry measurement. Another possibility is to insert a retarder that causes a phase shift of $\delta = \pi/2$. If one measures once with and once without the retarder, one obtains two solutions for the determination equation for Δ:

$$\cos(\Delta + \delta) = \frac{\beta}{\sqrt{1-\alpha^2}} \tag{8.27}$$

From Fig. 8.9, it can be seen that in the case that Δ is between zero and 180°, the sign changes in both measurements, while in the case that Δ is between 180° and 360°, the sign does not change. Therefore, a retarder is folded in at each measurement point in commercial ellipsometers.

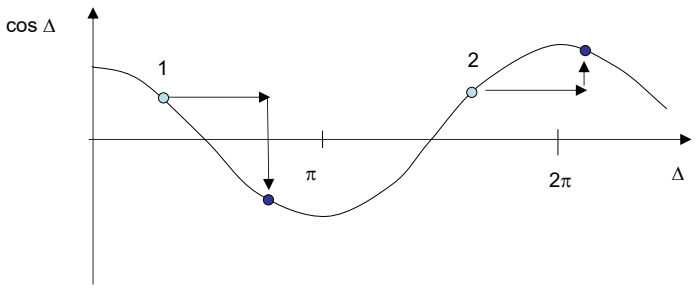

Figure 8.9: By folding in a retarder, the ambiguity of the measurement with a rotating analyzer can be resolved. When evaluating $cos\Delta$, the sign of b changes only if Δ is between 0 and π.

Calibration of an Ellipsometer

The derivation of the ellipsometer signal has so far assumed that we know all quantities relative to the plane of incidence of our measurement. This is generally not the case initially. When setting up an ellipsometer, it must first be calibrated. During this calibration, the position of the plane of incidence as well as the transmission direction of the polarizers relative to the plane of incidence must be determined. The experimental measurement signal is initially given by:

$$I^{exp} = 1 + \alpha' \cos 2\omega t + \beta' \sin 2\omega t \tag{8.28}$$

$$I^{exp} = 1 + (\alpha'^2 + \beta'^2)^{1/2} \cos(2\omega t - \Theta') \tag{8.29}$$

with

$$\Theta' = \arctan\left(\frac{\beta'}{\alpha'}\right) \tag{8.30}$$

In comparison, we have as a theoretical signal:

$$I^{theo} = 1 + \eta\alpha \cos\left(2(\omega t - A_c - \phi/2)\right) + \eta\beta \sin\left(2(\omega t - A_c - \phi/2)\right) \tag{8.31}$$

with

$$\alpha = \frac{\cos 2(P - P_c) - \cos 2\Psi}{1 - \cos 2(P - P_c)\cos 2\Psi} \tag{8.32}$$

and

$$\beta = \frac{\sin 2(P - P_c)\sin 2\Psi \cos\Delta}{1 - \cos 2(P - P_c)\cos 2\Psi} \tag{8.33}$$

This can also be brought to the form:

$$I^{theo} = 1 + \eta(\alpha^2 + \beta^2)^{1/2} \cos(2\omega t - \Theta) \tag{8.34}$$

$$\Theta = \arctan\frac{\beta}{\alpha} + 2A_c + \phi \tag{8.35}$$

Here, P_c and A_c is the position of the plane of incidence according to the coordinate system of polarizer and analyzer (reading angle) and η is the damping of the modulated part compared to the DC part. These three quantities need to be calibrated.

- **Residue Calibration**
  First, the position of the plane of incidence should be determined. If the polarizer is brought near the plane of incidence, the reflected light is almost linearly polarized since there is no intensity in the s-component. In the vicinity of $P \sim P_c$, the so-called residue R can be set up:

$$R = 1 - (\alpha'^2 + \beta'^2) \equiv 1 - \eta^2(\alpha^2 + \beta^2) \tag{8.36}$$

This expression is *independent* of A_c.

$$R = 1 - \eta^2 + \left[\eta \frac{\sin\Delta \sin 2\Psi \sin 2(P - P_c)}{1 - \cos 2\Psi \cos 2(P - P_c)}\right]^2 \tag{8.37}$$

For $P - P_c \ll 1$ the following applies:

$$R = 1 - \eta^2 + \left[\frac{2 \sin\Delta \sin 2\Psi}{1 - \cos 2\Psi}\right]^2 \tag{8.38}$$

This is a parabola of the form $R = C_0 + C_1 P + C_2 P2$. The minimum of the parabola is at the location $P = P_c$. That is, in the calibration, the residue is recorded while varying P and a parabola is fitted to this curve. From the minimum, P_c can be determined.

The values for A_c, η, and ϕ can be determined if the plane of incidence is known. For this purpose, the polarizer is moved once into the plane of incidence and once at 90° to it. From the comparison of Eq. 8.34 and 8.29, the unknowns can then be determined. For $P - P_c = 0°$ we get $\alpha = 1$ and $\beta = 0$ and for $P - P_c = 90°$ we get $\alpha = -1$ and $\beta = 0$. Thus, the signal is independent of the properties of the sample and the remaining unknowns can be determined.

- **Phase Calibration**

  In phase calibration, the arguments of the arctan in Eq. 8.34 and 8.29 are compared:

$$\Theta' = \arctan\frac{\beta'}{\alpha'} = \arctan\frac{\beta}{\alpha} + 2A_c + \phi \tag{8.39}$$

or

$$\Theta' = \arctan\left[\frac{\sin 2\Psi \sin 2(P - P_c)\cos\Delta}{\cos 2(P - P_c) - \cos 2\Psi}\right] + 2A_c + \phi \tag{8.40}$$

The value for Θ' is determined experimentally from the measured values for α' and β'. Two values for Θ' are considered, which are measured for two settings of P that are shifted by 90° from each other:

$$\tan\left[\Theta'(P + \pi/2) - \Theta'(P)\right] = \frac{K \sin 2(P - P_c)}{L + M \sin^2(P - P_c)} \tag{8.41}$$

It can be seen that this behaves like $\sin(P - P_c)$ in the vicinity of $P \sim P_c$ up to prefactors K, L and M. That is, the zero crossing of this function marks the plane of incidence and thus P_c. After determining this plane of incidence, all other quantities such as A_c, η and ϕ can be determined analogously to the residue calibration.

- **Simultaneous Calibration**

  The disadvantage of residue and phase calibration is the fact that the individual parameters are determined one after the other. That is, an error in the determination of the plane of incidence is carried forward into the determination of A_c, η and ϕ. This is avoided by simultaneous calibration. Here, a scan of the polarizer over 180° is performed and the Fourier coefficients are determined in each case. This distribution of Fourier coefficients is fitted to Eq. 8.34 by varying P_c, A_c, η, ϕ, Ψ and Δ. After the Fourier coefficients have been determined at typically 200 angles over 180°, the ill-posed problem can be resolved in this way. This type of calibration is now implemented in most modern ellipsometers.

Method of the Rotating Compensator

Alternatively to the method of the rotating analyzer, it is also possible to use the compensator ($\lambda/4$ plate) as the rotating element (see Fig. 8.10). This has a number of advantages as explained below. The fundamental experimental difficulty, however, is the fact that a phase shift must be realized as accurately as possible. This phase shift is also wavelength-dependent, which complicates the construction of a spectroscopic ellipsometer. For this reason, spectroscopic ellipsometers with a rotating compensator have only recently become commercially available.

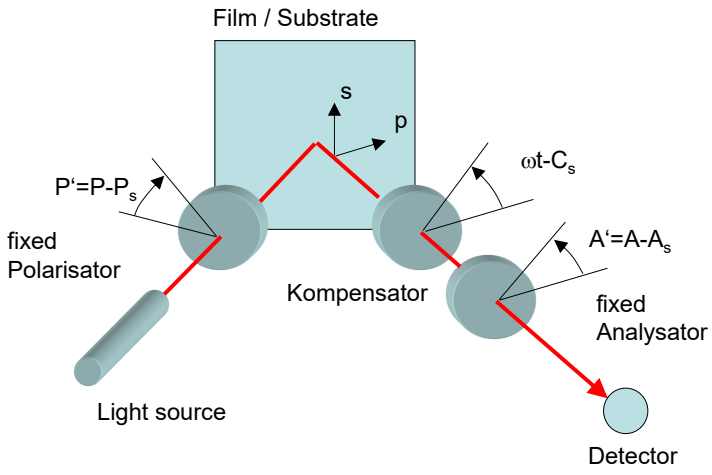

Figure 8.10: Ellipsometer with rotating compensator.

In the beam path of the ellipsometer with rotating compensator, the light beam passes through a stationary polarizer, is reflected by the sample, passes through the rotating compensator, and then through the stationary

analyzer. Considering this beam path through an ellipsometer with a rotating compensator, the transmission can be described with the matrices as:

$$\vec{E}_{out} = \left[\hat{D}(-A)\hat{T}_{analyser}\hat{D}(A)\right]\left[\hat{D}(-C)\hat{T}_{compensator}\hat{D}(C)\right]\hat{R}\left[\hat{D}(-P)\hat{T}_{polariser}\hat{D}(P)\right]\vec{E}_{in} \tag{8.42}$$

If this matrix multiplication is performed, the magnitude squared of the electric field strength after the analyzer is determined.

$$I = I_0\left(1 + \alpha'_2\cos(2\omega_C t) + \beta'_2\sin(2\omega_C t) + \alpha'_4\cos(4\omega_C t) + \beta'_4\cos(4\omega_C t)\right) \tag{8.43}$$

It can be seen that, unlike the rotating analyzer ellipsometer, components at $2\omega_c$ and also components at $4\omega_c$ appear. The prefactors are initially:

$$\alpha_m = \alpha'_m\cos(mC_s) + \beta'\sin(mC_s) \qquad m = 2, 4 \tag{8.44}$$

$$-\beta_m = -\alpha'_m\sin(mC_s) + \beta'\cos(mC_s) \qquad m = 2, 4 \tag{8.45}$$

The conversion of α' to α and β' to β transforms the Fourier coefficients to the axes of the plane of incidence. The prefactors α and β are:

$$\alpha_2 = (p\sin\delta\sin 2\chi\sin 2A')/\alpha_0 \tag{8.46}$$

$$\beta_2 = (-p\sin\delta\sin 2\chi\cos 2A')/\alpha_0 \tag{8.47}$$

$$\alpha_4 = \left[p\sin^2(\delta/2)\cos 2\chi\cos 2(A'+Q)\right]/\alpha_0 \tag{8.48}$$

$$\beta_4 = \left[p\sin^2(\delta/2)\cos 2\chi\sin 2(A'+Q)\right]/\alpha_0 \tag{8.49}$$

$$\alpha_0 = 1 + \left[p\cos^2(\delta/2)\cos 2\chi\cos 2(A'-Q)\right] \tag{8.50}$$

p is the degree of polarization ($0 < p < 1$) with $p = 1$ for completely polarized light. Q is the angle of the main axis of the elliptical polarization after reflection and χ, the corresponding phase shift. From the measured signals α and β, these quantities can be determined via:

$$Q = \frac{1}{2}\tan^{-1}\left(\frac{\beta_4}{\alpha_4}\right) - A' \tag{8.51}$$

$$\chi = \frac{1}{2}\tan^{-1}\left[\frac{\alpha_2 \cos(A'+Q)\tan(\delta/2)}{2\alpha_4 \sin A'}\right] \tag{8.52}$$

$$p = \alpha_2\left[\sin 2A' \sin\delta \sin 2\chi - \alpha_2 \cos^2(\delta/2)\cos 2\chi \cos 2(A'-Q)\right]^{-1} \tag{8.53}$$

$$\cos 2\Psi = \frac{\cos 2P' - \cos 2Q \cos 2\chi}{1 - \cos 2Q \cos 2\chi \cos 2P'} \tag{8.54}$$

$$\tan\Delta = -\frac{\tan 2\chi}{\sin 2Q} \tag{8.55}$$

The calibration of an ellipsometer with a rotating compensator also begins with the determination of the plane of incidence. Subsequently, certain polarization states can be prepared, by means of which the remaining unknowns can be calibrated.

An ellipsometer with a rotating compensator has numerous advantages over one with a rotating polarizer or analyzer.

- **Helicity can be determined**

  From the Fourier coefficients α_m and β_m, the absolute magnitude of Δ can also be determined. Thus, the helicity of the polarization ellipse is also known.

- **Sensitivity also in the range $\Delta \sim 0°$ and $\Delta \sim 180°$**

  The measurement accuracy of the ellipsometer is constant throughout the entire range of Δ. An ellipsometer with a rotating analyzer can poorly detect linearly polarized light, as the light signal is completely extinguished when the analyzer is set perpendicular to this polarization. This zero crossing is strongly influenced by noise and the background of the measurement.

- **Depolarization measurable**

  After the degree of polarization is determined, effects such as scattering from particles or inhomogeneities in the layer can be taken into account. In addition, transparent substrates can be analyzed in which the light transmission through the substrate must be incoherently superimposed.

- **Source polarization**

  After the analyzer and the polarizer are fixed, the polarization dependence of the source and the detector plays no role.

8.3.3 Measurement Process and Evaluation

In an ellipsometry measurement, the ellipsometric angles Ψ and Δ are determined. Alternatively, the properties of the sample can also be expressed by the complex refractive index or the dielectric constant. In the case of a semi-infinite medium, these last two quantities have a concrete physical meaning. In the case of thin films, this refractive index and this dielectric constant are only effective values that result from the reflection at a complex layer system. The measured ellipsometric angles must be compared with an optical model of these quantities to determine the unknown refractive indices and layer thicknesses.

If one has only one measurement point expressed by Ψ and Δ, the problem is initially underdetermined, as one wants to determine three quantities, n and κ as well as the layer thickness d, for a thin film. This is usually not possible. However, if one has the possibility to vary the wavelength or the angle of incidence, this underdeterminedness can be resolved, as one now has a variety of measurement data for the same sample.

In an ellipsometry measurement, there are two essential modes. (i) In an in-situ measurement, a plasma process is continuously monitored. This real-time measurement is also referred to as kinetic ellipsometry. The information about the layer structure including its history is contained in a trajectory in the parameter space Ψ and Δ. Through the time evolution of these parameters, the underdeterminedness can also be resolved if one assumes that the refractive index is only a slowly varying function with the layer thickness. (ii) As a second method, the sample is measured spectrally resolved ex-situ, in combination with a variation of the angle of incidence, data of high quality can be produced, which make the comparison between model and measurement unambiguous.

The optimal angle of incidence is in the vicinity of the Brewster angle. At this angle, a significant portion of the light is refracted into the sample. Thus, the reflected light contains much information about the nature of the layer system.

As an example of a kinetic ellipsometry measurement, Fig. 8.11 is shown. A typical coating on a silicon sample begins at $\Psi \sim 10°$ and $\Delta \sim 180°$. Subsequently, the Ψ, Δ values shift with increasing layer thickness. As an example, the coating with two different materials is shown. From the shape of the trajectory, the refractive index can be derived. Together with the optical model, the growth rate can be determined from the sequence of points. For completely transparent samples, the curve runs back into itself. For absorbing samples, a continuously varying curve is created.

If the film is very strongly absorbing (see Fig. 8.12), it is observed that

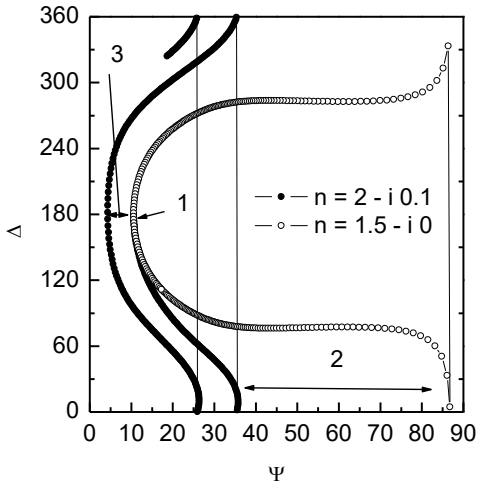

Figure 8.11: Coating with different optical constants.

beyond a certain layer thickness, the Ψ, Δ values no longer change. From this point on, the incident light wave can no longer reach the interface between sample and substrate. That is, the light "sees" only the surface.

The ellipsometry data are characterized by a high layer thickness sensitivity. Changes in the layer thickness in the sub-angstrom range are detectable. Comparison with independent measurement methods has also shown that the evaluation of the data provides reliable results even for the smallest layer thicknesses.

8.4 Vibrational Spectroscopy

Let us now consider the absorption of light by excitation of molecular vibrations. Absorption of infrared light only occurs if the molecule has a static dipole moment. That is, homonuclear molecules do not have an infrared spectrum.

If we consider the dipole moment of a vibrating molecule with the displacement x, the dipole moment can change through the vibration if $\frac{\partial p_{el}}{\partial x} \neq 0$

$$p_{el}(x) = p_{el}(0) + \frac{\partial p_{el}}{\partial x} x \tag{8.56}$$

If an external electric field $\vec{E}$ is applied, it can polarize the molecule according to its polarizability α. This can also change with the vibration of the molecule as:

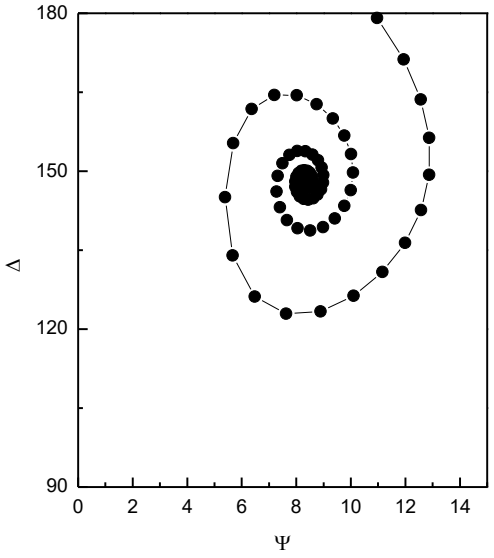

Figure 8.12: Ellipsometry measurement of a very strongly absorbing film.

$$\alpha(x) = \alpha(0) + \frac{\partial \alpha}{\partial x} x \tag{8.57}$$

The total electric dipole moment results from the static and the induced part as:

$$p = p_{el}(x) + \alpha \vec{E} \tag{8.58}$$

With the ansatz $x = x_0 \cos(\omega t)$ for the molecular vibration at frequency ω and the incident light $\vec{E} = E_0 \cos \omega_0 t$, we obtain:

$$p_{el}(x) = p_{el}(0) + \underbrace{\frac{\partial p_{el}}{\partial x} x_0 \cos \omega t}_{IR-spectrum} + \underbrace{\alpha(0) E_0 \cos \omega_0 t}_{Rayleigh-spectrum} + \underbrace{\frac{\partial \alpha}{\partial x} x_0 \frac{E_0}{2} \cos(\omega_0 \pm \omega) t}_{Raman-spectrum} \tag{8.59}$$

In addition to the static part according to $p_{el}(0)$, three parts are recognized: **IR absorption or emission** of the vibrating dipole, which changes its dipole moment during this vibration; **Rayleigh scattering** as the elastic scattering of light on the molecule (or atom); **Raman scattering** as the inelastic scattering of the photons on the vibrating molecule. In inelastic scattering, either a vibration/rotation can be excited, i.e., the scattered light

is energetically lower, the so-called **Stokes** lines, or a vibration/rotation is de-excited, and the scattered light is energetically higher than the incident light, the so-called **anti-Stokes** lines (see Fig. 8.13).

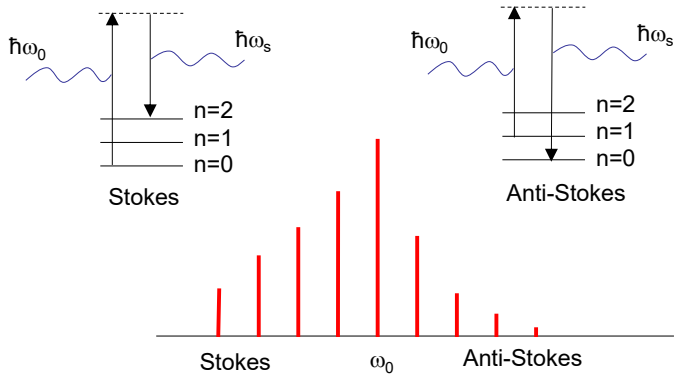

Figure 8.13: In inelastic light scattering, Raman scattering, a vibrational quantum can be excited (Stokes lines) or de-excited (anti-Stokes).

Infrared spectroscopy and Raman spectroscopy are considered complementary to each other. This can be illustrated by the example of the IR and Raman sensitivity of some vibrational modes.

For this purpose, consider a two-atom molecule that performs a stretching vibration. If the atoms are equal, the polarizability changes with the stretching, since the electron shell and the atomic nuclei shift relative to each other to stabilize the stretched form of the molecule. However, the dipole moment does not change. Therefore, such a vibration is Raman-active but not infrared-active. In a two-atom molecule with two different atoms, both IR and Raman absorption occur.

In a three-atom molecule with a heavier atom in the center, a symmetric and an anti-symmetric vibration can occur. In the symmetric vibration, the polarizability changes, but the dipole moments of the two bonds cancel each other out. That is, this symmetric vibration is IR-inactive but Raman-active. In the anti-symmetric vibration, on the other hand, no Raman scattering occurs, since the decrease in polarizability of one bond is compensated by the increase in polarizability of the other bond (see Fig. 8.14). The dipole moment, on the other hand, changes with the vibration. Such an oscillation is infrared-active but Raman-inactive.

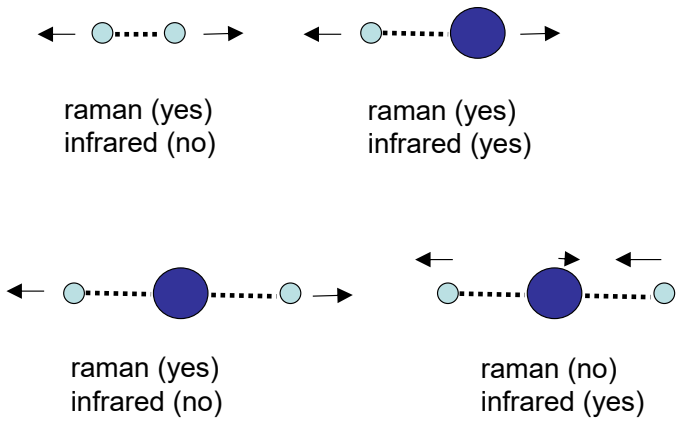

Figure 8.14: Depending on the dependence of the dipole moment on the displacement of the atoms and the corresponding polarizability, a vibration can be infrared- and/or Raman-active.

8.4.1 Infrared Spectroscopy

Fourier Transform Infrared Spectrometer

To determine the rotational-vibrational spectra of molecules, for example, the spectrum of a light source, which is partially absorbed by molecules, is measured spectrally resolved using a monochromator. This monochromator selects only a small wavelength range, which in the infrared has the disadvantage that the light intensities become very small ($I \propto \hbar\omega$).

An elegant method to circumvent this problem is Fourier transform infrared spectroscopy (Fig. 8.15). Here, the light from an infrared light source is passed through a **Michelson interferometer**. One mirror of this interferometer is movable and is moved continuously. First, consider a monochromatic radiation source that emits light ($E = E_0 \cos \omega_0 t$) of a frequency ω_0. By superimposing the light from both interferometer arms, a cosine-shaped signal is obtained on the detector as a function of the mirror path s_2.

$$I = c\epsilon_0 E^2 = c\epsilon_0 E_0^2 \left[\cos(\omega_0 t + k s_1) + \cos(\omega_0 t + k s_2)\right]^2 RT \tag{8.60}$$

E_0 is the amplitude of the electric field strength of the light. R is the reflectivity of the fixed and the movable mirror. T is the transmission of the beam splitter. The two paths s_1 and s_2 differ by the movement of the mirror with a velocity v:

$$s_2 = s_1 + vt \tag{8.61}$$

On the detector, this results in the time-averaged signal:

$$\langle I(t)\rangle_t = RTI_0 \left[1 + \cos\left(\omega_0 \frac{v}{c} t\right)\right]^2 \tag{8.62}$$

That is, the modulation of the signal on the detector occurs at a frequency that is transformed down by a factor of v/c. If a Fourier transform of this modulated signal is performed,

$$I(\omega) = \int_{t=0}^{\infty} \langle I(t)\rangle_t \cos\left(\omega_0 \frac{v}{c} t\right) dt \tag{8.63}$$

A line corresponding to the frequency ω_0 is obtained in the frequency spectrum. For a spectrally broad light source, the Fourier transform yields the entire frequency spectrum. That is, with this method, *all* frequencies are measured *simultaneously*. The light intensity is large, which facilitates the measurement technique. If a sample is now placed in the beam path, the corresponding absorption spectrum is observed.

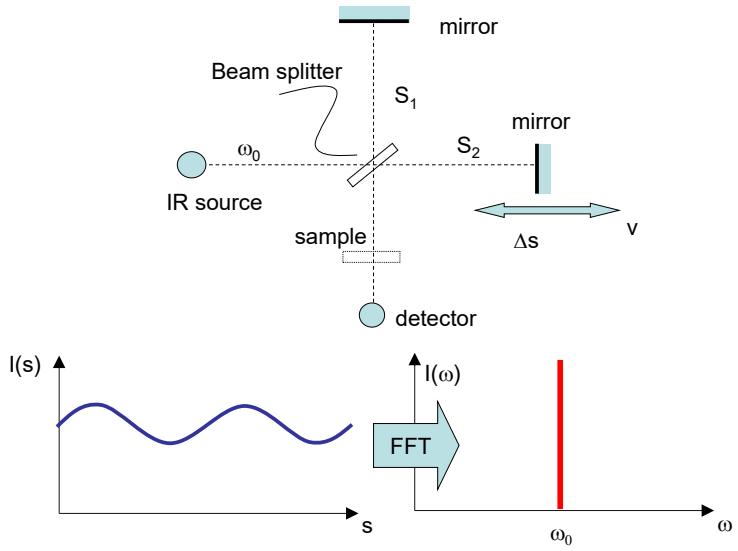

Figure 8.15: Fourier transform spectroscopy. A spectrally broad light source is passed through a Michelson interferometer in which one mirror is continuously moved. The Fourier transform of the detector signal gives the frequency spectrum of this light source. This is illustrated for *one* frequency component ω_0 of the light source.

The resolution of an FTIR spectrometer is calculated from the condition that two frequencies can only be separated when the signal has been measured for at least a time Δt according to:

$$\Delta\omega\Delta t \geq 2\pi \tag{8.64}$$

Thus, the resolution is given by the travel length of the mirror as:

$$\Delta\omega = \frac{2\pi}{\Delta s}v \tag{8.65}$$

That is, a large travel length is required to achieve good resolution. This is very laborious since the movement of the mirror must be absolutely linear. This is realized by a HeNe interferometer that is superimposed on the IR beam path and only serves to measure the position of the mirror very precisely.

An arbitrarily sharp line can only be measured if the travel length becomes infinite. Since this is not possible, a finite line width is obtained. Due to the fact that the Fourier transform runs from 0 to ∞, but the signal only from 0 to Δt, additional frequencies arise in the spectrum due to the truncation of the signal at Δt. This sharp truncation can be mitigated by introducing an **apodization function** $D(t)$, which is superimposed on the signal.

$$I(\omega) = \int_{t=0}^{\infty} \langle I(t)\rangle_t D(t) \cos\left(\omega_0 \frac{v}{c} t\right) dt \tag{8.66}$$

Here, a trapezoidal function is often chosen for D.

Methods of Sensitivity Enhancement

In infrared spectroscopy, the absorption coefficient of the vibrations is usually relatively small. That is, in order to resolve the absorption of the physical surface directly, it is necessary to increase the sensitivity of the method. There are several optical configurations for this, as illustrated in Fig. 8.16.

- **Metallic Substrate**

  In the case of a metallic substrate, the electric field must have a wave node perpendicular to the plane of incidence. The field parallel to the plane of incidence is then maximized (see Fig. 8.16a). Due to this maximum field strength, the absorption is particularly sensitive to the presence of a thin film on this metallic substrate. This configuration is often used in surface physics, which often considers metallic, catalytic surfaces as the subject of investigation. In plasma technology,

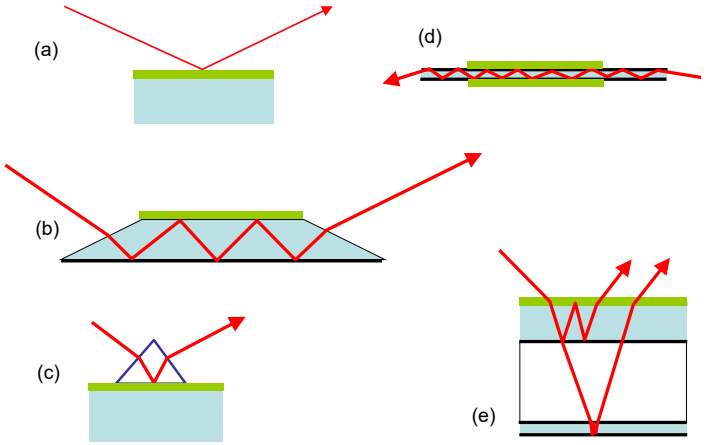

Figure 8.16: Methods to increase the sensitivity of an infrared measurement: (a) metallic substrate; (b) internal total reflection ITR; Â© attenuated total reflection; Â© glass fiber; (d) optical cavity resonator.

this configuration is only relevant in systems in which metal is also deposited.

- **Attenuated Total Reflection (ATR)**

  In attenuated total reflection, light is coupled into a trapezoidally cut crystal (see Fig. 8.16b). The angle of incidence and the refractive index of the light are chosen such that the wave is totally reflected at the interface coating-crystal during internal reflection. The electric field strength decreases exponentially in the film (see Fig. 8.17):

$$E = E_{z=0} \exp(-\gamma z) \tag{8.67}$$

  with

$$\gamma = \frac{2\pi}{\lambda_s}(\sin^2\Theta - n_{as}^2)^{1/2} \tag{8.68}$$

  $\lambda_s = \frac{\lambda_{Vakuum}}{n_s}$, $n_{as} = \frac{n_a}{n_s}$ with n_a the refractive index of the film and n_s the refractive index of the substrate.

$$E_{y,z=0} = \frac{2\cos\Theta}{(1-\epsilon_{as})^{1/2}} E_{in} \tag{8.69}$$

with $\epsilon_{as} = \frac{\epsilon_a}{\epsilon_s} = \left(\frac{n_a}{n_s}\right)^2$

$$E_{x,z=0} = \frac{2\left(\sin^2\Theta - \epsilon_{as}\right)^{1/2}}{\left(1-\epsilon_{as}\right)^{1/2}\left[\left(1+\epsilon_{as}\right)\sin^2\Theta - \epsilon_{as}\right]^{1/2}}\cos\Theta E_{in} \tag{8.70}$$

$$E_{y,z=0} = \frac{2\cos\Theta}{\left(1-\epsilon_{as}\right)^{1/2}\left[\left(1+\epsilon_{as}\right)\sin^2\Theta - \epsilon_{as}\right]^{1/2}}\sin\Theta E_{in} \tag{8.71}$$

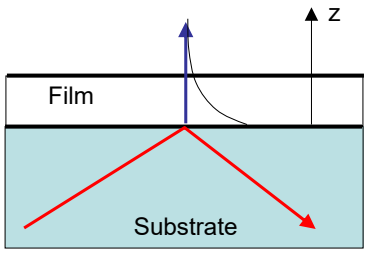

Figure 8.17: Exponential decay of the field strength in total reflection.

A disadvantage of total reflection is the fact that many reflections must be collected. Due to the beam offset of the light inside the wafer, it is necessary to realize a large-area coating in order to collect information over a large lateral area. The substrates used are, for example, silicon wafers, which are usually transparent in the infrared. For the alignment of the infrared beam, this poses the problem that alignment with visible light is no longer possible.

In a simpler configuration, attenuated total reflection is also used for the analysis of thin films in reflection. If a sample has no optical quality and is not transparent, it is not suitable for a measurement in transmission or reflection. For this purpose, an ATR prism (ATR, attenuated total reflection) is used, which is pressed onto the surface. The infrared beam is then coupled in via a facet of the prism and undergoes total reflection at the interface prism-sample (see Fig. 8.16c).

Another elegant variant of internal total reflection is the use of an infrared-transparent glass fiber from which the cladding has been removed (see Fig. 8.16d). Such a fiber is stretched through a plasma system and its transmission is measured. If coating now occurs on this

glass fiber, the transmission is attenuated, which is visible as a signal on the detector.

- **Optical Cavity Resonator**

  A similar increase in sensitivity as internal total reflection is offered by the use of an optical cavity resonator (see Fig. 8.16e). Here, a wafer is first oxidized to create SiO_2 on both sides in the range of 1 μm. At this layer thickness, a resonant enhancement of the field strength occurs at the surface of this wafer. This enhancement occurs for the component perpendicular to the plane of incidence. The back side of the wafer can additionally be coated with metal.

  However, the amplification can only be realized over a limited wavelength range, since the resonance condition must be tuned to the system to be investigated.

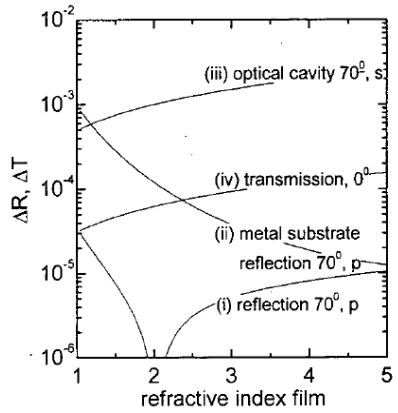

Figure 8.18: Comparison of the sensitivity of individual substrate configurations with respect to the detection of a SiH vibration at 2100 cm^{-1}.

Time Resolution

The temporal resolution of infrared spectroscopy is usually strongly limited, as the corresponding detection systems in the infrared do not work sensitively enough, so that a long measurement time is required to achieve a certain signal-to-noise ratio. If periodic processes can be observed, this limitation can be overcome. This is achieved with the **Step-Scan** method. Here, the course of a physical process (scan) is measured for a single *fixed* mirror position of the FTIR spectrometer. The mirror is then moved (step) and the

course of this process is measured repeatedly. By means of a back calculation, the interferograms for the individual points in time can then be reassembled. Time resolutions down to the ns range are possible here.

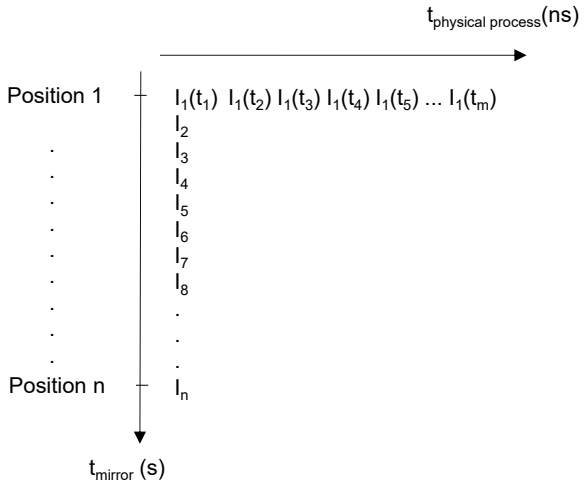

Figure 8.19: In the step-scan method, a periodic process is measured at a fixed mirror position.

Raman Spectroscopy

Concept of Raman Spectrometer

In Raman spectroscopy, the inelastic scattering of light is analyzed. Due to the small cross section for scattering ($\propto \omega^4$), a strong laser must be used for the primary light source. The choice of the laser wavelength initially determines the type of electronic excitation. In the case of carbon films and a laser wavelength in the visible range, the π-electron system is excited. The Raman effect then depends on the change in the polarizability of the material during this excitation. The scattered light is shifted in frequency, which is recorded as the Raman spectrum.

In terms of construction, an intense laser is transmitted through a sample or reflected by it. By spectral filtering, the intense peak of elastic scattering (Raleigh scattering) must be separated. The obtained Raman spectra are then evaluated.

However, the primary laser beam leads to heating of the sample. The temperature increase ΔT_{max} is:

$$\Delta T_{max} = \frac{(1-R)P}{2\sqrt{\pi}\lambda w} f(\alpha w) \tag{8.72}$$

with R the reflectivity, P the laser power on a spot with diameter w, λ the thermal conductivity and f a function describing the absorption in the material. If the absorption is weak, f yields a number less than 1, if the absorption is strong $f = 1$. This heating of the sample can be avoided by irradiating the laser in a pulsed manner, or by expanding the laser through a cylindrical lens and imaging the lines onto a CCD chip via a spectrograph. Thus, the power is distributed over a larger area, resulting in a lower temperature increase.

The signal height can be increased similarly to infrared spectroscopy by optical resonators. A special case here is the SERS (surface enhanced Raman scattering) method. Here, it has been observed that the line intensity of thin films increases very strongly if they are located on a rough metallic surface. It has been shown that the primary laser radiation resonantly excites plasmons in the metal, which strongly increase the electric field strength at the surface. Due to these strongly oscillating fields, there is a field enhancement and any absorption is sensitively detected.

Raman Spectroscopy on Crystalline Samples

When considering Raman spectroscopy on crystalline samples, the structure factor becomes important, which describes the coherent superposition of the scattering events. The cross section is given by:

$$\frac{d\sigma^2}{d\Omega d\omega_s} = \left(\frac{\omega_s}{c}\right)^4 \left(\frac{V^2\omega_s}{2\pi\omega_i}\right) S(\vec{k},\omega) \tag{8.73}$$

with ω_s the frequency of the scattered light, ω_i the frequency of the incident light, V the scattering volume. The scattering condition is based on the conservation of momentum and energy given by:

$$\vec{k} = \vec{k}_i - \vec{k}_s \tag{8.74}$$

$$\omega = \omega_i - \omega_s \tag{8.75}$$

$$\tag{8.76}$$

The structure factor combines the coherent superposition of the polarizabilities at two different locations r and r'. For an energy loss according to ω this is:

$$S(\vec{k},\omega) = \frac{1}{V^2}\Im \int dr dr' dt \langle \delta\alpha^*(\vec{r},z)\delta\alpha(\vec{r}',0)\rangle e^{-\imath\vec{k}(\vec{r}-\vec{r}')-\imath\omega t} \tag{8.77}$$

The change in polarizability can be represented in first approximation as a function of the *position* of the atoms $u(r,t)$:

$$\delta\alpha = Au(\vec{r},t) \tag{8.78}$$

The correlation function of the positions of the atoms can be derived from the phonon spectrum according to:

$$\langle u^(\vec{r},t)u(\vec{r},0)\rangle = \frac{1}{V}\sum_q \langle u^(\vec{q})u(\vec{q})\rangle e^{i\vec{q}(\vec{r}-\vec{r}')+\imath\omega t} \tag{8.79}$$

This can be summarized as

$$S(\vec{k},\omega) = \frac{N}{V^2}\frac{1}{V}\sum |A(\vec{q})|^2\delta(\omega-\omega_0(\vec{q}))\langle u^*(\vec{q})u(\vec{q})\rangle |F(\vec{k}-\vec{1})|^2 \tag{8.80}$$

with

$$F(\vec{k}-\vec{q}) = \int dr e^{\imath(\vec{k}-\vec{q})\vec{r}} \tag{8.81}$$

In first approximation $\langle u^*(\vec{q})u(\vec{q})\rangle = \frac{n(\omega)+1}{\omega}$ with $n(\omega)$ the occupation number of the phonons. One finally obtains:

$$S(\vec{k},\omega) = \frac{N}{V^2}\frac{n(\omega)+1}{\omega}\frac{1}{V}\sum |A(\vec{q})|^2\delta(\omega-\omega_0(\vec{q}))|F(\vec{k}-\vec{1})|^2 \tag{8.82}$$

Chapter 9

Measurement Methods for Mechanical Properties

In plasma technology, hard materials are an important application area. Therefore, determining hardness is a frequent requirement for layer diagnostics. Materials with great hardness often also exhibit high internal stresses, which must be absorbed by a substrate.

9.1 Stress and Strain

9.1.1 Fundamentals

The quantities stress σ and strain ϵ are linearly interlinked. This is referred to as Hooke's Law:

$$\boxed{\sigma = E\epsilon} \tag{9.1}$$

where E is the modulus of elasticity. When a body is stretched in one direction, it contracts in the perpendicular direction. This component is expressed by the Poisson's ratio ν:

$$\boxed{\epsilon_{yy} = -\nu\epsilon_{xx}} \tag{9.2}$$

Equations 9.1 and 9.2 can be linked as follows for the case of isotropic stress (no off-diagonal elements of E):

$$\epsilon_{xx} = \frac{1}{E}\left[\sigma_{xx} - \nu\left(\sigma_{yy} + \sigma_{zz}\right)\right] \tag{9.3}$$

$$\epsilon_{yy} = \frac{1}{E}\left[\sigma_{yy} - \nu\left(\sigma_{xx} + \sigma_{zz}\right)\right] \tag{9.4}$$

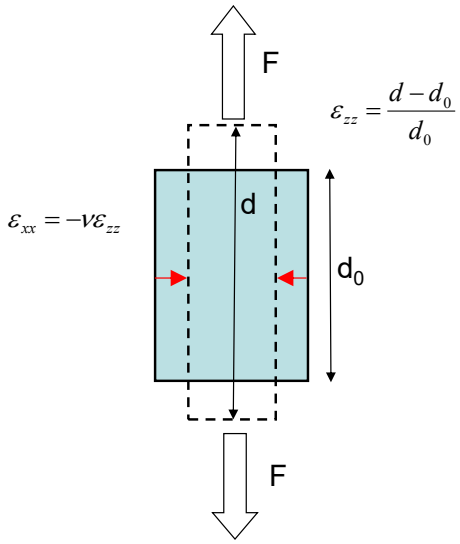

Figure 9.1: Tensile and compressive stress in a layer.

$$\epsilon_{zz} = \frac{1}{E}\left[\sigma_{zz} - \nu\left(\sigma_{yy} + \sigma_{xx}\right)\right] \tag{9.5}$$

That is, the strain in the x-direction ϵ_{xx} is initially dependent on the stress in the x-direction σ_{xx} but also, via the Poisson's ratio, dependent on the stress in the y- and z-directions. The term $-\nu$ expresses that, for example, a tensile stress in the x-direction leads to a compression in the z-direction and vice versa.

Now let's consider the case of a thin film, which is typical in plasma technology. A thin film cannot absorb stress in the z-direction. For this reason, $\sigma_{zz} = 0$. The stress in the film itself is isotropic. That is, $\sigma_{xx} = \sigma_{yy} = \sigma_f$. Thus, we obtain:

$$\epsilon_{xx} = \frac{1}{E}\left[\sigma_f - \nu\left(\sigma_f + 0\right)\right] \tag{9.6}$$

or

$$\epsilon_{xx} = \frac{1}{E}(1 - \nu)\sigma_f \tag{9.7}$$

This can be rearranged to:

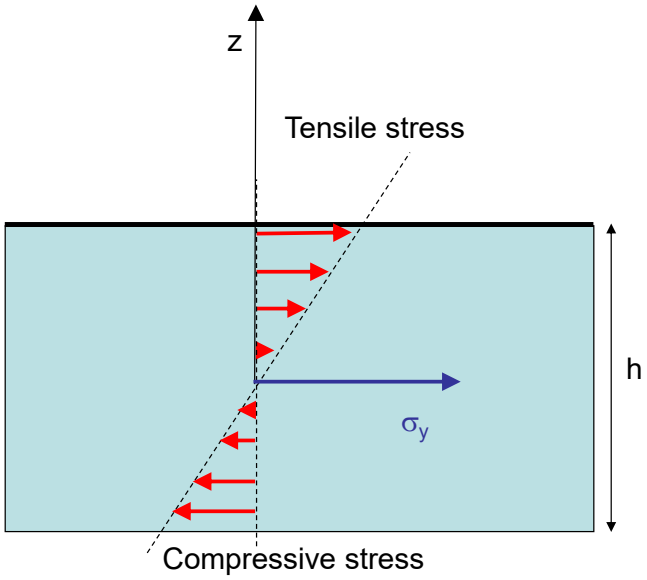

Figure 9.2: Stress profile in a coated wafer.

$$\sigma_f = \underbrace{\frac{E}{1-\nu}}_{Y} \epsilon xx \tag{9.8}$$

Y is referred to as the biaxial modulus of elasticity or also *Young's* modulus of elasticity:

$$\boxed{Y = \frac{E}{1-\nu}} \tag{9.9}$$

For the strain in the z-direction of a thin film, we obtain:

$$\epsilon_{zz} = \frac{-2\nu}{E}\sigma_f \tag{9.10}$$

9.1.2 Stress Distribution Wafer - Coating

Now we want to analyze the system of coated substrate or wafer in more detail. The coating on a wafer is carried out, for example, in a plasma process in which significant ion bombardment occurs. This creates a compressive or tensile stress in the material. As a consequence, the wafer is bent by this

stress in the thin film. That is, the bending or curvature of this wafer is a measure of the built-in stress in the thin film.

First, let's consider the wafer of thickness h, which is deformed by an acting bending moment M (e.g., compressive stress in the film). There is a tensile stress on the top side and a compressive stress on the bottom side, as illustrated in Fig. 9.2. Since the entire system must be force-free, it always holds that:

$$\int \sigma dz = 0 \tag{9.11}$$

As the simplest approach, we set $\sigma_{xx}(z) = z\alpha$. The bending moment M, which corresponds to these internal stresses, is:

$$M = \int_{-h/2}^{h/2} \sigma_{xx} z dz = \alpha \frac{h^3}{12} \tag{9.12}$$

From this, α can be determined for a given bending moment M, and we obtain:

$$\sigma_{xx} = \frac{12M}{h^3} z \tag{9.13}$$

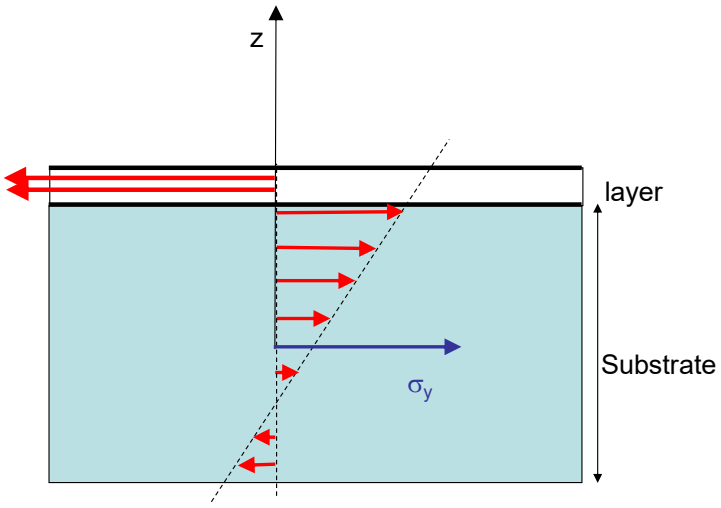

Figure 9.3: Radius of curvature of a bent substrate.

The wafer is bent by the occurring stresses, and a radius of curvature R is observed. How is the strain now linked with the stress in the material? The strain (or compression) ϵ_{xx} is obtained from Fig. 9.3 as:

$$\epsilon_{xx} = \frac{(R+z)\Theta - R\Theta}{R(\Theta)} = \frac{z}{R} \tag{9.14}$$

or with the biaxial stress in a thin film:

$$\frac{z}{R} = \epsilon_{xx} = \frac{\sigma_s}{Y_s} = \frac{12M}{h^3} z \frac{1}{Y_s} \tag{9.15}$$

That is, a bending moment M acting on a wafer of thickness h leads to a curvature with radius of curvature R according to:

$$\frac{1}{R} = \frac{12}{Y_s h^3} M \tag{9.16}$$

When coating, we now assume that this bending moment is caused by the thin film on the surface. This bending moment on the substrate by the stress σ_f in the thin film of thickness d_{layer} is:

$$M = \underbrace{\sigma_f d_{layer}}_{=Force} \underbrace{\frac{dsubstrate}{2}}_{=Lever} \tag{9.17}$$

Combining Eq. 9.17 and Eq. 9.16, we obtain:

$$\frac{1}{R} = \frac{12}{Y_{substrate} d_{substrate}^3} \left(\sigma_{layer} d_{layer} \frac{d_{substrate}}{2} \right) \tag{9.18}$$

That is, the stress in the layer σ_{layer} can be obtained by measuring the radius of curvature of a wafer with known mechanical properties. This is expressed by the **Stoney equation**:

$$\boxed{\frac{1}{R} = \frac{6}{Y_{substrate} d_{substrate}^2} \sigma_{layer} d_{layer}} \tag{9.19}$$

The Stoney equation describes the stress induced by a layer in a substrate. But what about the opposite? If we bend the substrate, a strain is created in the thin film:

$$\epsilon_{layer} = \frac{z}{R} = \frac{\frac{d_{substrate}}{2} + \frac{d_{layer}}{2}}{R} = \frac{d_{substrate}}{2R} \tag{9.20}$$

$$\sigma_{layer} = E_{layer} \epsilon_{layer} = \frac{E_{layer} d_{substrate}}{2R} \tag{9.21}$$

Since $d_{substrate} \ll R$, σ_{layer} is very small. That is, by bending the substrate, we can hardly induce any stress in the layer.

9.1.3 Measurement Technology

There are several methods for determining the layer stress, which can be used either ex-situ or in-situ.

Laser Scanning

When evaluating using a laser scanner, the curvature of a substrate is measured. An unbent substrate results in a point-like image of the reflected laser beam, which is scanned over the sample (see Fig. 9.4). If the substrate is bent by the layer stress, the image enlarges. With this method, it is possible to detect radii of curvature up to 10 km with a scan length of 100 mm.

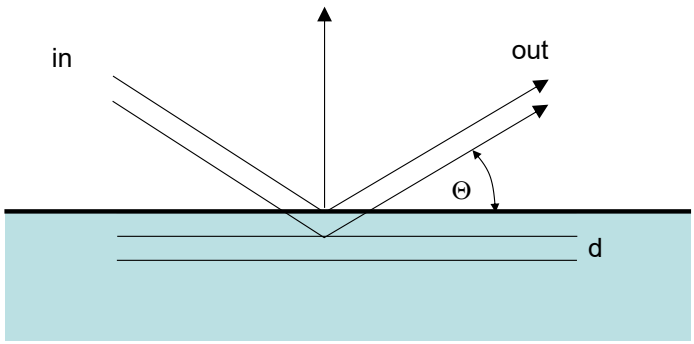

Figure 9.4: Laser scanner for determining the radius of curvature of a sample. The expansion of the laser spot on the detector is a measure of the curvature.

Profilometer

Similar to a laser scanner, the curvature of a wafer can also be measured by mechanically scanning a wafer with a profilometer.

X-ray Diffraction

The stress in a layer leads to a change in the average distance between the atoms. This is visible in X-ray diffraction for the case of polycrystalline materials (titanium nitride, boron nitride). The Bragg condition for constructive diffraction is (see Fig. 9.5):

$$d \sin \Theta = \frac{\lambda}{2} \tag{9.22}$$

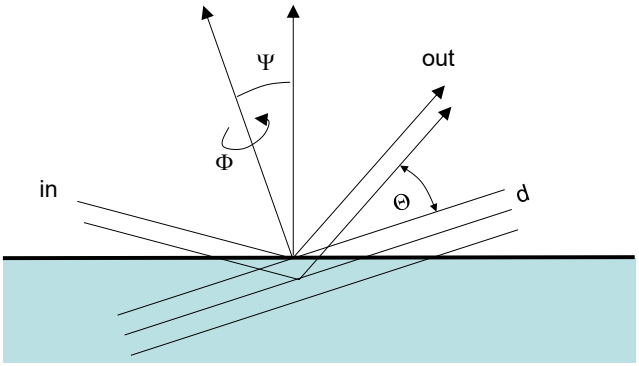

Figure 9.5: Bragg condition in X-ray diffraction.

The measured lattice plane distance d can differ from the tabulated values for the unstressed solid d_0. This corresponds to the strain ϵ according to:

$$\epsilon = \frac{d - d_0}{d_0} \tag{9.23}$$

Since the strain usually acts in the layer plane and the lattice plane distance is measured perpendicular to it, Poisson's ratio is needed to determine the final layer stress. With $\epsilon_x x = -\nu \epsilon_z z$, we obtain for the layer stress:

$$\sigma_{Schicht} = -\frac{E}{2\nu} \epsilon_{zz} = -\frac{E}{2\nu} \left(\frac{d - d_0}{d_0} \right) \tag{9.24}$$

In this equation, both the layer stress $\sigma_{Schicht}$ and the modulus of elasticity E of the material can be unknown. For this general case, it is necessary to perform the X-ray diffraction in an angle-resolved manner (see Fig. 9.6).

The strain of the lattice planes ϵ_{11}, which is visible at any angle, is calculated from the strains of the principal directions to:

$$\epsilon_\Psi = \sin 2\Psi \cos 2\Psi \epsilon_{xx} + \sin 2\Psi \sin 2\Phi \epsilon_{yy} + \cos^2 \Psi \epsilon_{zz} \tag{9.25}$$

Since $\epsilon_{zz} = -\nu \epsilon_{xx} = -\nu \epsilon_{yy}$, we can derive:

$$\epsilon_\Psi = \frac{1 + \nu}{E} \sigma_f \sin^2 \Psi - \frac{2\nu}{E} \sigma_f \tag{9.26}$$

The strain is generally:

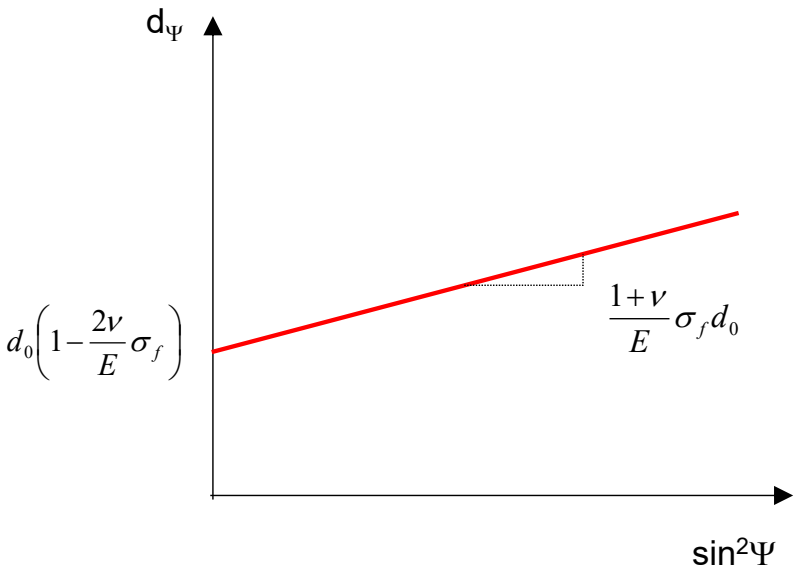

Figure 9.6: Bragg condition of X-ray diffraction with tilted sample.

$$\epsilon_\Psi = \frac{d_\Psi - d_0}{d_0} \tag{9.27}$$

Thus, from Eq. 9.26 and Eq. 9.27, we obtain:

$$d_\Psi = \frac{1-\nu}{E}\sigma_{Schicht} d_0 \sin^2\Psi + \left(1 - \frac{2\nu}{E}\sigma_f\right) d_0 \tag{9.28}$$

If we now plot the quantity d_Ψ against $\sin^2\Psi$, we can derive E and $\sigma_{Schicht}$ from the slope of the line and the intercept. This is illustrated in Fig. 9.7.

9.2 Hardness

Hardness is fundamentally not a physical quantity, unlike the modulus of elasticity. Formally, hardness is only defined with respect to a particular measurement method. In all methods, a test body with a known force is pressed into the workpiece. This force is related to the size of the impression. The hardness H is thus:

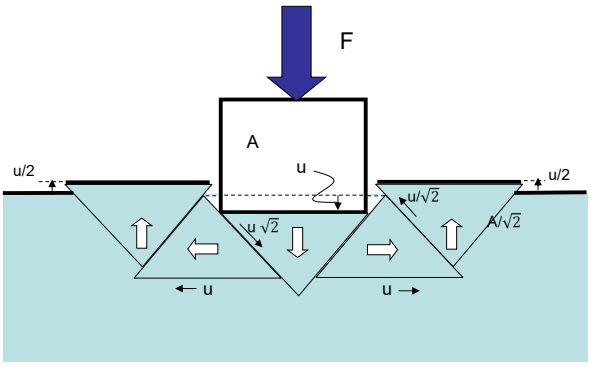

Figure 9.7: Evaluation of X-ray diffraction at variable angles of incidence.

$$H = \frac{F_{max}}{A} \tag{9.29}$$

where A is the cross-sectional area of the impression. In a simple two-dimensional model, the hardness of a sample can be linked with the internal stresses in the film as illustrated in Fig. 9.8.

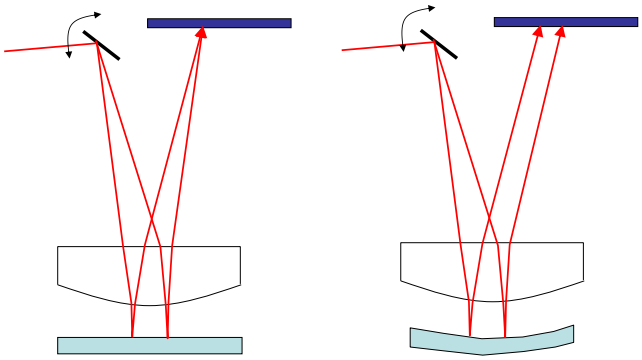

Figure 9.8: Link between hardness and stress in the layer.

The deformation of the sample is approximated by the displacement of 5 triangles with a base area of A and an edge area of $A/\sqrt{2}$. Work must be done against the shear stress at the interfaces of these triangles. This initially seems to be an artificial assumption, but the deformation is often microscopically the slipping of individual bodies in the polycrystalline layers

relative to each other. It is assumed here that the shear stress is about half of the compressive or tensile stress σ_y in the material. This shear stress is then:

$$k = \frac{\sigma_y}{2} \tag{9.30}$$

A body is now pressed into a workpiece with a force F over a distance u and displaces the triangles as illustrated in Fig. 9.8. Two triangles are each displaced to the left and right by u, and two triangles are pushed out of the material by a distance $u/2$. Work must be done against the shear stress at the interfaces of the triangles and also at the interfaces with the surrounding material during this displacement. This work Fu is balanced by the displacement of all triangles against the layer stress. The work done by displacing the middle triangle relative to the adjacent triangles is the slipping of the two surfaces by a distance $u\sqrt{2}$:

$$2\left[\underbrace{\frac{1}{\sqrt{2}}}_{area} A \underbrace{k}_{stress}\right] \underbrace{\sqrt{2}u}_{path} \tag{9.31}$$

Displacing the two triangles to the right and left along the surfaces A by the distance u at the boundary with the surrounding material is:

$$2\left[A_{area} \underbrace{k}_{stress}\right] u_{path} \tag{9.32}$$

Finally, the two triangles next to the indentation stem are pushed out of the sample, and we obtain the shearing at four interfaces. Overall, this results in:

$$Fu = 2\left(\frac{Ak}{\sqrt{2}}\right)\sqrt{2}u + 2Aku + 4\left[\frac{Ak}{\sqrt{2}}\right]\frac{u}{\sqrt{2}} \tag{9.33}$$

and thus

$$\frac{F}{A} = 6k \tag{9.34}$$

Hardness is thus linked with the internal stress as:

$$\boxed{H = \frac{F}{A} = 3\sigma_y} \tag{9.35}$$

9.2.1 Classification

There are several measurement methods for classifying hardness.

- **Brinell**

  In metallurgy, the Brinell hardness is often used. Here, a macroscopic ball (diameter cm) is pressed into the workpiece (see Fig. 9.9), and the deformation is related to the applied force.

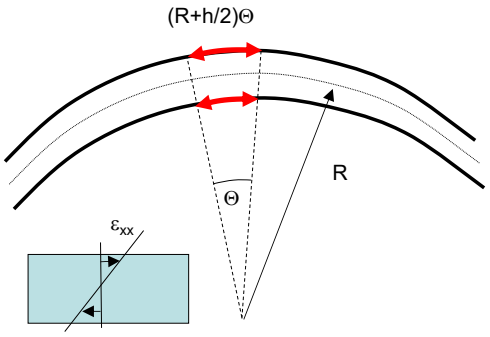

Figure 9.9: Deformation by the penetration of a body into the layer.

$$\mathrm{BHN} = \frac{F}{\frac{\pi}{2} D \left(D - \sqrt{D^2 - D_i^2} \right)} \tag{9.36}$$

- **Vickers**

  In the Vickers hardness test, a diamond indenter (as the hardest material) is used, where a facet is pressed into the workpiece. This creates an impression of area D_2.

$$\mathrm{HK} = 14.229 \frac{F}{D_2} \tag{9.37}$$

- **Rockwell**

  In the Rockwell hardness test, the gradient of the force buildup during penetration into the workpiece is evaluated. The determination of the area of the impression itself is thus no longer necessary.

- **Mohs**

  The Mohs hardness is an empirical scale from 1 to 10 in which the scratchability of two substances is compared. The test substances range from gypsum to diamond. The Mohs hardness is the test substance with which the sample can just be scratched.

These measurement methods have so far been validated for bulk materials. However, for determining the hardness of thin films, the finiteness of the sample must be considered. When pressing in the test body, only the mechanical properties of the coating should be decisive and not those of the substrate. This can be achieved by limiting the size of the impressions to the micrometer or nanometer range. With these methods, thin films are then also accessible.

9.2.2 Nanoindentation

In the so-called nanoindenter, a test body is pressed into a sample with a force in the millinewton range. The hardness can be determined from the force-displacement curve. Newer models also have the possibility to optically capture the shape of the impression. A typical nanoindentation measurement setup is shown in Fig. 9.10.

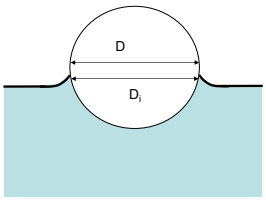

Figure 9.10: A μ- or nanoindenter measures the force when pressing a tip into the sample. The change in distance is measured via a capacitor C.

The force-displacement curve during pressing can be divided into several phases. Initially, the surface is deformed *plastically* and *elastically* until a maximum force is reached. Subsequently, the sample is unloaded, assuming that this unloading occurs purely *elastically*. At the point of maximum force, this is typically held for 30 seconds. If the penetration depth still changes during this time, this is referred to as *creep* of the material. This is illustrated in Fig. 9.11 using the example of the two materials Al and Al_2O_3. After

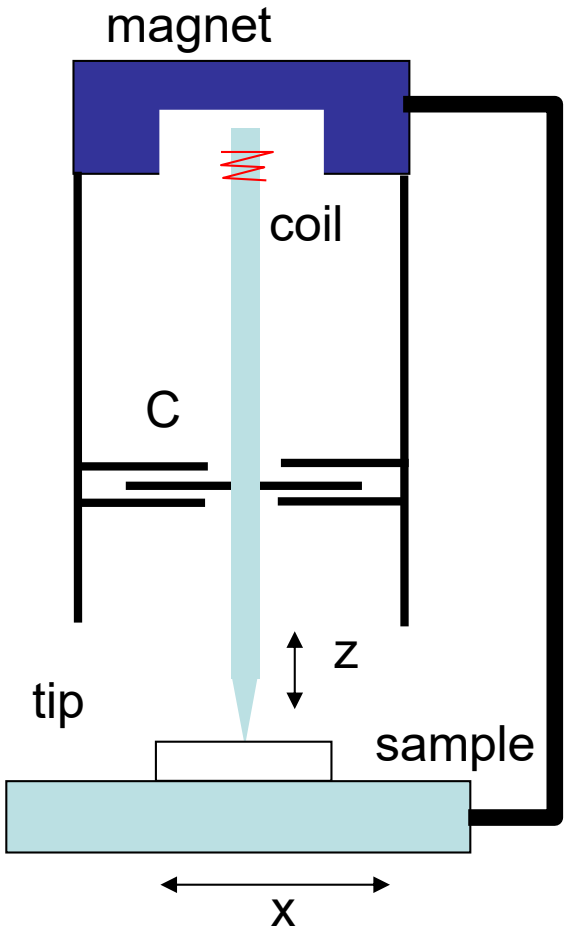

Figure 9.11: Loading and unloading curves of Al and Al_2O_3.

unloading the test body, the impression of the initial plastic deformation remains (see Fig. 9.12).

Modern instruments for hardness determination use a high-resolution SEM or AFM to determine the size of the impression of the plastic deformation. If such a device is not available, it is also possible to derive the size of the impression from the loading and unloading curve. This is done using the Oliver & Pharr method. The prerequisite is again that the unloading curve occurs completely elastically. If a test body with a horizontal boundary surface is used, the entire surface remains in contact with the solid until the test body lifts off the sample. In the elastic region, a linear dependence of force on distance is expected. That is, the unloading curve is a straight line that

intersects the x-axis in Fig. 9.12 at a depth corresponding to the last contact of the plastically deformed body. Since most test bodies, however, have complex three-dimensional shapes, the loading and unloading curve follows a general power law of the form:

$$F \propto (h - h_0)^m \tag{9.38}$$

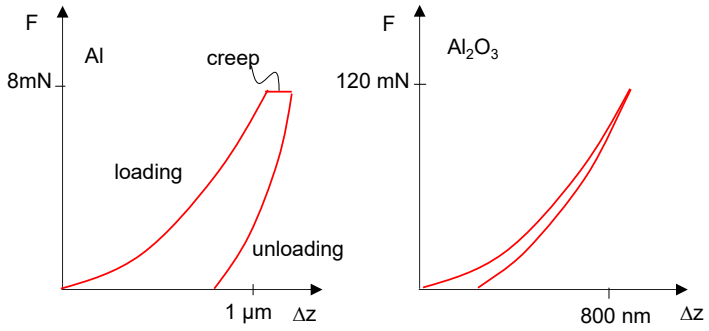

Figure 9.12: Plastic and elastic depth of the impression.

For a square body, $m = 1$, for a conical body $m = 2$, and for a spherical body $m = 1.5$. Now, from the unloading curve, we must try to determine the size of the impression of the plastic deformation. This is done as follows: (i) first, we determine the slope of the curve at the point of maximum load S_{max} and maximum penetration depth h_{max}. This slope is extrapolated to the x-axis, and we obtain the penetration depth h_i. The penetration depth h_c at the transition from elastic to plastic deformation is obtained from:

$$h_c = h_{max} - \epsilon\,(h_{max} - h_i) \tag{9.39}$$

ϵ again takes into account the shape of the indenter with $\epsilon = 1$ for a cube, $\epsilon = 0.72$ for a cone, and $\epsilon = 0.75$ for a sphere.

After determining the penetration depth h_c at the transition from plastic to elastic deformation, the cross-sectional area $A = f(h_c)$ can be calculated for a known geometry. The hardness is then again $H = F/A$.

From the elastic region, the modulus of elasticity can again be determined. For a known contact area A in the region S_{max}, the modulus of elasticity is given as:

$$S_{max} = \frac{2}{\sqrt{\pi}} E_r \sqrt{A} \tag{9.40}$$

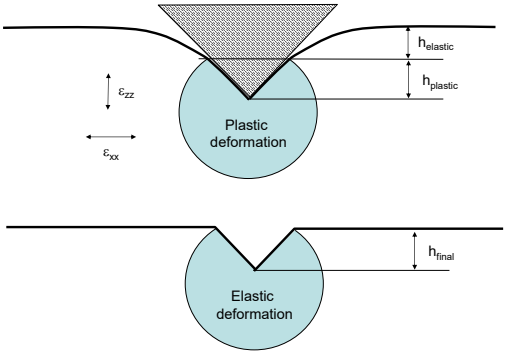

Figure 9.13: Evaluation of unloading curve.

E_r takes into account that not only the system indenter-sample but also the indenter itself has elastic properties. E_r is calculated from:

$$\frac{1}{E_r} = \frac{1-\nu_{indenter}2}{E_{indenter}} + \frac{1-\nu^2_{sample}}{E_{sample}} \tag{9.41}$$

When evaluating the force-displacement curve, it should be noted that we initially assumed a semi-infinite medium. In plasma technology, thin films are often important in which the region of plastic deformation can reach up to the interface. Therefore, the depth of the impression should typically be only 1/10 of the thickness of the layer.

Here is the converted text with the LaTeX code strictly kept:

In more complex layer systems, it is also essential to track the distribution of layer stress in the individual layers. Depending on the load distribution, apparently paradoxical effects can occur if a soft film increases the hardness of a underlying layer because the stress is distributed more uniformly.

In addition to nanoindentation, there are other methods for measuring hardness. For example, it is possible to measure the layer stress in real-time if a free standing cantilever is exposed to a plasma process. The cantilever is increasingly bent by the growing layer. This bending is measured via the deflection of a laser beam.

In another ex-situ method, a coated wafer is chemically detached until a self-supporting film is created. The backside is then subjected to a pressure that causes the layer to bulge. The height of this bulge is a measure of the hardness of the layer.

In addition to measuring hardness, there are methods to characterize wear. Here, a test body with a defined force is moved over the sample. The amount of material removed is measured. A typical setup is the movement

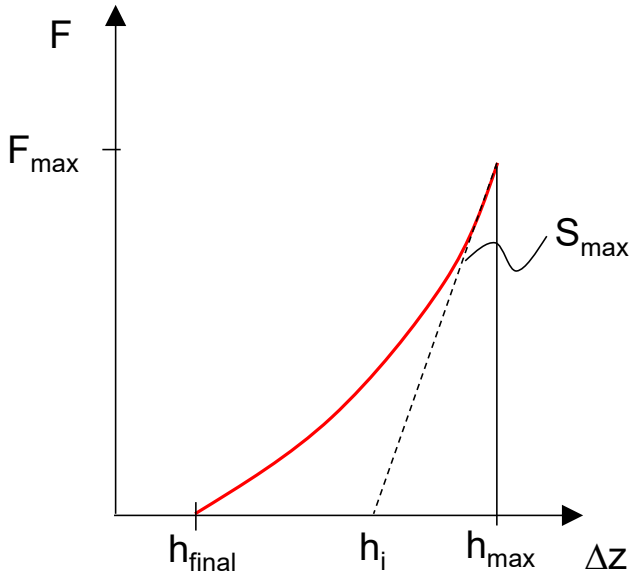

Figure 9.14: Influence of the finite substrate thickness on the evaluation of nanoindentation.

of a ball or a stylus over a rotating disk.

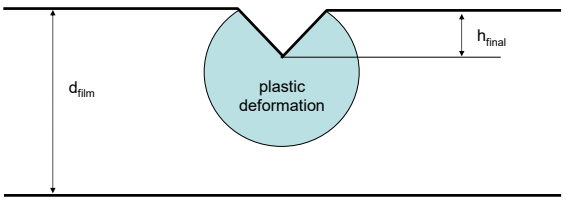

Figure 9.15: Method of the bent cantilever and bulge test.

Chapter 10

Measurement Methods Interface Properties

10.1 Surface Energy

In plasma technology, there are many applications where the interface of a workpiece is intended to have special properties regarding wettability. The wetting of a surface can be controlled by adjusting the so-called surface energy. If this surface energy is high, the system can reduce the total energy through wetting. If the surface energy is low, the wetting remains low as well.

Surface energy is defined as the work that must be expended to create a surface of a solid. If we consider the cleavage of a solid, two new surfaces are created as illustrated in Fig. 10.1. The work that must be done during cleavage is:

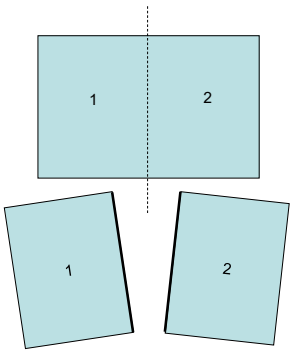

Figure 10.1: Definition of surface energy.

$$W_{12} = 2\sigma \tag{10.1}$$

Since two surfaces are created, the surface energy is σ. If two different materials 1 and 2 are involved, the work expended is:

$$W_{12} = \sigma_1 + \sigma_2 - V_{12} \tag{10.2}$$

because the interface between medium 1 and 2 disappears, and thus a portion V_{12} must be subtracted. There are different *empirical* formulas for this interaction component. The simplest approach according to:

$$V_{12} = |\sigma_1 - \sigma_2| \tag{10.3}$$

could not reproduce the measured values satisfactorily. However, the geometric mean describes the interaction contribution well:

$$V_{12} = 2\Phi\sqrt{\sigma_1\sigma_2} \tag{10.4}$$

The size Φ is a scaling factor. Therefore, we obtain:

$$W_{12} = \sigma_1 + \sigma_2 - 2\Phi\sqrt{\sigma_1\sigma_2} \tag{10.5}$$

The interaction of two media can occur in different ways: (i) induced dipole-dipole interaction for non-polar substances; (ii) dipole-dipole interaction for polar substances; (iii) hydrogen bonding. Therefore, the surface energy contains several contributions:

$$\sigma = \sigma^d + \sigma^p + \sigma^h \tag{10.6}$$

where σ^d is the contribution for the induced dipole-dipole interaction (d: dispersive), σ^p is the contribution of the dipole-dipole interaction (p: polar), and σ^h is the contribution of the hydrogen bonding (h: hydrogen).

The following important assumption is made: The interaction component V_{12} between two media contains terms only if *both* media contain the same type of bonding. Thus, a non-polar medium 1 can only interact with the non-polar bonding character in medium 2. That is, for the terms in V_{12}:

$$V_{12} \propto \sqrt{\sigma_1\sigma_2} = 2\left(\sqrt{\sigma_1^d\sigma_2^d} + \sqrt{\sigma_1^p\sigma_2^p} + \sqrt{\sigma_1^h\sigma_2^h}\right) \tag{10.7}$$

Mixed terms of the form $\sigma_1 d\sigma_2 p$ do *not* occur! In this sense, a hierarchy of interaction energies can be established. If, for example, the wetting of a layer (medium 1) with a non-polar solvent (medium 2) is considered, we obtain:

$$W_{12} = \sigma_1 + \sigma_2 - 2\sqrt{\sigma_1^d \sigma_2^d} \tag{10.8}$$

However, if a polar solvent is used, a portion of the induced and direct dipole-dipole interaction is obtained:

$$W_{12} = \sigma_1 + \sigma_2 - 2\left(\sqrt{\sigma_1^d \sigma_2^d} + \sqrt{\sigma_1^p \sigma_2 p}\right) \tag{10.9}$$

The portion of the polar interaction cannot be investigated independently of the non-polar interaction because the induced dipole-dipole interaction is much weaker but *always* present. If hydrogen bonding is also considered, we obtain:

$$W_{12} = \sigma_1 + \sigma_2 - 2\left(\sqrt{\sigma_1^d \sigma_2^d} + \sqrt{\sigma_1^p \sigma_2^p} + \sqrt{\sigma_1^H \sigma_2^H}\right) \tag{10.10}$$

Alternatively to the geometric mean, the arithmetic mean is also possible:

$$4\frac{\sigma_1^d \sigma_2^d}{\sigma_1^d + \sigma_2^d} \tag{10.11}$$

The determination of the surface energy usually occurs with the drop method. Here, a liquid (l: liquid) with known components σ_l^d and σ_l^p is dropped onto a surface, and the contact angle is measured as illustrated in Fig. 10.2.

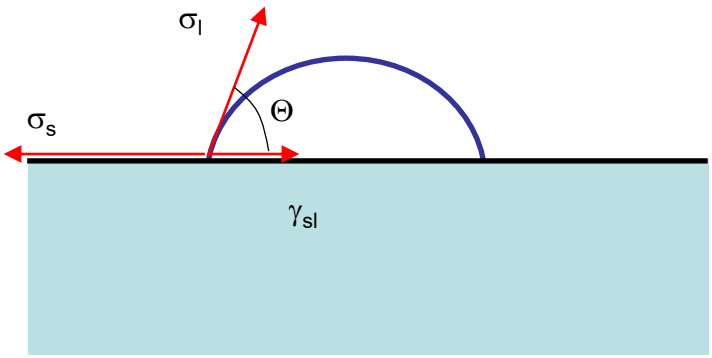

Figure 10.2: Contact angle of a drop.

From the force equilibrium at the circumference of the base area of the drop, we recognize:

$$\boxed{\sigma_s = \gamma_{sl} + \sigma_l \cos\Theta} \tag{10.12}$$

The angle Θ is determined by observing the drop with a telescope. However, the quantities σ_s and σ_l are unknown in this equation. This can be resolved with several methods:

10.1.1 Method according to Zisman

According to the method by Zisman, liquids with different σ_l are used. If the $\cos\Theta$ for different values is plotted, it can be extrapolated to the point $\cos\Theta = 1$. $\cos\Theta = 1$ corresponds to $\Theta = 0°$, i.e., complete wetting. That is, if a liquid is chosen whose surface energy exactly matches that of the solid, complete **spreading** can occur, and the surface is completely wetted. The extrapolation of the measured values is shown in Fig. 10.3.

$$\cos\Theta = 1 \tag{10.13}$$

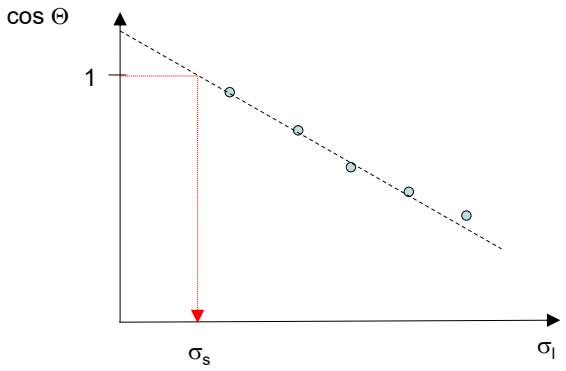

Figure 10.3: Method according to Zisman.

10.1.2 Method according to Fowkes

With the Zisman method, σ_s can be determined. However, the distinction between the non-polar and polar components is not yet possible. This requires the use of both polar and non-polar solvents as media for the drop. For the determination of σ_s^d and σ_s^p, the Fowkes method proceeds in two steps:

- **Non-polar liquids**

  First, the non-polar component is determined. We had for the interaction energy at the interface between liquid and coating:

$$\gamma_{sl} = \sigma_s + \sigma_l - 2\sqrt{\sigma_s^d \sigma_l^d} \tag{10.14}$$

  and the force equilibrium at the interface.

$$\sigma_s = \gamma_{sl} + \sigma_l \cos\Theta \tag{10.15}$$

  Combining these two equations, we obtain:

$$\cos\Theta = 2\sqrt{\sigma_s^d}\frac{1}{\sqrt{\sigma_l^d}} - 1 \tag{10.16}$$

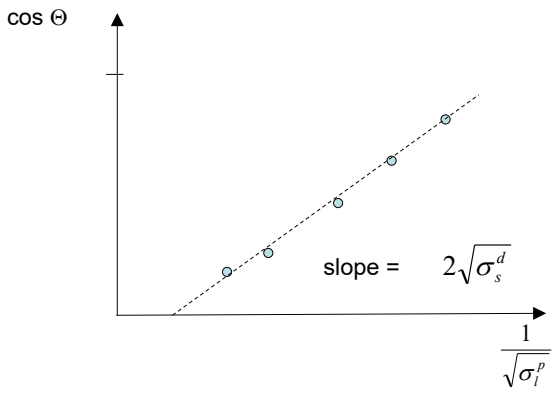

Figure 10.4: Method according to Fowkes, non-polar component.

  This equation can be evaluated graphically. After measuring the contact angles of different liquids with known component σ_l^d, a straight line is obtained when plotted according to Fig. 10.4, from which σ_s^d can be derived.

- **Polar liquids**

  In a second step, σ_s^p is determined. Polar solvents are now used:

$$\gamma_{sl} = \sigma_s + \sigma_l - 2\left(\sqrt{\sigma_s^d \sigma_l^d} + \sqrt{\sigma_s^p \sigma_l^p}\right) \tag{10.17}$$

The force equilibrium is again:

$$\sigma_s + \gamma_{sl} + \sigma_l \cos\Theta \tag{10.18}$$

The work done when applying the drop is:

$$W_{sl} = \sigma_s + \sigma_l - \gamma_{sl} \tag{10.19}$$

This work done can also be divided into a non-polar and polar component:

$$W_{sl} = W_{sl}^p + W_{sl}^d \tag{10.20}$$

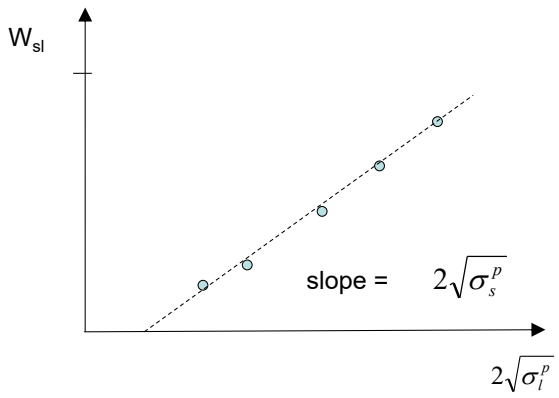

Figure 10.5: Method according to Fowkes, polar component.

From 10.18 and 10.19, it can be derived that:

$$W_{sl} = \sigma_l(1 + \cos\Theta) \tag{10.21}$$

$W_{sl}p = W_{sl} - W_{sl}d$ can be expressed as:

$$W_{sl}p = \sigma_l(\cos\Theta + 1) - 2\sqrt{\sigma_s^d \sigma_l^d} \tag{10.22}$$

In this equation, σ_l^d and σ_l of the polar liquid are known, and σ_s^d of the layer is known from the first part of the method. Therefore, for a given

non-polar liquid, the value of W_{sl}^p can be determined. From this value, σ_s^p can then be determined according to:

$$W_{sl}p = 2\sqrt{\sigma_l^p \sigma_s^p} \tag{10.23}$$

10.1.3 Method according to Owens, Wendt

According to the method by Owens and Wendt, the polar and non-polar components of the interaction can be determined simultaneously. Combining the equations:

$$W_{sl} = \sigma_s + \sigma_l - 2\left(\sqrt{\sigma_s^d \sigma_l^d} + \sqrt{\sigma_s^p \sigma_l^p}\right) \tag{10.24}$$

and

$$\sigma_s = \gamma_{sl} + \sigma_l \cos\Theta \tag{10.25}$$

they can be brought into a form $a = mx + b$ with terms according to:

$$\underbrace{\frac{(1+\cos\Theta)\sigma_l)}{\sqrt{\sigma_l^d}}}_{y} = \underbrace{\sqrt{\sigma_s^p}}_{m}\underbrace{\sqrt{\frac{\sigma_l^p}{\sigma_l^d}}}_{x} + \underbrace{\sqrt{\sigma_s^d}}_{b} \tag{10.26}$$

That is, if the contact angle is determined for several liquids with known σ_l^p and σ_l^d, a straight line with the slope σ_l^d and its intercept at $x = 0$, σ_l^d can be determined.

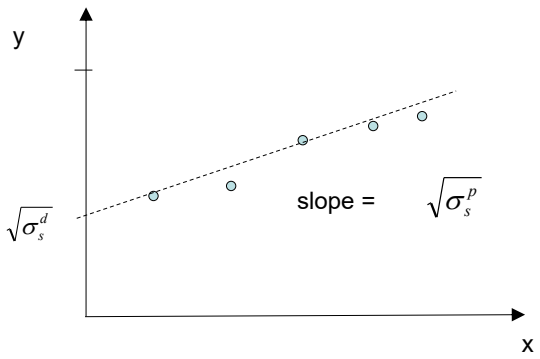

Figure 10.6: Method according to Owens, Wendt.

Appendix A

Vacuum Physics

The processing of surfaces using plasmas often takes place in systems that operate under reduced pressure. At low pressures, the chemistry of a reactive plasma and the quality of the surfaces can be better controlled than in processes that occur at atmospheric pressure. For this reason, a brief overview of vacuum generation is provided here, although only the most common methods are described.

A.1 Fundamentals

A.1.1 Pressure and Pumping Capacity

To generate a vacuum, a pump is connected to a recipient and this recipient is evacuated (see Fig. A.1). The achievable vacuum generally depends on the type of pump, the construction of the system, and its leak rate. Several vacuum ranges are roughly distinguished:

$$\begin{aligned} \text{RoughVacuum(RV)} &\quad 1000 - 1 \text{ mbar} \\ \text{FineVacuum(FV)} &\quad 1 - 10^{-3} \text{ mbar} \\ \text{HighVacuum(HV)} &\quad 10^{-3} - 10^{-7} \text{ mbar} \\ \text{Ultra} - \text{HighVacuum(UHV)} &\quad < 10^{-7} \text{ mbar} \end{aligned}$$

First, a distinction is made between **Total Pressure** and **Partial Pressure**. The partial pressure p_i corresponds to the pressure exerted by only one type of particle i. The total pressure p_{total} is obtained as the sum of all partial pressures according to:

$$p_{total} = p_1 + p_2 + p_3 + ... \tag{A.1}$$

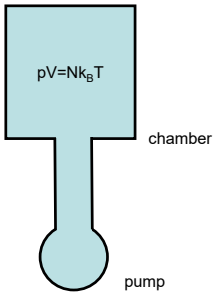

Figure A.1: Evacuation of a recipient with a pump via a pipe.

According to the ideal gas law, pressure, volume, and temperature are linked via:

$$\boxed{pV = N_A k_B T} \tag{A.2}$$

The average velocity of the gas particles, according to kinetic gas theory, is:

$$\boxed{\bar{v} = \sqrt{\frac{8k_B T}{\pi m}}} \tag{A.3}$$

When evacuating a recipient, the pumping process can be characterized as a **Volumetric Flow** or as a **Mass Flow**. The volumetric flow is:

$$\boxed{S_V = \frac{dV}{dt} \qquad [\mathrm{m3h^{-1}}, \mathrm{ls^{-1}}]} \tag{A.4}$$

This is also referred to as **Pumping Speed** S_V. The mass flow is calculated as:

$$\frac{dM}{dt} = \rho \frac{dV}{dt} = \frac{m}{k_B T} p \frac{dV}{dt} \tag{A.5}$$

The mass flow primarily depends on pS_V. This is also referred to as **Pumping Capacity** S_L:

$$\boxed{S_L = p\frac{dV}{dt} \qquad [\mathrm{kgh^{-1}}, \mathrm{kgs^{-1}}]} \tag{A.6}$$

Each pump has a certain pumping capacity or pumping speed depending on its design principle. A recipient to be evacuated has a certain leak rate,

which is caused by the imperfections of the connections. In equilibrium, the mass flow through the leak rate is equal to the mass flow through the pump. As sealing systems for the recipient, plastic seals are distinguished, which, due to their leak rate, reach into the high vacuum range, and metal seals, which are indispensable for ultra-high vacuum.

In plasma systems, however, gas is passed through the recipient. Here, the pumping capacity must essentially remove the mass inflow through the gas supply Φ. Gas flows are usually measured in particles per time. The following units have become established for this purpose:

sccm	Standard Cubic Centimeters per Minute
sccs	Standard Cubic Centimeters per Second
slm	Standard Liters per Minute

The particle quantity always corresponds to the number of gas particles at standard pressure in the specified volume (according to the ideal gas law, $N_A = 6 \cdot 10^{23}$ particles correspond to a volume of 22.4 l). The pressure of a gas of mass m that is established is obtained from the pumping speed S_V of the pump, the gas flow Φ, and the leak rate $L_{leakage}$ of the recipient. The change in particle density is:

$$\frac{dN}{dt} = \Phi + L_{leackage} - S_V \frac{p}{k_B T} \tag{A.7}$$

due to the pumping capacity $\frac{dN}{dT}\big|_{Pump} = S_V \frac{p}{k_B T}$. In equilibrium, the time derivative can be neglected, and we obtain:

$$\frac{p}{k_B T} S_V = \Phi + L \tag{A.8}$$

or for the pressure achieved in the recipient:

$$p = \frac{\Phi + L_{leakage}}{S_V} k_B T \tag{A.9}$$

In the case of reactive plasmas, this equation can be strongly modified. For example, if we consider a coating plasma, the conversion of stable molecules into reactive particles in the plasma can lead to the gas being completely converted into coating. That is, pumping of the system is no longer necessary in this case!

For the design of a vacuum system, the pumping capacity of the pump is not decisive, but the pumping capacity that can directly act on the recipient. This differs from the pump's pumping capacity because there are usually still

connecting pipes between the pump and the recipient. These connections have an individual **Conductance**, which effectively reduces the pumping capacity. This is explained below.

A.1.2 Conductance

Laminar and Molecular Flow

In gas transport in a given geometry, a distinction is made between **Laminar or Viscous** flow, where the collisions of gas particles with each other are significant, and **Molecular** flow, where the mean free path is greater than the vessel dimension. Here, collisions with the surrounding walls are significant for gas transport. The mean free path can be represented as a collision process in the image of hard spheres with radius r as:

$$\lambda = \frac{1}{\pi\sqrt{2}n(2r)^2} \tag{A.10}$$

with n the particle density. The individual cases of flow can be derived by comparing the mean free path with the vessel dimension d: **Viscous Flow** $\lambda < d$; **Knudsen Flow** $\lambda \sim d$; **Molecular Flow** $\lambda > d$. As a dimensionless number, the Knudsen number is often used for this purpose:

$$Kn = \frac{\lambda}{d} \tag{A.11}$$

Conductance

The mass transport through a geometry (pipe, orifice, etc.) now depends on the pressure difference at the inlet and outlet and the conductance of the arrangement. L_m denotes the mass conductance

$$\frac{dM}{dt} = L_m\,(p_2 - p_1) \tag{A.12}$$

and L_s the volumetric conductance

$$p\frac{dV}{dt} = L_s\,(p_2 - p_1) \tag{A.13}$$

In the following, the conductance of some arrangements will be determined.

- **Conductance of an Orifice**

The simplest case is the conductance of an orifice. From kinetic gas theory, we know that the flux J of particles onto an area A is given as:

$$\frac{dN}{dt} = J = \frac{1}{4} n\bar{v}A \tag{A.14}$$

with $\bar{v}$ the average gas velocity. The volumetric flow is then:

$$\frac{dV}{dt} = \frac{d}{dt}\left(\frac{N}{p}k_B T\right) = \frac{1}{p}k_B T\frac{1}{4}n\bar{v}A \tag{A.15}$$

with $n = N/V = p/(k_B T)$ we obtain:

$$\frac{dV}{dt} = \frac{1}{4}A\bar{v} \tag{A.16}$$

If we compare this directly with Eq. A.13

$$p_2\frac{dV}{dt} = L_s(p_2 - p_1) \tag{A.17}$$

with the condition that the pressure behind the orifice $p_1 \ll p_2$, we obtain the conductance as:

$$L_{Orifice} = \frac{1}{4}A\bar{v} \tag{A.18}$$

We see that the conductance of an orifice is *independent* of the density of the particles. This is an indication that the mean free path should be greater than the dimension of this orifice. That is, we are considering molecular flow.

- **Conductance of a Pipe**

  The most common case is gas flow through a pipe, as illustrated in Fig. A.2. In the case of laminar flow, the friction of the gas particles with each other, as well as the friction of the gas particles on the walls of the pipe, is decisive. Due to this boundary condition, the flow velocity at the wall is directly equal to zero and then increases towards the center of the pipe. This results in a parabolic velocity profile.

  The mass flow is obtained from the law of **Hagen-Poiseuille** as:

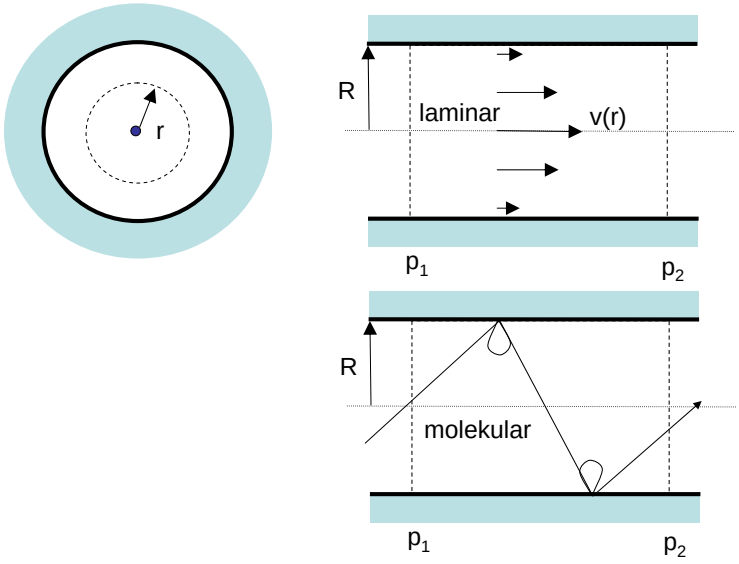

Figure A.2: Gas flow in a pipe with laminar and molecular flow.

$$\boxed{p\frac{dV}{dt} = \frac{\pi}{128}\frac{d^4}{\eta l}\left(\frac{p_1+p_2}{2}\right)(p_1-p_2)} \tag{A.19}$$

with p_1 and p_2 the pressure at the inlet and outlet of the pipe, η the viscosity, and l the length of the pipe. A comparison with Eq. A.13 also shows that the conductance is:

$$L_{Pipe,laminar} = \frac{\pi}{128}\frac{d^4}{\eta l}\left(\frac{p_1+p_2}{2}\right) \tag{A.20}$$

We see that the throughput scales with the fourth power of the diameter and depends on the average pressure $(p_1+p_2)/2$. For this reason, very thin cross-sections in an arrangement massively limit the conductance of the entire arrangement.

In the case of molecular flow, however, the mean free path is greater than the dimension of the pipe. Here, the particles are reflected between the walls of the pipe (see Fig. A.2). Upon each reflection, they leave the surface again with a cosine-shaped angular distribution. The superposition of the trajectories of many particles finally leads to a conductance that scales only with the third power of the radius:

$$L_{Pipe,molecular} = \frac{8}{3}\frac{R^3}{l}\sqrt{\frac{\pi N_A k_B T}{2m}} \tag{A.21}$$

This conductance is also independent of the pressure, as must always be the case for molecular flow. For the conductance of pipes, compact rule-of-thumb formulas can be given:

- **Laminar Flow**
  For $\bar{p} = \frac{p_1+p_2}{2}$ in [mbar] and d in [cm].

$$L = 135\frac{d^4}{l}\bar{p} \qquad [\mathrm{ls}^{-1}] \tag{A.22}$$

- **Molecular Flow**

$$L = 12.1\frac{d^3}{l} \qquad [\mathrm{ls}^{-1}] \tag{A.23}$$

  It is important to note that in the range of molecular flow, the conductance becomes independent of the pressure.

The conductance for pipes can also be extended to bends and curves if an effective length l_{eff} is introduced. For a bend with angle Θ, as illustrated in Fig. A.3, the following effective length is obtained from the nominal length l_{axial}:

$$l_{eff} = l_{axial} + 1.33\frac{\Theta}{180^\circ}d \tag{A.24}$$

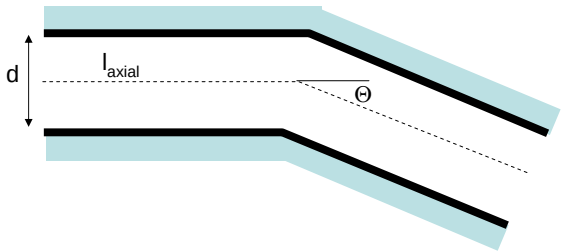

Figure A.3: Effective conductance for bends in pipes can be considered by an effective length.

with d the diameter of the pipe.

A.1.3 Design of Vacuum Systems

As already noted above, the effective pumping speed S_{eff} at a recipient depends on the nominal pumping speed S of the pump and the conductance L of the arrangement between the pump and the vessel. As in the series connection of conductances, we obtain:

$$\frac{1}{S_{eff}} = \frac{1}{S} + \frac{1}{L} \tag{A.25}$$

The conductance of an entire arrangement corresponds to a series connection of conductances, and we obtain:

$$\frac{1}{L} = \frac{1}{L_1} + \frac{1}{L_2} + \frac{1}{L_3} + \frac{1}{L_4} + ... + \frac{1}{L_n} \tag{A.26}$$

A.2 Vacuum Generation

In the following, the most common pumps for generating vacuums will be described.

A.2.1 Diaphragm Pump

An important representative of pumps for generating a rough vacuum are diaphragm pumps. They achieve a final pressure in the range of mbar, with the aspirated air not coming into contact with lubricants. They are therefore referred to as *oil-free*. This is particularly important for applications where backflow of lubricants from the pumps back into the recipient should be avoided. This is a significant advantage of diaphragm pumps compared to oil-sealed piston pumps.

In a diaphragm pump, a diaphragm is clamped between a pump head and the housing wall. This diaphragm is moved via an eccentric and thereby sucks gas from an inlet valve, compresses it, and then expels the gas via an outlet valve (see Fig. A.4).

If the diaphragm is coated with Teflon, a diaphragm pump can also be made very resistant to chemicals. The disadvantage of diaphragm pumps is their low gas throughput, as the variation in volumes during pumping must be realized by bending the diaphragm. Furthermore, the final pressure achieved is lower than that of oil-sealed piston pumps. This can be compensated by using multi-stage diaphragm pumps. With four-stage pumps, a final pressure in the range of 10^{-3} mbar is achieved. Diaphragm pumps are suitable only for plasma applications with low gas throughput or in combination with

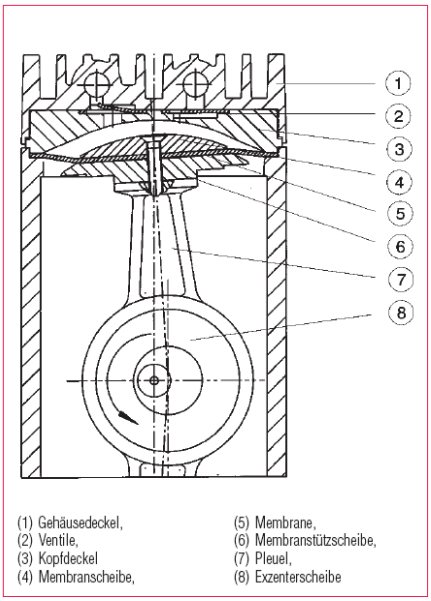

Abb. 2.1
Schematische Darstellung des Aufbaues einer Membranpumpenstufe (Vacuubrand)

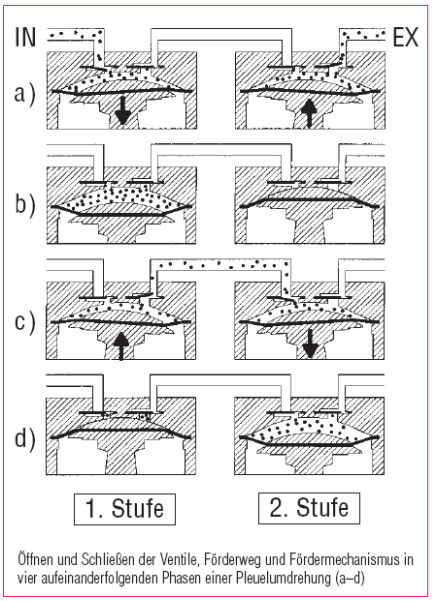

Abb. 2.2
Veranschaulichung der Funktionsweise einer zweistufigen Membranpumpe (Vacuubrand)

Figure A.4: Principle of a diaphragm pump. Single-stage and dual-stage design.

turbomolecular pumps that allow a foreline pressure in the range of 1 mbar. They are ideally suited for applications where the vacuum must remain oil-free, such as for differential pumping stages in mass spectrometry.

A.2.2 Rotary Vane Pump

In the rotary vane pump, two vanes are located in a slotted rotor, which are pressed against the outer wall of the pump chamber by centrifugal forces. There, they seal off via an oil film (see Fig. A.5).

A multi-stage arrangement yields final pressures up to 10^{-3} mbar. Large gas volumes can be pumped with rotary vane pumps.

When pumping different media, condensation of moisture in the medium may occur during compression of the gas before expulsion. This can be avoided by operating the pump with a **Gas Ballast**, i.e., during compression, the pump also sucks in ambient air and thus keeps the humidity in the compression chamber below 100

Such a gas ballast can also be used to add inert gases to keep the concentration of flammable gases in the exhaust low or to keep their concentration

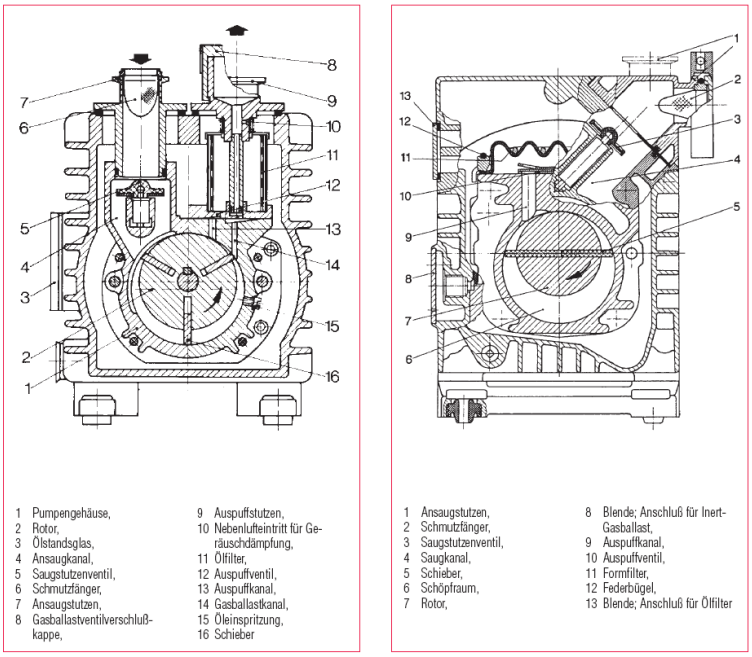

Figure A.5: Principle of a rotary vane pump.

below the ignition point.

A.2.3 Root Pump (Lobe Pump)

Root pumps, or lobe pumps, are characterized by a low final pressure and a very high gas throughput. They are designed for applications where very large gas volumes need to be pumped. In the lobe pump principle, two symmetrically shaped rotors run against each other (see Fig. A.7). The rotors run past each other without contact, with only a gap of a few tenths of a millimeter. For this reason, they can run at very high speeds, which explains the high pumping capacity.

To prevent oil vapors, an **Adsorption Trap** is connected between the recipient and the pump, where the gas must flow over a zeolite with a large surface area.

A.2.4 Turbomolecular Pump

For pumping in the molecular flow range, the conductance of the intake is no longer dependent on the pressure. That is, in this pressure range, the

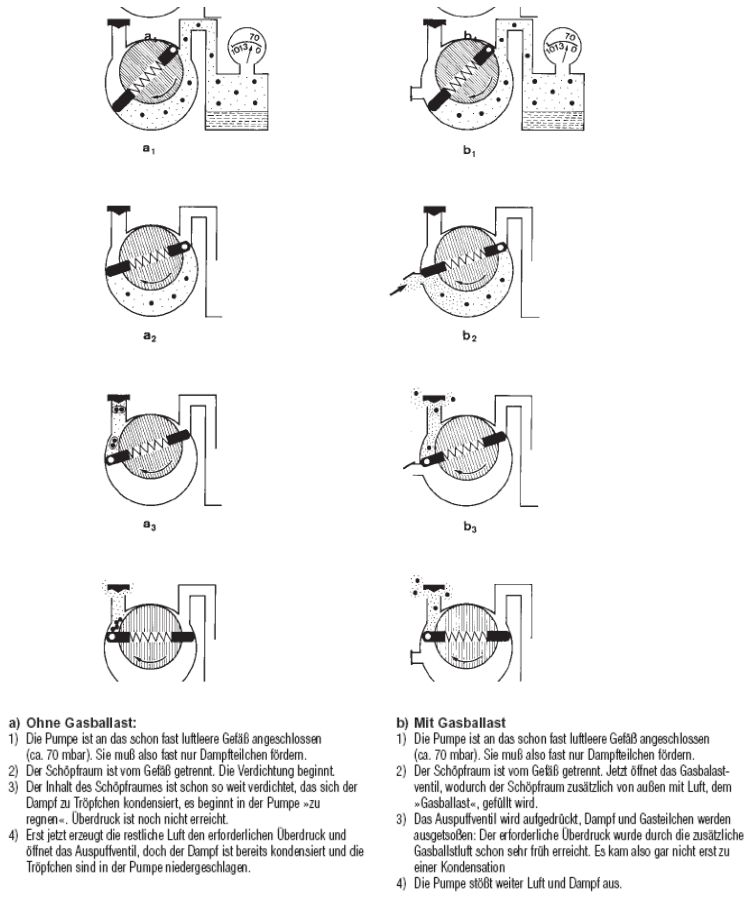

Figure A.6: By using a gas ballast, condensation of moisture in the outlet can be suppressed. Additionally, inert gas can be added to the pumped reactive gas.

absolute cross-section of the pump line is decisive. The most widespread in this range are turbomolecular pumps (see Fig. A.8).

In turbomolecular pumps, a rotor rotates opposite a stator with obliquely positioned rotor blades. If a gas particle hits such a rotor blade, it is accelerated in the direction of the outlet opening. The rotational speeds of these rotors are in the range of 10,000 to 30,000 revolutions per minute. The rotors are often magnetically levitated. With turbomolecular pumps, a final pressure in the range of 10^{-10} mbar can be achieved.

Turbomolecular pumps can generate a compression ratio of the order of 10^8. This compression ratio is usually smaller for very light gases such as hydrogen, as hydrogen has a large gas velocity and can therefore more easily backflow against the rotors.

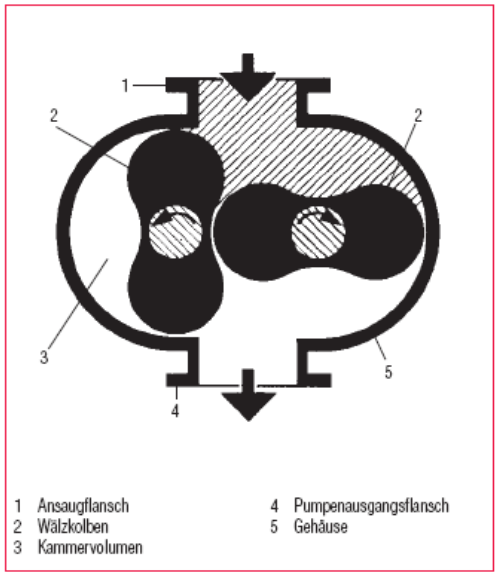

Abb. 2.17
Schematischer Querschnitt einer Wälzkolbenpumpe

Figure A.7: Root pump.

The operating principle of a turbomolecular pump can be illustrated in Fig. A.9: First, consider a gas with an average isotropic velocity v_{Gas}. This gas hits the rotating rotor with its obliquely positioned rotor blades. The velocity of the rotor is v_{Rotor}, which is typically in the range of 300...400 ms^{-1}. In the stationary reference system of the rotor, the rotor sees a *distorted* velocity distribution of the gas atoms, as indicated in Fig. A.9. A certain section of this velocity distribution (hatched area in Fig. A.9) can pass the rotor without collision. For the consideration of backflow, we rotate the image. Now, a different section of the velocity distribution can pass through the rotor without collision (hatched area in Fig. A.9). The comparison of the sections for the two flow directions shows that effective pumping occurs when the proportion for forward flow is much larger than the proportion for backflow (the consideration of adsorption and desorption of particles from the rotor blades changes this dependence only slightly).

This also means that good compression is only achieved when the rotor speed is close to the gas velocity, as only then is the velocity distribution in the rotor reference system sufficiently distorted. For nitrogen, gas velocities in the range of 400 ms^{-1} are achieved, thus resulting in good pumping action. For hydrogen, however, a gas velocity in the range of 1600 ms^{-1} is present, which results in a poor compression ratio for H_2. Values are only achieved

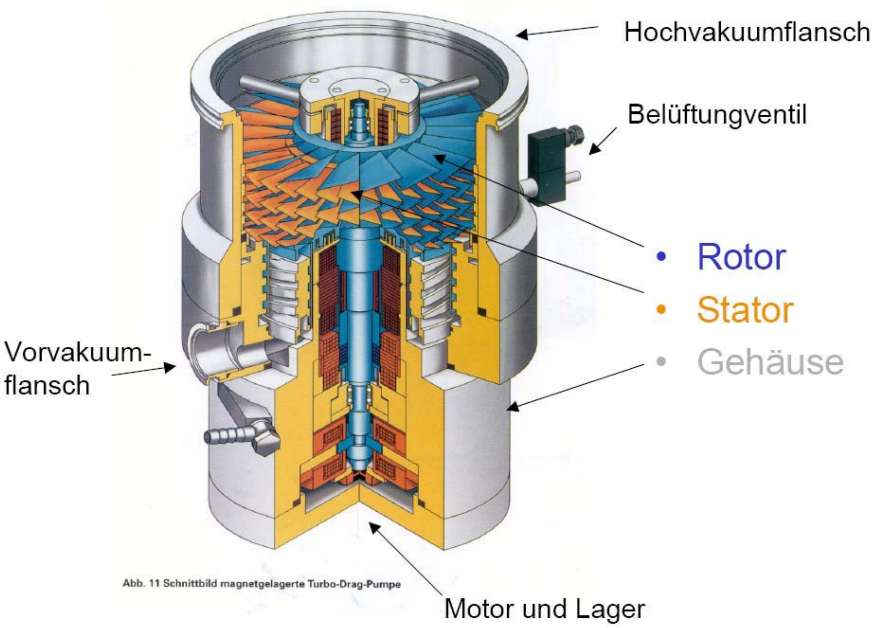

Figure A.8: Cross-section of a turbomolecular pump.

in the range of 10^4.

The disadvantage of the poor compression ratio for hydrogen is avoided by turbomolecular pumps with post-compression, a so-called **Holweck stage**. Here, the gas passes through a system of nested cylinders at the outlet, which extends the path from the rotors to the outlet. Through this labyrinth, a high compression ratio is also achieved for hydrogen. The disadvantage of this type is a smaller gas throughput. Alternatively to this Holweck stage, a series connection of turbopumps can be designed, in which the poor compression of a single turbopump is compensated by the second. In the latter approach, the gas throughput can also be large.

To protect the bearings of this pump type from reaction with a reactive gas, a **Purge Gas** can be introduced, which explicitly protects the bearing at the often oil-sealed outlet side. Gases can also be introduced via this seal gas valve to reduce the ignition point of the exhaust gas.

A.2.5 Ion Getter Pump

In an ion getter pump, a gas discharge is ignited via a high voltage. The gas of this discharge is provided by the residual gas in the recipient. The gas particles are ionized and implanted into the surfaces. The surfaces of this ion

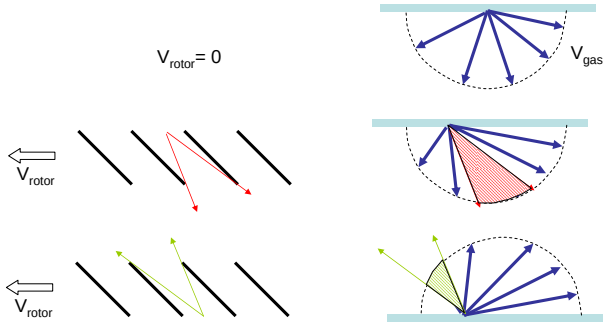

Figure A.9: Operating principle of a turbomolecular pump.

getter pump consist of titanium, which is sputtered by the impinging ions. The titanium atoms hit the surrounding surfaces and form a very reactive metal film. This metal film *getters* additional gas particles (see Fig. A.11). In the case of non-reactive gases, such as noble gases, only the implantation contributes to the pumping effect.

A.3 Vacuum Measurement

A.3.1 Gas-Type Independent Sensors

In the rough vacuum range, spring and diaphragm vacuum gauges are most common. Here, a diaphragm is deflected by the pressure difference between the recipient and the environment. The deflection itself is calibrated and thus serves to display the pressure.

Modern implementations of this measurement principle are capacitive pressure sensors. Here, the diaphragm forms the central part of a series connection of capacitors. By bending this diaphragm, an oscillating circuit containing these capacitors can be detuned. According to this method, pressures can be determined very well. In particular, this pressure measurement is *independent* of the gas type. However, these tubes are sensitive to coating, as the deformation of the diaphragm could then change. For this reason, heated types exist that can suppress the adsorption of gases. The measurement range of this type extends down to 10^{-3} mbar.

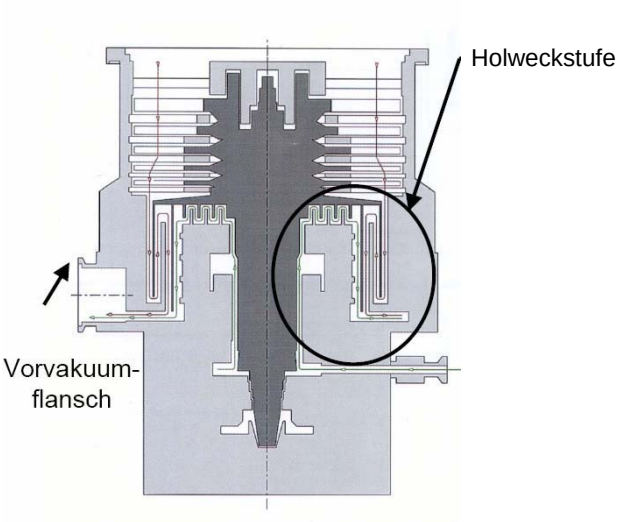

Figure A.10: Holweck stage of a turbomolecular pump.

A.3.2 Gas-Type Dependent Sensors

Friction Gauge

In a friction gauge, gas friction is used as a measure of pressure. Here, a steel ball is suspended frictionlessly in a magnetic field. The ball is set into rotation (400 Hz) electromagnetically. A gas flow slows down this ball. In a measurement cycle, this ball is accelerated and then slowed down by the gas flow. The time constant of this deceleration is a measure of the pressure. Since the deceleration time depends on the absolute pressure, measurement times between 5 and 40 seconds are obtained.

Pirani Tube

In a **Pirani Tube** , a wire is heated to 100° to 150 ° degrees. The thermal conductivity of the surrounding gas determines the heating current that must flow to maintain the temperature. As the pressure decreases, the thermal conductivity and thus the heating current decrease. In the rough vacuum range, convection is decisive for the display. Accordingly, the display is then inaccurate. Pirani tubes operate in the range of 10^{-3} mbar to 1 mbar. At lower pressures, the change in thermal conductivity is too small.

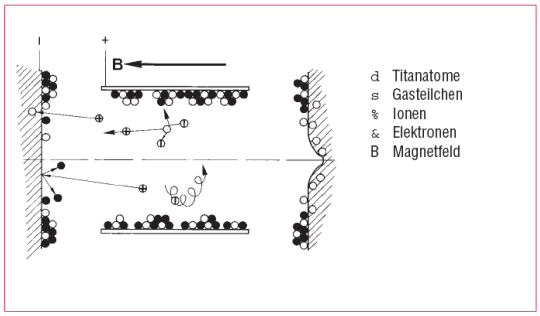

Abb. 2.62
Elektrodenkonfiguration einer Dioden-Ionenzerstäuberpumpe

Figure A.11: Ion getter pump.

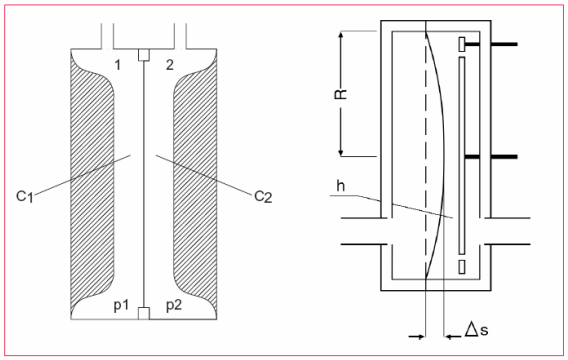

Abb. 3.5
Kapazitiver Sensor, (Prinzip)

Figure A.12: Capacitive pressure gauge.

Penning Gauge

In a Penning gauge or cold cathode vacuum gauge, a discharge is ignited via a high voltage. The discharge current is a measure of the density of gas particles. The confinement of this plasma is further increased by an additional magnetic field, so that even at very low pressures, a significant current still flows.

Ionization Gauge

In an ionization gauge, an electron current is generated via a heated filament. Yttrium oxide-coated iridium is usually used as the filament, which emits electrons even at low temperatures.

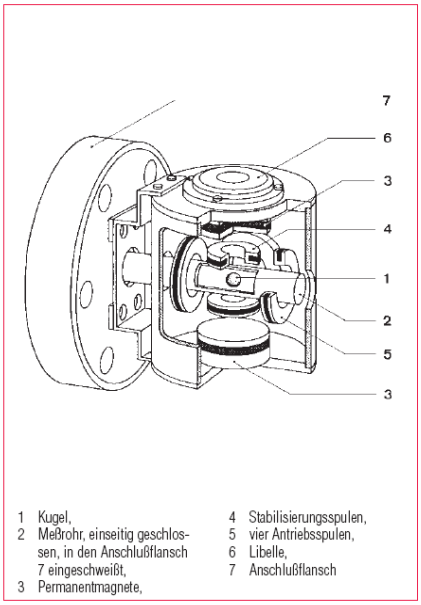

Abb. 3.9
Schnitt durch den Meßkopf des Reibungs-Vakuummeters VISCOVAC VM 212.

Figure A.13: Friction gauge.

The electrons are emitted from the heated cathode and accelerated towards the anode. On their way, they can ionize gas particles. These gas particles are captured on an ion collector, which is at a negative potential with respect to the cathode. There, they contribute to the current, which is thus a measure of the prevailing pressure.

At high pressures, this method is limited by the mean free path of the gas particles. That is, ionization gauges operate at most up to the range of 10^{-2} mbar. Towards very low pressures, the ionization gauges are limited by the X-ray effect. Here, the electrons at the anode release photons, which in turn release electrons from the ion collector via the photoelectric effect. This loss of electrons from the ion collector is detected as ion current.

The ionization gauges can be connected differently, as illustrated in Fig. A.15. The anode is labeled A, the cathode K, and the ion collector J: (a) In a conventional arrangement, electrons are generated at a central filament and accelerated outward through a grid anode. They oscillate around the grids of the anode and thus increase the probability of ionization. The ion collector is a concentric grid on the outside. Â© The most common connection is the Bayard-Alpert tube. Here, the X-ray effect is greatly reduced because

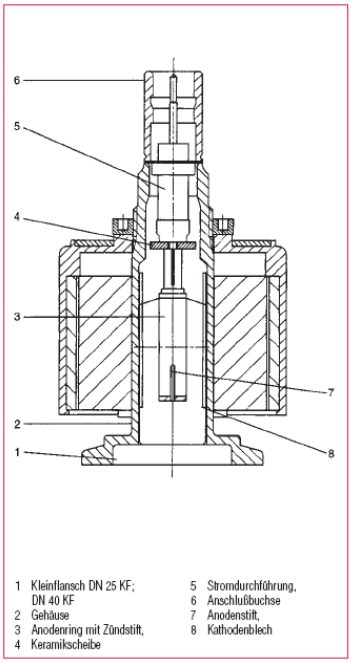

Figure A.14: Penning gauge.

the ion collector is designed as a very thin wire, minimizing the impact of photons. Ions, however, are trapped by the electric field of the wire.

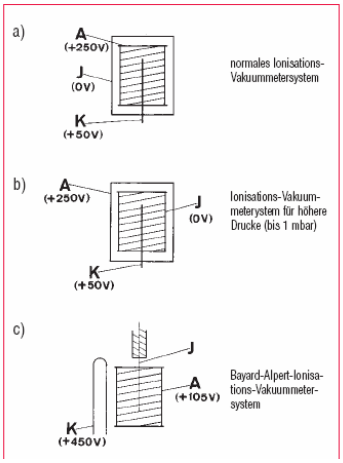

Figure A.15: Possible connections of an ionization vacuum gauge.

Appendix B

Optics of Thin Films

B.1 Interface Between Two Media

B.1.1 Angles

Consider an electromagnetic wave at the interface between two media 1 and 2. Since there are no external charges present, the tangential components of the electric field and the normal components of the D-field must be identical. With $\vec{D} = \epsilon\vec{E}$, the conditions are:

$$\vec{E}_{t1} = \vec{E}_{t2} \tag{B.1}$$
$$\epsilon_1\vec{E}_{n1} = \epsilon_2\vec{E}_{n2} \tag{B.2}$$

Since we are also considering a non-magnetic material, the components of the magnetic field are:

$$\vec{B}_{t1} = \vec{B}_{t2} \tag{B.3}$$
$$\vec{B}_{n1} = \vec{B}_{n2} \tag{B.4}$$

With the approach for $\vec{E} = Ae^{i\vec{k}\vec{r}-i\omega t}$, the continuity conditions for the location $\vec{r} = 0$ according to Fig. result in:

$$E_{et} + E_{rt} = E_{gt} \tag{B.5}$$
$$A_{et}e^{\imath\omega_e t} + A_{rt}e^{\imath\omega_r t} = A_{gt}e^{\imath\omega_g t} \tag{B.6}$$

Since the phase must be preserved, it is immediately apparent that:

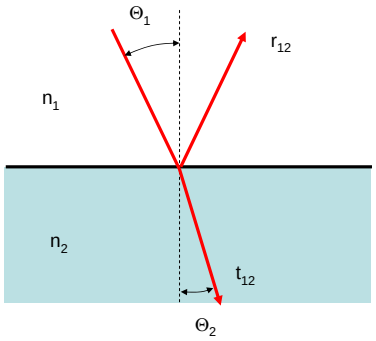

Figure B.1: Reflection of a light beam at an interface between two media 1 and 2.

$$\omega_e = \omega_r = \omega_g \tag{B.7}$$

i.e., the frequency remains the same, but the wavelength in the medium can change due to:

$$\frac{c}{n} = \frac{\nu}{\lambda} \tag{B.8}$$

Assume that the location on the interface can be arbitrary. Therefore, for all locations, the following must hold:

$$\vec{k}_e\vec{r} = \vec{k}_r\vec{r} = \vec{k}_g\vec{r} \tag{B.9}$$

i.e., projecting onto the xy-plane results in:

$$\vec{k}_{ex} = \vec{k}_{rx} = \vec{k}_{gx} \tag{B.10}$$

From the figure, it can be seen that:

$$k_{ex} = k_e \sin\alpha \tag{B.11}$$
$$k_{rx} = k_r \sin\alpha' \tag{B.12}$$
$$k_{gx} = k_g \sin\beta \tag{B.13}$$

with

$$k = n\frac{\omega}{c} \tag{B.14}$$

we finally obtain:

$$n_1 \sin\alpha = n_1 \sin\alpha' = n_2 \sin\beta \tag{B.15}$$

After that, $\alpha = \alpha'$, i.e., the angle of incidence is equal to the angle of reflection, and

$$\boxed{n_1 \sin\alpha = n_2 \sin\beta} \tag{B.16}$$

This is referred to as **Snell's Law**. It should be noted that the refractive indices are generally complex numbers. That is, if we consider the direction of propagation in a medium, for example, $\sin\beta$ is a complex number. For the true direction of propagation, only the real part of n counts here. However, when calculating layer stacks, it is essential to treat the expression for $\sin\beta$ fully as a complex number in the calculation.

To calculate the Fresnel coefficients, the quantity $\cos(\Theta_1)$ is required. This quantity must formally be treated as a complex number in the case of absorbing materials.

$$\cos(\Theta_2) = \sqrt{1 - \frac{n_1}{n_2}\sin^2(\Theta_1)} \tag{B.17}$$

This relationship also applies to a layer stack, as Snell's Law links all layers. For the direction of propagation in an arbitrary layer i, with Θ_0 as the angle of incidence, we obtain:

$$\cos(\Theta_\mathrm{i}) = \sqrt{1 - \frac{1}{n_\mathrm{i}}\sin^2(\Theta_0)} \tag{B.18}$$

B.1.2 Amplitudes

Now let's consider the amplitudes of the electric field. In the following, we divide the amplitudes into a component parallel (index p) to the plane of incidence and one perpendicular (index s) to it.

$$A_{ls} + A_{rs} = A_{gs} \tag{B.19}$$

With $\vec{B} = \frac{n}{c}\hat{\vec{k}} \times \vec{E}$ ($\hat{\vec{k}} = \frac{\vec{k}}{|k_0|}$), we obtain:

$$k_{ey}A_{ls} + k_{ry}A_{rs} = k_{gy}A_{gs} \tag{B.20}$$

With $k_{ey} = -k_{ry}$ and $k_{ey} = k_e \cos\alpha$ and $k_{gy} = k_g \cos\alpha$, we obtain:

$$k_g n_1 = k_e n_2 \tag{B.21}$$

Thus, we have:

$$r_{\mathrm{s},12} = \frac{A_{rs}}{A_{es}} = \frac{n_1 \cos(\Theta_1) - n_2 \cos(\Theta_2)}{n_1 \cos(\Theta_1) + n_2 \cos(\Theta_2)} \tag{B.22}$$

and

$$t_{\mathrm{s},12} = \frac{A_{gs}}{A_{es}} = \frac{2n_1 \cos(\Theta_1)}{n_1 \cos(\Theta_1) + n_2 \cos(\Theta_2)} \tag{B.23}$$

Analogously, for the components perpendicular to the plane of incidence, we obtain for the components parallel to the plane of incidence:

$$r_{\mathrm{p},12} = \frac{n_2 \cos(\Theta_1) - n_1 \cos(\Theta_2)}{n_2 \cos(\Theta_1) + n_1 \cos(\Theta_2)} \tag{B.24}$$

and

$$t_{\mathrm{p},12} = \frac{2n_1 \cos(\Theta_{1,\mathrm{p}})}{n_2 \cos(\Theta_{1,\mathrm{p}}) + n_1 \cos(\Theta_{2,\mathrm{p}})} \tag{B.25}$$

When considering the law of refraction, there are two special cases:

- **Brewster Angle**

  At a certain angle of incidence, the angle between the reflected beam and the refracted beam becomes 90 degrees. For the case where the light is polarized in the plane of incidence, the intensity of the reflected beam becomes zero:

  $$\tan \alpha = \frac{n_2}{n_1} \tag{B.26}$$

  This can be understood microscopically. If we consider the solid atoms as oscillating dipoles, there is no radiation in the direction of this dipole moment. Therefore, radiation in the direction of the reflected beam is also no longer possible, as illustrated in Fig. B.2.

- **Total Reflection**

  If a light beam falls from the optically denser medium onto an interface with the optically thinner medium, the refracted beam can run parallel to the surface at a certain critical angle. From this critical angle, total reflection occurs, and only an evanescent wave enters the optically thinner medium.

  $$\sin \alpha = \frac{n_1}{n_2} \tag{B.27}$$

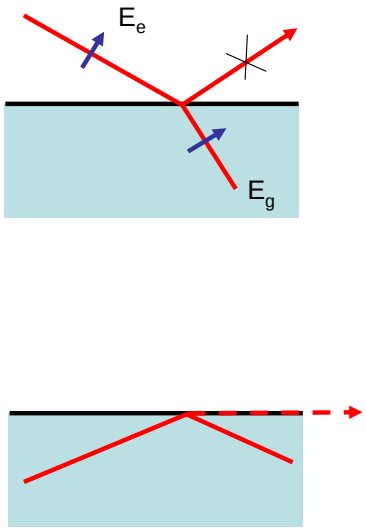

Figure B.2: Brewster angle and angle of total reflection.

B.1.3 Transmission Through a Thin Film

When transmitting through a thin film, it is essential to consider the multiple interferences, as illustrated in Fig. B.3. To calculate the reflected amplitude, we must sum over all light bundles and coherently superpose them. This results in:

$$r = r_{12} + t_{12}r_{23}t_{21}e^{-i2\beta} + t_{12}r_{23}r_{21}r_{23}t_{21}e^{-i4\beta} + ... \tag{B.28}$$

Here, β is the phase shift in the thin film:

$$\beta = \frac{2\pi}{\lambda} nd\cos\Theta \tag{B.29}$$

Eq. B.28 can be rewritten as a sum over n multiple interferences according to:

$$r = r_{12} + t_{12}t_{21}e^{-i2\beta}\sum_{l=0}^{n}\underbrace{\left(r_{21}r_{23}e^{-i2\beta}\right)}_{=q} \tag{B.30}$$

with $q < 1$. Thus, we obtain a geometric series that can be written as:

$$r = r_{12} + t_{12}t_{21}e{-}\imath 2\beta\frac{qn-1}{q-1} \tag{B.31}$$

and in the limit $n \to \infty$ we obtain:

$$r = r_{12} + t_{12}t_{21}r_{23}e^{-\imath 2\beta}\frac{1}{1 - r_{21}r_{23}e^{-\imath 2\beta}} \tag{B.32}$$

Since $r_{21} = -r_{12}$ and $t_{12} + r_{12} = 1$, we obtain:

$$r = r_{12} + (1 - r_{12})(1 + r_{12})r_{23}e^{-\imath 2\beta}\frac{1}{1 + r_{12}r_{23}e^{-\imath 2\beta}} \tag{B.33}$$

and finally as the final result:

$$\boxed{r = \frac{r_{12} + r_{23}e^{-\imath 2\beta}}{1 + r_{12}r_{23}e^{\imath 2\beta}}} \tag{B.34}$$

This equation applies to *both* polarization directions, perpendicular and parallel to the plane of incidence. Analogously to the derivation of Eq. B.34, we obtain for the transmission of a thin film:

$$\boxed{t = \frac{t_{12}t_{23}e^{-\imath\beta}}{1 + r_{12}r_{23}e^{-\imath 2\beta}}} \tag{B.35}$$

The reflectivity as a measure of the reflection capability of the intensity is:

$$R_{12} = r_{12} \cdot r_{12}^* \tag{B.36}$$

In the case of transmission through an interface, we obtain:

$$T_{12} = \frac{\cos(\Theta_1)}{\cos(\Theta_2)}t_{12}t_{12}^* \tag{B.37}$$

The prefactors disappear in the case of transmission through a thin film T_{12}, where the medium on both sides is identical.

B.2 Reflection and Transmission of Light on a Layer Stack

How do we now calculate the transmission or reflection of an entire layer stack? This is achieved using a recursive method that starts with the lowest layer and iteratively proceeds through the layer stack. In a first step, the Fresnel coefficients of each interface are calculated. Here, i is the index of each layer with i=0 for the substrate and $i = l$ for the topmost layer:

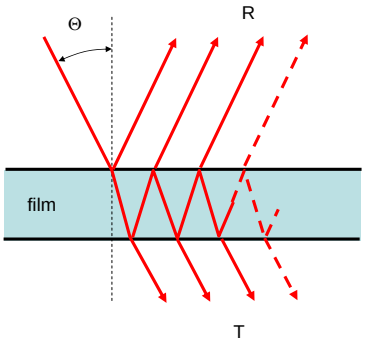

Figure B.3: Reflection of light on a thin film.

$$r_{p,i-1:i} = \frac{n_{\mathrm{i}} \cos(\Theta_{\mathrm{i}-1}) - n_{\mathrm{i}-1} \cos(\Theta_{\mathrm{i}})}{n_{\mathrm{i}} \cos(\Theta_{\mathrm{i}-1}) + n_{\mathrm{i}-1} \cos(\Theta_{\mathrm{i}})} \tag{B.38}$$

$$r_{s,i-1:i} = \frac{n_{\mathrm{i}-1} \cos(\Theta_{\mathrm{i}-1}) - n_{\mathrm{i}} \cos(\Theta_{\mathrm{i}})}{n_{\mathrm{i}-1} \cos(\Theta_{\mathrm{i}-1}) + n_{\mathrm{i}} \cos(\Theta_{\mathrm{i}})} \tag{B.39}$$

The reflection coefficient at the lowest layer 1 is (interface 1:2):

$$r_{\mathrm{total},1} = \frac{r_{21} + r_{10} e^{-\imath 2\beta_1}}{1 + r_{21} r_{10} e^{-\imath 2\beta_1}} \tag{B.40}$$

The recursion consists in using this reflection coefficient for the Fresnel coefficient of the interface 2:3. The recursion formula is thus:

$$r_{\mathrm{total,i}} = \frac{r_{\mathrm{i+1,i}} + r_{total,i-1} e^{-\imath 2\beta_i}}{1 + r_{i+1,i} r_{total,i-1} e^{-\imath 2\beta_i}} \tag{B.41}$$

B.3 Coherent and Incoherent Transmission

B.3.1 Transmission and Reflection on a Thin Film

What changes now if we assume that the light transmission through a film no longer occurs in a coherent manner, as the phase relationship between two light bundles is no longer preserved. This can be taken into account by setting the real part of β to zero and adding the intensities of the individual light bundles instead of the field strengths. Analogously to the consideration of a thin film, we must now sum the intensities of the multiple reflections *incoherently*:

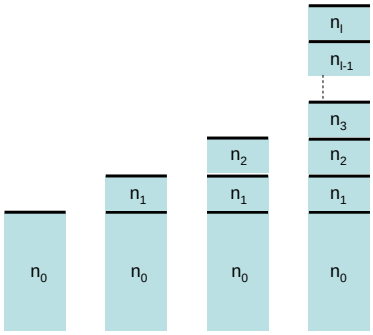

Figure B.4: Reflection on a layer stack.

$$R = R_{12} + T_{12}R_{23}T_{21}e^{4\beta} + T_{12}T_{21}R_{23}e^{4\beta}R_{21}R_{23}e^{4\beta} + ... \tag{B.42}$$

This can also be written as a sum over n reflections:

$$R = R_{12} + T_{12}R_{23}T_{21}e^{4\beta}\sum_{l=0}^{n}\left(R_{21}R_{23}e^{4\beta}\right)l \tag{B.43}$$

with $n \to \infty$ we finally obtain:

$$R = R_{12} + T_{12}R_{23}T_{21}e^{4\beta}\frac{1}{1 - R_{12}R_{23}e^{4\beta}} \tag{B.44}$$

Analogously, the transmission can be derived:

$$T = T_{12}T_{23}e^{2\beta} + T_{12}T_{23}e^{2\beta}R_{23}R_{21}e^{4\beta} + ... \tag{B.45}$$

We obtain:

$$T = \frac{T_{12}T_{23}e^{2\beta}}{1 - R_{12}R_{23}e^{4\beta}} \tag{B.46}$$

B.3.2 Optical Cavity Resonator

The difference between coherent and incoherent transmission is illustrated using the example of an optical cavity resonator (see Fig. B.5). An optical cavity resonator consists of a resonant, transparent layer whose thickness is adjusted so that the electric field strength at the interfaces is maximized. If a

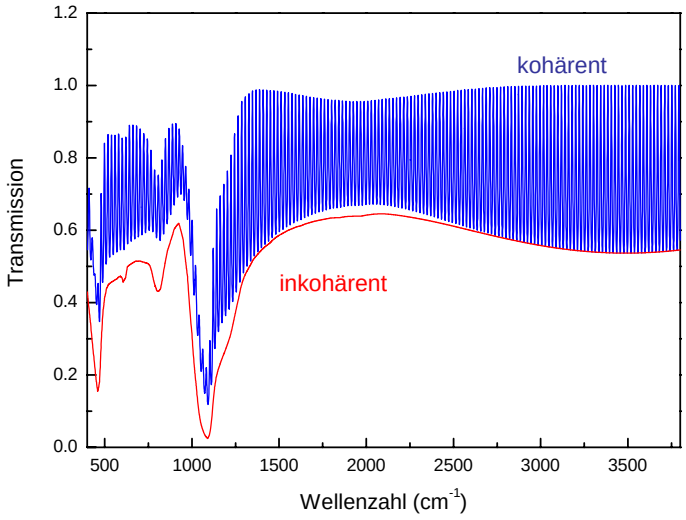

Figure B.5: Transmission of an oxidized Si wafer (oxide thickness 1000 nm). The transmission through the wafer itself was considered both coherently and incoherently.

thin film is then applied to this substrate, a small absorption in this film leads to a significant change in the reflectivity. A simple method to produce such a cavity resonator is the oxidation of a silicon wafer. The thick oxide layer then acts as a cavity resonator at a given wavelength. If we consider an infrared measurement, for example, the wavelength is in the μm range, which results in an oxide thickness in the μm range. The coherence length of a thermal light source, as used in infrared spectrometers, is in the range of a few μm to mm, depending on the desired wavenumber resolution. Thus, the case can occur where the reflection or transmission in the cavity resonator itself is coherent, but the transmission and reflection at the infrared-transparent silicon wafer below must be calculated incoherently.

The thin film on the cavity resonator and the cavity resonator itself are considered as a layer stack whose reflection and transmission capabilities are calculated coherently. This results in the following intensity factors: R_{film} for the reflection at the film surface; T_{top} and T_{film} is the transmission of the incident light from the environment into the silicon wafer; R_{top} is the reflection of the light from within the silicon wafer to the back of the cavity resonator; R_{bottom} is the reflection of the light from the silicon wafer at the back of the wafer.

For the transmission or reflection in the region of the wafer itself, we

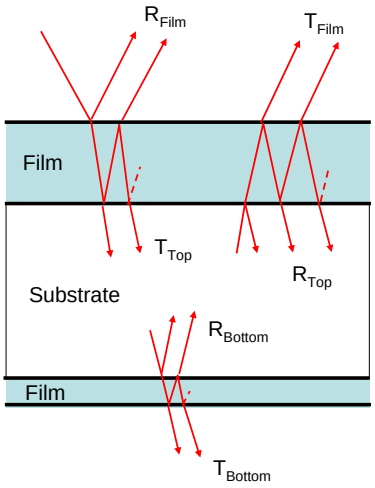

Figure B.6: Reflection on an optical cavity resonator.

consider the incoherent case. Here, the real part of the phase coefficient β is set to zero. Similar to the consideration of the reflection of a thin film, we again obtain a geometric series with the result:

$$R_{\text{total}} = R_{\text{film}} + \frac{T_{\text{top}} T_{\text{film}} R_{\text{bottom}} e^{-4\text{Im}\beta_{\text{substrate}}}}{1 - R_{\text{bottom}} R_{\text{top}} e^{-4\text{Im}\beta_{\text{substrate}}}} \tag{B.47}$$

The transmission results analogously:

$$T_{\text{total}} = \frac{T_{\text{top}} T_{\text{bottom}} e^{-2\text{Im}\beta_{\text{substrate}}}}{1 - R_{\text{bottom}} R_{\text{top}} e^{-4\text{Im}\beta_{\text{substrate}}}} \tag{B.48}$$

Appendix C

Mie Scattering

The scattering of light by particles of the size of the wavelength can no longer be described by the theory of thin films. For this, the Mie theory is required. The cross-section for the scattering of light by particles of size a is:

$$\sigma \sim \frac{a^6}{\lambda^4} \tag{C.1}$$

It can be seen that the scattered intensity for very small particles is usually very small. By analyzing the scattered light and the change in the polarization state, the size of the particles and their number can be derived.

C.1 Theory

The theoretical description of the scattering of a plane light wave by a sphere is outlined below.

C.1.1 Scattering by a Sphere

The solution of the Maxwell equations for the propagation of an electromagnetic wave can be expressed by the scalar wave equation:

$$\Delta\psi + k^2 m^2 \psi = 0 \tag{C.2}$$

For the scattering problem, we use polar coordinates of the form

$$\psi(r, \theta, \phi) = R(r)\Theta(\theta)\Phi(\phi) \tag{C.3}$$

The wave equation yields in polar coordinates for the new variables r, θ, and ϕ

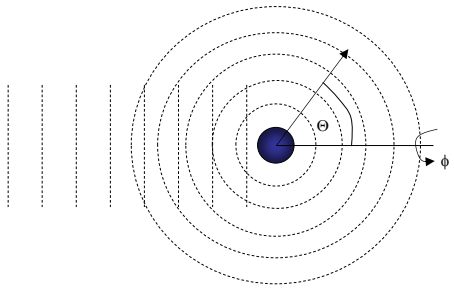

Figure C.1: Scattering of a plane wave by a homogeneous sphere.

$$\frac{d2\Phi}{d\phi 2} + m\Phi^2 = 0 \tag{C.4}$$

$$\frac{1}{\sin\theta} dd\theta \left(\sin\theta \frac{d\Theta}{\theta}\right) \left[n(n+1) - \frac{m^2}{\sin^2\theta}\right] = 0 \tag{C.5}$$

$$\frac{d}{dr}\left(r^2 \frac{dR}{dr}\right) + [k^2 r^2 - n(n+1)]R = 0 \tag{C.6}$$

The constants m and n must be determined by the boundary conditions. The solution of Eq. C.4 is of the form:

$$\Phi = \cos(m\phi) \qquad \Phi = \sin(m\phi) \tag{C.7}$$

The solution of Eq. C.5 are associated Legendre polynomials:

$$P_n^m \tag{C.8}$$

The solution of Eq. C.6 are spherical Bessel functions:

$$j_n(z) \tag{C.9}$$

The solution ψ can additionally be expanded into a vector field using $\mathbf{M}$

$$\mathbf{M} = \nabla \times (\mathbf{c}\psi) \tag{C.10}$$

With this vector field $\mathbf{M}$, another vector field $\mathbf{N}$ is constructed:

$$\mathbf{N} = \frac{\nabla \times \mathbf{M}}{k} \tag{C.11}$$

The electric and magnetic fields $\mathbf{E}$ and $\mathbf{H}$ are given by linear combinations of $\mathbf{M}$ and $\mathbf{N}$.

C.1.2 The Incident, Internal, and Scattered Wave

The scattering problem is solved by seeking a solution that superimposes the incident and scattered waves. All waves must be expressed in polar coordinates. The scattered wave is:

$$\psi_{\ln}(\Theta, \varphi, r) = \cos(l\varphi) P_n^l \cos(\Theta) z_n(mkr) \tag{C.12}$$

or

$$\psi_{\ln}(\Theta, \varphi, r) = \sin(l\varphi) P_n^l \cos(\Theta) z_n(mkr) \tag{C.13}$$

The incident wave is in polar coordinates with the solutions u and v:

$$u = e^{\imath\omega t} \cos\varphi \sum_{n=1}^{\infty} (-i)^n \frac{2n+1}{n(n+1)} P_n^1(\cos\Theta) j_n(kr) \tag{C.14}$$

$$v = e^{\imath\omega t} \sin\varphi \sum_{n=1}^{\infty} (-i)^n \frac{2n+1}{n(n+1)} P_n^1(\cos\Theta) j_n(kr) \tag{C.15}$$

The outgoing wave outside the sphere is in polar coordinates with the solutions u and v:

$$u = e^{\imath\omega t} \cos\varphi \sum_{n=1}^{\infty} -a_n (-i)^n \frac{2n+1}{n(n+1)} P_n^1(\cos\Theta) h_n^{(2)}(kr) \tag{C.16}$$

$$v = e^{\imath\omega t} \sin\varphi \sum_{n=1}^{\infty} -b_n (-i)^n \frac{2n+1}{n(n+1)} P_n^1(\cos\Theta) h_n^{(2)}(kr) \tag{C.17}$$

The outgoing wave inside the sphere is in polar coordinates with the solutions u and v:

$$u = e^{\imath\omega t} \cos\varphi \sum_{n=1}^{\infty} m c_n (-i)^n \frac{2n+1}{n(n+1)} P_n^1(\cos\Theta) j_n(mkr) \tag{C.18}$$

$$v = e^{\imath\omega t} \sin\varphi \sum_{n=1}^{\infty} m d_n (-i)^n \frac{2n+1}{n(n+1)} P_n^1(\cos\Theta) j_n(mkr) \tag{C.19}$$

The boundary conditions at the interface between the sphere and the surrounding medium are used to determine the coefficients a_n, b_n, c_n, d_n for $r = a/2$. For this, we use the substitutions:

$$x = ka = \frac{2\pi}{\lambda} \tag{C.20}$$

and

$$y = mka \tag{C.21}$$

We obtain the following conditions for the coefficients a_n and b_n for the outgoing wave:

$$a_n = \frac{\psi_n^{'}(y)\psi_n(x) - m\psi_n(y)\psi_n^{'}(x)}{\psi_n^{'}(y)\varsigma_n(x) - m\psi_n(y)\varsigma_n^{'}(x)} \tag{C.22}$$

and

$$b_n = \frac{m\psi_n^{'}(y)\psi_n(x) - \psi_n(y)\psi_n^{'}(x)}{m\psi_n^{'}(y)\varsigma_n(x) - \psi_n(y)\varsigma_n^{'}(x)} \tag{C.23}$$

The individual functions ψ_n are derived from spherical Bessel functions:

$$\psi n(z) = \sqrt{\frac{\pi}{2}z}J_{n+1/2}(z) \tag{C.24}$$

$$\varsigma n(z) = -\sqrt{\frac{\pi}{2}z}N_{n+1/2}(z) \tag{C.25}$$

The individual functions π_n are derived from associated Legendre polynomials:

$$\pi_n(\cos\Theta) = \frac{dP_n(\cos\Theta)}{d\cos\Theta} \tag{C.26}$$

$$\tau_n(\cos\Theta) = \cos\Theta\pi_n(\cos\Theta) - \sin\Theta\frac{d\pi_n(\cos\Theta)}{d\cos\Theta} \tag{C.27}$$

Finally, we obtain the ratio of the amplitudes parallel and perpendicular to the plane of incidence S_1 and S_2:

$$S_1(\Theta) = \sum_{n=1}^{\infty}\frac{2n+1}{n\,(n+1)}\left\{a_n\pi_n\left(\cos\Theta\right) + b_n\tau_n\left(\cos\Theta\right)\right\} \tag{C.28}$$

and

$$S_2(\Theta) = \sum_{n=1}^{\infty}\frac{2n+1}{n\,(n+1)}\left\{b_n\pi_n\left(\cos\Theta\right) + a_n\tau_n\left(\cos\Theta\right)\right\} \tag{C.29}$$

The individual terms in the sum correspond to dipole, quadrupole radiation, etc. The number of relevant terms increases with the size of the particles. An example of such a scattering calculation is shown in Fig. C.2.

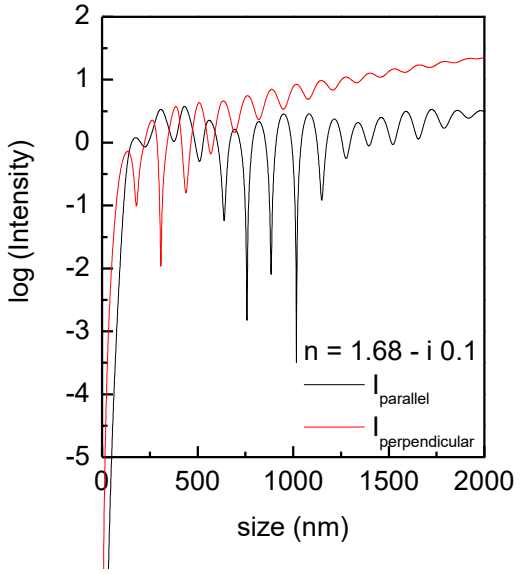

Figure C.2: Scattering intensities parallel and perpendicular to the plane of incidence for homogeneous spheres of varying size at a wavelength of 488 nm.

C.2 Mie Ellipsometry

The ellipsometric angles Ψ and Δ can be derived from the scattering amplitudes. The scattering process can be expressed as a Jones vector:

$$\begin{bmatrix} E_{p,OUT} \\ E_{s,OUT} \end{bmatrix} = \frac{e^{\imath kr}}{-\imath kr} \begin{bmatrix} S_2 & 0 \\ 0 & S_1 \end{bmatrix} \begin{bmatrix} E_{p,IN} \\ E_{s,IN} \end{bmatrix} \tag{C.30}$$

For non-spherical particles, off-diagonal elements appear in the scattering matrix S. With the ratio of the amplitudes from Eq. C.28 and C.29, the ellipsometric angles are obtained directly using:

$$\tan \Psi e^{i\Delta} = \frac{S_2}{S_1} \tag{C.31}$$

C.3 Influence of Particle Size Distribution

When scattering from an ensemble of particles of different sizes, the phases are randomized and intensities must be added instead of field amplitudes. In the coherent case, we had

$$I_p = \left| \sum_i^N S_{2,i} \right|^2 \tag{C.32}$$

In the incoherent case, this becomes:

$$I_p = \sum_i^N |S_{2,i}|^2 \tag{C.33}$$

In the case of a monodisperse particle distribution, the incoherent addition of the individual scattering events leads to a depolarization of the incident light. The signal in an ellipsometer with a rotating analyzer was:

$$I_i = I_{0,i} \left(1 + a_i \cos(2\omega t) + b_i \sin(2\omega t)\right) \tag{C.34}$$

The scattering by a particle i corresponds to a specific Fourier coefficient a_i and b_i. The summation over the intensities of different particles can therefore be expressed by corresponding weights f_i:

$$I = \sum_i^N f_i I_{0,i} \left(1 + a_i \cos(2\omega t) + b_i \sin(2\omega t)\right) \tag{C.35}$$

This can be separated into:

$$I = \sum_i^N I_{0,i} + \cos(2\omega t) \sum_i^N I_{0,i} a_i + \sin(2\omega t) \sum_i^N I_{0,i} b_i \tag{C.36}$$

The incident light has a constant intensity $I_0 = N I_{0,1}$. Thus, we obtain:

$$I = I_0 \left(1 + \cos(2\omega t) \sum_i^N a_i + \sin(2\omega t) \sum_i^N b_i \right) \tag{C.37}$$

or the effective Fourier coefficients:

$$a_{eff} = \frac{1}{N} \sum_{i=1}^N a_i \tag{C.38}$$

and

$$b_{eff} = \frac{1}{N} \sum_{i=1}^{N} b_i \tag{C.39}$$

This shows that the summation over the Fourier coefficients corresponds to a summation over intensities. In the case of monodisperse particles, this means that the phase shift between the perpendicular and parallel components is preserved even if the scattering occurs simultaneously by many particles.

Randomization of the phase only occurs if unequal particle sizes also result in a distribution of Fourier coefficients. These coefficients for a single particle i were:

$$a_i = \frac{\cos 2P - \cos 2\Psi_i}{1 - \cos 2\Psi_i \cos 2P} \tag{C.40}$$

and

$$b_i = \frac{\sin 2P \sin 2\Psi \cos \Delta_i}{1 - \cos 2\Psi_i \cos 2P} \tag{C.41}$$

The ellipsometric angles Ψ_i and Δ_i are derived from Eq. C.31 for given particle sizes. A size distribution can be taken into account by summing the Fourier coefficients for different sizes with corresponding weights.

$$a_{eff} = \frac{1}{N} \sum_{i=1}^{N} f_i a_i(d) \tag{C.42}$$

with a distribution f_i. For the distribution, a log-normal distribution is often used, as it arises from agglomeration in aerosols. With an average size d_m and a geometric standard deviation σ, we obtain:

$$f(d) = \frac{1}{\sqrt{2\pi} \ln(\sigma)\, d} \exp\left\{ -\frac{[\ln d - \ln d_m]^2}{2 [\ln \sigma]^2} \right\} \tag{C.43}$$

For a simple Gaussian size distribution, we set:

$$f(d) = \frac{1}{2\sigma} \exp\left\{ -\frac{(d - d_m)^2}{2\sigma^2} \right\} \tag{C.44}$$

The experimental determination of the size distribution is carried out by varying an external parameter during the measurement. In the case of a kinetic measurement, this is the growth of the particles. The trajectory in

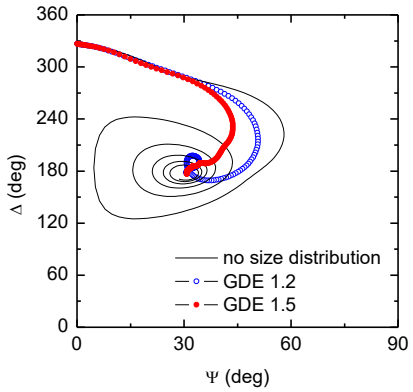

Figure C.3: Ellipsometry data for scattering by a particle ensemble with a size distribution corresponding to a geometric standard deviation of 1.2 and 1.5.

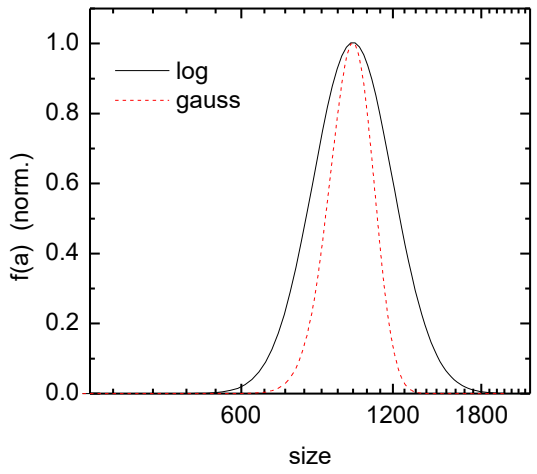

Figure C.4: Comparison between a Gaussian and a log-normal distribution.

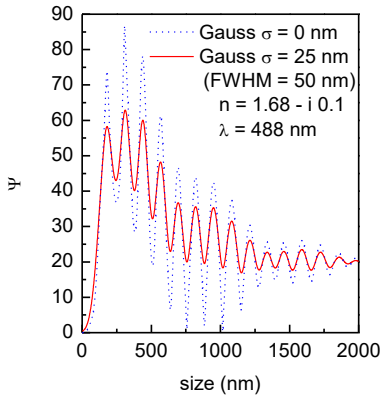

Figure C.5: Averaging by a particle size distribution according to a Gaussian distribution.

the Ψ,Δ-plane contains the information about the size distribution. Alternatively, another external parameter such as the scattering angle, the light wavelength, or the polarizer angle can be varied. As an example, a polarizer variation for a particle distribution with a Gaussian distribution is shown in Fig. C.6.

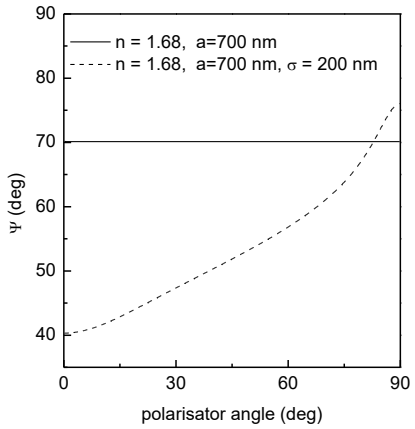

Figure C.6: Variation of the angle Ψ with the variation of the polarizer angle for a monodisperse and a Gaussian distribution with a full width at half maximum of 50 nm.

Appendix D

Data Analysis Using Bayesian Probability Theory

When quantitatively evaluating data obtained from plasmas, the number of unknowns is often large, or the characteristics of a plasma are only known approximately. To evaluate the obtained data, "expert knowledge" is often used to exclude ambiguities. This procedure has a significant disadvantage: Through the implicit reference to expert knowledge, a biased evaluation of the data takes place. If this expert knowledge is based on incorrect boundary conditions, information that could be contained in the data is neglected from the outset. In contrast, Bayesian probability theory enables a bias-free evaluation of data with explicit assessment of any prior knowledge.

D.1 Bayes's Theorem

In Bayesian theory, probabilities are calculated for certain events. This is to be distinguished from the statistical approach, where a probability is only assigned to an event after a large number of trials (frequency approach). However, in many experiments, it is not possible to perform an arbitrary number of trials, and therefore, it is necessary to calculate a probability even for a small number of trials.

The probability of an event A given certain information I is denoted as:

$$p(A|I) \tag{D.1}$$

For these probabilities, the sum rule applies:

$$p(A|I) + p(\bar{A}|I) = 1 \tag{D.2}$$

$\bar{A}$ denotes an event in which hypothesis A does not occur. The product rule is:

$$\begin{aligned} p(A,B|I) &= p(A|B,I)p(B|I) && \text{(D.3)} \\ &= p(B|A,I)p(A|I) && \text{(D.4)} \end{aligned}$$

The product rule can be transformed into the **Bayes's Theorem**:

$$\boxed{p(A|B,I) = \frac{1}{p(B|I)} p(B|A,I)p(A|I)} \qquad \text{(D.5)}$$

The meaning of the Bayesian formula can be described intuitively. Consider a dataset that is to be described by a certain model. In the notation of Bayes's theorem, this means:

$$p(\text{Model}|\text{Data},I) = \frac{1}{p(\text{Data}|I)} p(\text{Data}|\text{Model},I)p(\text{Model}|I) \qquad \text{(D.6)}$$

The left side corresponds to the probability of a certain model given the data. This is usually the quantity to be determined. The first term on the right side corresponds to the normalization; the second term corresponds to the probability of the data given the model. This term corresponds to the forward calculation, which is equivalent to the *least-squares* expression χ^2. The last term is the so-called prior, the probability of the model itself.

The art of Bayesian statistics essentially consists in the unbiased evaluation of the model through the priors. In short, priors are sought that formalize the maximum ignorance about the input parameters of a model. This will be illustrated below.

D.2 Priors

If, for example, we consider a distribution function that is to reflect a dataset, we can demand of the principal form of the distribution function that it is maximally *uninformative*. That is, without the presence of a dataset, this distribution function should contain no information.

To characterize the information content of a distribution function, we first consider the discrete form of a distribution function for N particles:

$$f_i = \frac{n_i}{N} \qquad \text{(D.7)}$$

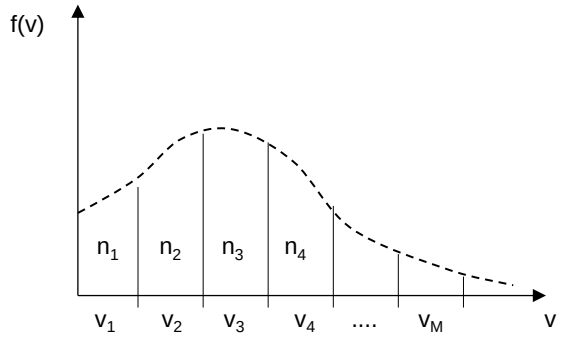

Figure D.1: Discrete distribution function.

The number of ways to distribute these N particles into M bins is:

$$\frac{N!}{n_1!n_2!...n_M!} \tag{D.8}$$

The total number of possibilities is:

$$M^N \tag{D.9}$$

Thus, the probability p of having a certain distribution function is:

$$p = \frac{N!}{n_1!n_2!...n_M!} M^{-N} \tag{D.10}$$

We take the logarithm of this probability:

$$\ln p = -N \ln M + \ln N! - \sum_i^M \ln n_i! \tag{D.11}$$

Using the Stirling formula $\ln n! = n \ln n - n$, we obtain:

$$\ln p = -N \ln M - N \sum_i^M f_i \ln f_i \tag{D.12}$$

The probability is maximized if the term

$$\boxed{S = -N \sum_i^M f_i \ln f_i} \tag{D.13}$$

is maximized. This is referred to as the **Entropy of the Distribution Function**. In the following, we want to derive typical priors in which the distribution function has maximum entropy.

Prior for the Knowledge that the Parameter is Positive

The simplest prior can be generated if we only assume that the value should be positive and should lie within a certain interval. If this interval for the quantity x is determined as the range $0 < x < a$, then the prior for this situation is:

$$\boxed{p(x) = \frac{1}{a}} \tag{D.14}$$

Prior for Known Averages

Assume that in a model, the average μ of a quantity x is known as prior information. The distribution function f_i gives the probability according to:

$$\mu = \int xp(x)dx = \sum_i xf_i \tag{D.15}$$

The entropy of the distribution function f is maximized under this constraint. With the Lagrangian:

$$\pounds = -\sum_i^M f_i \ln f_i + \lambda_0 \left[\mu - \sum_i f_i x\right] \tag{D.16}$$

As a solution, we obtain:

$$\boxed{p(x|\mu, I) = \frac{1}{\mu} \exp\left(-\frac{x}{\mu}\right)} \tag{D.17}$$

That is, a value for x smaller than μ is measured much more frequently than a large value, as one can easily visualize: in many events that belong to a certain average, there are more permutations if small values occur more frequently.

Prior for Known Averages Plus Error

Now we seek the maximum of this entropy under the constraint that the first and second moments of the distribution function are constant:

$$\sum f_i v_i = \mu \tag{D.18}$$

$$\sum f_i \left(v_i - \mu\right)^2 = \sigma^2 \tag{D.19}$$

The Lagrangian is formed according to:

$$L = -\sum_i^M f_i \ln f_i + \lambda_0 \left[\mu - \sum f_i v_i\right] \lambda_0 \left[\sigma^2 - \sum f_i \left(v_i - \mu\right)^2\right] \tag{D.20}$$

With the condition

$$\frac{\partial L}{\partial f_i} = 0 \tag{D.21}$$

we obtain as a solution:

$$\boxed{f_i = \frac{1}{\sigma\sqrt{2\pi}} e^{-\frac{(v_i-\mu)2}{2\sigma 2}}} \tag{D.22}$$

We obtain the **Gaussian distribution**. This also corresponds to a derivation of the Maxwellian velocity distribution. This form of the distribution function arises when many elastic collisions occur, and the system is in equilibrium. The constancy of the first and second moments is thus equivalent to a condition for the conservation of momentum and energy.

Appendix E

Question Catalog

E.1 Chapter 1: Introduction

- Plasma processes
- Difference between low-pressure plasmas and thermal plasmas
- Why are rf-plasmas used for coating insulating substrates?
- How does a coating magnetron work?

E.2 Chapter 2: Ion Fluxes on Surfaces

- Explain the cause of the formation of a boundary layer in a simple way?
- How does the so-called self-bias occur?
- Which approach is used to calculate the potential profile in a plasma boundary layer?
- What is the Bohm criterion?
- Which boundary condition applies in the boundary layer or the pre-layer?
- How are ion energy distributions measured?
- What does an ion energy distribution in an rf-plasma typically look like? What influence do collisions in the boundary layer have?

E.3 Chapter 3: Neutral Particle Fluxes on Surfaces

- Which equation is used to calculate the concentration profile of neutral species in a discharge? What does the density profile look like in a planar arrangement? How does the density profile change under the assumption that the neutrals are partially reflected at the wall?
- Under what conditions does a Maxwell distribution occur?
- What is referred to as ambipolar diffusion?
- What is the surface loss probability and how is it measured?

E.4 Chapter 4: Basics of Surface Physics

- How is the surface coverage defined?
- What is the surface energy and how can it be determined?
- What condition must the surface energies satisfy for a system to show island or layer growth?
- What is an electronic surface state and why is it localized?
- How is the range of electrons in a solid as a function of energy?
- How does photoelectron spectroscopy and Auger spectroscopy work?

E.5 Chapter 5: Interaction of Neutrals with Surfaces

- What is the difference between physisorption and chemisorption?
- What is the relationship between the overlap of the wave function and the strength of the chemical bond?
- What is the work function and how can it be changed by an adsorbate?
- What is the sticking coefficient and how does it change with the temperature of the surface and the velocity of the incident particle?
- What is referred to as Langmuir adsorption?

- How does the dependence of the sticking coefficient on coverage change under the assumption of Langmuir adsorption or surface diffusion?
- What does the potential energy diagram look like for an incident particle in front of a surface? What is thermally activated chemisorption? What does this diagram look like in higher dimensions using the example of the H2 molecule?
- What is vibrationally assisted sticking?
- What is the difference between the Eley-Rideal and the Langmuir-Hinshelwood mechanism?

E.6 Chapter 6: Interaction of Ions with Surfaces

- Which approach is used to calculate the screening of an atom in a solid?
- What is the kinematic factor? What is the maximum energy transferred in the collision?
- What is the differential cross-section?
- How does the differential Rutherford cross-section scale with energy and scattering angle? What does this mean for the range of ions in a solid?
- What types of energy loss are there and how do they scale with the energy of the incident ion?
- How does the sputtering yield depend on the energy of the incident ion? What is the angular distribution and energy distribution of the sputtered particles?
- What is the surface binding energy?

E.7 Chapter 7: Applications

- What methods are there to produce a-Si:H films? What are these films used for? What are the current problems in understanding the film growth?

- What methods are there to produce a-C:H films? What are these films used for? What are the characteristic properties depending on the preparation conditions?
- How is the residence time calculated as a characteristic quantity in material turnover in reactive plasmas?
- How does the etching of silicon wafers in CF plasmas work?
- How is the anisotropy and selectivity ensured in the etching process?

Index